Tasting Flavoured Dark Matter

A Study of Simplified Flavoured Dark Matter Models

Zur Erlangung des akademischen Grades eines

Doktors der Naturwissenschaften (Dr. rer. nat.)

von der KIT-Fakultät für Physik
des Karlsruher Instituts für Technologie (KIT)
genehmigte

Dissertation

von

M.Sc. Harun Acaroğlu

Tag der mündlichen Prüfung: 10. Februar 2023

Referentin: Prof. Dr. Margarete Mühlleitner
Korreferent: Prof. Dr. Felix Kahlhöfer
Betreuende Wissenschaftlerin: Dr. Monika Blanke

Abstract

In this thesis we study three simplified flavoured dark matter models with t-channel mediated interactions between the dark sector and the Standard Model. In the first model a Majorana fermionic dark matter triplet is coupled to right-handed up-type quarks of the Standard Model, allowing this model to connect the dark matter problem with large effects in CP violating charm decays. In the second model the dark particles are assumed to be complex scalars which couple to right-handed charged leptons of the Standard Model, yielding a rich phenomenology that allows for large couplings of dark matter to leptons. Finally, an extended version of the lepton-flavoured dark matter model with additional couplings of the dark species to left-handed leptons is studied. The additional coupling of the two fields that mediate the interactions of dark matter with left- and right-handed leptons to the Higgs doublet allows this model to constitute a joint solution for the DM problem and the muon $(g-2)$ anomaly.

Levha-i Tabîat

“Tezyîn ediyor cihânı kudret,
Yâ Rabb! Bu ne cilve-i meşiyyet?

Kim verdi bu revnakı bahâra,
Döndürdü yeri tecellîzâra.

Tevlîd ediyor meşîme-i hâk,
Binlerce şukûfe-i tarabnâk.

Baktıkça zemîn-i dil-nişîne,
Benzer küre-i zümrüde yine.

Elmas-ı ferahfezâya benzer,
Her jale-i berg-i renkperver.

Yâ Rabb! Beni sâhib-i intibâh et!
Bir şâir-i âteşîn-nigâh et!

Ettikçe nazar şu kâinâta,
Mazhar olayım tecelliyâta!“

Erzurumlu Ömer Nasûhî Efendi rh.

Teşekkürât

Mübesmilen, muhamdilen ve musalvilen evvela ebeveynim Türkan ve Recep Acaroğlu'na üzerimdeki nihayetsiz emekleri sebebiyle en samimi ve en kalbî şükranlarımı arz ederim. Hicret ve gurbet hayatı yaşamanıza rağmen biz cocuklarınıza sağladığınız imkanlar bir yana, bizleri sevgi, muhabbet ve şefkatle yetiştirdiğiniz ve her ne olursa olsun bizlere daima evleviyet verdiğiniz için cenâb-ı mevlâ hazretleri sizlerden razı ve memnun olsun, her ikinize de saadet-i dareyn nasip eylesin. Abim Orkun Acaroğlu'na, bana hem okul vetiresinde hem de üniversite hayatı itibariyle öncülük edip daima iyi bir örnek olması hasebiyle müteşekkir olduğum gibi, kardeşim Turgut Acaroğlu'na da kücüklük yıllarımızdan bi'l-itibar dostluğunu ve hürmetini benden esirgememesi sebebiyle minnettarım.

Üniversite hayatımın ilk safhasını oluşturan lisans ve yüksek lisans vetirelerinde beni daima destekleyen büyüklerim, ki ezcümle Hüseyin Armutçu, Salih Armutçu, Mehmet Arslan, Bayram Aslan, Muzaffer Beygirci, Sevban Böğürcü, Faruk Gügen, Aydemir Kaplangiray, Serhat Pehlivan, Ahmet Cemil Tural, Ramazan Yılmaz'a ve bilhassa Mustafa ve Muhammed Gerçek dostlarıma, yani kısacası bütün *Aachis* topluluğuna da aynı şekilde müteşekkirim. Uhrevî ilimler nokta-i nazarından bana muallimlik etmiş olan Hüseyin Armutçu, Ömer Tüzün, Kemal Acar, Burak Şahin ve elan beni okutan Şevket Açıkgöz hocalarımla birlikte, her konuda bana örnek olmakla beraber bu yola koyulmama vesile olan Ali Kemal Alkan hocama dahî en kalbî teşekkürlerimi arz ederim. Nezdimde ayrı bir değere sahip olan Karlsruhe'deki talebelerimden de cenâb-ı hak hazretleri, bana karşı gösterdikleri sadakat, hürmet ve itibarlarından nâşî razı olsun. Sabilik yıllarımdan bu yana bana tam manasıyla dostluk etmiş olan Zafer Yılmaz ve Ahmet Enes Özcan kardeşlerime dahî desteklerini asla esirgemedikleri için minnettarım.

Son olarak refîka-i hayatım Gülhanım Acaroğlu'na, nihayetsiz destekleri ve bilâ kayd ü şart benim için katlandığı meşakkatler için, bu tezin içerdiği harfler adedince şükranlarımı arz ederim. Mevlâ-yı zü'l-celâl hazretleri senden razı olsun.

Acknowledgements

First of all I would like to thank my supervisors Monika Blanke and Margarete Milada Mühlleitner for accepting me as a PhD student at the KIT. I'd like to thank Monika for the excellent supervision during the last three years. I appreciate that you always took your time to help me with fruitful discussions and advises whenever necessary, even when being contacted on a short notice. Further, I'd like to thank you both for also supporting me outside of physics by allowing me to simultaneously pursue a second PhD degree but also by always supporting me whenever I applied for a scholarship or similar. I would like to also thank Felix Kahlhöfer for offering me to be the second supervisor of my dissertation.

I am particular grateful to Prateek Agrawal who hosted me as an academic visitor at the University of Oxford for half a year. I really enjoyed being part of your working group and profited a lot from the many fruitful discussions we had. I am especially thankful to you for continuing our collaboration even after I returned to Germany. From my colleagues in Oxford I would like to thank Michele Fava for being the friendliest office mate and having plenty interesting discussions and conversations with me.

I would like to thank Monika and my former office mate Mustafa Tabet—whom all scatter plots in the thesis are dedicated to—for proofreading my thesis and providing many useful comments. I want to also thank Mustafa for helping me with any Mathematica related problems and giving me plenty of general advises that I typically ignored initially just to re-encounter the things he warned me about at later times.

I am thankful to Martin Lang, Lucas Kunz, Mustafa Tabet, Fabian Lange, Robert Ziegler and Manuel Egner for enduring my endless desire to talk within the last three years. Although I am convinced that Uli Nierste can truly compete with me in this regard, you have to admit that what I had to say was at least entertaining or polarising enough to keep you in mood. In general, I am very thankful to all the TTP members for the wonderful atmosphere at the institute.

I want to also acknowledge the hard work and excellent administrative support of Martina Schorn, Regina Hühn, Barbara Lepold and Michelle Jose from Oxford.

Finally, I am grateful for the financial and educational support I received from the Avicenna-Studienwerk e.V. as well as the Karlsruhe School of Elementary Particle and Astroparticle Physics (KSETA) during my PhD programme. Further, I am thankful to the Karlsruhe House of Young Scientists (KHYS) for financially supporting my academic visit at the University of Oxford through the Research Travel Grant programme.

Contents

List of Figures

List of Tables

Acronyms

CERN	European Organization for Nuclear Research
CKM	Cabibbo–Kobayashi–Maskawa
CMB	Cosmic Microwave Background
DM	Dark Matter
EDM	Electric Dipole Moment
EW	Electroweak
FCNC	Flavour Changing Neutral Current
FNAL	Fermi National Accelerator Laboratory
HFLAV	Heavy Flavour Averaging Group
KEK	High Energy Accelerator Research Organisation
ΛCDM	Lambda Cold Dark Matter
LEP	Large Electron Positron Collider
LFV	Lepton Flavour Violating
LHC	Large Hadron Collider
LO	Leading Order
MDM	Magnetic Dipole Moment
MFV	Minimal Flavour Violation
mDM	Millicharged Dark Matter
MSSM	Minimal Supersymmetric Standard Model
NFW	Navarro-Frenk-White
NLO	Next-to-Leading Order
NP	New Physics
PDF	Parton Distribution Function
QCD	Quantum Chromodynamics
QDF	Quasi-Degenerate Freeze-Out
RG	Renormalisation Group

SD	Spin-Dependent
SFF	Single Flavour Freeze-Out
SI	Spin-Independent
SM	Standard Model
SUSY	Supersymmetry
UV	Ultraviolet
VEV	Vacuum Expectation Value
WIMP	Weakly Interacting Massive Particle

Chapter 1
Introduction

Over the last decades the observation of a whole set of phenomena that indicate the existence of an undetected form of matter which seems to have no interactions with light has been particularly interesting yet at the same time challenging for particle physicists and cosmologists working at the *new physics* (NP) frontier. This new type of matter is referred to as *dark matter* (DM) and is currently being regarded as the most convincing hint at NP. The reason is that the *Standard Model* (SM) of particle physics, which without a doubt constitutes the so far most remarkable success of quantum field theory in general, lacks a coherent and convincing explanation for DM and thereby motivates searches for NP beyond the SM.

While the evidence for its existence is overwhelming [1, 2], the particle physics properties of DM still remain obscure. This leaves theorists with numerous opportunities in terms of model building and hence, mapping this vast theory space to experimental data constitutes a major challenge. Adopting a systematic approach by examining simplified models and categorising signals and phenomenological features of large classes of models can thus be very beneficial in taking on this challenge. Moreover, identifying classes which are at the same time capable of addressing other problems, puzzles or anomalies of physics can provide further motivation for the respective models and render them particularly appealing.

One such class of models is represented by the flavoured DM framework [3–12], which proposes that the DM field comes in multiple generations and is often associated with an according flavour symmetry. These models are motivated by the paradigm of a weakly-coupled DM particle with weak-scale mass, i.e. the paradigm of a *weakly interacting massive particle* (WIMP), in combination with the non-observation of DM in detection and collider experiments. The additional dark species allow for a much more dynamic thermal production of DM in the early Universe, such that the correct DM relic density can be obtained while at the same time satisfying stringent constraints from detection and collider experiments, ultimately reconciling the absence of signal in respective experiments with the WIMP paradigm [13]. On more general grounds, the existence of flavour constitutes a central aspect of the SM and hence assuming DM to also carry flavour quantum numbers can be regarded as an intuitive assumption. However, flavoured DM models are subject to stringent constraints from flavour observables implying a non-generic flavour structure of interactions between DM and the SM at the weak scale. Thus, early analyses of these models were limited to the paradigm of *minimal flavour violation* (MFV) [14–19], which assumes that the only sources of flavour violation are the SM Yukawa couplings. A consequence of this premise is that the coupling matrix of DM to SM matter has to be expressed in terms of the latter, which in turn yields a highly restricted flavour structure.

A more general framework for the systematic study of flavoured DM models is the so-called *dark minimal flavour violation* (DMFV) framework, which was introduced in Reference [20] and allows for a non-trivial flavour structure of the interactions between DM and the SM by assuming them to constitute a new source of flavour violation in addition

to the SM Yukawa couplings. In this sense the DMFV framework goes beyond the scope of MFV and hence it generally gives rise to a very rich phenomenology which—depending on the actual DMFV model—is potentially able to fit other anomalies as well. Still, even within the DMFV framework our ignorance about fundamental properties of DM leaves us with many options in terms of model building. Apart from the choice of the particle nature of DM and its corresponding mediator particle, one is also left with a large variety of options in terms of the SM fields that DM interacts with. Here, the DMFV framework allows for couplings to all fermion types of the SM. The cases of DM being a Dirac fermion coupling to the various SM quark fields have already been studied intensively [20–23], and its coupling to the right-handed charged leptons has been investigated in Reference [24].

In this thesis we study a total of three simplified flavoured DM models. The first two models belong to the DMFV class and consider either up-type flavoured Majorana DM or lepton-flavoured complex scalar DM, respectively, both with purely right-handed interactions between DM and the SM. In the former model, the Majorana nature of DM allows this model to simultaneously address large effects in CP violating charm decays, as measured by the LHCb collaboration [25], while DM with lepton portal interactions generally features less stringent constraints from direct detection since leading contributions to the DM–nucleon scattering rate arise at the one-loop level. The last model does not belong to the DMFV class, as it constitutes an extension of the lepton-flavoured DM model, where DM is assumed to additionally couple to left-handed leptons. However, similar to DMFV models it assumes all new flavour-violating interactions to be related to a single new coupling matrix. Further, in this model the fields that mediate the interactions of DM with left- and right-handed leptons are Yukawa-coupled to the SM Higgs doublet. Hence, this model allows for a connection of the DM problem with the $(g-2)_\mu$ anomaly [26, 27], ultimately rendering it particularly appealing.

This thesis is organised as follows: in Part I we introduce the reader to the DM problem. We discuss evidence for its existence and provide an overview of the current experimental status in Chapter 2. We review the WIMP paradigm and the thermal freeze-out of DM in the early Universe. In Chapter 3 we discuss the DMFV framework and its formal definition and further identify two scenarios for the freeze-out of flavoured DM. Part II is dedicated to the analysis of the up-type flavoured Majorana DM model. We discuss the model details in Chapter 4 and then continue with a phenomenological analysis in Chapter 5. We first examine constraints from collider searches, neutral D meson mixing, the observed DM relic density and direct detection experiments individually and then perform a combined analysis. Further, we check if this model is capable of generating sizeable NP contributions to the direct CP asymmetry in charm decays. We conclude our analysis of this model in Chapter 6. The lepton-flavoured complex scalar DM model with purely right-handed couplings to the SM is the subject of Part III. Again, we first present the model details in Chapter 7 and study its phenomenology in Chapter 8 by discussing constraints from collider searches, *lepton flavour violating* (LFV) decays, the observed DM relic density and direct as well as indirect DM detection experiments. The summary of our results regarding this model is given in Chapter 9. Finally, we present a joint solution for the DM problem and the muon $(g-2)$ anomaly in Part IV. The details of this model are presented in Chapter 10 and we examine experimental constraints to study its phenomenology in Chapter 11. In this case relevant limits come from collider searches, LFV decays, precision tests of the SM, the observed DM relic density and DM detection experiments. After analysing all constraints individually, we perform a combined analysis and examine if this model can accommodate the experimental central value of $(g-2)_\mu$ within its viable parameter space. We provide a summary of our findings from this part in Chapter 12. The thesis is then concluded in Chapter 13, where we return to the global

picture by identifying and summarising the most important results.

Part I

Overview

This part serves as an overview of the DM problem and the DMFV framework—a model building framework we use in this analysis in order to address the former problem. We first provide a short summary of evidence and searches for DM and then continue by discussing the formal definition of the DMFV class of DM models. We also review the paradigm of the thermal freeze-out of DM here with a particular emphasis on flavoured DM.

Chapter 2
The Dark Matter Problem

In this chapter we briefly introduce the DM problem by presenting important evidence that points towards the existence of DM and by further reviewing how it is searched for today. The reader is also introduced to the WIMP paradigm and we provide a short discussion of the thermal freeze-out of DM.

2.1 Evidence and Searches for Dark Matter

The existence of DM is backed up by many observations [28]. Historically, the circular velocity profile of galaxies has been particularly important and constitutes convincing evidence that led to the discovery of the existence of DM [29]. Such a profile is also referred to as a galaxy's rotation curve and is based on measurements of the circular velocities of stars and gas within the respective galaxy as a function of their distance from its centre. Classically, i.e. according to Newtonian dynamics, this velocity depends on the overall mass M_r enclosed within the distance r at which a star or gas rotates around the galactic centre as well as r itself and generally reads

$$v_c = \sqrt{\frac{GM_r}{r}}\,. \tag{2.1}$$

Here, G is the gravitational constant and the enclosed mass M_r is defined as

$$M_r = \int_0^r 4\pi\tilde{r}^2\rho(\tilde{r})\,d\tilde{r}\,, \tag{2.2}$$

where $\rho(r)$ is the mass density profile of the galaxy. The rotation curves of several galaxies have been measured particularly in the 1970s [30–40] and these observations have shown that at large distances r where the galaxy dependent mass distribution of luminous matter approaches zero, the circular velocity does not behave as $v_c \propto r^{-1/2}$ but flattens out and takes a roughly constant, non-zero value. This led to the conclusion that there needs to be a significant amount of non-luminous and therefore dark type of matter that surrounds the luminous components of a galaxy in order to yield the correct circular velocities at large distances r. This surrounding dark component is referred to as a galaxy's DM halo and its corresponding mass density ρ_{DM} can be modelled in several ways. In Figure 2.1a, for example, we show the rotation curve of the galaxy NGC 3198 obtained in Reference [41] where the *Navarro-Frenk-White* (NFW) profile [42]

$$\rho_{\mathrm{NFW}}(r) = \frac{\rho_s r_s^3}{r\,(r_s + r)^2}\,, \tag{2.3}$$

was used to model the DM density together with its experimental measurement from Reference [43]. In this expression, r_s and ρ_s are galaxy dependent characteristic parameters. In Figure 2.1a the dashed and dot-dashed lines show the resulting velocity profile if only

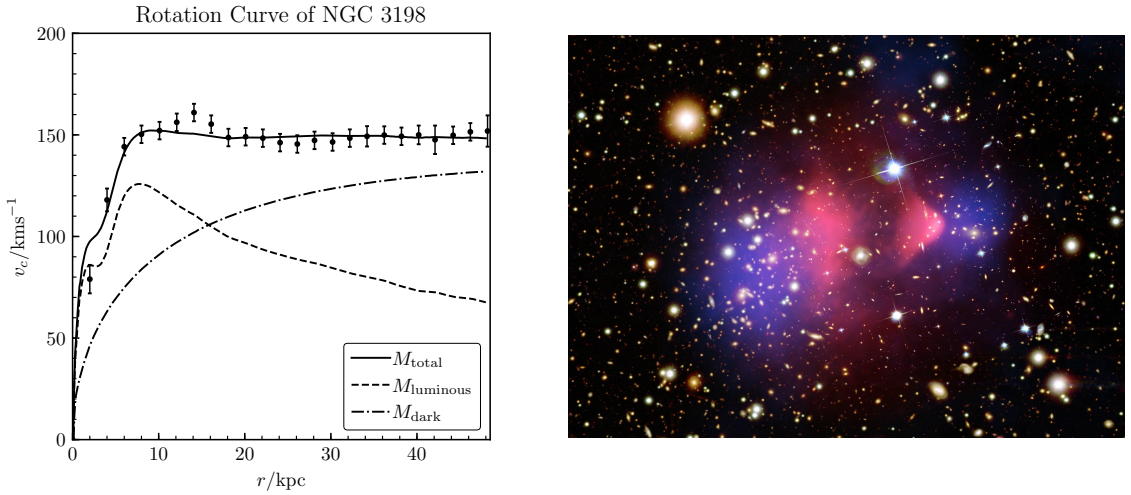

(a) Rotation Curve of NGC 3198 **(b)** Composite Image of the Bullet Cluster

Figure 2.1 | Evidence for the existence of DM. The left panel shows the rotation curve of the galaxy NGC 3198 as measured by Reference [43] and modelled by Reference [41]. The right panel shows a composite image of the bullet cluster based on X-ray [44] and weak gravitational lensing [45] measurements.

luminous matter or dark matter, respectively, is considered and the solid line shows the velocity profile if all components are taken into account. As one can see, the luminous matter content alone, which consists of stars as well as gas and can generally be detected using optical and radio telescopes, yields circular velocities that exhibit a qualitative and quantitative discrepancy with respect to the experimental data. While the peak of the circular velocity at $r \simeq 8.5\,\text{kpc}$ yields a too small value, the overall behaviour of v_c at large r also deviates significantly from data. The velocities calculated from luminous matter decrease with increasing distances from the galactic centre while the experimental measurement yields a roughly constant value for $r \gtrsim 8.5\,\text{kpc}$. This discrepancy explicitly demonstrates the necessity of additional mass in the galaxy and particularly in its outer parts, in order to yield a flat rotation curve as indicated by the data. Assuming a halo of dark, i.e. electromagnetically neutral and therefore spectroscopically non-detectable particles that surround the luminous matter of the galaxy yields a rotation curve that fits the experimental data accurately. This is illustrated by the black solid line in Figure 2.1a.

Moving from galaxies to the largest gravitationally bound structures of the Universe, we find that galaxy clusters provide additional evidence for the existence of DM. Historically, the application of the virial theorem to the Coma cluster in order to determine its mass-to-luminosity ratio [46] yielded one of the earliest hints at the existence of DM. Within this approach, stars are estimated to only account for less then two percent of the Coma clusters total mass, while hot intracluster gas accounts for roughly ten percent [47] hinting at the existence of additional, non-baryonic mass within the cluster. Further evidence stems from the X-ray spectrum of the hot intracluster gas, which consists of bremsstrahlung emitted by accelerated charged elementary and composite particles as well as line emissions which stem from ionised heavy elements such as iron. By fitting this spectrum through appropriate models one can calculate a relation between the cluster's temperature and total mass. In case of the Coma cluster for example, the former is measured to yield a mean value of roughly $T \approx 9\,\text{keV}$ over the entire cluster which corresponds to a total mass compatible

with the estimate based on the virial theorem [1, 47]. One particularly interesting and prominent observation within the context of galaxy clusters is related to the so-called bullet cluster, which consists of two colliding sub-clusters shown in Figure 2.1b. In this composite image of the bullet cluster, the magenta regions indicate the distribution of hot X-ray emitting intracluster gas based on respective measurements performed by the Chandra observatory [44]. The blue regions indicate the distribution of both baryonic and non-baryonic matter obtained through the weak gravitational lensing of background galaxies [45]. Thus, the latter represents a reconstruction of the bullet cluster's total gravitational potential based on its total mass, while the former only shows the potential caused by baryonic matter, as the baryon number of clusters is mainly dominated by hot gas. In Figure 2.1b it can be seen that the two reconstruction approaches yield different gravitational centres, which allows us to deduce that the bullet cluster contains a significant amount of DM.

At even larger scales, the *cosmic microwave background* (CMB) anisotropies as well as their angular power spectrum provide further striking evidence for the existence of non-baryonic DM [48, 49] and allow the Universe's matter and energy density to be measured. Currently, the most precise measurement was made by the Planck space observatory and it found the baryon and DM densities to be [2]

$$\Omega_{\mathrm{b}} h^2 = 0.0224 \pm 0.0001\,, \tag{2.4}$$

$$\Omega_{\mathrm{DM}} h^2 = 0.1200 \pm 0.0010\,, \tag{2.5}$$

where $h = 0.674$ is the scaling factor for the Hubble expansion rate.

It is due to this overwhelming amount of evidence for its existence that throughout the last decades physicists have grown a particular interest in the detection of DM. To gain insights on its particle physics properties, this unknown type of matter that accounts for roughly 85% of the Universe's matter budget, has been searched for in several experiments. Generally, these experiments can be categorised with respect to the type of signal they aim to detect and their underlying conceptual particle physics processes are gathered in Figure 2.2.

One such class of experiments are colliders that try to detect signals from the direct production of DM particles through the collision of SM matter. In Figure 2.2 this process corresponds to the case where time flows from left to right. Since DM has to be electrically neutral[1] and may only interact weakly with the SM, collider experiments cannot produce a direct signal, but rather search for DM in the missing transverse energy ($\not{E}_T$) spectrum. Important experiments in this category are the CDF [52, 53] and D0 [54, 55] experiments at the *Fermi National Accelerator Laboratory*'s (FNAL) Tevatron collider, the Belle II [56] experiment of the *High Energy Accelerator Research Organisation*'s (KEK) SuperKEKB collider, the ALEPH [57], DELPHI [58], L3 [59] and OPAL [60] experiments at the *European Organization for Nuclear Research*'s (CERN) *Large Electron Positron Collider* (LEP) as well as the ATLAS [61], CMS [62] and LHCb [63] experiments at its *Large Hadron Collider* (LHC). The LHC is a proton-proton collider with a centre-of-mass energy of $\sqrt{s} = 13.6\,\mathrm{TeV}$ that currently constitutes the largest operating particle collider in the world and is thus particularly important within the context of DM searches.

Experiments that search for DM in signals produced by processes that correspond to the case of the time flowing up- or downwards in the Feynman diagram of Figure 2.2 are called

[1] In fact, measurements of the CMB anisotropy power spectrum allow for a tiny amount of DM accounting for $0.01\% - 0.4\%$ of the total DM density to be charged with an electric charge of $Q_{\mathrm{DM}}/e \simeq \mathcal{O}(10^{-6} - 10^{-4})$ [50, 51]. The allowed masses for this tiny amount of so-called *millicharged DM* (mDM) range from 0.1 MeV to 1 MeV [51].

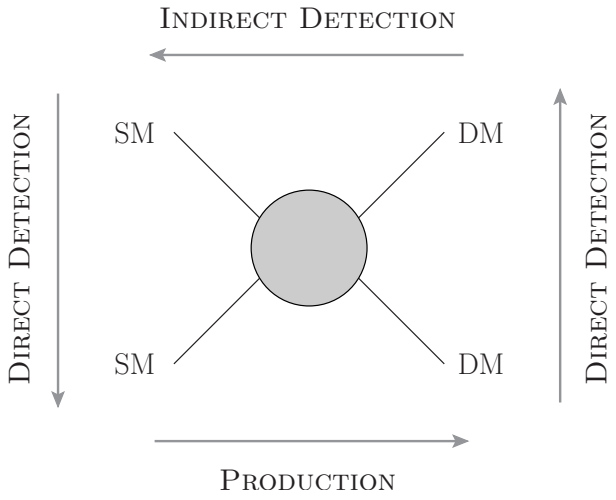

Figure 2.2 | Conceptual Feynman diagrams for DM searches. The grey arrows indicate the direction of the time-flow for different types of experiments. The labels SM and DM represent baryonic and non-baryonic matter, respectively.

direct detection experiments. Here, the signal is assumed to be generated by galactic DM particles scattering off SM matter and consists of the resulting recoil energy of the latter. Possible scattering targets in these experiments are nuclei, bound electrons, free electrons as well as atoms as a whole. Important direct detection experiments are the CDEX [64], CDMSlite [65], SuperCDMS [66], COSINE-100 [67], CRESST [68], DAMA/LIBRA [69], DAMIC [70], DAMIC-M [71], DarkSide-50 [72], DEAP-3600 [73], DARWIN [74], PICASSO [75], PICO [76], EDELWEISS [77–79], LUX [80], LUX-ZEPLIN [81], NEWS-G [82], PandaX [83], PandaX II [84], PandaX-4T [85], XENON100 [86] and XENON1T [87] experiments.

Finally, DM is also searched for in indirect detection experiments, which generally aim to detect a signal from the flux of SM matter produced through the annihilation of DM. In Figure 2.2 these processes correspond to the case of a time-flow from right to left. Here, the flux of γ-rays, neutrinos and charged leptons are particularly interesting. Indirect detection searches have been or are still performed through the MAGIC [88], VERITAS [89], HAWC [90], IceCube [91], ANTARES [92], Super-Kamiokande [93], PAMELA [94], Pierre Auger [95], Fermi-LAT [96], H.E.S.S. [97], AMS [98] and AMS-02 [99] experiments.

2.2 Dark Matter Thermal Freeze-Out

The evidence discussed in the last section does not only hint at the existence of DM but also provides constraints on some of its properties. Here, the observation of large-scale structures [100, 101] demands DM to be *cold*, i.e. to be non-relativistic [102–104]. Further important properties are that—as already mentioned—DM needs to be electrically neutral [105, 106] but also stable at cosmological scales, which means that it needs to have a lifetime larger than the age of the Universe [107–114]. Most importantly, DM needs to have been produced in the early Universe through a mechanism that yields the correct relic density as observed today.

In terms of the evolution of the Universe, the *Lambda Cold Dark Matter* (ΛCDM) model is currently the most successful theory in describing cosmological phenomena at large scales [115], while it suffers from some problems at smaller scales [116] that can potentially be solved through DM self-interactions [117]. It is particularly successful in

predicting cosmic abundances of light elements through the paradigm of a hot big bang and thermal decoupling, which suggests that the same mechanism could also be applied to DM. According to this paradigm, the production of DM as the relic of a thermal decoupling process can be outlined as follows.

The primordial Universe is dense and hot such that its SM matter content forms a thermal bath. If DM is assumed to interact with the SM, the process of annihilations of DM particles into SM matter and the production of DM particles out of SM matter establishes an equilibrium between DM and this thermal bath. Once the Universe cools down to temperatures smaller than the DM mass, the thermal bath is no longer energetic enough to produce DM, leading to a decreasing DM number density due to ongoing annihilations. However, since the Universe does not only cool down but also expand, the annihilation rate of DM decreases with time, as the dark particles become more and more dilute. Once this rate drops below the expansion rate of the Universe, i.e. the Hubble rate H, the dilution of DM particles is large enough to have them decouple from thermal equilibrium such that one is left with a constant amount of cold DM [13, 118]. The decoupling of DM from thermal equilibrium is also referred to as *thermal freeze-out*.

The dynamics of this freeze-out procedure are governed by the Boltzmann equation

$$\frac{dn}{dt} = -3Hn - \langle \sigma v \rangle \left(n^2 - n_{\text{eq}}^2 \right) , \tag{2.6}$$

where n and n_{eq} describe the DM number density and its value at thermal equilibrium, respectively, while $\langle \sigma v \rangle$ is the thermally averaged DM annihilation rate. It includes all possible annihilation channels of DM. The first term on the right hand side of Equation (2.6) accounts for the dilution of DM due to the expansion of the Universe, while the second and third terms describe the change in the number density due to annihilations of DM into SM matter as well as the inverse process of SM matter producing DM. The comoving DM relic density after the freeze-out is approximately constant and is defined as [118]

$$\Omega_{\text{DM}} = \frac{m_{\text{DM}} n_0}{\rho_c} = \frac{m_{\text{DM}} T_0^3}{\rho_c} \frac{n_0}{T_0^3} \sim \frac{m_{\text{DM}} T_0^3}{\rho_c} \frac{n_f}{T_f^3} , \tag{2.7}$$

where we have used that the DM yield $Y = n/s$ with $s \sim T^3$ being the entropy density remains constant after freeze-out. Here, m_{DM} is the DM mass, ρ_c is the critical density, n_f as well as T_f are the number density and temperature at the freeze-out and T_0 is the temperature of the Universe today. Using this expression one can calculate an estimate for Ω_{DM} by demanding that the annihilation rate drops below the expansion rate of the Universe, i.e.

$$n_f \langle \sigma v \rangle = H \sim \frac{T_f^2}{m_{\text{P}}} , \tag{2.8}$$

where the last similarity is an approximation that holds for the early, radiation dominated Universe [119] and m_{P} is the Planck mass. For the comoving DM relic density we can then write

$$\Omega_{\text{DM}} \sim \frac{m_{\text{DM}} T_0^3}{T_f \rho_c m_{\text{P}}} \frac{1}{\langle \sigma v \rangle} = \frac{x_f T_0^3}{\rho_c m_{\text{P}}} \frac{1}{\langle \sigma v \rangle} \sim x_f \frac{1.5 \times 10^{-28}\, \text{cm}^3 \text{s}^{-1}}{\langle \sigma v \rangle} , \tag{2.9}$$

where we have used $x_f = m_{\text{DM}}/T_f$. Since the freeze-out of DM typically occurs at values $x_f \simeq 10 - 30$ [13, 118, 119], we find that the DM relic density mainly depends on the thermally averaged annihilation rate and is inversely proportional to it. This behaviour is illustrated in Figure 2.3, where we show the resulting comoving number density of DM after the freeze-out for different values of x_f or $\langle \sigma v \rangle$, respectively.

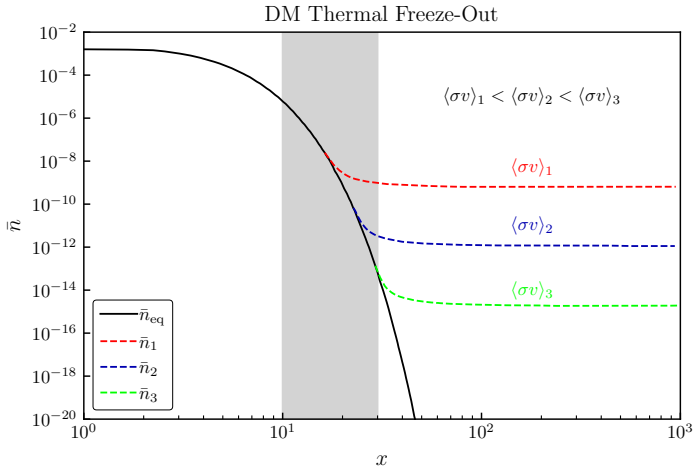

Figure 2.3 | Illustration of the thermal freeze-out of DM. We show the resulting comoving DM number density $\bar{n}$ in dependence of the parameter $x = m_{\rm DM}/T$ for three different annihilation rates that satisfy $\langle\sigma v\rangle_1 < \langle\sigma v\rangle_2 < \langle\sigma v\rangle_3$. The grey area indicates the typical region of freeze-out with $x_f \simeq 10 - 30$. The illustrated curves have been adopted from Reference [120].

One remarkable observation about our findings in Equation (2.9) is that in order to reproduce the observed relic density given in Equation (2.5) the DM annihilation rate needs to be roughly[2]

$$\langle\sigma v\rangle \simeq 10^{-26}\,\text{cm}^3\text{s}^{-1}\,, \tag{2.10}$$

which corresponds to the typical rate of a pair of weakly coupled particles annihilating at the TeV scale. Here we have assumed the freeze-out to occur at $x_f = 20$. For comparison, the above mentioned rate of two weakly coupled particles annihilating at a NP scale of $m_{\rm NP} = 1\,\text{TeV}$ is given by

$$\langle\sigma v\rangle_{\rm weak} \sim \frac{\alpha_W^2}{m_{\rm NP}^2} \simeq 10^{-26}\,\text{cm}^3\text{s}^{-1}\,. \tag{2.11}$$

This numerical coincidence suggests that WIMPs produced as the result of a thermal freeze-out might constitute a possible solution to the DM problem and is thus referred to as the *WIMP miracle*. The existence of WIMPs at the TeV scale is even further motivated and generally predicted by proposed solutions to the Higgs or weak hierarchy puzzle of the SM.

Since as pointed out above the DM density after freeze-out mainly depends on the thermally averaged annihilation rate, we want to also comment on its definition before concluding this section. In all generality it is given as [121]

$$\langle\sigma v\rangle = \frac{f_{\rm nat}}{8m_{\rm DM}^4 T K_2^2(m_{\rm DM}/T)} \int_{4m_{\rm DM}^2}^{\infty} \sigma(\sqrt{s} - 4m_{\rm DM}^2)\sqrt{s} K_1\left(\sqrt{s}/T\right) ds\,, \tag{2.12}$$

where the functions K_i are modified Bessel functions of order i, σ is the Lorentz invariant cross section for the DM annihilation process and s is the usual Mandelstam variable. The factor $f_{\rm nat}$ depends on the particle nature of DM and reads $f_{\rm nat} = 1/2$ if DM is not a

[2] Note the additional factor of h^2 when comparing Equation (2.9) and (2.5).

self-conjugate particle, like e.g. a Dirac fermion or a complex scalar. Otherwise it is equal to one. Note that the integral in Equation (2.12) cannot be solved analytically. However, since WIMPs typically freeze-out in the non-relativistic regime with $v \ll c$, one can expand the annihilation rate for small velocities to find [121, 122]

$$\langle \sigma v \rangle = f_{\text{nat}} \left[a + b \langle v^2 \rangle + \mathcal{O}\left(\langle v^4 \rangle \right) \right] . \tag{2.13}$$

The coefficients of this low-velocity expansion can then be determined analytically without solving any integrals at all [123, 124]. It is important to note however that this expansion breaks down if DM annihilates into a pole, i.e. if it resonantly exchanges an s-channel mediator [125, 126].

Chapter 3
Dark Minimal Flavour Violation

We use this chapter to introduce the formal definition of the DMFV framework and provide an overview of DMFV models that have already been studied. Further, we extend our review of the DM thermal freeze-out from Section 2.2 to the case of flavoured DM and define two flavoured freeze-out scenarios that we will use in our phenomenological analyses.

3.1 The Dark Minimal Flavour Violation Framework

DMFV is a framework for simplified flavoured DM models with non-trivial flavour structures that was introduced in Reference [20]. In this framework, the SM is typically extended by a DM flavour triplet $\phi = (\phi_1, \phi_2, \phi_3)^T$ which couples to SM fermions via a corresponding mediator particle ψ, where the lightest state of the fields ϕ_i is assumed to account for the observed amount of DM in the Universe.[3] Generically, this interaction is described by the Lagrangian

$$\mathcal{L}_{\text{int}}^{\text{DMFV}} = \lambda_{ij}\, \bar{f}_i \phi_j \psi + \text{h.c.}\,, \tag{3.1}$$

where λ is a complex 3×3 coupling matrix that parametrises the interaction strength between dark particles and the SM. In this notation, the fermion f can be either of the SM fields u_R, d_R, ℓ_R, Q_L or L_L. The quantum numbers of the DM field ϕ and the mediator field ψ depend on their particle natures as well as the choice for the fermion f. The field extension and the interaction term in Equation (3.1) extend the approximate flavour symmetry of the SM to

$$\mathcal{G}_{\text{DMFV}} = U(3)_Q \times U(3)_L \times U(3)_u \times U(3)_d \times U(3)_\ell \times \mathcal{G}(3)_\phi\,, \tag{3.2}$$

where the symmetry group $\mathcal{G}(3)_\phi$ depends on the particle nature of the DM field ϕ. If it is a self-conjugate particle, the symmetry that DM is associated with is an $O(3)_\phi$ while for non-self-conjugate particles it is a $U(3)_\phi$. In DMFV this extended flavour symmetry is accompanied by the assumption that besides the SM Yukawa couplings Y_u, Y_d and Y_ℓ the only new source of flavour-violation is constituted by the coupling matrix λ. This ansatz is referred to as the *DMFV hypothesis* and carries the DMFV framework beyond the scope of the well studied case of MFV [14–19].

DMFV models with Dirac fermionic DM coupling to right-handed down-type quarks d_R [20], right-handed up-type quarks u_R [21, 23], right-handed charged leptons ℓ_R [24] as well as the left-handed quark doublets Q_L [22] have already been studied in earlier analyses. In this work we consider the cases of Majorana fermionic DM coupling to right-handed up-type quarks u_R and complex scalar DM coupling to right-handed charged leptons ℓ_R. We further study a model that does not belong to the DMFV class, in which complex scalar DM couples to right- and left-handed charged leptons. Note that in the following

[3] The choice of the Greek letters ϕ and ψ shall neither imply that ϕ is always a scalar nor that ψ is always a fermion here.

we adopt a notation in which we call the heaviest dark flavour ϕ_1 and the lightest dark flavour ϕ_3.

3.2 Flavoured Freeze-Out Scenarios

It is important to note that the discussion of the thermal freeze-out of DM provided in the last section is only valid for a single DM species. Since in all the models that we study in this work DM comes in three generations, the Boltzmann equation from Equation (2.6) that describes the dynamics of the freeze-out needs to be adapted accordingly. In this case the number densities n_i of each DM generation ϕ_i receive additional contributions through conversions of the form $\phi_i f_k \to \phi_j f_l$ as well as the decays $\phi_i \to \phi_j \bar{f}_k f_l$, where i, j, k and l are flavour indices. Since however, due to the latter processes the heavier states ϕ_1 and ϕ_2 will decay into the lightest state on scales as large as the age of the Universe[4], the total number density of the dark relic n after the freeze-out can be written as

$$n = \sum_i n_i \,, \tag{3.3}$$

which evolves according to the coupled three flavour Boltzmann equation [127]

$$\frac{dn}{dt} = -3Hn - \sum_{ij} \langle \sigma v \rangle_{ij} \left(n_i n_j - n_i^{\text{eq}} n_j^{\text{eq}} \right) \,. \tag{3.4}$$

Here the annihilation rate includes all possible final states that a DM pair $\phi_i \phi_j$ can annihilate into. In the following we define two benchmark scenarios for the thermal freeze-out of flavoured DM that we will consider in the phenomenological analysis of the three models we study in this work.

The first is the so-called *quasi-degenerate freeze-out* (QDF) scenario in which we assume the mass splittings between the different dark flavours to be negligibly small[5]. Hence, the decay of the heavier states into the lightest state ϕ_3 is kinematically sufficiently suppressed such that they are stable at the time scale of the freeze-out. Moreover, since the number density of SM particles f in the thermal bath is much higher than each n_i, the conversions between different DM generations ϕ_i happen at a much faster rate than DM annihilations. This establishes a relative equilibrium between the dark flavours and the thermal bath and hence the number densities n_i satisfy [127]

$$\frac{n_i}{n} \simeq \frac{n_{i,\text{eq}}}{n_{\text{eq}}} \,, \tag{3.5}$$

where $n_{i,\text{eq}}$ and n_{eq} describe the number density of a single flavour i and the total number density in equilibrium. Using this expression we can re-express Equation (3.4) and write

$$\frac{dn}{dt} = -3Hn - \langle \sigma v \rangle_{\text{eff}}^{\text{QDF}} \left(n^2 - n_{\text{eq}}^2 \right) \,, \tag{3.6}$$

where we have defined

$$\langle \sigma v \rangle_{\text{eff}}^{\text{QDF}} = \sum_{ij} \langle \sigma v \rangle_{ij} \frac{n_{i,\text{eq}}}{n^{\text{eq}}} \frac{n_{j,\text{eq}}}{n^{\text{eq}}} = \frac{1}{9} \sum_{ij} \langle \sigma v \rangle_{ij} \,, \tag{3.7}$$

[4] Following the line of argument in Appendix D of Reference [20], it can be shown that these decays happen at a fast enough rate such that they are not subject to constraints from big bang nucleosynthesis or energy injections into the cosmic microwave background.

[5] The origin of these mass splittings as well as numerical definitions of each freeze-out scenario will be discussed and introduced for each model separately in the according sections.

and used that $n_{i,\mathrm{eq}}/n_{\mathrm{eq}} \simeq 1/3$. In other words, in this benchmark scenario each dark flavour contributes equally to the freeze-out and the Boltzmann equation reduces to the single flavour case from Equation (2.6). Hence, following the low-velocity expansion from Equation (2.13) we can write

$$\langle \sigma v \rangle_{\mathrm{eff}}^{\mathrm{QDF}} = \frac{f_{\mathrm{nat}}}{9} \left[a + b \langle v^2 \rangle + \mathcal{O}\left(\langle v^4 \rangle \right) \right] , \tag{3.8}$$

where in this expression the coefficients a and b include the sum over all possible annihilation channels.

The second benchmark scenario we consider is called the *single flavour freeze-out* (SFF) and is defined through a significant mass splitting between the lightest state ϕ_3 and the heavier flavours. While the flavour-changing scatterings $\phi_i f_k \to \phi_j f_l$ still maintain a relative equilibrium between the different dark flavours, the number density of the heavy states ϕ_1 and ϕ_2 is now suppressed by a Boltzmann factor with the respective mass splitting as its argument. This is due to the kinematical enhancement of the decay of the heavier flavours into the lightest state, since now the lifetime of the heavy states is small compared to the time of the freeze-out.[6] Hence, in this scenario we find

$$n_{1,2} \ll n_3 , \tag{3.9}$$

and thus

$$n = \sum_i n_i \simeq n_3 . \tag{3.10}$$

This again reduces Equation (3.4) to the single flavour Boltzmann equation

$$\frac{dn_3}{dt} = -3Hn_3 - \langle \sigma v \rangle_{33} \left(n_3^2 - n_{3,\mathrm{eq}}^2 \right) , \tag{3.11}$$

where the annihilation rate includes all possible final states. In this scenario it is only the lightest state ϕ_3 that contributes to the freeze-out and hence the sum over initial state flavours and the factor of 1/9 we had found for the QDF scenario are absent. Adopting the low-velocity expansion from Equation (2.13) we provide the joint expression

$$\langle \sigma v \rangle_{\mathrm{eff}} = f_{\mathrm{nat}} f_{\mathrm{sc}} \left[a + b \langle v^2 \rangle + \mathcal{O}\left(\langle v^4 \rangle \right) \right] , \tag{3.12}$$

for both scenarios, where we have $f_{\mathrm{sc}} = 1/9$ in the QDF scenario and $f_{\mathrm{sc}} = 1$ in the SFF scenario. Also, depending on the scenario the coefficients a and b either include a sum over initial state flavours or do not.

[6] We have checked the accuracy of the SFF approximation in an ongoing analysis [128] by numerically solving the coupled three-flavour Boltzmann equations.

Part II

Up-Type-Flavoured Majorana Dark Matter

This part is based on the publication

> H. Acaroğlu and M. Blanke, *Tasting flavoured Majorana dark matter*, *JHEP* **05** (2022) 086 [2109.10357] ,

and here we study a simplified model of Majorana fermionic up-type flavoured DM in the DMFV framework. The SM field content is extended by a DM flavour triplet that couples to right-handed up-type quarks through a coloured and charged scalar mediator. This interaction is governed by a new 3×3 coupling matrix λ, which according to the DMFV ansatz constitutes a new source of flavour-violation. We study the phenomenology of this model by analysing constraints from collider experiments, neutral D meson mixing, the observed DM relic density and direct detection experiments. Throughout this analysis we point out crucial differences between our case of Majorana fermionic DM and the version of this model where DM is assumed to be a Dirac fermion studied in Reference [21]. To determine the viable parameter space of this model we further perform a combined analysis of all constraints and determine which flavour for the DM particle is preferred by experimental data. Finally, we investigate if this model is capable of generating sizeable contributions to the direct CP asymmetry $\Delta A_{\mathrm{CP}}^{\mathrm{dir}}$ in charm decays. We find that the viable parameter space identified in the combined analysis allows for a significant enhancement of $\Delta A_{\mathrm{CP}}^{\mathrm{dir}}$ with respect to the SM estimate such that the experimental central value can be reproduced.

Chapter 4
Model Details

While DM remains undetected in various experiments, the absence of signal can imply important properties of DM. One such property is its particle nature, which generally has a severe impact on the phenomenology of DM. In this sense, Majorana fermionic DM is particularly interesting and at the same time well-studied, as the neutralino—a DM candidate predicted by *Supersymmetry* (SUSY) models [130]—is a Majorana particle. On more general grounds, Majorana DM is capable of easing the tension between the absence of experimental signals and the WIMP paradigm, as in this class of DM models leading contributions to the DM–nucleon scattering cross section vanish. Moreover, the Majorana nature of DM gives rise to Majorana specific contributions to several observables, which in some cases tend to relax respective experimental constraints. Hence, combining Majorana fermionic DM with the paradigm of flavoured DM constitutes an interesting benchmark case.

This chapter covers the details of an up-type flavoured Majorana DM model that we study throughout this part. We first present how the model is set up in the DMFV framework and then continue with a discussion of the coupling matrix λ and its parametrisation. The chapter is concluded by a review of this model's mass spectrum and a discussion of how DM is stabilised in it.

4.1 Field Content and Interactions

We present a DMFV model that extends the SM by the Majorana fermionic flavour triplet $\chi = (\chi_1, \chi_2, \chi_3)^T$ and the complex scalar mediator field ϕ. The dark fields transform as singlets under the SM gauge group with the representation $(\mathbf{1}, \mathbf{1}, 0)_{1/2}$ whereas the scalar field carries electric as well as colour charge and is thus represented by $(\mathbf{3}, \mathbf{1}, 2/3)_0$. Here we have used the shorthand notation $(SU(3)_C, SU(2)_L, U(1)_Y)_{\text{spin}}$. The DM flavour triplet χ is coupled to the right-handed up-type quarks u_R through the scalar mediator ϕ and this interaction is governed by the new flavour-violating 3×3 complex coupling matrix λ. Following the line-out that we have presented in Section 3.1, this model extends the approximate flavour symmetry of the SM by an additional $O(3)_\chi$ under which the field χ transforms as a triplet. The Lagrangian of this simplified model reads

$$\begin{aligned}\mathcal{L} = \mathcal{L}_{\text{SM}} + \frac{1}{2}(i\bar{\chi}\partial\!\!\!/\chi - M_\chi\bar{\chi}\chi) - (\lambda_{ij}\bar{u}_{Ri}\,\chi_j\phi + \text{h.c.}) + (D_\mu\phi)^\dagger(D^\mu\phi) \\ - m_\phi^2\,\phi^\dagger\phi + \lambda_{H\phi}\,\phi^\dagger\phi H^\dagger H + \lambda_{\phi\phi}\left(\phi^\dagger\phi\right)^2 ,\end{aligned} \tag{4.1}$$

where χ is a four-component Majorana spinor $\chi = (\chi_L, i\sigma_2\chi_L^*)^T$ and χ_L is a two-component Weyl spinor. The factor of $1/2$ in the kinetic term of the field χ is due to its Majorana fermionic particle nature. The latter also determines the symmetry group that the DM flavour triplet is associated with to be an $O(3)_\chi$ and not a $U(3)_\chi$, since otherwise the mass term of χ would violate the flavour symmetry. Following the DMFV ansatz we assume

that the coupling λ is the only new source of flavour violation aside from the SM Yukawa couplings and that the lightest state of the fields χ_i accounts for the observed DM relic in the Universe.

While the quartic coupling $\lambda_{\phi\phi}$ parametrising self-interactions of the scalar mediator ϕ has no impact on our analysis and is only given for completeness here, some remarks are in order for the Higgs portal coupling $\lambda_{H\phi}$. This coupling generates contributions to the effective coupling of the SM Higgs to gluons and photons through loop processes, which are suppressed by two powers of the mediator mass m_ϕ. We will find that for the NP scales allowed by the LHC searches we discuss in Section 5.1 these contributions are expected to be small and can thus be neglected. More importantly, $\lambda_{H\phi}$ induces a DM–Higgs coupling at the one-loop level that in principle contributes to the annihilation of DM in the early Universe and DM–nucleon scattering. While we will comment on the implications of these contributions in the according sections, we want to stress here that the main goal of our analysis is to elucidate possible structures of the flavour-violating coupling λ allowed by current experimental data. Hence, the general approach of our analysis will be to neglect the impact of the quartic couplings $\lambda_{H\phi}$ and $\lambda_{\phi\phi}$.

4.2 Parametrisation of the Dark-Matter–Quark Coupling λ

To parametrise the coupling matrix λ we follow a similar procedure as for the SM Yukawa couplings Y_u and Y_d. This coupling is a complex 3×3 matrix and thus contains a total of 18 degrees of freedom, consisting of nine real parameters and nine complex phases. In analogy to the parametrisation of the SM Yukawa couplings, we want to make use of the flavour symmetry $O(3)_\chi$ and identify the physical degrees of freedom in λ. To this end we perform a singular value decomposition and express it as

$$\lambda = UDV\,, \tag{4.2}$$

where U and V are unitary matrices. The matrix D is diagonal and has only positive real entries. This ansatz creates three additional redundant degrees of freedom, since unitary matrices have a total of nine free parameters accounting to a total number of 21 parameters for λ after the singular value decomposition. However, these redundancies can be removed through a diagonal rephasing of Equation (4.2) according to

$$U' = U\,\mathrm{diag}(e^{i\alpha_1}, e^{i\alpha_2}, e^{i\alpha_3})\,, \tag{4.3}$$

$$V' = \mathrm{diag}(e^{-i\alpha_1}, e^{-i\alpha_2}, e^{-i\alpha_3})\,V\,, \tag{4.4}$$

which reduces the number of complex phases in λ back to nine.

One can now remove additional unphysical degrees of freedom from λ by using the flavour symmetry the DM field χ is associated with. As already mentioned in the last section, the Majorana mass term

$$M_\chi \bar{\chi}\chi = M_\chi\, i(\chi_L^\dagger \sigma_2 \chi_L^* - \chi_L^T \sigma_2 \chi_L)\,, \tag{4.5}$$

is only invariant under orthogonal transformations, i.e. Majorana fermions can only transform under real representations. Thus the DM triplet χ transforms under an $O(3)_\chi$ symmetry that we want to use to remove three real degrees of freedom from V. Following Reference [131] we therefore decompose V into

$$V = OdP\,, \tag{4.6}$$

where O as well as P are orthogonal matrices and d is a diagonal matrix that contains three complex phases. One can now transform χ_L according to

$$\chi_L \to P^{-1}\chi_L\,, \tag{4.7}$$

and remove the orthogonal matrix P from V. For the parametrisation of λ this yields

$$\lambda = UDOd\,. \tag{4.8}$$

Note that this analysis already reveals a fundamental difference to the case of Dirac fermionic DM in DMFV [20–24]. In such models DM is associated with a $U(3)_\chi$ symmetry and thus the matrix V can be fully removed from λ. This reduces the total number of free parameters to nine for Dirac fermionic DMFV models, while in our case of Majorana fermionic DM we are left with a total of 15 physical degrees of freedom in λ.

For the parametrisation of the unitary matrix U we adopt the expression from References [21, 132] and write

$$\begin{aligned} U &= U_{23}\,U_{13}\,U_{12} \\ &= \begin{pmatrix} 1 & 0 & 0 \\ 0 & c_{23}^\theta & s_{23}^\theta e^{-i\delta_{23}} \\ 0 & -s_{23}^\theta e^{i\delta_{23}} & c_{23}^\theta \end{pmatrix} \begin{pmatrix} c_{13}^\theta & 0 & s_{13}^\theta e^{-i\delta_{13}} \\ 0 & 1 & 0 \\ -s_{13}^\theta e^{i\delta_{13}} & 0 & c_{13}^\theta \end{pmatrix} \begin{pmatrix} c_{12}^\theta & s_{12}^\theta e^{-i\delta_{12}} & 0 \\ -s_{12}^\theta e^{i\delta_{12}} & c_{12}^\theta & 0 \\ 0 & 0 & 1 \end{pmatrix}, \end{aligned} \tag{4.9}$$

where we have introduced the shorthand notation $s_{ij}^\theta = \sin\theta_{ij}$ and $c_{ij}^\theta = \cos\theta_{ij}$. In this expression the rephasing from Equation (4.3) has already been used to remove three complex phases from U. The matrix O can be written in terms of three orthogonal matrices and reads

$$\begin{aligned} O &= O_{23}\,O_{13}\,O_{12} \\ &= \begin{pmatrix} 1 & 0 & 0 \\ 0 & c_{23}^\phi & s_{23}^\phi \\ 0 & -s_{23}^\phi & c_{23}^\phi \end{pmatrix} \begin{pmatrix} c_{13}^\phi & 0 & s_{13}^\phi \\ 0 & 1 & 0 \\ -s_{13}^\phi & 0 & c_{13}^\phi \end{pmatrix} \begin{pmatrix} c_{12}^\phi & s_{12}^\phi & 0 \\ -s_{12}^\phi & c_{12}^\phi & 0 \\ 0 & 0 & 1 \end{pmatrix}, \end{aligned} \tag{4.10}$$

where we again use the shorthand notation $c_{ij}^\phi = \cos\phi_{ij}$ and $s_{ij}^\phi = \sin\phi_{ij}$. For the diagonal matrices D and d we write

$$D = \mathrm{diag}(D_1, D_2, D_3)\,, \tag{4.11}$$

$$d = \mathrm{diag}(e^{i\gamma_1}, e^{i\gamma_2}, e^{i\gamma_3})\,. \tag{4.12}$$

In total the coupling matrix λ is then expressed in terms of the parameters

$$\theta_{23},\, \theta_{13},\, \theta_{12},\, \phi_{23},\, \phi_{13},\, \phi_{12},\, \delta_{23},\, \delta_{13},\, \delta_{12},\, \gamma_1,\, \gamma_2,\, \gamma_3,\, D_1,\, D_2,\, D_3\,. \tag{4.13}$$

When scanning over these parameters in the numerical analysis of experimental constraints we will restrict them to the ranges

$$\theta_{ij} \in [0, \frac{\pi}{4}], \quad \phi_{ij} \in [0, \frac{\pi}{4}], \quad \delta_{ij} \in [0, 2\pi), \quad \gamma_i \in [0, 2\pi), \quad D_i \in [0, 2]\,. \tag{4.14}$$

Here, the ranges of the mixing angles θ_{ij} and ϕ_{ij} avoid a double counting of the parameter space, while the couplings D_i are conservatively restricted to a maximum value of $D_i = 2$ in order to guarantee perturbativity.

4.3 Mass Spectrum and Dark Matter Stability

While the $O(3)_\chi$ symmetry ensures that the masses m_{χ_i} of the different dark flavours are equal at *leading order* (LO) in the coupling λ, the *ultraviolet* (UV) completion of the theory can still induce non-universal mass corrections at tree-level or one-loop. Even if these are absent, already within the simplified model there will be unavoidable contributions to the DM mass splittings from one-loop *renormalisation group* (RG) running. However, as the DMFV hypothesis ensures that λ constitutes the only new source of flavour-violation, the mass matrix M_χ in the Lagrangian of Equation (4.1) cannot be generic. Instead, in analogy to the usual spurion expansion of MFV [15], we expand the DM mass matrix in powers of the flavour-violating coupling λ and write

$$M_{\chi,ij} = m_\chi \left\{ \mathbb{1} + \frac{\eta}{2}(\lambda^\dagger\lambda + \lambda^T\lambda^*) + \mathcal{O}(\lambda^4) \right\}_{ij} . \tag{4.15}$$

Here we have introduced the parameter η which accounts for our ignorance about the UV completion of the theory. Depending on the actual source of the mass corrections, this parameter can be at most an $\mathcal{O}(1)$ number, as it would be the case for DMFV preserving tree-level contributions. If on the other hand the corrections are induced through loop-effects, η receives a loop suppression and is thus much smaller[7].

Note that the expansion from Equation (4.15) includes the second term in the round brackets since mass matrices of Majorana fermions need to be symmetric. In the case of Dirac fermionic DM such a term is thus not present [20–22]. More importantly, we find that inserting the parametrisation of λ derived in the last section into Equation (4.15) yields

$$M_{\chi,ij} = m_\chi \left\{ \mathbb{1} + \frac{\eta}{2} \left(d^* O^T D^2 O d + d O^T D^2 O d^* \right) + \mathcal{O}(\lambda^4) \right\}_{ij} , \tag{4.16}$$

i.e. including higher-order corrections to the mass matrix results in a non-diagonal M_χ. This misalignment between mass and gauge eigenstates of χ constitutes another formal difference between Majorana and Dirac fermionic DM in DMFV, since for the latter the mass matrix M_χ remains diagonal even after applying the spurion expansion [20–22]. However, the gauge and mass eigenstates of the field χ can be related to each other through an Autonne–Takagi factorisation [133, 134] of M_χ, where we write

$$M_\chi = W^T M_\chi^D W . \tag{4.17}$$

Since the mass matrix M_χ is real, the matrix W here is orthogonal, while M_χ^D is a diagonal matrix with positive and real entries. The mass and gauge eigenstates of χ are then related through the transformation $\chi_L \to W\chi_L$, which in turn transforms the DM–quark coupling λ to

$$\tilde{\lambda} = \lambda W^T . \tag{4.18}$$

Following the notation that we introduced at the end of Section 3.1, we always rearrange the rows in W and relabel the fields χ_i in such a way that the diagonal mass matrix satisfies

$$M_\chi^D = \mathrm{diag}(m_{\chi_1}, m_{\chi_2}, m_{\chi_3}) , \tag{4.19}$$

with the hierarchy $m_{\chi_1} > m_{\chi_2} > m_{\chi_3}$. This means that the third generation χ_3 is the lightest state, which we assume to form the DM of the Universe.

[7] In any case, the absolute size of the mass corrections may not grow too large in order ensure the convergence of this expansion. Following References [20–22] we thus limit the corrections to $\delta m_{\chi_i} < 0.3\, m_\chi$ in the numerical analysis.

Another important formal difference between the Majorana and the Dirac DM ansatz in DMFV is related to the stability of DM. For quark-flavoured Dirac DM models this is guaranteed by a residual $\mathbb{Z}_3$ symmetry implied by the global flavour symmetry [20–22]. In our case however, this residual symmetry is absent, since the non-trivial representation of Majorana spinors is real. We hence impose a $\mathbb{Z}_2$ symmetry under which only the new fields χ_i and ϕ are charged. This symmetry forbids the decay of any of the χ_i or ϕ into SM fields only and thus stabilises the DM field χ_3 as long as its mass is smaller than the mediator mass. To this end, we set $\eta < 0$ such that the mass corrections for the dark particles χ_i are always negative and further demand

$$m_\phi > m_\chi \,. \tag{4.20}$$

Here, m_ϕ and m_χ are the tree-level mass parameters from Equation (4.1) and (4.15).

Chapter 5
Phenomenology

After having discussed the details of the model presented in the last chapter, we are now ready to study its phenomenology. To this end we will first analyse the restrictions that constraints from collider experiments, neutral D meson mixing, the observed DM relic density and detection experiments place on its parameter space. To provide a comprehensive picture of the allowed parameter space in the context of current experimental data, we then perform a combined analysis in which we demand that all the mentioned constraints are satisfied simultaneously. We conclude this chapter by reviewing if this model can predict sizeable contributions to the direct CP asymmetry $\Delta A_{\text{CP}}^{\text{dir}}$ in charm decays within its viable parameter space.

5.1 Collider Phenomenology

This section is dedicated to the analysis of constraints that collider searches for DM place on the parameter space of our model. Relevant searches are conducted at the LHC and imply particularly strong restrictions on the masses of the new particles χ_i and ϕ. Hence, we discuss these restrictions in the following in order to determine the experimentally excluded parameter space of our model.

We only focus on signatures given rise to by the pair-production of the mediator particle ϕ and its subsequent decay into quarks and missing transverse energy $\not{E}_T$. This is because Reference [135] shows that for models with a coloured t-channel mediator the most stringent limits arise for the latter signatures, which we expect to also hold true for our model.

LHC Signatures from Mediator Pair-Production

The production of the mediator ϕ can either take place through *quantum chromodynamics* (QCD) interactions or the NP interactions governed by the coupling matrix λ. In both processes the $\mathbb{Z}_2$ symmetry discussed in Section 4.3 guarantees that it is produced in pairs. All QCD production channels of the mediator pair $\phi^\dagger\phi$ are proportional to the strong coupling α_s and only depend on the mediator mass m_ϕ in terms of the NP parameters.

The NP pair-production mode of ϕ on the other hand, is governed by λ and consists of two incoming quarks that exchange a dark particle in the t-channel. Since the latter are Majorana particles, this channel additionally allows for the production of the same-sign mediator pairs $\phi\phi$ and $\phi^\dagger\phi^\dagger$. We show all three NP pair-production modes of ϕ in Figure 5.1. The two same-sign production channels are additionally proportional to the DM mass parameter m_{χ_i} of the dark particle χ_i that is exchanged in the t-channel, since it is the Majorana mass term from Equation (4.5) that mixes the fields χ_L and $\chi_L^\dagger$. However, the production of a $\phi\phi$ pair is enhanced by the up quark *parton distribution function* (PDF) [136], since a proton contains a pair of valence up quarks.

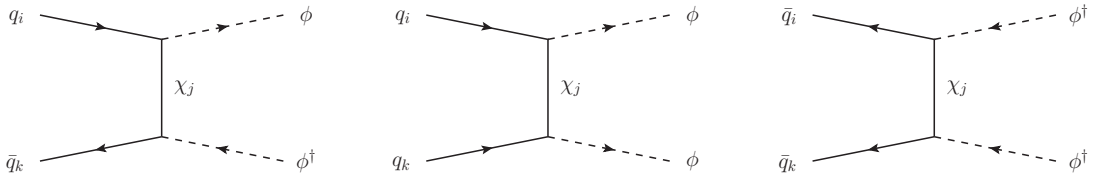

(a) $\phi\phi^\dagger$ production **(b)** $\phi\phi$ production **(c)** $\phi^\dagger\phi^\dagger$ production

Figure 5.1 | Feynman diagrams of the t-channel χ-exchange production modes of ϕ.

The subsequent decay of the pair of mediators then gives rise to signatures with at least two dark particles, as the $\mathbb{Z}_2$ symmetry would otherwise be violated. Here, the by far dominant decay modes are the ones where each ϕ decays into a quark and a dark particle as shown in Figure 5.2. The pair-production of ϕ together with this decay hence gives rise to the following parton-level processes relevant for the analysis of LHC constraints:

$$\begin{aligned} pp &\to \phi\,\phi^\dagger \to \chi_i\,\chi_j\,q_k\,\bar{q}_l\,, \\ pp &\to \phi\,\phi \to \chi_i\,\chi_j\,q_k\,q_l\,, \\ pp &\to \phi^\dagger\,\phi^\dagger \to \chi_i\,\chi_j\,\bar{q}_k\,\bar{q}_l\,, \end{aligned} \tag{5.1}$$

where i, j, k and l are flavour indices. The actual signatures that arise from these processes depend on the flavour indices k and l of the SM fields. Note that light quarks and antiquarks of the first and second generation lead to a jet in the final state while the dark particles χ_i are indistinguishable at the LHC and only appear as missing transverse energy $\not{E}_T$. Hence, both are very hard to distinguish in flavour, whereas top and antitop quarks can be distinguished through their semileptonic decays. In total this leads to the final state signatures $t\bar{t} + \not{E}_T$, $tt + \not{E}_T$, $\bar{t}\bar{t} + \not{E}_T$, $jj + \not{E}_T$ as well as $tj + \not{E}_T$.

As far as the mixed-flavour signature $tj + \not{E}_T$ generated by the decay of the mediator pair into two dark particles, one top quark and one light quark is concerned, Reference [137] has shown for the Dirac DM version of this model that it exhibits a significant discovery potential. Such a signature can also be generated in SUSY models with flavour-violating *scalar quark* (squark) couplings [138–143]. Generally, we expect the conclusions from Reference [137] to also hold true for this model. However, since currently there exist no dedicated searches for this signature we leave a detailed analysis for future work.

The flavour-conserving signatures $t\bar{t} + \not{E}_T$ and $jj + \not{E}_T$[8] are also generated in SUSY models and are the same as in searches for a pair of squarks in final states with quarks and missing transverse energy. Since squarks have the same quantum numbers as the mediator ϕ, the final state kinematics are the same as far as the QCD pair-production of ϕ is concerned. The t-channel χ-exchange production channel however, could in principle differ from the SUSY case, where either a gluino or a neutralino is exchanged in the t-channel. The reason is that the neutralino couplings are small and the gluino mass $m_{\tilde{g}}$ is experimentally constrained to $m_{\tilde{g}} \gg 1\,\text{TeV}$ [144, 145].[9] However, we do not expect a relevant impact on our results, as we implement the mediator pair-production explicitly when recasting SUSY limits. Since the searches that we use only consider hadronically decaying top and antitop quarks, the same-sign signatures $tt + \not{E}_T$ and $\bar{t}\bar{t} + \not{E}_T$ cannot be distinguished from $t\bar{t} + \not{E}_T$. Hence, we include them into the analysis and use the shorthand notation tops $+ \not{E}_T$ for the sum of all three signatures with top flavour in the final state.

[8] Note that this signature can in general also be generated through flavour-violating squark decays.

[9] Due to this constraint the gluino contribution is typically not even included in the simplified models for which the LHC squark searches calculate limits.

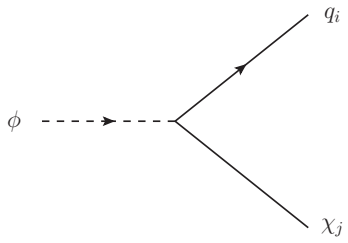

Figure 5.2 | Feynman diagram of the mediator ϕ decaying into q_i and χ_j.

The same-sign signatures $tt + \not{E}_T$ and $\overline{tt} + \not{E}_T$ constitute a unique feature of this model that has not received attention in the literature so far. Due to its PDF enhancement, the signature $tt + \not{E}_T$ is particularly interesting and could serve as a smoking-gun signature. Also, the same-sign signatures can be used in order to further analyse the particle nature of DM, as these are specific to Majorana fermionic DM. We will hence return to them at the end of this section.

Recast of LHC Limits

For the numerical analysis of the LHC constraints we recast the limits obtained by the CMS collaboration in Reference [146], where the full LHC run 2 dataset with an integrated luminosity of $136\,\text{fb}^{-1}$ is used. This analysis directly addresses the relevant signatures $\text{tops} + \not{E}_T$ and $jj + \not{E}_T$ and provides upper limits on their cross sections in tabular form. Since as already mentioned this analysis only considers hadronically decaying top and antitop quarks, its results for the signature with top flavour in the final state are not distinctive with respect to the charge of the final state particles.

To recast these limits we first implement the model into `FeynRules` [147] by using the Lagrangian from Equation (4.1). With this implementation we generate a `UFO` file [148] and use `MadGraph 5` [149] to calculate the LO signal cross section $\sigma \times \text{Br}$ for the signatures $\text{tops} + \not{E}_T$ and $jj + \not{E}_T$ separately. For the analysis of LHC constraints we follow References [20–22] and do not consider the mass splittings discussed in Section 4.3 and given in Equation (4.15). Such small splittings[10] only lead to additional soft and therefore hard to detect decay products of the heavy flavours into lighter states. We further set the mixing angles and phases in λ to zero, since we are primarily interested in the restrictions that the LHC searches place on the NP masses m_χ and m_ϕ. Allowing for flavour-violating couplings only reduces the branching ratio of a given flavour-conserving final state in comparison to the case of vanishing mixing angles. This in turn reduces the signal cross section of that final state and leads to a smaller exclusion in the mass plane $m_\phi - m_\chi$. Finally, we conventionally set the couplings D_1 and D_2 to the same value in this section, i.e. we define $D_1 = D_2 = D_j$. The results are gathered in Figure 5.3 and 5.4.

Figure 5.3 illustrates the restrictions that the recasted cross section limits from Reference [146] for the signature $\text{tops} + \not{E}_T$ place on the NP masses. We show the exclusion in the mass plane $m_\phi - m_\chi$ for fixed values of D_3 and varying values of D_j. For overall small couplings $D_i < 0.5$ we find that the QCD pair-production of the mediator ϕ dominates over the t-channel χ-exchange production. This can be inferred from Figure 5.3a, since increasing values of D_j shrink the excluded area. As the coupling D_j parametrises the coupling of the dark particles to up and charm quarks, increasing values lead to an increased production rate of ϕ pairs through the t-channel χ-exchange production mode.

[10] Remember that we had limited the mass corrections to the masses m_{χ_i} to $\delta m_{\chi_i} < 0.3\, m_\chi$ in order to ensure the convergence of the series in Equation (4.15).

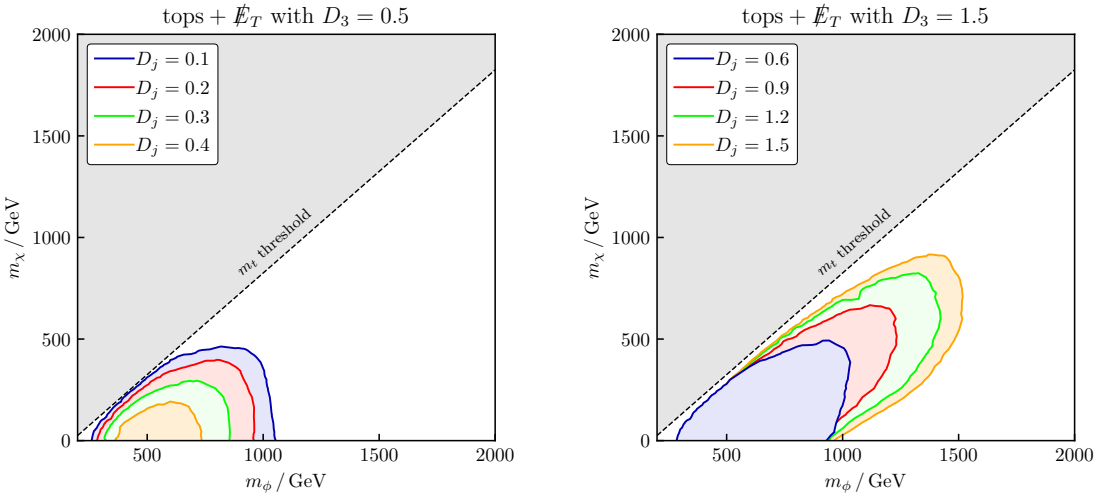

(a) $D_3 = 0.5$ and varying D_j **(b)** $D_3 = 1.5$ and varying D_j

Figure 5.3 | Constraints on the final state tops + $\not{E}_T$ obtained from Reference [146]. The coloured areas are excluded.

However, large couplings D_j at the same time reduce the branching ratio of the relevant final states with top flavour and therefore also reduce the signal cross section. Since the interplay of these concurring effects still leads to a reduced exclusion in the $m_\phi - m_\chi$ plane for increasing values of D_j, we deduce that the pair-production of ϕ in this region of the parameter space mainly happens through the QCD mode.

If on the other hand the couplings D_i are large, we find that increasing values of D_j lead to an increased exclusion in the $m_\phi - m_\chi$ plane. This is illustrated in Figure 5.3b and we can infer from this behaviour that for couplings $D_j > 0.5$ the χ-exchange production mode for mediator pairs is the dominant one. In this case, increasing values of D_j at the same time increase the production of ϕ at such a rate that it overcompensates for the reduced branching fraction of final states with top flavour and leads to a larger signal cross section in total. This is also due to the fact that a large coupling D_1 magnifies the production rate of the same-sign final state $tt + \not{E}_T$ enhanced by the PDFs of two valence up quarks in the initial state. In Figure 5.3b this enhanced production of the mentioned same-sign signature can be seen explicitly, as the excluded region grows rapidly for non-vanishing DM masses m_χ and large values of D_j. The DM mass dependence here is due to the Majorana nature of χ and the earlier mentioned fact that the Majorana mass term from Equation (4.5) parametrises the mixing between particle and antiparticle necessary for the production of same-sign signatures. We thus find that even in the strongest constrained case of $D_3 = D_j = 1.5$ shown in Figure 5.3b regions with a small m_χ and $m_\phi \gtrsim 1000\,\text{GeV}$ are still viable.

The results for the signature $jj + \not{E}_T$ are shown in Figure 5.4. Here we have fixed the coupling D_j and D_3 varies. As the t-channel pair-production of ϕ mainly depends on D_j, increasing values of D_3 only reduce the branching ratio of the mediator's decay into up or charm quarks. Thus, they always lead to a reduced exclusion in the $m_\phi - m_\chi$ plane, as can be seen in Figure 5.4a and 5.4b. Increasing values of D_j on the other hand, lead to significantly larger exclusions as now both the χ-exchange pair-production of ϕ as well as the branching ratio into the relevant final states with u- and c-jets are increased. This can be seen by comparing both panels of Figure 5.4. In Figure 5.4b we further see that just

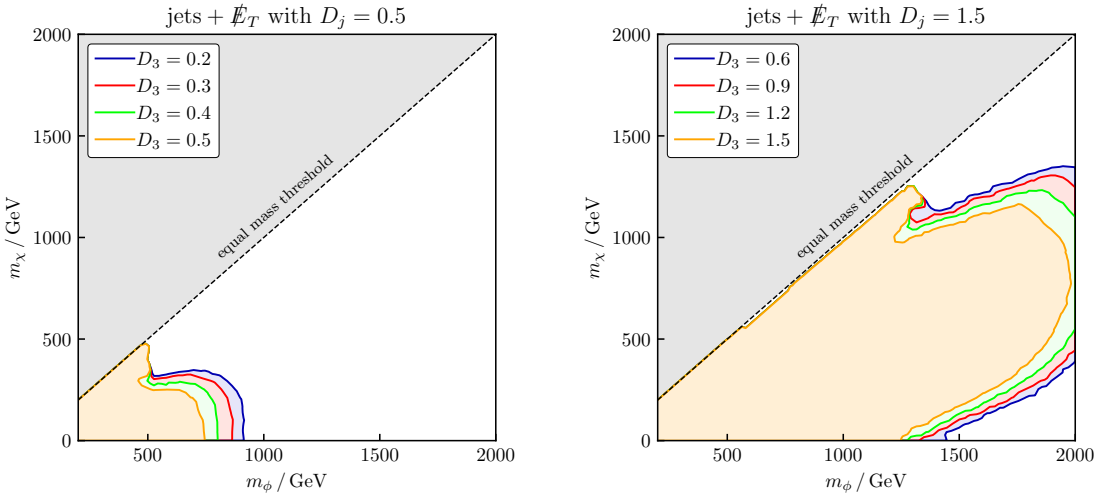

(a) $D_j = 0.5$ and varying D_3 **(b)** $D_j = 1.5$ and varying D_3

Figure 5.4 | Constraints on the final state $jj + \not{E}_T$ obtained from Reference [146]. The coloured areas are excluded.

as for the signatures with top flavour, increased values of D_j together with large masses m_χ lead to a significant production of the same-sign final states. We again find that for sufficiently large mediator masses $m_\phi \gtrsim 1500\,\text{GeV}$ small DM masses m_χ are therefore not excluded by LHC searches.

Comparing both Figure 5.3 and 5.4 we find that the restrictions placed on the parameter space of the model by the signature $jj + \not{E}_T$ are generally larger than the restrictions from signatures with top flavour. This is mainly due to the fact that for the signature $jj + \not{E}_T$ the mediator pair-production and its subsequent decay into the relevant final states are parametrised by the same coupling D_j, while for top-flavoured signatures the latter is parametrised by D_3. Hence, for the signature tops$+\not{E}_T$ increasing the production rate of ϕ pairs always comes at the cost of reducing their decay rate into the relevant final states with top flavour. Another reason why the constraints from final states with jets are larger is the increased multiplicity of the possible parton-level final states, as the signature $jj + \not{E}_T$ includes both final states with up as well as charm flavour.

We conclude that for both signatures the Majorana specific same-sign final states can lead to significant restrictions in the $m_\phi - m_\chi$ plane. One way to satisfy these constraints is to choose the coupling D_j to be small while D_3 can be large, since in this case the QCD pair-production of ϕ is dominant. Demanding the couplings to fulfil

$$0 < D_3 < 1.5\,, \tag{5.2}$$

$$0 < D_j < 0.5\,, \tag{5.3}$$

one can satisfy the LHC constraints with mediator masses $m_\phi \gtrsim 1000\,\text{GeV}$ and a free DM mass m_χ. We will find that the constraints from flavour physics and cosmology also support this choice for the couplings, which particularly holds true for the case of top-flavoured DM. Note that, however, it is also possible to satisfy the LHC constraints for larger values $D_j \gtrsim 1.0$. In this case it is necessary to restrict the NP masses to $m_\phi \gtrsim 1500\,\text{GeV}$ and $m_\chi \lesssim 200\,\text{GeV}$.

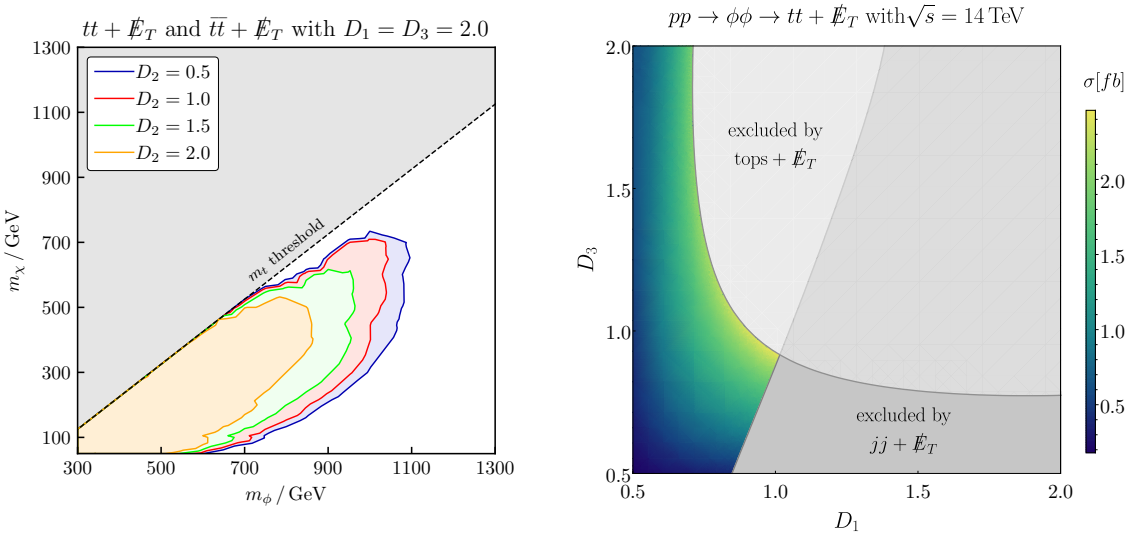

(a) constraints on the same-sign final states

(b) prediction of $tt + \not{E}_T$ for $\sqrt{s} = 14\,\text{TeV}$

Figure 5.5 | Constraints on the same-sign final states based on Reference [150] (left) and LO cross section of the process $pp \to \phi\phi \to tt + \not{E}_T$ in $\sqrt{s} = 14\,\text{TeV}$ collisions for $m_\phi = 1200\,\text{GeV}$ and $m_\chi = 400\,\text{GeV}$ (right). For the latter, the DM–charm coupling is fixed to $D_2 = 0$.

Majorana Specific LHC Signatures

As already discussed earlier, the Majorana nature of χ gives rise to the same-sign collider signatures $tt + \not{E}_T$ and $\bar{t}\bar{t} + \not{E}_T$ through the production of same-sign mediator pairs as shown in Figure 5.1b and 5.1c. The process with two positively charged top quarks in the final state is particularly interesting, since it is enhanced by two powers of the proton's up quark PDF. As this signature is absent in the case of Dirac fermionic DM and is suppressed in SUSY models due to the smallness of relevant couplings, we regard the di-top final state as a smoking-gun signature of our model and want to discuss it in more detail here. Experimentally, this final state can be distinguished from the usual opposite-sign final state $t\bar{t} + \not{E}_T$ through semileptonic top quark decays by measuring the charge of the lepton this decay produces.

Principally these signatures can also be used in combination with according searches for them in order to further constrain the parameter space of our model in the same fashion as above. Here we find that while dedicated searches for such same-sign signatures exist [150] they generally exhibit different final state kinematics than our model. The CMS search of Reference [150] for example, considers a SUSY model, in which a pair of gluinos is produced that both decay into a top or antitop associated with a stop. The stop is then assumed to decay into a light quark and a neutralino giving rise to the same-sign signatures $ttjj + \not{E}_T$ and $\bar{t}\bar{t}jj + \not{E}_T$. However, since this search assumes a small mass splitting of roughly 20 GeV between the stop and the neutralino, the jets in the final state are produced very softly. As a LO estimate we hence calculate the production rates of the two same-sign final states and compare them with the limits from Reference [150]. Further, we also present a prediction of the size of the di-top final state's LO signal cross section for future LHC runs with a centre-of-mass energy of $\sqrt{s} = 14\,\text{TeV}$ here.

The results are shown in Figure 5.5. The exclusion in the $m_\phi - m_\chi$ plane coming from searches in same-sign final states is shown in Figure 5.5a. We find that the exclusion is

maximal for vanishing DM–charm couplings D_2 and large DM–up and DM–top couplings D_1 and D_3. While large couplings D_1 increase the production rate of the same-sign intermediate states $\phi\phi$ and $\phi^\dagger\phi^\dagger$, large values of D_3 increase the branching ratio of the relevant final states with two top or antitop quarks. The same finding holds true for small DM–charm couplings, since an increasing coupling D_2 reduces the relevant branching ratios and leads to a smaller signal cross section. We further find the same DM mass dependence as in Figure 5.3 and 5.4 here, which again is due to the Majorana mass term that parametrises the same-sign pair-production of ϕ. However, we find the limits from searches in same-sign final states to be less restrictive than both searches considered in the previous section, such that they do not lead to additional exclusions in the $m_\phi - m_\chi$ plane.

In Figure 5.5b we have calculated the signal cross section for varying couplings D_1 and D_3 and for masses $m_\phi = 1200\,\text{GeV}$ and $m_\chi = 400\,\text{GeV}$. The DM–charm coupling is fixed to $D_2 = 0$ since large values only weaken the signal due to a reduced branching fraction of the relevant final state. We further show the exclusions from the above discussed searches in tops $+ \not{E}_T$ as well as $jj + \not{E}_T$ in form of the light-grey and grey areas, respectively. Since the production of same-sign mediator pairs is proportional to D_1, we find that the signal cross section grows for increasing values of D_1. At the same time, growing values of D_3 increase the decay rate of the mediator pair into two top quarks, which in turn again leads to a larger signal. As a result of the interplay of both of these effects in combination with the exclusions from the searches in tops $+ \not{E}_T$ and $jj + \not{E}_T$ we find that in the case of close-to-equal couplings $D_1 \approx D_3 \simeq 1.0$ the signal cross section is predicted to be of order $\mathcal{O}(\text{fb})$, which is well in reach of future LHC studies.

Before concluding this section we want to comment on another interesting feature of the same-sign signatures related to the particle nature of quark-flavoured DM.[11] These signatures can be used in order to define an asymmetry that can potentially be measured in order to determine if DM is a self-conjugate particle. For our case of fermionic DM, for instance, it can be utilised to distinguish between Dirac and Majorana DM. Since for the Dirac case the same-sign pair-production of ϕ is absent, we expect the mixed-flavour signatures $tj + \not{E}_T$ and $\bar{t}j + \not{E}_T$ to satisfy

$$\sigma_{\text{Dirac}}(tj + \not{E}_T) = \sigma_{\text{Dirac}}(\bar{t}j + \not{E}_T)\,. \tag{5.4}$$

In the Majorana case on the other hand, the same-sign intermediate states will contribute to both mixed-flavour signatures mentioned above. However, since the pair-production of $\phi\phi$ with positive charge is additionally enhanced by the PDFs of the two valence up quarks in a proton, we expect

$$\sigma_{\text{Majorana}}(tj + \not{E}_T) > \sigma_{\text{Majorana}}(\bar{t}j + \not{E}_T)\,, \tag{5.5}$$

for Majorana fermionic DM, provided that the DM–up couplings are not negligible. In this case the same-sign signatures can be utilised in order to define the charge asymmetry

$$a_{tj} = \frac{\sigma(tj + \not{E}_T) - \sigma(\bar{t}j + \not{E}_T)}{\sigma(tj + \not{E}_T) + \sigma(\bar{t}j + \not{E}_T)}\,, \tag{5.6}$$

which yields $a_{tj} = 0$ for Dirac and $a_{tj} > 0$ for Majorana fermions. Hence, a potential measurement of the charge asymmetry a_{tj} could shed light on the particle nature of DM

[11] The same-sign signatures generally do not exist for lepton-flavoured DM models, due to the lack of a direct coupling of DM to quarks. In these models, the LHC production channel of DM consists of a Drell–Yan process that does not allow for the production of same-sign mediator pairs due to charge conservation, see Part III and IV.

and is principally possible through semileptonic decays of the final state top or antitop quark. While we leave an elaborate feasibility study for future work, we want to conclude this section by presenting a prediction for a_{tj} based on the viable parameter space we will find in the combined analysis of Section 5.5. The maximally feasible charge asymmetry reads

$$a_{tj}^{\max} \simeq 0.9\,, \tag{5.7}$$

for both freeze-out scenarios discussed in Section 3.2 with the corresponding total signals

$$\sigma_{\text{tot}}^{\text{QDF}} \simeq 4\,\text{fb}\,, \tag{5.8}$$
$$\sigma_{\text{tot}}^{\text{SFF}} \simeq 8\,\text{fb}\,, \tag{5.9}$$

defined as $\sigma_{\text{tot}} = \sigma(tj + \not{E}_T) + \sigma(\bar{t}j + \not{E}_T)$. As far as the SM background is concerned, Reference [137] has shown for the Dirac fermionic version of our model that the NP signal in the final state $tj + \not{E}_T$ is detectable in large parts of the parameter space. We expect these findings to also apply to our case of Majorana DM since the background is the same, while the signal is larger compared to the Dirac case due to Majorana specific same-sign contributions. In summary, these preliminary results motivate a dedicated study of the same-sign signatures and the charge asymmetry a_{tj}.

5.2 Flavour Physics Phenomenology

In DMFV the non-trivial flavour structure of the coupling matrix λ can generally lead to large effects in flavour observables. For the case of quark flavoured DM the most important constraints arise for $\Delta F = 2$ observables, i.e. observables related to the oscillation of neutral mesons, which can receive large contributions from NP induced *flavour changing neutral currents* (FCNC). Hence, it is important to identify flavour-safe scenarios in which these contributions do not violate experimental limits. Since DM couples to up-type quarks in our model, the relevant process consists of neutral D meson mixing with $\Delta C = 2$. We use this section in order to discuss the constraints that $D^0 - \bar{D}^0$ mixing places on the coupling matrix λ. To this end we first derive relevant expressions for the NP contributions to $D^0 - \bar{D}^0$ mixing using the formalism of effective Hamiltonians. Detailed introductions to this formalism for the description of flavour-violating processes can be found in References [151, 152]. Using these expressions we then constrain the flavour-structure of λ through existing experimental limits on the $D^0 - \bar{D}^0$ mixing system.

Note that our model also generates contributions to the $\Delta F = 1$ processes of rare D meson and flavour-violating top quark decays. The constraints from rare D meson decays are generally weaker than the ones from $D^0 - \bar{D}^0$ mixing and the flavour-violating top quark decays are only weakly constrained in general [153]. Hence, we follow Reference [21] and do not consider possible restrictions placed on the structure of λ by these two processes here.

Neutral D Meson Mixing

At LO the NP contributions to $D^0 - \bar{D}^0$ mixing are generated at the one-loop level through the box diagrams shown in Figure 5.6 and are governed by the flavour-violating coupling matrix λ, i.e. they are proportional to λ^4. While the normal box diagram shown in Figure 5.6a exists for Dirac as well as Majorana fermions, the crossed diagram from Figure 5.6b is only given rise to in the latter case. Evaluating these diagrams and using the techniques

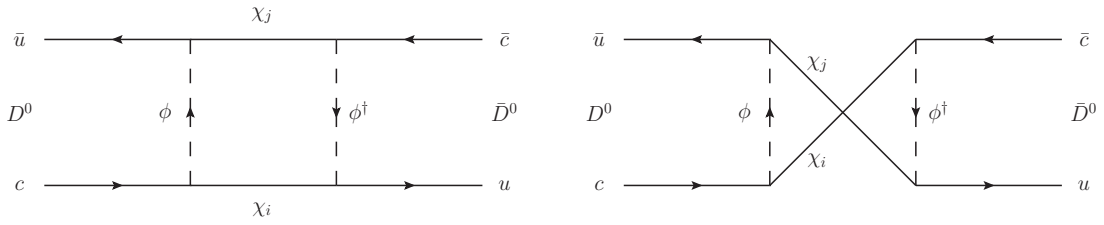

(a) standard box diagram **(b)** crossed box diagram

Figure 5.6 | Feynman diagrams for the NP contributions to $D^0 - \bar{D}^0$ mixing at LO.

provided in the References [151, 152] we write for the effective Hamiltonian that describes the NP contributions to $D^0 - \bar{D}^0$ mixing

$$\mathcal{H}_{\text{eff}}^{\Delta C=2,\,\text{NP}} = \frac{1}{128\pi^2 m_\phi^2} \sum_{ij} \lambda_{uj}\lambda_{ci}^* \Big[\lambda_{ui}\lambda_{cj}^* \cdot F(x_i, x_j) - 2\lambda_{uj}\lambda_{ci}^* \cdot G(x_i, x_j) \Big] \times Q_{uc}^{VRR} + \text{h.c.} \tag{5.10}$$

Here we have defined

$$Q_{uc}^{VRR} = (\bar{u}_\alpha \gamma_\mu P_R c_\alpha)(\bar{u}_\beta \gamma^\mu P_R c_\beta)\,, \tag{5.11}$$

for the effective four-fermion operator and imply a summation over the colour indices α and β. The functions F and G are loop functions and read

$$F(x_i, x_j) = \left(\frac{x_i^2 \log x_i}{(x_i - x_j)(1 - x_i)^2} + \frac{x_j^2 \log x_j}{(x_j - x_i)(1 - x_j)^2} + \frac{1}{(1 - x_i)(1 - x_j)} \right), \tag{5.12}$$

$$G(x_i, x_j) = -\left(\frac{\sqrt{x_i x_j} x_i \log x_i}{(x_i - x_j)(1 - x_i)^2} + \frac{\sqrt{x_i x_j} x_j \log x_j}{(x_j - x_i)(1 - x_j)^2} + \frac{\sqrt{x_i x_j}}{(1 - x_i)(1 - x_j)} \right), \tag{5.13}$$

with $x_i = m_{\chi_i}^2 / m_\phi^2$. Note that both loop functions have the same sign within the interval $x_i \in [0, 1]$ and even satisfy $2G(1, 1) = F(1, 1)$ for $x_i = x_j = 1$. Hence, the two diagrams shown in Figure 5.6 can interfere destructively due to the relative sign in Equation (5.10). This effect is well known from SUSY, where the box diagram contains gluinos and squarks [154]. It is important to note however, that in contrast to the squark–gluino couplings, the coupling matrix λ is not flavour-universal and thus a destructive interference can only happen if the pre-factors of the two loop functions F and G in Equation (5.10) have the same sign. We return to this interference in our numerical analysis.

The effective Hamiltonian from Equation (5.10) can be used in order to express the off-diagonal elements of the $D^0 - \bar{D}^0$ mass matrix as

$$\begin{aligned} M_{12}^{D,\,\text{NP}} &= \frac{1}{2m_{D^0}} \langle \bar{D}^0 | \, \mathcal{H}_{\text{eff}}^{\Delta C=2,\,\text{NP}} \, | D^0 \rangle^* \\ &= \frac{\eta_D m_{D^0} f_D^2 \hat{B}_D}{384\pi^2 m_\phi^2} \sum_{ij} \lambda_{uj}^* \lambda_{ci} \Big[\lambda_{ui}^* \lambda_{cj} \cdot F(x_i, x_j) - 2\lambda_{uj}^* \lambda_{ci} \cdot G(x_i, x_j) \Big]\,, \end{aligned} \tag{5.14}$$

where we have used

$$\langle \bar{D}^0 | \, Q_{uc}^{VRR}(\mu) \, | D^0 \rangle = \frac{2}{3} m_{D^0}^2 f_D^2 \hat{B}_D\,, \tag{5.15}$$

for the hadronic matrix element. In this expression, f_D and $\hat{B}_D$ are the decay constant and the bag parameter, respectively, which are both calculated in lattice QCD at the

low-energy scale $\mu = 3\,\text{GeV}$ [155, 156]. The parameter η_D in Equation (5.14) accounts for threshold corrections that are generated when matching the effective theory and the SM as well as for *next-to-leading order* (NLO) contributions induced by the renormalisation group running between the weak scale with $\mu = M_W$ and the low-energy scale $\mu = 3\,\text{GeV}$ [157]. As far as the matching between the SM and our simplified DMFV model is concerned, the mediator ϕ will contribute to the running of the strong coupling α_s since it carries colour charge. However, we expect this contribution to be small as it is suppressed by two powers of the NP scale m_ϕ, for which we have found $m_\phi \gtrsim 1\,\text{TeV}$ in Section 5.1. Hence, we follow Reference [20–22] and neglect these matching corrections. Also note that the NP scale is far above the D^0 meson scale, and thus the diagrams of Figure 5.6 cannot contribute to the absorptive part Γ_{12}^D of the mixing matrix, as they only generate off-shell contributions.

In the numerical analysis of the flavour constraints we again ignore the mass splittings from Equation (4.15) between the different dark flavours χ_i. Inserting these corrections into Equation (5.14) would lead to higher-order DMFV corrections of order $\mathcal{O}(\lambda^6)$ which we expect to be small. In fact, we have checked numerically that including these corrections only leads to differences of a few percent for the loop functions $F(x_i, x_j)$ and $G(x_i, x_j)$. We hence set $x_i = x_j = x$ in Equation (5.14) and perform the sum to find

$$M_{12}^{D,\text{NP}} = \frac{\eta_D m_{D^0} f_D^2 \hat{B}_D}{384\pi^2 m_\phi^2} \Big[\xi_f \cdot f(x) - 2\,\xi_g \cdot g(x)\Big]\,, \tag{5.16}$$

where we have defined the factors

$$\xi_f = \sum_{ij} \lambda_{ui}^* \lambda_{ci} \lambda_{uj}^* \lambda_{cj} = \left(\lambda\lambda^\dagger\right)_{cu}^2\,, \tag{5.17}$$

$$\xi_g = \sum_{ij} \lambda_{ci} \lambda_{ci} \lambda_{uj}^* \lambda_{uj}^* = \left(\lambda\lambda^T\right)_{cc} \left(\lambda\lambda^T\right)_{uu}^*\,, \tag{5.18}$$

and the special case loop functions

$$f(x) = \lim_{y\to x} F(x,y) = \frac{1+x}{(1-x)^2} + \frac{2x}{(1-x)^3}\log x\,, \tag{5.19}$$

$$g(x) = \lim_{y\to x} G(x,y) = -\frac{2x}{(1-x)^2} - \frac{x(1+x)}{(1-x)^3}\log x\,. \tag{5.20}$$

Using these expression we can now calculate the NP contributions to the neutral D meson mixing observables x_{12}^D and ϕ_{12}^D defined as

$$x_{12}^D = 2\,\tau_{D^0}\,|M_{12}^D| \;\; = 2\,\tau_{D^0}\,|M_{12}^{D,\text{SM}} + M_{12}^{D,\text{NP}}|\,, \tag{5.21}$$

$$\phi_{12}^D = \text{Arg}\left(\frac{M_{12}^D}{\Gamma_{12}^D}\right) = \text{Arg}\left(M_{12}^{D,\text{SM}} + M_{12}^{D,\text{NP}}\right)\,. \tag{5.22}$$

Note that in ϕ_{12}^D we have set $\Gamma_{12}^{D,\text{NP}} = 0$ for the above explained reason and also neglected $\Gamma_{12}^{D,\text{SM}}$ as it is real to an excellent approximation in the SM in the standard parametrisation of the *Cabibbo–Kobayashi–Maskawa* (CKM) matrix.

Constraints from $D^0 - \bar{D}^0$ Mixing

The numerical values of the constants in Equation (5.16) as well as the model independent experimental limits on x_{12}^D and ϕ_{12}^D are gathered in Table 5.1. As far as the SM contributions to x_{12}^D and ϕ_{12}^D are concerned, we neglect the CP-violating phase $\phi_{12}^{D,\text{SM}}$ as

it is estimated to be of order $\mathcal{O}(10^{-3})$ [160], i.e. we assume $M_{12}^{D,\mathrm{SM}}$ to be real. The SM contribution to x_{12}^D on the other hand is dominated by non-perturbative long-distance effects and thus suffers from larger theory uncertainties. Since estimations predict values of order $\mathcal{O}(10^{-2})$ [161], considering the large uncertainties we conservatively assume the SM contribution to lie within the range

$$x_{12}^{D,\mathrm{SM}} \in [-3\%, 3\%]\,. \tag{5.23}$$

Using these assumptions one can derive an upper limit for the real and imaginary part of $M_{12}^{D,\mathrm{NP}}$ by demanding the total values of x_{12}^D and ϕ_{12}^D to lie within their 95% C.L. given in Table 5.1. The $D^0 - \bar{D}^0$ mixing limits then reduce to

$$\mathrm{Re}\, M_{12}^{D,\mathrm{NP}} \leq 2.91 \times 10^{-14}\,\mathrm{GeV}\,, \tag{5.24}$$

$$\mathrm{Im}\, M_{12}^{D,\mathrm{NP}} \leq 2.47 \times 10^{-16}\,\mathrm{GeV}\,. \tag{5.25}$$

The results of the numerical analysis are gathered in Figures 5.7–5.9. The viable mixing angles θ_{ij} in dependence of the splittings $\Delta_{ij} = |D_i - D_j|$ are shown in Figure 5.7 for the masses $m_\phi > m_\chi$ and $m_\phi = m_\chi$[12]. For both of these cases the most restrictive constraints are placed on the mixing angle θ_{12}, which we find to strongly depend on the splitting Δ_{12}. A large splitting requires a vanishing mixing angle while the latter can be chosen freely if Δ_{12} is small. The same qualitative behaviour also holds true for θ_{13} and θ_{23}. However, for these mixing angles we find that in spite of a lower point density, large values are allowed even if the corresponding splitting Δ_{ij} is not small. Vanishing splittings generally lead to free mixing angles, since the factor ξ_f from Equation (5.17) approaches zero in the limit of degenerate couplings D_i as the product $\lambda\lambda^\dagger = UD^2U^\dagger$ becomes diagonal. Comparing Figure 5.7a and 5.7b shows that the case $m_\phi = m_\chi$ only leads to a marginally weakened bound on the splittings Δ_{ij}.

Since the factor ξ_g is proportional to the diagonal elements of $\lambda\lambda^T$ and its complex conjugate, the contribution from the crossed box diagram of Figure 5.6b does not vanish in the limit of zero mixing angles and hence puts restrictions on the absolute value of the couplings D_i. These restrictions are illustrated in Figure 5.8 where we show the viable values in the $D_i - D_j$ plane. The most stringent constraints here are placed on the couplings D_1 and D_2 and we find most viable points within the interval $D_1, D_2 \in [0.0, 0.5]$, see

Table 5.1 | Numerical values and limits used for the analysis of the $D^0 - \bar{D}^0$ mixing constraints [155–159]. The limits on x_{12}^D and ϕ_{12}^D are given at 95% C.L. and were obtained from the *Heavy Flavour Averaging Group*'s (HFLAV) website [159].

$\hat{B}_D$	0.75 ± 0.02
f_D	$209.0 \pm 2.4\,\mathrm{MeV}$
η_D	0.772
m_{D^0}	$1864.83 \pm 0.05\,\mathrm{MeV}$
τ_{D^0}	$410.1 \pm 1.5\,\mathrm{fs}$
x_{12}^D	$[0.21\%, 0.63\%]$
ϕ_{12}^D	$[-2.8°, 1.7°]$

[12] Note that the latter case of an equal DM and mediator mass is excluded by the DM stability condition $m_\chi < m_\phi$. We nevertheless also discuss this case here in order to provide a more general discussion of the flavour constraints and the possible interference of the two box diagrams from Figure 5.6.

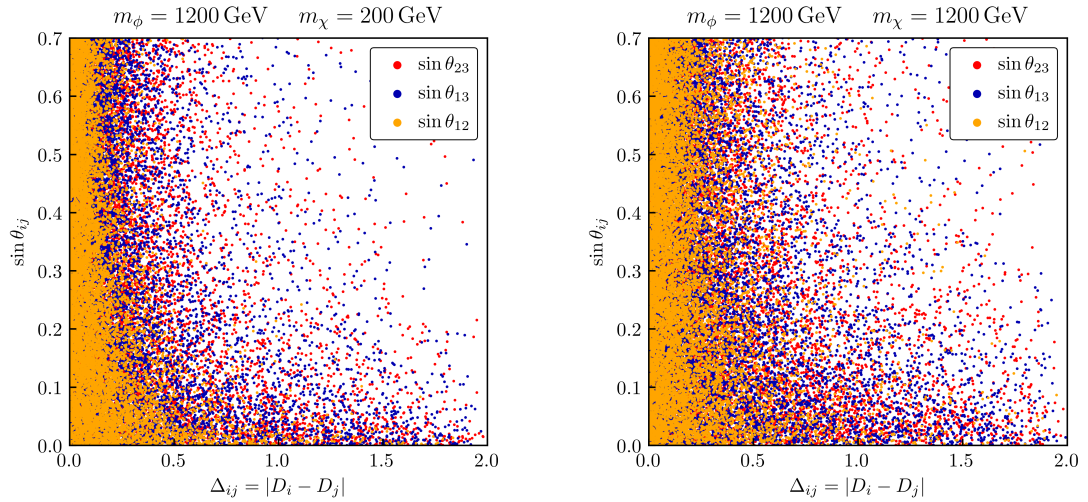

(a) $m_\phi = 1200\,\text{GeV}$ and $m_\chi = 200\,\text{GeV}$ **(b)** $m_\phi = 1200\,\text{GeV}$ and $m_\chi = 1200\,\text{GeV}$

Figure 5.7 | $D^0 - \bar{D}^0$ mixing constraints on the mixing angles θ_{ij} as a function of the splitting $\Delta_{ij} = |D_i - D_j|$ for two choices of m_ϕ and m_χ.

Figure 5.8a. The coupling D_3 on the other hand, can be chosen freely which is illustrated in Figure 5.8b. This is due to the fact that ξ_g mainly depends on the couplings D_1 and D_2 which parametrise the coupling of DM to up and charm quarks. In the limit of vanishing mixing angles and phases, this factor reduces to $\xi_g \approx D_1^2 D_2^2$ and hence the contributions from the crossed box diagram can also be sufficiently suppressed to satisfy the bound if either of the couplings D_1 or D_2 is small while the other one may be large. We have checked this behaviour to also hold true in the case of other choices for the masses m_χ and m_ϕ.

This allows us to conclude that, barring cancellations between the two contributions shown in Figure 5.6, the $D^0 - \bar{D}^0$ mixing constraints demand

$$\begin{aligned} 0 < D_3 &\leq 2.0\,, \\ 0 < D_1, D_2 &\leq 0.5\,, \end{aligned} \tag{5.26}$$

while it allows for large mixing angles within this part of the parameter space. Comparing this to our findings from Section 5.1, we find that both results perfectly match each other as the LHC constraints are also satisfied within these ranges. It is however important to note that while the majority of viable points in Figure 5.8 lie within the region identified above, there are also some that are significantly outside of it. In these cases, the viable parameter space is extended due to the aforementioned destructive interference between the two box diagrams shown in Figure 5.6.

In the following we want to illustrate how this interference effect extends the viable parameter space compared to the case of Dirac DM. To this end we show the imaginary parts of the coupling combinations ξ_f and ξ_g defined above for two choices of m_ϕ and m_χ in Figure 5.9. We find that for both mass choices the allowed points scatter around a linear function, which can be explained analytically as follows. The constraints on ϕ_{12}^D given in Table 5.1 are very stringent and roughly demand $\phi_{12}^D \simeq 0$, where ϕ_{12}^D is given by

$$\phi_{12}^D = \arctan \frac{\text{Im}\, M_{12}^{D,\text{NP}}}{\text{Re}\, M_{12}^{D,\text{NP}} + \text{Re}\, M_{12}^{D,\text{SM}}}\,. \tag{5.27}$$

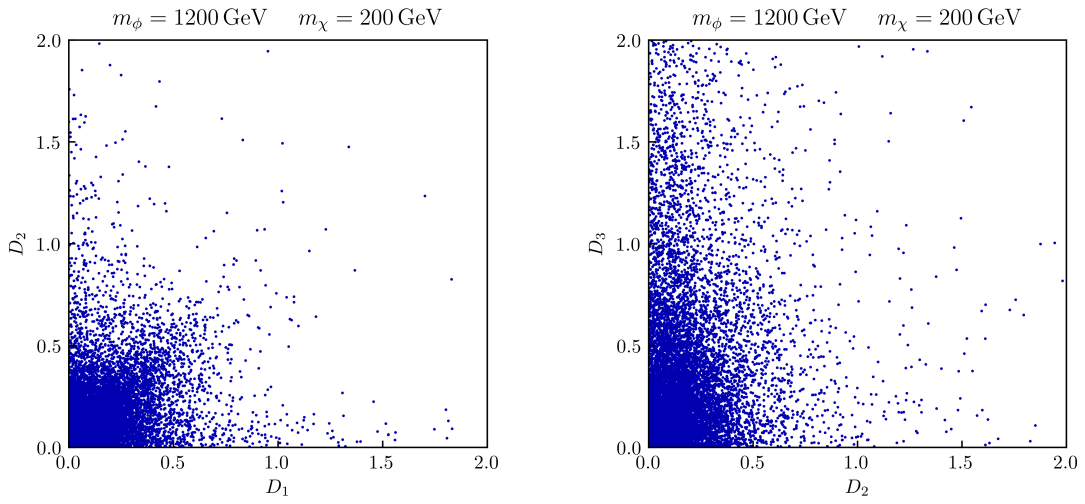

(a) $D_1 - D_2$ plane **(b)** $D_2 - D_3$ plane

Figure 5.8 | Viable points in the $D_i - D_j$ plane for $m_\phi = 1200\,\text{GeV}$ and $m_\chi = 200\,\text{GeV}$ when considering the $D^0 - \bar{D}^0$ mixing constraints.

Hence, the experimental bound on the CP-violating phase forces the imaginary part of $M_{12}^{D,\text{NP}}$ to be small, which for the factors ξ_f and ξ_g translates to the condition

$$\text{Im}\,\xi_f \approx \text{Im}\,\xi_g \frac{2g(x)}{f(x)}\,. \tag{5.28}$$

This can be seen explicitly in Figure 5.9a where we show the case of equal DM and mediator masses, i.e. $x = 1$. In this case the loop functions satisfy $2g(1) = f(1) = 1/3$ and hence Equation (5.28) reduces to $\text{Im}\,\xi_f \approx \text{Im}\,\xi_g$ yielding a slope that is equal to one. As can be seen in Figure 5.9b, for any other point in the mass plane $m_\phi - m_\chi$ the slope of the linear function that the allowed points scatter around is given by the actual value of $2g(x)/f(x)$. Note that we also found a number of allowed points well beyond the ranges for ξ_f and ξ_g shown in Figure 5.9 in our scan. While maximum values as large as $\text{Im}\,\xi_{f,g} \sim \mathcal{O}(1)$ can be reached, the point density decreases for increasing imaginary parts of both coupling factors.

The scattering of the points in Figure 5.9 around the linear relation from Equation (5.28) is tied to the fact that the experimental bound actually requires the CP-violating phase to lie within the range given in Table 5.1 instead of demanding it to be zero. Also, we here only show the imaginary parts of the factors $\xi_{f,g}$ constrained by the CP violation in $D^0 - \bar{D}^0$ mixing, since the CP-conserving and therefore real amplitude $M_{12}^{D,\text{SM}}$ suffers from large non-perturbative uncertainties. Generally, the same interference can also be seen for $M_{12}^{D,\text{SM}}$ with the sole difference of a larger scattering around the corresponding linear function for the real parts of $\xi_{f,g}$ due to these uncertainties.

For Dirac fermionic DM the crossed box diagram from Figure 5.6b proportional to ξ_g is absent, and hence the limit on ϕ_{12}^D requires $\text{Im}\,\xi_f \simeq 0$ in that case. We therefore conclude that the Majorana nature of the particles χ_i indeed extends the viable parameter space of our model with respect to the Dirac case and the above discussed destructive interference particularly allows for large imaginary parts of ξ_f and ξ_g in our model. We return to the practical implication of this finding in Section 5.6.

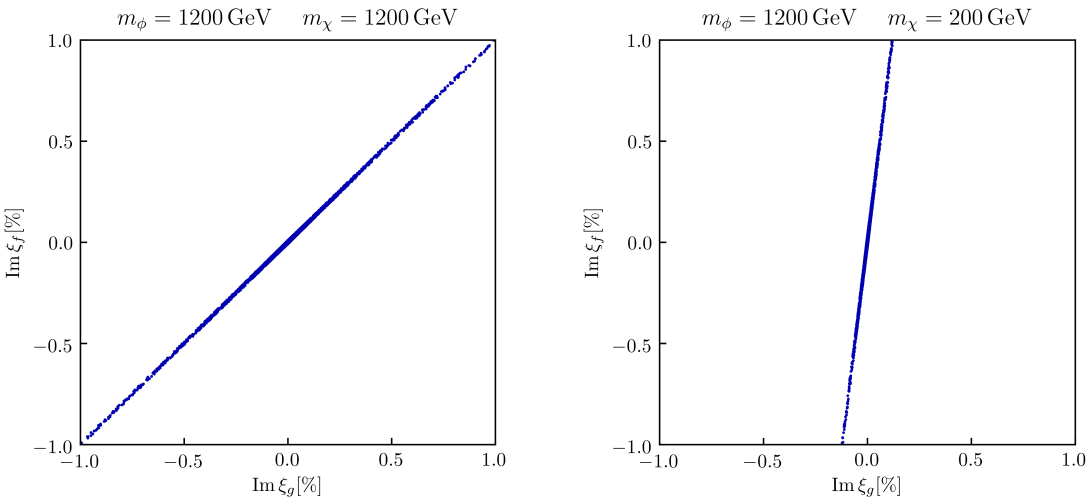

(a) $m_\phi = 1200\,\text{GeV}$ and $m_\chi = 1200\,\text{GeV}$ **(b)** $m_\phi = 1200\,\text{GeV}$ and $m_\chi = 200\,\text{GeV}$

Figure 5.9 | Imaginary part of the two factors ξ_f and ξ_g in percent.

5.3 Dark Matter Relic Density

As discussed in detail in Chapter 4 our model assumes the lightest dark flavour[13] to form the observed DM of the Universe. Hence, demanding that the abundance of χ_3 today equals the measured DM relic density also places constraints on the coupling matrix λ. We dedicate this section to the analysis of these constraints.

In terms of the production mechanism of a cold dark relic we assume a thermal freeze-out of DM as discussed in Section 2.2 and particularly focus on the two freeze-out scenarios defined in Section 3.2. To this end, we first define both scenarios numerically and then discuss relevant processes for the calculation of the thermally averaged annihilation rate. We conclude this section by analysing the allowed structure of λ within the context of the DM relic density bound for both freeze-out scenarios.

DM Annihilations and Thermal Freeze-Out

The two freeze-out scenarios identified in Section 3.2 depend on the mass splittings

$$\Delta m_{i3} = \frac{m_{\chi_i}}{m_{\chi_3}} - 1\,, \tag{5.29}$$

between the heavier flavours with $i \in \{1, 2\}$ and the lightest flavour χ_3. For this model we define both scenarios numerically as follows:

- In the QDF scenario we demand that the splittings Δm_{i3} are smaller than 1% and hence set $\eta = -0.01$ in Equation (4.15). As DMFV corrections to the DM mass matrix are at least generated at the one-loop level through RG running, smaller absolute values for η would be implausible.

- The SFF scenario is defined through a significant splitting and hence we here demand that Δm_{i3} is larger than 10% but at the same time small enough to ensure the

[13] Remember that we have conventionally chosen the third generation to be the lightest of all dark particles.

(a) t-channel annihilation **(b)** u-channel annihilation

Figure 5.10 | Feynman diagrams for the annihilation of two DM particles into two SM quarks at LO. Note that the u-channel diagram only exists for Majorana fermions.

convergence of Equation (4.15). We thus choose $\eta = -0.0575$ for this scenario which yields maximum splittings of $\Delta m_{i3}^{\max} \simeq 30\%$ for couplings $D_i \in [0, 2]$.

We further assume the freeze-out to occur at $T_f \approx m_{\chi_3}/20$ in both scenarios.

The relevant annihilation processes for the thermal freeze-out of DM are gathered in Figure 5.10. Note that the coannihilation process $\chi_i \phi \to q_j g$ where a ϕ is exchanged in the t-channel also exists but suffers from a suppression by the Boltzmann factor

$$k = e^{-\frac{m_\phi - m_{\chi_3}}{T_f}} \simeq e^{-20\frac{m_\phi - m_{\chi_3}}{m_{\chi_3}}}, \tag{5.30}$$

while the process $\phi^\dagger \phi \to \bar{q}_i q_j$ is even suppressed by k^2. Both of these annihilations[14] are thus only relevant for very small splittings between m_ϕ and m_{χ_3}. We neglect these contributions in the following and only consider the two diagrams shown in Figure 5.10 as we are not interested in the near-degeneracy limit $m_\phi \approx m_{\chi_3}$ in our analysis.

Evaluating both diagrams we find

$$\overline{|M|^2} = \overline{|M_t|^2} + \overline{|M_u|^2} - 2\,\mathrm{Re}\,\overline{M_{tu}}\,, \tag{5.31}$$

for the spin-, colour- and flavour-averaged squared amplitude $\overline{|M|^2}$. The relative sign of the interference term $\overline{M_{tu}}$ between the t- and u-channel contributions in this expression is due to the crossing of fermion lines in the diagram of Figure 5.10b. The summands in Equation (5.31) are given as

$$\overline{|M_t|^2} = \frac{3}{4} \sum_{ij} \sum_{kl} c^t_{ijkl} \frac{(m^2_{\chi_i} + m^2_{q_k} - t)(m^2_{\chi_j} + m^2_{q_l} - t)}{(t - m^2_\phi)^2}\,, \tag{5.32}$$

$$\overline{|M_u|^2} = \frac{3}{4} \sum_{ij} \sum_{kl} c^u_{ijkl} \frac{(m^2_{\chi_i} + m^2_{q_l} - u)(m^2_{\chi_j} + m^2_{q_k} - u)}{(u - m^2_\phi)^2}\,, \tag{5.33}$$

$$\overline{M_{tu}} = \frac{3}{4} \sum_{ij} \sum_{kl} c^{tu}_{ijkl} \frac{m_{\chi_i} m_{\chi_j} (s - m^2_{q_k} - m^2_{q_l})}{(u - m^2_\phi)(t - m^2_\phi)}\,, \tag{5.34}$$

where s, t and u are Mandelstam variables and the indices i, j, k and l are flavour indices. The factor of $3/4$ in each of these expressions is due to the colour and spin average and the couplings c^α are given as

$$c^t_{ijkl} = |\tilde{\lambda}_{ki}|^2 |\tilde{\lambda}_{lj}|^2\,, \tag{5.35}$$

[14] Note that there also exist corresponding charge conjugated diagrams for both of these processes, while the latter case, i.e. the case of mediator pair annihilation can additionally produce same sign quarks in the final state.

$$c^{u}_{ijkl} = |\tilde{\lambda}_{li}|^2 |\tilde{\lambda}_{kj}|^2 \,, \tag{5.36}$$

$$c^{tu}_{ijkl} = \tilde{\lambda}^*_{ki} \tilde{\lambda}_{lj} \tilde{\lambda}^*_{li} \tilde{\lambda}_{kj} \,, \tag{5.37}$$

where $\tilde{\lambda}$ is defined according to Equation (4.18).

For the calculation of the thermally averaged annihilation cross section we use the low-velocity expansion discussed at the end of Section 2.2 and adopt the expression from Equation (3.12), i.e.

$$\langle \sigma v \rangle_{\text{eff}} = f_{\text{sc}} \left[a + b \langle v^2 \rangle + \mathcal{O}\left(\langle v^4 \rangle \right) \right] \,, \tag{5.38}$$

where $\langle v^2 \rangle = 6T_f/m_\chi \approx 0.3$ and we have set $f_{\text{nat}} = 1$ since DM is a Majorana fermion in our model. As discussed in Section 3.2, the factor f_{sc} depends on the freeze-out scenario and is equal to one for the SFF scenario while it takes the value $f_{\text{sc}} = 1/9$ for the QDF case. The coefficients a and b corresponding to the s- and p-wave contributions to $\langle \sigma v \rangle_{\text{eff}}$ have been calculated using the techniques provided in Reference [123, 124] and can be found in Appendix A.1. In the limit of vanishing final state masses $m_{q_k} = m_{q_l} = 0$ and equal initial state masses $m_{\chi_i} = m_{\chi_j} = m_\chi$ they are given by

$$a = \frac{3}{32\pi m_\chi^2 (1+\mu)^2} \sum_{ij} \sum_{kl} \left(c^{t}_{ijkl} + c^{u}_{ijkl} - 2\, c^{tu}_{ijkl} \right) \,, \tag{5.39}$$

$$\begin{aligned} b = \frac{1}{128\pi m_\chi^2 (1+\mu)^4} \sum_{ij} \sum_{kl} \Big(& 22\, c^{tu}_{ijkl} - 7 \left(c^{t}_{ijkl} + c^{u}_{ijkl} \right) \\ & - 18 \left(c^{t}_{ijkl} + c^{u}_{ijkl} - 2\, c^{tu}_{ijkl} \right) \mu + \left(c^{t}_{ijkl} + c^{u}_{ijkl} + 6\, c^{tu}_{ijkl} \right) \mu^2 \Big) \,, \end{aligned} \tag{5.40}$$

where we have used $\mu = m_\phi^2/m_\chi^2$. Note that using equal initial state masses in the expressions above is justified for both freeze-out scenarios. For a QDF the mass splittings between the different dark flavours are negligibly small[15], while for a SFF the masses of the two annihilating particles are indeed equal as only χ_3 contributes to the freeze-out. For the latter freeze-out scenario m_χ thus has to be replaced by m_{χ_3} in the expressions above. For the same reason however, the sum over initial state flavours in Equation (5.39) and (5.40) needs to be omitted for the SFF scenario and the couplings c^α reduce to

$$c^{t}_{33kl} = c^{u}_{33kl} = c^{tu}_{33kl} = c_{kl} = |\tilde{\lambda}_{k3}|^2 |\tilde{\lambda}_{l3}|^2 \,. \tag{5.41}$$

This in turn causes the s-wave coefficient a from Equation (5.39) to vanish as we find

$$a = 0 \,, \tag{5.42}$$

$$b = \sum_{kl} c_{kl} \frac{1+\mu^2}{16\pi m_\chi^2 (1+\mu)^4} \,, \tag{5.43}$$

i.e. we encounter a p-wave suppression of annihilations into massless final states for the SFF scenario.

Further remarks are in place regarding the sum over final state flavours in the expressions for the s- and p-wave coefficients of both scenarios. It is important to note that the final state with a top–antitop pair is kinematically forbidden for masses $m_\chi < m_t$, where m_t is the top quark mass. Hence, in this case only final states with a single top-flavoured quark are allowed and the case $k = l = 3$ needs to be excluded from the sum. For even smaller masses $m_\chi < m_t/2$, the former final states become kinematically inaccessible as well and the sum over final state flavours hence reduces to $k, l \in \{1, 2\}$.

[15] We have checked numerically that using different initial state masses in the QDF scenario only causes negligible differences in $\langle \sigma v \rangle_{\text{eff}}$ of order $\mathcal{O}(1\%)$.

Constraints from the DM Relic Density

In order to analyse the constraints that the observed relic density places on the model parameters numerically, we use the partial wave expansion for $\langle\sigma v\rangle_{\text{eff}}$ discussed above and compare it with the annihilation rate necessary to produce the experimentally observed amount of DM. For masses $m_{\chi_3} > 10\,\text{GeV}$ the latter rate is found to be approximately constant and reads [162, 163]

$$\langle\sigma v\rangle_{\text{eff}}^{\text{exp}} = 2.2 \times 10^{-26}\,\text{cm}^3/\text{s}\,. \tag{5.44}$$

For the calculation of $\langle\sigma v\rangle_{\text{eff}}$ we include the s- and p-wave contributions in both scenarios and use the coefficients a and b with their full final state mass dependence as given in Appendix A.1. To derive constraints on λ and the NP masses we demand that $\langle\sigma v\rangle_{\text{eff}}$ equals the experimental value from Equation (5.44) within a 10% tolerance region. The numerical values for the quark masses are adopted from Reference [158].

The results of the numerical analysis are gathered in Figure 5.11 and 5.12. In Figure 5.11a we show the viable values in the $D_1 - D_2$ plane for the QDF scenario. Remembering that the QDF mass splitting condition itself also restricts the values of these two couplings, the overall pattern corresponds to the overlap of the areas in which both the relic density constraint as well as the QDF mass splitting condition are satisfied. We find that these areas exhibit a circular pattern and that smaller DM masses m_χ require larger couplings D_1 and D_2. Since in the QDF scenario the annihilation rate is not p-wave suppressed, the leading term is given by the s-wave contribution from Equation (5.39). In the limit of a negligible top quark mass $m_t \ll m_\chi$ the annihilation rate reduces to

$$\langle\sigma v\rangle_{\text{eff}}^{\text{QDF}} = \frac{1}{96\pi}\frac{m_\chi^2}{\left(m_\chi^2 + m_\phi^2\right)^2}\sum_{ij}\sum_{kl}\left(c^t_{ijkl} + c^u_{ijkl} - 2\,c^{tu}_{ijkl}\right) + \mathcal{O}\left(\langle v^2\rangle\right)\,, \tag{5.45}$$

and one can write for the sum over the couplings c^α

$$\sum_{ij}\sum_{kl} c^t_{ijkl} = \sum_{ij}\sum_{kl} c^u_{ijkl} = \text{Tr}\left[\tilde{\lambda}^\dagger\tilde{\lambda}\right]^2 = \text{Tr}\left[D^2\right]^2\,, \tag{5.46}$$

$$\sum_{ij}\sum_{kl} c^{tu}_{ijkl} = \text{Tr}\left[\tilde{\lambda}^T\tilde{\lambda}^*\tilde{\lambda}^\dagger\tilde{\lambda}\right] = \text{Tr}\left[Od^2O^TD^2Od^{*2}O^TD^2\right]\,. \tag{5.47}$$

While the first of these two traces can be evaluated trivially and reads

$$\text{Tr}\left[D^2\right]^2 = \left(D_1^2 + D_2^2 + D_3^2\right)^2\,, \tag{5.48}$$

the second one is more complex. It is bounded from above and its maximum value given for vanishing mixing angles ϕ_{ij} and phases γ_i reads[16]

$$\text{Tr}\left[Od^2O^TD^2Od^{*2}O^TD^2\right] \leq \text{Tr}\left[D^4\right] = D_1^4 + D_2^4 + D_3^4\,. \tag{5.49}$$

We hence conclude that the destructive interference between the t- and u-channel diagrams shown in Figure 5.10 can never lead to a p-wave suppression in the QDF scenario, since we find the s-wave contribution to the annihilation rate to be bounded from below, i.e. we find

$$\langle\sigma v\rangle_{\text{eff}}^{\text{QDF}} \geq \frac{1}{24\pi}\frac{m_\chi^2}{\left(m_\chi^2 + m_\phi^2\right)^2}\left(D_1^2D_2^2 + D_1^2D_3^2 + D_2^2D_3^2\right) + \mathcal{O}\left(\langle v^2\rangle\right)\,. \tag{5.50}$$

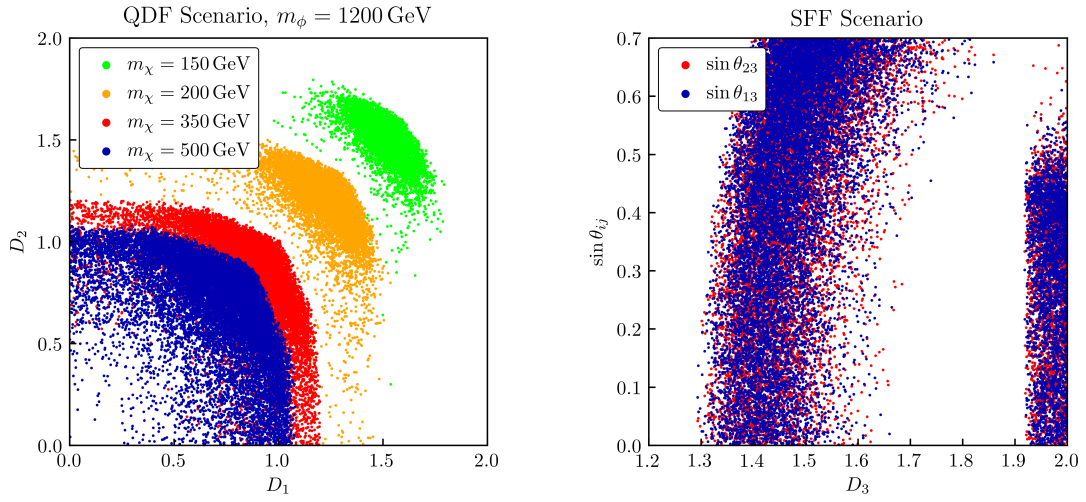

(a) $D_1 - D_2$ plane in the QDF scenario for varying m_χ and $m_\phi = 1200\,\text{GeV}$

(b) Viable $\sin\theta_{i3}$ and D_3 in the SFF scenario for $m_\chi = 220\,\text{GeV}$ and $m_\phi = 950\,\text{GeV}$

Figure 5.11 | Restrictions that the relic density constraints place on the model parameters for both freeze-out scenarios.

This short analysis explains the circular pattern in Figure 5.11a for large m_χ, as the relic density constraint in this case reduces to

$$\left(D_1^2 + D_2^2 + D_3^2\right)^2 - \text{Tr}\left[Od^2O^T D^2 Od^{*2} O^T D^2\right] \approx \text{const.}\,, \tag{5.51}$$

for a given point in the $m_\phi - m_\chi$ plane[17]. This condition corresponds to the shell of a three-dimensional sphere which is deformed by the second trace in the equation above and the restrictions that the QDF mass splitting condition puts on the couplings D_i. The green and orange points in Figure 5.11a further show that we encounter the same behaviour for $m_\chi \approx m_t$ and particularly for $m_\chi < m_t$ where the final state with a top–antitop pair becomes inaccessible. We further find that small DM masses require large couplings due to the analytically evident m_χ dependence of $\langle\sigma v\rangle_{\text{eff}}$ but also due to the reduced number of total annihilation channels in the regimes $m_\chi < m_t$ and $m_\chi < m_t/2$, respectively. As we have limited the couplings to $D_i \in [0, 2]$ this poses a lower limit on the DM mass m_χ.

Figure 5.11b shows the restrictions that the relic density constraints place on the mixing angles θ_{13} and θ_{23} as well as the coupling D_3 in the SFF scenario. We here show the case of top-flavoured DM, i.e. the case where the lightest dark flavour couples predominantly to the top quark. We find that small couplings D_3 require the mixing angles to be small as well. The reason is that for top-flavoured DM, large mixing angles enhance annihilations into final states with either only one top-flavoured quark (top or antitop quark) or no top flavour at all. As discussed above, the latter annihilation channels suffer from a p-wave suppression due to the smallness of the up and charm quark masses. While this is not the case for the channel with a single top-flavoured quark in the final state, these annihilations are still suppressed by the smallness of the second final state quark's mass. They are thus roughly three orders of magnitude smaller than the contributions to the

[16] The mixing angles ϕ_{ij} and the phases γ_i were defined in Equation (4.10) and (4.12), respectively.

[17] We have checked numerically that the trace in Equation (5.51) is typically much smaller than the first summand.

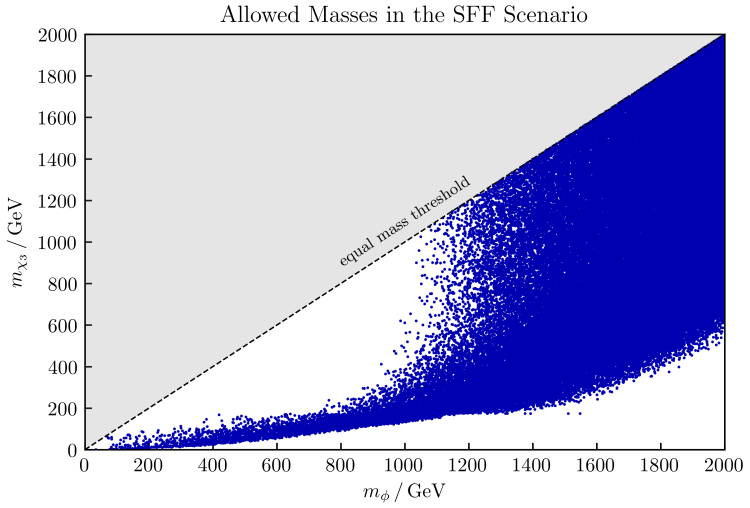

Figure 5.12 | Relic density constraints on the $m_\phi - m_{\chi_3}$ plane for the SFF scenario.

s-wave coefficient a from annihilations into a top–antitop pair. We conclude that large mixing angles only lead to suppressed additional annihilations while they at the same time reduce the rate of the dominant annihilation channel $\chi_3\chi_3 \to t\bar{t}$ and therefore also reduce the overall annihilation rate. Hence, for the smallest allowed values of D_3 the mixing angles may not grow too large, as this would lead to a too small annihilation rate or a too large relic density, respectively. For growing values of D_3 large mixing angles become viable as the annihilation rate into a top–antitop pair is increased in this case. Once the coupling grows as large as $D_3 \gtrsim 1.65$ however, the rate $\chi_3\chi_3 \to t\bar{t}$ tends to be too large and hence sizeable mixing angles are required in order to suppress the total annihilation rate through the mechanism explained above. It is important to note that this suppression mechanism becomes weaker for increasing values of D_3. This is due to the fact that the p-wave suppressed annihilations into light quarks as well as annihilations into final states with a single top-flavoured particle also grow with D_3. Thus, for values $D_3 \gtrsim 1.80$ the total annihilation rate cannot be suppressed sufficiently any longer through large mixing angles, such that the resulting DM density is always too small. This only holds true as long as annihilations into a top–antitop pair are possible: once the DM mass drops below the top quark mass threshold, these annihilations become kinematically inaccessible. In the limit of vanishing mixing angles ϕ_{ij} and phases γ_i the DM mass of top-flavoured DM is given by $m_{\chi_3} \approx m_\chi(1 - |\eta|D_3^2)$, i.e. m_{χ_3} decreases with increasing values of D_3. We hence find that for $D_3 \gtrsim 1.92$ the annihilation channel $\chi_3\chi_3 \to t\bar{t}$ becomes forbidden and the total annihilation rate is thus pushed back into the tolerance region. In this case only very large mixing angles θ_{i3} are excluded as they would further enhance the accessible annihilation channels and lead to a too large annihilation rate or too small DM relic density, respectively.

Note that in Figure 5.11b there are no differences between the two mixing angles θ_{13} and θ_{23}, which is due to the fact that we do not fix the value of one angle while looking at the other and vice versa. Also recall that we only illustrate the case of top-flavoured DM in Figure 5.11b. Since we allow for a rearrangement of the matrix W from Equation (4.17) in order to ensure that χ_3 is always the lightest state, its mass corrections can generally also depend on D_1 or D_2 which corresponds to the cases of up- and charm-flavoured DM. For these cases the parameters shown in Figure 5.11b are basically free and the only constraint

comes from the SFF scenario itself. Its mass splitting condition here demands the coupling D_3 to be sufficiently smaller than D_1 or D_2, respectively.

In Figure 5.12 we show the viable masses m_ϕ and m_{χ_3} in the SFF scenario. Just as for the QDF scenario, the upper limit on the couplings D_i again translates into a lower limit on the DM mass, since the annihilation rate is roughly proportional to the sum over $m_{\chi_3}^2 D_i^4$. However, in this case we additionally find an upper bound on m_{χ_3} for mediator masses $m_\phi \lesssim 1000\,\text{GeV}$ which can be explained as follows. For large DM masses the couplings need to be correspondingly small in order to keep the annihilation rate within the tolerance interval. The mass splitting condition of the SFF scenario however, always forces one coupling D_i to be significantly larger than the other two[18]. Hence, the relic density constraint cannot be satisfied in the SFF scenario for arbitrarily large values of m_{χ_3} as long as the mediator mass is comparably small. Since the annihilation rate is additionally suppressed by $1/m_\phi^2$, we find that for values $m_\phi \gtrsim 1000\,\text{GeV}$ this suppression compensates for the single sizeable coupling D_i and values of the DM mass m_{χ_3} up to the equal mass threshold become viable.

5.4 Dark Matter Detection Experiments

We have seen so far that the Majorana nature of DM had important implications for the collider, flavour and relic density constraints as it generated Majorana specific contributions in all three fields. In terms of the detection phenomenology of DM, choosing it to be a Majorana fermion has even more profound implications and leads to severe differences when comparing the resulting phenomenology to the Dirac case. We hence dedicate this section to the discussion of constraints from detection experiments.

Most importantly, we expect the Majorana nature of χ to render limits from indirect detection to be very lenient. The reason is the above mentioned p-wave suppressed annihilation rate of χ_3 into up or charm flavoured final states. As the DM halo velocity in the Milky Way is approximately given by $\langle v^2 \rangle \simeq 10^{-6}$, these final states lead to a severely suppressed indirect detection signal. Annihilations into top-flavoured final states can neither lead to relevant signals, since for comparably small DM masses the annihilation rate suffers from a phase space suppression due to the large top quark mass. Since the indirect detection constraints are additionally generally less significant for large DM masses m_χ, we expect them to not place any relevant restrictions on λ at all and hence only focus on direct detection experiments in this section.

Relevant Processes for Direct Detection

The DM–nucleon scattering cross section generally splits up into a *spin-dependent* (SD) and a *spin-independent* (SI) part in the non-relativistic limit. Typically, the constraints for SI scattering are much stronger since in this case DM coherently scatters off all nucleons in the nucleus and the signal is thus enhanced. In the case of SD scattering on the other hand, such an enhancement is absent as it only couples to the modulus of the total spin, while the nucleon spins cancel in pairs [6]. It is thus often an accurate approximation to solely consider SI scatterings when analysing direct detection constraints [20–22].

For our case of Majorana DM however, the leading contributions to the SI part of the DM–nucleon scattering cross section corresponding to scalar $(\bar{\chi}\chi\bar{q}q)$ and vector $(\bar{\chi}\gamma^\mu\chi\,\bar{q}\gamma_\mu q)$ type interactions are absent. The latter interactions are identically zero, since for Majorana fermions bilinears which are antisymmetric under C parity vanish.

[18] Remember that we have chosen $\eta < 0$, i.e. the mass corrections δm_{χ_i} are always negative.

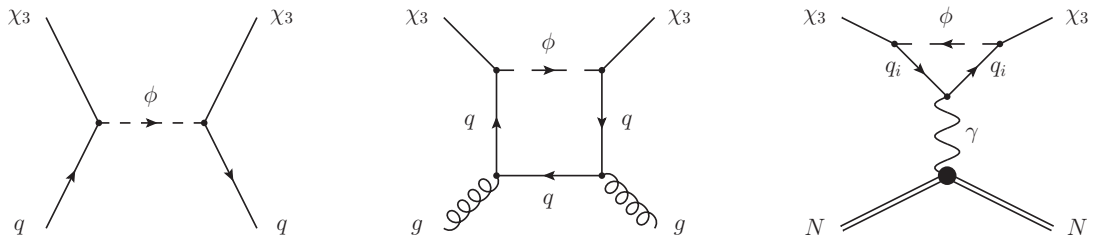

(a) tree-level scattering **(b)** DM–gluon scattering **(c)** photon penguin

Figure 5.13 | Tree-level and loop induced Feynman diagrams for DM–nucleon scattering. Note that there exist several additional DM–gluon scattering diagrams and one additional photon-mediated penguin diagram that we don't show here. All penguin diagrams can moreover be mediated by a Higgs or Z boson as well.

The scalar interactions on the other hand vanish for Majorana DM with chiral interactions, as present in our model [6,164,165]. We hence also consider SD contributions in our analysis and additionally go beyond LO when calculating the SI contributions by including one-loop induced scatterings between DM and gluons. The relevant diagrams are gathered in Figure 5.13.

Note that at the one-loop level there also exists a photon-mediated penguin diagram for SI scatterings through which DM can couple to nucleons. This interaction is shown in Figure 5.13c and is induced by the electric and magnetic dipole, the charge-radius as well as the anapole operators. There is no such contribution from the electric dipole operator $(\bar{\chi} i\sigma^{\mu\nu}\gamma_5\chi F_{\mu\nu})$ in our model, as the NP interaction Lagrangian in Equation (4.1) involves a chiral interaction and is thus not CP-violating. On the other hand, the magnetic dipole $(\bar{\chi} i\sigma^{\mu\nu}\chi F_{\mu\nu})$ as well as the charge-radius operators $(\bar{\chi}\gamma^{\mu}\chi\partial^{\nu}F_{\mu\nu})$ vanish for Majorana fermions due to the above explained reason. Thus, the only contributions are generated by the anapole moment [166], which however are found to be very small [167]. The resulting scattering cross section is far beyond the sensitivity of current experiments and we hence neglect this diagram in our analysis. The contributions from equivalent penguin diagrams mediated by a Z boson are proportional to the external momentum [166] and are hence negligible as well.

We further neglect similar one-loop penguin diagrams which are mediated by a Higgs boson instead of a photon. The impact of such a contribution has already been discussed in the context of neutralino DM in the *Minimal Supersymmetric Standard Model* (MSSM) [168,169]. In our model, the size of the effective DM–Higgs coupling depends on the Yukawa coupling of the up-type quark in the loop as well as the Higgs portal coupling $\lambda_{H\phi}$. While the process with a top quark in the loop can particularly yield a relevant contribution to SI DM–nucleon scattering, it is always possible to suppress it by choosing $\lambda_{H\phi}$ properly. Since the latter coupling is not constrained by the rest of our analysis, we follow the arguments provided in Section 4.1 and use this freedom to assume that the Higgs penguin is negligible.

We are hence left with the tree-level diagram of Figure 5.13a as well as the one-loop DM–gluon scatterings from Figure 5.13b. To calculate the resulting DM–nucleon scattering cross section we write

$$\sigma^N_{\mathrm{SD}} = \frac{3}{16\pi}\frac{m_N^2 m_{\chi_3}^2}{(m_N + m_{\chi_3})^2}\left(\sum_{q=u,d,s}\Delta q^N a_q\right)^2 , \tag{5.52}$$

for its SD part [164, 165, 170] and

$$\sigma_{\mathrm{SI}}^{N} = \frac{4}{\pi} \frac{m_N^2 m_{\chi_3}^2}{(m_N + m_{\chi_3})^2} |f_N|^2 \,, \tag{5.53}$$

for its SI part [6, 164, 165]. In these expressions a_q is the Wilson coefficient of the SD quark–nucleon interaction, Δq^N is the spin content of the nucleon $N = \{p, n\}$ in terms of the quark q and m_N is the nucleon mass. The factor f_N is the matrix element of the SI quark–nucleon interaction.

As χ_3 only couples to up-type quarks in our model, Equation (5.52) reduces to

$$\sigma_{\mathrm{SD}}^{N} = \frac{3}{16\pi} \frac{m_N^2 m_{\chi_3}^2}{(m_N + m_{\chi_3})^2} \left(\Delta u^N a_u\right)^2 \,, \tag{5.54}$$

with the corresponding Wilson coefficient

$$a_u = \frac{|\tilde{\lambda}_{u3}|^2}{m_\phi^2 - (m_{\chi_3} + m_u)^2} \,. \tag{5.55}$$

For the SI scattering cross section we follow the formalism of References [171–173] and write

$$\mathcal{L}_{\mathrm{SI}}^{\mathrm{eff}} = \sum_{q=u,d,s,c} \mathcal{L}_q^{\mathrm{eff}} + \mathcal{L}_g^{\mathrm{eff}} \,, \tag{5.56}$$

for the effective interaction Lagrangian. Scatterings between DM and quarks are described by

$$\mathcal{L}_q^{\mathrm{eff}} = f_q \bar{\chi}\chi \, \mathcal{O}_q^{(0)} + \frac{g_q^{(1)}}{m_{\chi_3}} \bar{\chi} i(\partial^\mu \gamma^\nu + \partial^\nu \gamma^\mu) \chi \mathcal{O}_{q,\mu\nu}^{(2)} + \frac{g_q^{(2)}}{m_{\chi_3}^2} \bar{\chi} (i\partial^\mu)(i\partial^\nu) \chi \mathcal{O}_{q,\mu\nu}^{(2)} \,, \tag{5.57}$$

whereas loop-induced DM–gluon scatterings are described by

$$\mathcal{L}_g^{\mathrm{eff}} = f_G \bar{\chi}\chi \, \mathcal{O}_g^{(0)} + \frac{g_G^{(1)}}{m_{\chi_3}} \bar{\chi} i(\partial^\mu \gamma^\nu + \partial^\nu \gamma^\mu) \chi \mathcal{O}_{g,\mu\nu}^{(2)} + \frac{g_G^{(2)}}{m_{\chi_3}^2} \bar{\chi} (i\partial^\mu)(i\partial^\nu) \chi \mathcal{O}_{g,\mu\nu}^{(2)} \,. \tag{5.58}$$

In the notation of Reference [165] the tensor operators from above are given as

$$\mathcal{O}_{q,\mu\nu}^{(2)} = \frac{1}{2} \bar{q} \left(\gamma^{\{\mu} i D_-^{\nu\}} - \frac{g^{\mu\nu}}{4} i \not{D}_- \right) \,, \tag{5.59}$$

$$\mathcal{O}_{g,\mu\nu}^{(2)} = -G^{a,\mu\rho} G^{a,\nu}{}_{\rho} + \frac{g^{\mu\nu}}{4} \left(G_{\alpha\beta}^a\right)^2 \,, \tag{5.60}$$

and the scalar operators read

$$\mathcal{O}_q^{(0)} = m_q \bar{q} q \,, \tag{5.61}$$

$$\mathcal{O}_g^{(0)} = G_{\mu\nu}^a G^{a,\mu\nu} \,. \tag{5.62}$$

The matrix element f_N of SI contributions can be written in terms of the mass fractions f_{T_q} of light quarks in the nucleon as well as the second moments of the quark, antiquark and gluon PDFs $q(2)$, $\bar{q}(2)$ and $G(2)$, respectively. It reads

$$\frac{f_N}{m_N} = \sum_{q=u,d,s,c} f_{Tq} f_q + \frac{3}{4}\left[q(2)+\bar{q}(2)\right]\left(g_q^{(1)}+g_q^{(2)}\right) - \frac{8\pi}{9\alpha_s} f_{T_G} f_G + \frac{3}{4} G(2)\left(g_G^{(1)}+g_G^{(2)}\right) . \tag{5.63}$$

Here, the Wilson coefficients for DM–quark interactions read [165]

$$f_q = \frac{|\tilde{\lambda}_{q3}|^2 m_{\chi_3}}{16(m_\phi^2-(m_{\chi_3}+m_q)^2)^2} , \tag{5.64}$$

$$g_q^{(1)} = \frac{|\tilde{\lambda}_{q3}|^2 m_{\chi_3}}{8(m_\phi^2-(m_{\chi_3}+m_q)^2)^2} , \tag{5.65}$$

$$g_q^{(2)} = 0 . \tag{5.66}$$

It is important to note that these Wilson coefficients are suppressed by an additional power of the NP scale m_ϕ when compared to the corresponding coefficient for SD scattering a_u from Equation (5.55). This is due to the fact that these coefficients are only generated through an NLO expansion of the propagator in the tree-level diagram of Figure 5.13a. The Wilson coefficients f_G, $g_G^{(1)}$ and $g_G^{(2)}$ of the gluonic operators $\mathcal{O}_g^{(0)}$ and $\mathcal{O}_{g,\mu\nu}^{(2)}$ can be found in Appendix A.2.

In terms of the evolution of the Wilson coefficients for SI scattering from the NP scale m_ϕ down to the scattering scale $\mu = 2\,\text{GeV}$ we use the results from Reference [174] and also adopt the anomalous dimension and matching matrices given there. We further use the `RunDec` package [175] for the running and decoupling of quark masses and the strong coupling α_s. The numerical values of the hadronic matrix elements as well as the input quark masses for the RG running can be found in the appendix of Reference [165].

Constraints from Direct Detection

To study the restrictions that direct detection experiments place on our model parameters, we calculate the SD and SI scattering cross sections as discussed above and compare each with the respective experimental upper limit. Currently, the PICO-60 experiment [176] provides the strongest constraints on SD WIMP–proton scattering for which Equation (5.54) reads

$$\sigma_{\text{SD}}^p = \frac{3}{16\pi}\frac{m_p^2 m_{\chi_3}^2}{(m_p+m_{\chi_3})^2}\left(\Delta u^p a_u\right)^2 . \tag{5.67}$$

The world-leading result for SI scatterings is provided by the XENON1T experiment [177]. Averaging the SI WIMP–nucleon cross section from Equation (5.53) over all nucleons in the nucleus we write

$$\sigma_{\text{SI}} = \frac{4\mu^2}{\pi A^2}|Z f_p + (A-Z) f_n|^2 , \tag{5.68}$$

where $\mu = m_N m_{\chi_3}/(m_N+m_{\chi_3})$ is the reduced mass of the DM–nucleon system and $A = 131$ and $Z = 54$ are the mass and atomic numbers of Xenon. Using these expressions we scan over the mass plane $m_\phi - m_{\chi_3}$ and determine the coupling strength for which both cross sections saturate their respective experimental upper limit given at 90% C.L. For σ_{SI} we additionally assume a flavour-universal DM–quark coupling, i.e. we fix all DM–quark couplings to one value $|\tilde{\lambda}_{i3}|$. The results are shown in Figure 5.14.

For the calculation of the SD scattering rate σ_{SD}^p we have only included the dominant tree-level contribution from Figure 5.13a and hence the PICO-60 limit solely constrains the coupling $|\tilde{\lambda}_{u3}|$ as can be seen in Figure 5.14a. We find that in large parts of the parameter

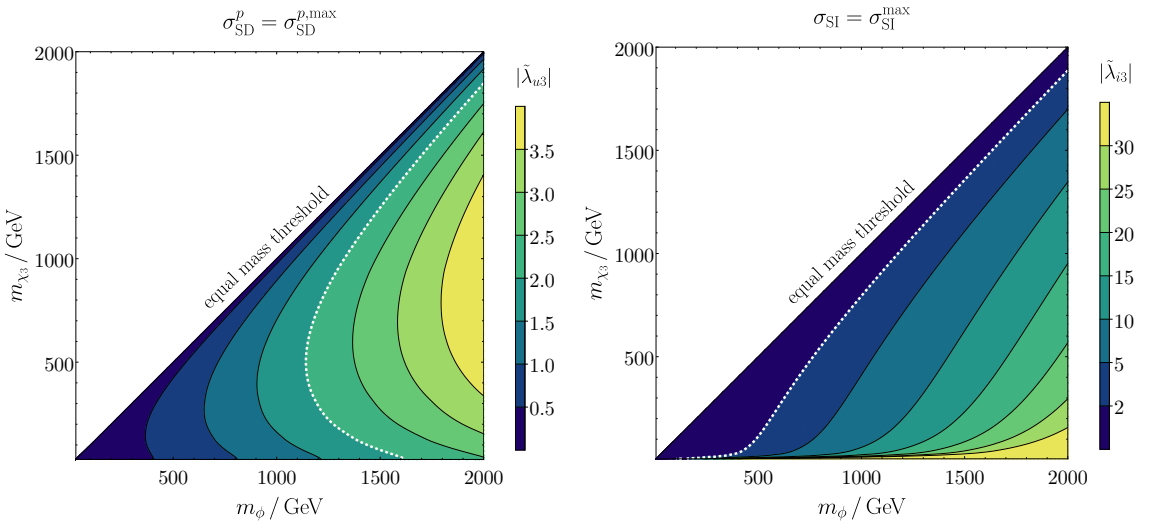

(a) SD scattering **(b)** SI scattering

Figure 5.14 | Direct detection limits on $\tilde{\lambda}$ from the PICO-60 and XENON1T experiments. For the latter we have set $|\tilde{\lambda}_{u3}| = |\tilde{\lambda}_{c3}| = |\tilde{\lambda}_{t3}| \equiv |\tilde{\lambda}_{i3}|$. The area included by the white dashed line and the equal mass threshold indicates in which mass regime the constraints are relevant.

space the limits can be completely evaded. For masses $m_\phi \gtrsim 1200\,\text{GeV}$ it is always possible to find an m_{χ_3} for which the DM–up coupling can take its maximally[19] allowed value $|\tilde{\lambda}_{u3}| = 2.0$ (white dashed contour) without violating the experimental bound. For even larger values $m_\phi \gtrsim 1500\,\text{GeV}$ the limit becomes only relevant in the close-to-degeneracy region $m_\phi \approx m_{\chi_3}$ and for small DM masses $m_{\chi_3} \lesssim 100\,\text{GeV}$.

The constraints on the SI scattering rate $\sigma_{\rm SI}$ are even more lenient as can be seen in Figure 5.14b. This was to be expected as the leading contributions to the SD scattering cross section $\sigma^p_{\rm SD}$ are generated by dimension-six operators while the leading terms for SI scatterings arise from the dimension-seven and dimension-eight operators discussed above. Hence, the SI scattering rate $\sigma_{\rm SI}$ suffers from a severe suppression by the NP scale m_ϕ. We find that this suppression causes the SI scattering limits to be only relevant in the close-to-degeneracy region for mass splittings between m_ϕ and m_{χ_3} of at most 10%.

We conclude that the direct detection constraints are much less stringent for our model than the previously discussed limits from collider and flavour experiments as well as the observed DM relic density. We find that the Majorana nature of χ_3 severely suppresses SI scatterings and thus renders SD scatterings to be the dominant ones.

5.5 Combined Analysis

To provide a global picture of the viable parameter space of our model, we perform a combined analysis in this section. To this end we demand that all the constraints discussed in the previous sections are satisfied simultaneously. After identifying viable structures for the coupling matrix $\tilde{\lambda}$, we conclude this section by analysing the flavour of the lightest dark particle χ_3.

[19] Remember that we had limited the couplings D_i to $D_i \in [0, 2]$ for perturbativity reasons. This choice translates into an according upper bound $|\tilde{\lambda}_{ij}| \leq 2.0$ on each entry of $\tilde{\lambda}$.

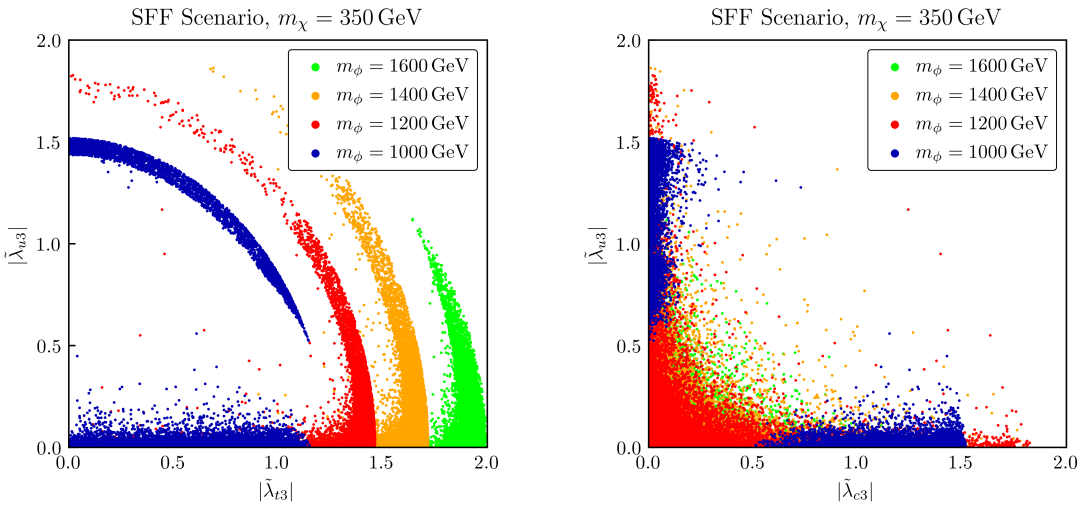

(a) $|\tilde{\lambda}_{t3}| - |\tilde{\lambda}_{u3}|$ plane **(b)** $|\tilde{\lambda}_{c3}| - |\tilde{\lambda}_{u3}|$ plane

Figure 5.15 | Viable couplings $|\tilde{\lambda}_{i3}|$ for $m_\chi = 350\,\text{GeV}$ and varying m_ϕ within the context of all constraints in the SFF scenario.

Combined Constraints

We show the results of the combined analysis of all constraints in Figure 5.15 and 5.16. The LHC constraints are considered in form of the choices for the masses m_ϕ and m_χ here. Note that the structure of $\tilde{\lambda}$ is also restricted by the choice of the freeze-out scenario, since the latter is defined through the mass splittings between the different dark flavours which in turn are determined by the hierarchy of $\tilde{\lambda}$.

The results for the SFF scenario are gathered in Figure 5.15. In Figure 5.15a we show viable points in the $|\tilde{\lambda}_{t3}| - |\tilde{\lambda}_{u3}|$ plane and Figure 5.15b likewise shows the allowed values for $|\tilde{\lambda}_{c3}|$ and $|\tilde{\lambda}_{u3}|$. In this scenario the relic density constraint discussed in Section 5.3 reduces to the condition

$$|\tilde{\lambda}_{u3}|^2 + |\tilde{\lambda}_{c3}|^2 + |\tilde{\lambda}_{t3}|^2 \approx \text{const.}\,, \tag{5.69}$$

as χ_3 is the only flavour that contributes to the thermal freeze-out. This explains the outer edge of the bands that can be seen in Figure 5.15a. The lower edge of these bands on the other hand, is caused by the $D^0 - \bar{D}^0$ mixing constraints which force either $|\tilde{\lambda}_{u3}|$ to be small if $|\tilde{\lambda}_{c3}|$ is large or vice versa. This can be seen very well in Figure 5.15b, where most of the allowed points are located close to the axes with $|\tilde{\lambda}_{u3}| \simeq 0$ and $|\tilde{\lambda}_{c3}| \simeq 0$. The points with $|\tilde{\lambda}_{u3}| \simeq 0$ are then scattered at the bottom in Figure 5.15a while the points with $|\tilde{\lambda}_{c3}| \simeq 0$ form the circular bands.

The m_ϕ dependence of the allowed values in the $|\tilde{\lambda}_{t3}| - |\tilde{\lambda}_{u3}|$ plane shown in Figure 5.15a is primarily due to the relic density constraint. For low mediator masses we find that DM needs to be mainly up- or charm-flavoured, which can be seen explicitly for $m_\phi = 1000\,\text{GeV}$. In this case the thermally averaged annihilation cross section is enhanced by the smallness of the mediator mass. As annihilations into massless final states are p-wave suppressed in the SFF scenario, DM then needs to predominantly couple to either up or charm quarks in order to compensate for this enhancement of the annihilation rate by the small mediator mass. Larger values for m_ϕ sufficiently suppress the annihilation rate, such that top-flavoured DM becomes viable as well. If m_ϕ however grows too large, we find that both up- and charm-flavoured DM are excluded and DM needs to predominantly

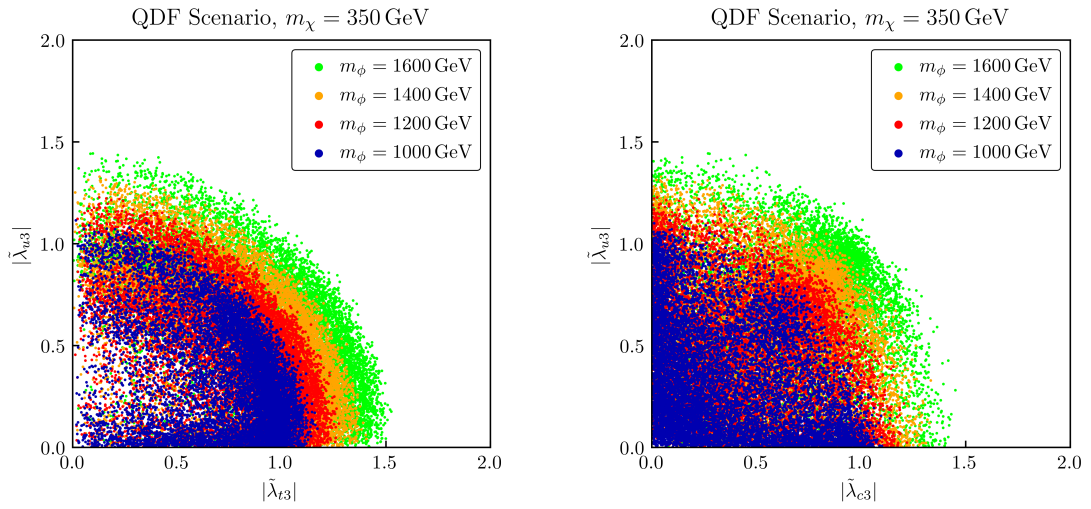

(a) $|\tilde{\lambda}_{t3}| - |\tilde{\lambda}_{u3}|$ plane

(b) $|\tilde{\lambda}_{c3}| - |\tilde{\lambda}_{u3}|$ plane

Figure 5.16 | Viable couplings $|\tilde{\lambda}_{i3}|$ for $m_\chi = 350\,\text{GeV}$ and varying m_ϕ within the context of all constraints in the QDF scenario.

couple to top quarks as can be seen for $m_\phi = 1600\,\text{GeV}$ in Figure 5.15a. The reason is that in this case the suppression of the annihilation rate by sizeable mediator masses together with the above mentioned p-wave suppression of annihilations into up and charm quarks results in a too small annihilation cross section or too large relic density, respectively.

The results for the QDF scenario are shown in Figure 5.16. Since in this case all dark flavours contribute equally to the thermal freeze-out, the relic density condition reduces to

$$\sum_{ij} |\tilde{\lambda}_{ij}|^2 \approx \text{const.}\,, \tag{5.70}$$

and hence the emerging patterns are much less clear than in the SFF scenario. This spherical condition again causes an upper bound on the couplings $|\tilde{\lambda}_{i3}|$, but in this case the lower edge of the bands from the SFF case is absent and hence we are left with the circular patterns that can be seen in Figure 5.16. The varying point density in Figure 5.16a indicates that in the QDF scenario top-flavoured DM is experimentally favoured over up- and charm-flavoured DM. From Figure 5.16b one can infer that the neutral D meson mixing constraints exclude less parameter space in the QDF scenario, as in this case the density of the viable points is not only high close to the axes but also on the diagonal. The reason is that the QDF mass splitting condition implies a near degeneracy condition on the couplings D_i, which in turn suppresses NP contributions to $D^0 - \bar{D}^0$ mixing since $\tilde{\lambda}$ becomes close-to-diagonal for near-degenerate couplings D_i.

In both scenarios we find that for Majorana DM direct detection constraints do not place additional restrictions on the coupling matrix λ or $\tilde{\lambda}$, respectively. We hence conclude that the allowed parameter space is mainly determined by the flavour, relic density and LHC constraints.

Flavour Analysis

Our discussion of the combined constraints from above already contains some aspects related to the flavour of the lightest DM particle χ_3. In the following we want to provide

a more quantitative analysis of the latter. To this end we first define the DM particle χ_3 to be i-flavoured if

$$|\tilde{\lambda}_{i3}| > |\tilde{\lambda}_{j3}|\,, \tag{5.71}$$

with $i \neq j$ and $i, j \in \{u, c, t\}$. In other words, the particle χ_3 has the flavour i if it predominantly couples to the up-type quark of flavour i. We further define the quantity

$$n_i = \frac{N_i}{N}\,, \tag{5.72}$$

where N corresponds to the total number of viable parameter points generated in our randomised scan that satisfy a given constraint, and N_i is the number of this allowed points for which χ_3 has the flavour i. To provide a numerical analysis of the flavour of χ_3 we collect the different n_i in the triple $n_{\text{constr.}} = \{n_u, n_c, n_t\}$ for each experimental constraint separately as well as for points that satisfy all constraints at the same time. Note that our random generation of points prior to the application of the experimental constraints does not favour a specific flavour for χ_3. The results of this analysis are shown in Table 5.2 for $m_\phi = 1400\,\text{GeV}$ and several choices of m_χ. In the QDF scenario the dependence on the latter mass parameter was found to be much weaker than in the SFF scenario and hence we restrict ourselves to just one value of m_χ in this case.

As expected from our results found in Section 5.4, the constraints that direct detection experiments place on the parameter space of our model do not have any implications for the flavour of χ_3 in neither of the freeze-out scenarios. Over large parts of the parameter space, these constraints are too weak to constrain our model at all and hence the flavour of χ_3 quantified by n_{direct} is not constrained by DM–nucleon scatterings either.

For the constraints from $D^0 - \bar{D}^0$ mixing we find much stronger implications for the DM flavour, quantified by n_{mixing}. Since a neutral D meson consists of up and charm quarks, the mixing amplitude is sensitive to the coupling of the new particles χ_i and ϕ to the former particles. Hence, the flavour constraints generally prefer top-flavoured DM over up and charm flavour. This especially holds true for the SFF scenario, which demands that one coupling D_i is larger than the other two in order to generate a significant mass splitting between χ_3 and the heavier states. For up- and charm-flavoured DM one thus always ends up with large couplings $|\tilde{\lambda}_{u3}|$ or $|\tilde{\lambda}_{c3}|$ leading to at least one sizeable contribution to the mixing amplitude from Equation (5.14). This is why in the SFF scenario the mixing constraints strongly disfavour up and charm flavour. The QDF scenario however, demands the couplings D_i to be only marginally split in order to generate a near-degenerate mass spectrum for the dark flavours. Hence, in this case the overall size of all three couplings D_i

Table 5.2 | Numerical results of the flavour analysis for $m_\phi = 1400\,\text{GeV}$. The constraints from direct detection experiments and neutral D meson mixing do not exhibit a significant dependence on m_χ, so that in the SFF scenario only one numerical result is shown that applies to all four m_χ values.

Scenario	m_χ / GeV	n_{direct} / %	n_{mixing} / %	n_{relic} / %	n_{combined} / %
SFF	300	{33, 33, 34}	{2, 4, 94}	{5, 4, 91}	{0, 0, 100}
	350			{23, 19, 58}	{0, 1, 99}
	400			{36, 33, 31}	{1, 2, 97}
	450			{39, 36, 25}	{2, 3, 95}
QDF	350	{33, 33, 34}	{22, 24, 54}	{34, 34, 32}	{23, 23, 54}

can be small, which in turn also allows for up- and charm-flavoured DM while top flavour is still preferred.

The relic abundance constraints are blind towards the flavour of the DM particle in the QDF scenario, as the initial state flavours are summed over in Equations (5.32)–(5.34), rendering all nine couplings $|\tilde{\lambda}_{ij}|$ relevant. This sum is omitted in the SFF scenario, since only the lightest flavour contributes to the freeze-out, so that only the third column of $\tilde{\lambda}$ is constrained. Hence, in this scenario we encounter strong implications for the flavour of the DM particle quantified by n_{relic}. One of them is the aforementioned interplay between the p-wave suppression of the annihilation rate into final states with up- or charm-flavour and the enhancement of the latter rate for small mediator masses. As already discussed in the combined analysis, low mediator masses hence require the DM particle to be up- or charm-flavoured in order to compensate for this enhancement. We find the inverse behaviour with respect to varying DM masses, since the annihilation rate is roughly proportional to m_χ^2. Thus, in contrast to its $1/m_\phi^2$ dependence, growing values of m_χ do not suppress but enhance the overall annihilation rate. Small values of m_χ therefore require top-flavoured DM since annihilations into a top–antitop pair are not p-wave suppressed. In turn, for growing values of m_χ up and charm flavour both become more viable, as the total annihilation cross section is enhanced by the increased DM mass and even p-wave suppressed annihilations can yield the correct total annihilation rate now.

The distribution of possible DM flavours when all constraints are satisfied at the same time is quantified by n_{combined} and shown in the last column of Table 5.2. We find that up- and charm-flavoured DM is strongly disfavoured by experimental data in the SFF scenario. Only for large DM mass parameters $m_\chi \gtrsim 350\,\text{GeV}$ a tiny part of the viable parameter space corresponds to up- or charm-flavoured DM as the relic density constraint relaxes for these flavours here due to the above explained reasons. In spite of having a much weaker dependence on the DM mass, the QDF scenario shows a similar behaviour. Here, top-flavoured DM again is favoured, however the DM particle can also have up or charm flavour.

5.6 Direct CP Violation in Charm Decays

In Section 5.2 we had found that the additional $D^0 - \bar{D}^0$ mixing diagram with crossed fermion lines for our case of Majorana DM leads to less constrained CP-violating interactions than in the Dirac DM case. In contrast to the latter, flavoured Majorana DM models can hence induce potentially sizeable NP contributions to flavour- and CP-violating meson decays. Since the DM flavour triplet is coupled to up-type quarks in our model, the relevant contributions here are related to decays of neutral D mesons.

In terms of the latter, the two decays $D^0 \to K^+K^-$ and $D^0 \to \pi^+\pi^-$ are particularly interesting. The difference $\Delta A_{\text{CP}}^{\text{dir}}$ between the direct CP asymmetries of both of these processes has been measured by the LHCb collaboration and led to the discovery of CP violation in charm decays [25]. This measurement however, found the difference $\Delta A_{\text{CP}}^{\text{dir}}$ to be significantly larger than its SM estimate, which potentially[20] raises the need for a NP explanation. After having identified the viable parameter space of our model in the last section, we review in this section if it is capable of generating sizeable contributions to $\Delta A_{\text{CP}}^{\text{dir}}$.

[20] Note that SM calculations of $\Delta A_{\text{CP}}^{\text{dir}}$ suffer from large hadronic uncertainties that can also be the cause of the discrepancy between its theory prediction and experimental measurement. However, in our analysis we want to shed light on possible NP explanations.

Theoretical Approach

The LHCb collaboration measured the difference between the time-integrated direct CP asymmetries in $D^0 \to K^+K^-$ and $D^0 \to \pi^+\pi^-$ decays to be [25]

$$\Delta A_{\mathrm{CP,LHCb}}^{\mathrm{dir}} = (-0.157 \pm 0.029)\% \,. \tag{5.73}$$

In the SM this asymmetry can be estimated parametrically and yields the naive result

$$\Delta A_{\mathrm{CP,SM}}^{\mathrm{dir}} \sim \mathcal{O}((\alpha_s/\pi)(V_{ub}V_{cb}^*)/(V_{us}V_{cs}^*)) \sim 10^{-4} \,, \tag{5.74}$$

which is an order of magnitude below the experimental value. Reference [178] presents a more elaborate prediction based on QCD light-cone sum rules and finds

$$\Delta A_{\mathrm{CP,SM}}^{\mathrm{dir}} = (0.02 \pm 0.003)\% \,, \tag{5.75}$$

which in turn corresponds to a deviation of 4.7σ from the data. We interpret this discrepancy between the SM predictions and the LHCb result for $\Delta A_{\mathrm{CP}}^{\mathrm{dir}}$ as a hint at NP. Note however, that the possibility of a significantly larger $\Delta A_{\mathrm{CP,SM}}^{\mathrm{dir}}$ has also been argued for in the literature [179, 180].

For the calculation of the NP contributions to $\Delta A_{\mathrm{CP}}^{\mathrm{dir}}$ in our model we follow the approach of Reference [181]. There, the relevant hadronic matrix elements for the D^0 meson decay have been calculated through a naive QCD factorisation. In this approximation, the matrix element of the decay $D^0 \to K^+K^-$, for instance, reads

$$\langle K^+K^-| \, (\bar{u}\,\Gamma_1\, s)(\bar{s}\,\Gamma_2\, c) \, |D^0\rangle \approx \langle K^+| \, (\bar{u}\,\Gamma_1\, s) \, |0\rangle \, \langle K^-| \, (\bar{s}\,\Gamma_2\, c) \, |D^0\rangle \,, \tag{5.76}$$

and formally corresponds to the LO term in a heavy charm quark mass expansion. While the matrix elements thus suffer from large $1/m_c$ corrections, this ansatz enables the calculation of the NP and SM contributions to $\Delta A_{\mathrm{CP}}^{\mathrm{dir}}$ in an effective field theory approach. The latter asymmetry is given by

$$\Delta A_{\mathrm{CP}}^{\mathrm{dir}} = A_{K^+K^-}^{\mathrm{dir}} - A_{\pi^+\pi^-}^{\mathrm{dir}} \,, \tag{5.77}$$

and we adopt the expression

$$A_f^{\mathrm{dir}} = 2\, r_f \sin\delta_f \sin\phi_f \,, \tag{5.78}$$

for the time-integrated direct CP asymmetry of the decay $D^0 \to f$ with the final states $f \in \{K^+K^-, \pi^+\pi^-\}$ from Reference [181]. In this expression, δ_f and ϕ_f are the relative strong and weak phases of the two interfering decays $D^0 \to f$ as well as $\bar{D}^0 \to f$ and Equation (5.78) is only valid if their relative amplitude r_f is small. The contributions to r_f and ϕ_f can generally be expressed in terms of Wilson coefficients for the relevant set of $\Delta F = 1$ operators through the relation [181]

$$\begin{aligned} r_f e^{i\phi_f} \approx \left(C_1^{(1)p} + \frac{C_2^{(1)p}}{N_c}\right)^{-1} \Bigg(& \frac{(C_2^{(1)p})_{\mathrm{NP}}}{N_c} + C_4^{(1)} + \frac{C_3^{(1)}}{N_c} - \frac{C_{10}^{(1)}}{2} - \frac{C_9^{(1)}}{2N_c} - \frac{3\alpha_s}{4\pi}\frac{N_c^2-1}{N_c^2} C_{8g}^{(1)} \\ & + \gamma_f \left(C_6^{(1)} + \frac{C_5^{(1)}}{N_c} - \frac{C_8^{(1)}}{2} - \frac{C_7^{(1)}}{2N_c} - \frac{\alpha_s}{4\pi}\frac{N_c^2-1}{N_c^2} C_{8g}^{(1)} \right) + (C_i^{(1)} \leftrightarrow \tilde{C}_i^{(1)}) \Bigg) \,, \end{aligned} \tag{5.79}$$

where $N_c = 3$ is the number of colours and γ_f are the chirality factors of the final states f. They are approximately given as

$$\gamma_K \approx \frac{2m_K^2}{m_c m_s} \,, \qquad \gamma_\pi \approx \frac{2m_\pi^2}{m_c(m_d + m_u)} \,. \tag{5.80}$$

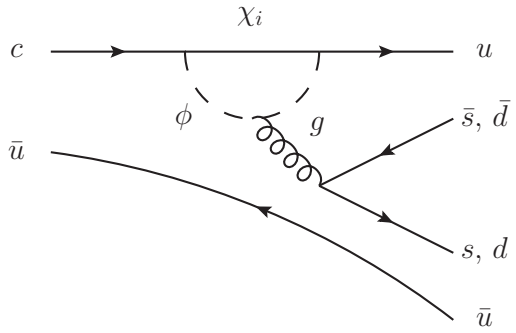

Figure 5.17 | Penguin diagram for NP contributions to $\Delta A_{\mathrm{CP}}^{\mathrm{dir}}$.

In Equation (5.79) we have dropped the Wilson coefficients of scalar operators, as they are absent in our model and their RG running is decoupled from the $\Delta F = 1$ operators included above. A complete list of the relevant operators that contribute to the CP asymmetry is given in Reference [181].

In our model, $\Delta A_{\mathrm{CP}}^{\mathrm{dir}}$ only receives sizeable NP contributions from the gluon penguins illustrated in Figure 5.17. Similar penguin diagrams from *electroweak* (EW) interactions are suppressed by a colour factor $1/N_c$ as well as the smallness of the hypercharge gauge coupling and can thus be neglected. This leaves us with the NP contributions[21]

$$\begin{aligned}
\tilde{C}_6^{(1)} &= \frac{\alpha_s}{4\pi} \sum_i \tilde{\lambda}_{ui} \tilde{\lambda}_{ci}^* \frac{1}{8m_\phi^2}\, u(x_i)\,, \\
\tilde{C}_3^{(1)} &= \tilde{C}_5^{(1)} = -\frac{1}{N_c} \tilde{C}_4^{(1)} = -\frac{1}{N_c} \tilde{C}_6^{(1)}\,, \\
\tilde{C}_{8g}^{(1)} &= \sum_i \tilde{\lambda}_{ui} \tilde{\lambda}_{ci}^* \frac{1}{4m_\phi^2}\, v(x_i)\,,
\end{aligned} \tag{5.81}$$

with $x_i = m_{\chi_i}^2/m_\phi^2$. Here we have introduced the loop functions [181]

$$\begin{aligned}
u(x) &= -\frac{2 - 7x + 11x^2}{36(1-x)^3} - \frac{x^3}{6(1-x)^4} \log x\,, \\
v(x) &= \frac{1 - 5x - 2x^2}{24(1-x)^3} - \frac{x^2}{4(1-x)^4} \log x\,.
\end{aligned} \tag{5.82}$$

The operator $C_1^{(1)p}$ from Equation (5.79) is generated when integrating out the W boson at the EW scale and is given by

$$C_1^{(1)p} = \lambda_p \frac{G_F}{\sqrt{2}}\,, \tag{5.83}$$

where the coupling factor λ_p is defined as $\lambda_p = V_{cp} V_{up}^*$. For decays into K mesons we here have $p = s$ and for the final state with $f = \pi^+\pi^-$ we have $p = d$. Following References [179, 181, 182] we assume $\mathcal{O}(1)$ strong phase differences.

For the numerical analysis we use LO RG running to evolve the Wilson coefficients from the NP scale down to the meson scale $\mu \approx m_{D^0}$. The anomalous dimensions are adopted from Reference [181], and for the running of the quark masses and the strong coupling α_s we again use the `RunDec` package [175]. The values for the CKM matrix elements are obtained

[21] At LO we here only find NP contributions to the Wilson coefficients $\tilde{C}_i^{(1)}$ of $V + A$ operators, since the DM triplet is coupled to right-handed up-type quarks in our model.

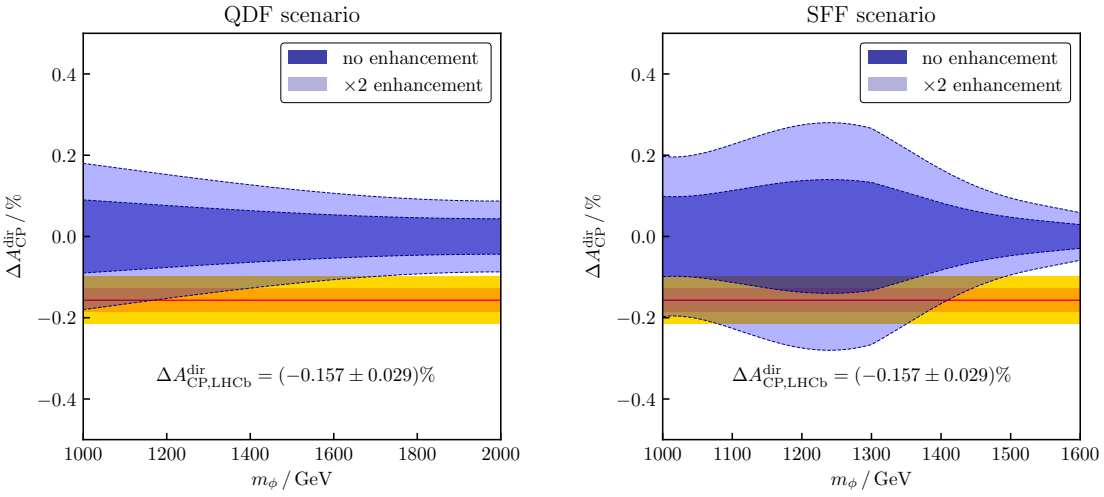

(a) QDF scenario, $m_\chi = 350\,\mathrm{GeV}$ **(b)** SFF scenario, $m_\chi = 350\,\mathrm{GeV}$

Figure 5.18 | $\Delta A_{\mathrm{CP}}^{\mathrm{dir}}$ in dependence of m_ϕ in the two freeze-out scenarios. The blue contours correspond to the ranges covered by our model, as discussed in the text. The red, orange and yellow bands display the LHCb measurement with its 1σ and 2σ uncertainty bands.

from the UTfit website [183]. Due to the large uncertainties stemming from the naive QCD factorisation of the hadronic matrix elements, we follow References [179,181,182] and allow for an enhancement factor of two for the relative amplitude r_f.

Note that the LHCb collaboration recently also measured the single asymmetries $\Delta A_f^{\mathrm{dir}}$ of both decays $D^0 \to K^+K^-$ as well as $D^0 \to \pi^+\pi^-$ and found them to have the same sign [184]. This measurement thus amounts to a U-spin symmetry[22] violation [182, 185–187] that goes beyond the SM estimate at the 1.9σ level [188]. We stress that this anomaly cannot be explained through the penguin diagram of Figure 5.17 that our model gives rise to, since this diagram is U-spin preserving and does not distinguish between down or strange quarks in the final state.

Results

To estimate the size of $\Delta A_{\mathrm{CP}}^{\mathrm{dir}}$ in our model numerically, we calculate its value within the viable parameter space found in the combined analysis in Section 5.5. The asymmetry is calculated for a set of viable points that satisfy all constraints for given masses m_ϕ and m_χ. This determines the range of possible values for $\Delta A_{\mathrm{CP}}^{\mathrm{dir}}$ for a tuple (m_ϕ, m_χ) and we additionally scan over these two masses in order to obtain a global estimate of the CP asymmetry. When calculating $\Delta A_{\mathrm{CP}}^{\mathrm{dir}}$ we use the QCD factorisation and effective field theory approach discussed above and consider the two cases of no enhancement for r_f as well as the case where r_f is enhanced by a factor of two.

The results for a fixed DM mass $m_\chi = 350\,\mathrm{GeV}$ and a varying mediator mass m_ϕ are shown for both freeze-out scenarios in Figure 5.18. We here only show the case of a varying mediator mass, since the DM mass dependence of $\Delta A_{\mathrm{CP}}^{\mathrm{dir}}$ was found to be less significant. For the QDF scenario shown in Figure 5.18a the $1/m_\phi^2$ dependence of the

[22] The U-spin symmetry is a $SU(2)$ subgroup of the SM's approximate flavour symmetry under which the pair $(d, s)^T$ is a doublet.

Wilson coefficients from Equation (5.81) can be seen very well, as increasing masses lead to decreasing values of $\Delta A_{\mathrm{CP}}^{\mathrm{dir}}$. For the case of a non-enhanced r_f we find that the 2σ band of the LHCb measurement can only be reached for masses $m_\phi \lesssim 1000\,\mathrm{GeV}$ which are excluded by LHC searches. When including a factor of two in r_f however, the experimental 2σ band is reached for masses $m_\phi \lesssim 1600\,\mathrm{GeV}$, while values for $\Delta A_{\mathrm{CP}}^{\mathrm{dir}}$ large enough to be consistent with the experimental 1σ band can be generated for mediator masses up to $m_\phi \simeq 1400\,\mathrm{GeV}$. Since decreasing mediator masses enhance the relevant Wilson coefficients from Equation (5.81), we find that for masses $m_\phi \lesssim 1200\,\mathrm{GeV}$ even the experimental central value can be accommodated in the QDF scenario in the case of an enhanced amplitude r_f.

The results for the SFF scenario are shown in Figure 5.18b and we here find that the CP asymmetry grows for increasing mediator masses up to the threshold $m_\phi \simeq 1300\,\mathrm{GeV}$, where $\Delta A_{\mathrm{CP}}^{\mathrm{dir}}$ starts to decrease for an increasing m_ϕ. Given the $1/m_\phi^2$ dependence of the relevant Wilson coefficients this behaviour is quite counter-intuitive but can be explained in the context of our findings from Section 5.5. In Figure 5.15 we had found for the SFF scenario that for mediator masses $m_\phi \lesssim 1400\,\mathrm{GeV}$ DM can be up- or charm-flavoured with close to maximum couplings $|\tilde{\lambda}_{u3}|$ or $|\tilde{\lambda}_{c3}|$. An increasing CP asymmetry for growing values of m_ϕ thus indicates that the resulting suppression of $\Delta A_{\mathrm{CP}}^{\mathrm{dir}}$ is overcompensated for by the increased couplings. For masses $m_\phi \gtrsim 1300\,\mathrm{GeV}$ the couplings $|\tilde{\lambda}_{u3}|$ or $|\tilde{\lambda}_{c3}|$ cannot grow any longer, as they are limited to $|\tilde{\lambda}_{i3}| \leq 2.0$. At the same time the relic density constraint requires DM to be top-flavoured, since annihilations into up- or charm-flavoured final states are p-wave suppressed. Hence, in this regime $\Delta A_{\mathrm{CP}}^{\mathrm{dir}}$ receives a severe suppression for increasing values of m_ϕ as can be seen in Figure 5.18b. We find that in the SFF scenario values of $\Delta A_{\mathrm{CP}}^{\mathrm{dir}}$ consistent with the experimental 1σ and 2σ bands can be accommodated without an enhancement of r_f within the ranges $1100\,\mathrm{GeV} \lesssim m_\phi \lesssim 1350\,\mathrm{GeV}$ and $1200\,\mathrm{GeV} \lesssim m_\phi \lesssim 1300\,\mathrm{GeV}$, respectively. Allowing the amplitude r_f to be enhanced by a factor of two, one can even reproduce the experimental mean value within the range $m_\phi \lesssim 1400\,\mathrm{GeV}$.

We conclude that in both freeze-out scenarios the large experimental value of $\Delta A_{\mathrm{CP}}^{\mathrm{dir}}$ can be reproduced in our model. The QDF scenario here requires the amplitude r_f to be enhanced by a factor of two, while in the SFF scenario values of $\Delta A_{\mathrm{CP}}^{\mathrm{dir}}$ compatible with its LHCb measurement at the 1σ level can also be generated without such an enhancement.

Chapter 6
Summary

In this part we have studied a DMFV model of Majorana fermionic DM $\chi = (\chi_1, \chi_2, \chi_3)^T$ coupling to right-handed up-type quarks u_R. The interaction between quarks and DM is parametrised by the new coupling matrix λ and is mediated by the coloured and charged scalar mediator ϕ. In order to identify viable structures of this coupling matrix, we have studied constraints from LHC searches, neutral D meson mixing, the observed DM relic density and direct detection experiments.

In Section 5.1 we have recasted limits obtained from searches for SUSY squarks in the two final states tops $+ \not{E}_T$ and $jj + \not{E}_T$ to our model. The Majorana nature of χ allows for additional same-sign pair-production channels of ϕ, leading to a larger exclusion in the $m_\phi - m_\chi$ plane especially for non-zero DM masses. For mediator masses $m_\phi \gtrsim 1000\,\text{GeV}$ the constraints from LHC searches can be satisfied by either choosing $0 \leq D_3 \leq 1.5$ and $0 \leq D_1, D_2 \leq 0.5$ or by allowing for larger couplings $D_{1,2}$ while keeping the DM mass m_χ small. We further investigated constraints placed on the model parameters from searches in same-sign final states and found them to be less restrictive than the searches from above. Finally, we predicted the size of the same-sign signature $tt + \not{E}_T$ in collisions with $\sqrt{s} = 14\,\text{TeV}$ to be of order $\mathcal{O}(\text{fb})$ and discussed how it can be used in order to gain insights on the particle nature of DM.

The restrictions that neutral D meson mixing places on the coupling matrix λ have been reviewed in Section 5.2. Again we found a Majorana specific contribution, consisting of a one-loop diagram with crossed fermions in the loop. We found that this diagram and the usual box diagram can interfere destructively, leading to an extension of the viable parameter space in our model when comparing to the Dirac fermionic case. Numerically, the $D^0 - \bar{D}^0$ mixing constraints can be satisfied for $0 \leq D_1, D_2 \leq 0.5$ and free mixing angles θ_{ij}, while the above mentioned destructive interference also allows for viable points outside of this range.

For the analysis of the relic density constraints in Section 5.3 we used the two benchmark scenarios for the thermal freeze-out of DM defined in Part I. In the SFF scenario the thermally averaged cross section for DM annihilations into massless final states is p-wave suppressed due to an additional u-channel diagram only present for Majorana fermions. In both scenarios the relic density constraint places a lower bound on m_χ for a given mediator mass. In the SFF scenario the interplay between the p-wave suppression of the annihilation rate into up- and charm-flavoured final states and it's DM mass dependence additionally leads to an upper bound on the DM mass m_χ, which is relaxed for large mediator masses $m_\phi \gtrsim 1000\,\text{GeV}$.

We looked into constraints from direct detection experiments in Section 5.4. Yet again, the Majorana nature of χ turned out to have strong implications for the phenomenology, as the dominant SI contributions to the DM–nucleon scattering cross section are absent. This causes the direct detection constraints to be very lenient and we found that they are dominated by the generally less sizeable SD contributions to the overall scattering cross section.

In Section 5.5 we then performed a combined analysis where we demanded all the constraints mentioned above to be satisfied at the same time. For both scenarios the viable parameter space is mainly determined by the neutral D meson mixing and relic density constraints. In the SFF scenario the combined analysis allows for discrete bands in each $|\tilde{\lambda}_{i3}| - |\tilde{\lambda}_{j3}|$ plane, which strongly depend on the NP masses m_ϕ and m_χ in particular. As the freeze-out of DM depends on all couplings $|\tilde{\lambda}_{ij}|$ in the QDF scenario, the features in the $|\tilde{\lambda}_{i3}| - |\tilde{\lambda}_{j3}|$ planes are far less pronounced, while the relic density constraint still reduces to a spherical condition. However, in this case the dependence on the DM and mediator mass in particular is marginal.

Finally, we investigated if our model can generate sizeable contributions to CP violation in charm decays in Section 5.6. To this end we estimated the CP asymmetry $\Delta A_{\text{CP}}^{\text{dir}}$ in $D^0 \to K^+K^-$ as well as $D^0 \to \pi^+\pi^-$ decays and compared it to its experimental measurement by the LHCb collaboration. Technically, we adopted an approach where the relevant hadronic matrix elements are calculated through a naive QCD factorisation corresponding to the LO term of a heavy charm quark mass expansion. In both freeze-out scenarios the value of $\Delta A_{\text{CP}}^{\text{dir}}$ can be enhanced significantly. The QDF scenario requires the relevant amplitude to be enhanced by a factor of two relative to the naive QCD factorisation limit, in order to be consistent with the experimental measurement. In the SFF scenario values of $\Delta A_{\text{CP}}^{\text{dir}}$ large enough to be compatible with the experimental 1σ band can also be generated without such an enhancement.

We conclude that changing the fermion nature of DM from Dirac to Majorana leads to a severely altered phenomenology, as this gives rise to additional Majorana specific contributions to relevant observables. In spite of stronger restrictions from collider searches, we found these contributions to relax the other constraints, as they either lead to a destructive interference in the neutral D meson mixing amplitude, a p-wave suppression of the DM annihilation rate or a suppression of leading SI contributions to DM–nucleon scattering. One can hence consider the case of Majorana fermionic DM to be phenomenologically advantageous, as it leads to smaller predicted signals in various experiments and is thus capable of reconciling the WIMP paradigm with the absence of signal in DM searches so far. As far as the altered collider phenomenology is concerned, we have seen that the Majorana nature of χ leads to same-sign signatures that exhibit a significant discovery potential particularly with respect to the particle nature of DM. The fact that this model allows for a NP explanation of the large CP violation in charm decays only further motivates up-type flavoured Majorana DM and renders the model even more attractive from a phenomenological point of view.

Part III

Lepton-Flavoured Scalar Dark Matter I

This part is based on

> H. Acaroğlu, P. Agrawal and M. Blanke, *Lepton-Flavoured Scalar Dark Matter in Dark Minimal Flavour Violation*, 2211.03809.

We here study a simplified DMFV model which extends the SM by a complex scalar DM flavour triplet and a corresponding fermionic charged mediator. The dark particles are coupled to right-handed charged leptons of the SM through this mediator and the interaction between DM and the SM is parametrised by a new 3×3 complex coupling matrix λ. Following the DMFV ansatz, this coupling constitutes the only new source of flavour violation while the lightest of the dark particles is assumed to account for the observed amount of DM in the Universe. To review the phenomenology of this model we study constraints from collider searches, lepton flavour violating decays, the observed DM relic density and direct as well as indirect detection experiments. We further perform a combined analysis by demanding all of these constraints to be satisfied simultaneously and find that the strongest restrictions come from lepton flavour violating decays, the observed DM relic density and direct detection. The interplay between the latter two constraints moreover renders collider searches irrelevant in further restricting the parameter space of the model while constraints from indirect detection experiments are generally weak due to a p-wave suppression of the thermally averaged DM annihilation rate.

Chapter 7
Model Details

Lepton-flavoured DM corresponds to a class of DM models with specific features [190–193]. Most importantly, the absence of a direct coupling to quarks leads to a suppressed signal in direct detection experiments, since the leading contribution to DM–nucleon scattering arises at the one-loop level in these models. For the same reason lepton-flavoured DM models are less constrained by LHC searches. The corresponding mediator particle of DM can only be produced by a Drell–Yan process and hence suffers from an s-channel suppression combined with the smallness of the electroweak coupling. As these properties can potentially ameliorate the tension between the WIMP paradigm and the absence of a signal in DM detection and production experiments, lepton-flavoured DM constitutes an interesting and well-motivated class of models. However, choosing DM to interact with leptons comes at the cost of stronger indirect detection constraints and a richer direct detection phenomenology due to the direct coupling to electrons and positrons.

This chapter presents the details of a lepton-flavoured DM model realised in the DMFV framework. We first discuss the general set-up, continue with a prametrisation of the DM–lepton coupling λ and finally conclude the chapter by reviewing the model's mass spectrum.

7.1 Field Content and Interactions

In this DMFV model the SM is extended by the dark complex scalar field $\phi = (\phi_1, \phi_2, \phi_3)^T$ associated with an approximate $U(3)_\phi$ flavour symmetry. This flavour triplet couples to right-handed charged leptons ℓ_R through the charged vector-like Dirac fermion ψ and its lightest flavour is assumed to account for the observed amount of DM. The DM field ϕ is a singlet under the SM gauge group and is represented by $(\mathbf{1}, \mathbf{1}, 0)_0$ and the vector-like mediator has the representation $(\mathbf{1}, \mathbf{1}, -1)_{1/2}$ where we again use the shorthand notation $(SU(3)_C, SU(2)_L, U(1)_Y)_{\text{spin}}$. The interaction between DM and the SM is governed by a new 3×3 complex coupling matrix λ, which according to the DMFV hypothesis is the only new source of flavour-violation. The Lagrangian of this model is given by

$$\begin{aligned}\mathcal{L} = \mathcal{L}_{\text{SM}} &+ (\partial_\mu \phi)^\dagger (\partial^\mu \phi) - M_\phi^2\, \phi^\dagger \phi + \bar{\psi}(i\not{D} - m_\psi)\psi - (\lambda_{ij} \bar{\ell}_{Ri} \psi\, \phi_j + \text{h.c.}) \\ &+ \lambda_{H\phi}\, \phi^\dagger \phi\, H^\dagger H + \lambda_{\phi\phi} \left(\phi^\dagger \phi\right)^2 . \end{aligned} \tag{7.1}$$

We stress that in contrast to the model studied in Part II the DM triplet is associated with a $U(3)_\phi$ symmetry here, since we chose it to be a complex scalar. Further, according to the DMFV ansatz the mass matrix M_ϕ as well as the quartic couplings $\lambda_{\phi\phi}$ and $\lambda_{H\phi}$ cannot be generic 3×3 matrices, as they would each constitute new sources of flavour-violation otherwise. We hence choose the two quartic couplings to be flavour-universal and diagonal.[23] The mass matrix M_ϕ is reviewed in more detail in Section 7.2.

[23] These couplings could generally also be non-diagonal and flavour-violating within the DMFV framework, if they are expressed in terms of the flavour-violating coupling λ similar to the usual spurion ansatz

It is important to note that the quartic couplings $\lambda_{\phi\phi}$ and $\lambda_{H\phi}$ represent a characteristic feature of complex scalar DM in DMFV. The Higgs portal coupling $\lambda_{H\phi}$ can generally lead to relevant contributions to DM–nucleon scattering as well as DM annihilations. The phenomenology of models, in which DM interacts solely through this channel with the SM is very well studied and can for example be found in Reference [194]. While the case of a sizeable Higgs portal and lepton portal coupling at the same time can lead to an interesting phenomenology, we leave such an analysis for future work and here focus on the case of negligible Higgs portal couplings $\lambda_{H\phi}$. We will however comment on possible implications of $\lambda_{H\phi}$ whenever necessary throughout our analysis. The self-coupling $\lambda_{\phi\phi}$ on the other hand, can induce perturbative DM self-interactions which in turn are subject to constraints from cosmological observations. For the parameter space that we find to be viable, the size of these interactions is too small to have an impact on the phenomenology and we hence also neglect this coupling.

This leaves us with the lepton portal coupling λ that we want to parametrise in the following. We first decompose it according to a singular value decomposition and write

$$\lambda = UDV\,, \tag{7.2}$$

where U and V are unitary matrices and D is a diagonal matrix with positive real entries D_i. In this expression one can now remove three complex phases from U by performing the diagonal rephasing of U and V given in Equation (4.3). Using the flavour symmetry $U(3)_\phi$ it is then possible to entirely remove the unitary matrix V by transforming the DM triplet according to $\phi \to V^{-1}\phi$ to find

$$\lambda = UD\,. \tag{7.3}$$

For the matrix U we use the same parametrisation as in Equation (4.9) containing three mixing angles θ_{ij} and three complex phases δ_{ij}.

The coupling matrix λ hence contains nine physical parameters

$$\theta_{23},\, \theta_{13},\, \theta_{12},\, \delta_{23},\, \delta_{13},\, \delta_{12},\, D_1,\, D_2,\, D_3\,. \tag{7.4}$$

When scanning over these parameters numerically we restrict them to the ranges

$$\theta_{ij} \in [0, \frac{\pi}{4}], \quad \delta_{ij} \in [0, 2\pi), \quad D_i \in [0, 2]\,, \tag{7.5}$$

to guarantee perturbativity and to avoid a double-counting of the parameter space.

7.2 Mass Spectrum and Dark Matter Stability

As already mentioned above, the mass matrix M_ϕ in the Lagrangian of Equation (7.1) cannot be generic, since this would violate the DMFV hypothesis. Effects from RG running as well as the UV completion of the theory however can lead to DMFV preserving mass corrections for the different dark flavours ϕ_i. Following the MFV spurion expansion approach [15] we parametrise these corrections by expanding the mass matrix M_ϕ in terms of the coupling matrix λ to find

$$M^2_{\phi,ij} = m^2_\phi \left\{ \mathbb{1} + \eta \left(\lambda^\dagger \lambda\right) + \mathcal{O}\left(\lambda^4\right) \right\}_{ij} = m^2_\phi \left\{ \mathbb{1} + \eta\, D_i^2 + \mathcal{O}\left(\lambda^4\right) \right\} \delta_{ij}\,, \tag{7.6}$$

where the parameter η depends on the details of the model and its UV completion.

in MFV [15].

We further follow the convention defined in Section 3.2 and always order and relabel the fields ϕ_i in such a way that the mass matrix

$$M_\phi^2 = \text{diag}(m_{\phi_1}^2, m_{\phi_2}^2, m_{\phi_3}^2)\,, \tag{7.7}$$

satisfies the hierarchy condition $m_{\phi_1} > m_{\phi_2} > m_{\phi_3}$. In other words, the lightest state of the flavour triplet ϕ is always ϕ_3 and as we assume it to form the DM of the Universe, it is necessary to ensure its stability. In quark-flavoured Dirac fermionic DMFV models this stability is guaranteed by an unbroken residual $\mathbb{Z}_3$ symmetry implied by the global flavour symmetry [20–22]. In our case of lepton-flavoured DM however, such a residual symmetry is not present as all NP fields are $SU(3)_C$ singlets [24]. To ensure the stability of ϕ_3 we hence charge the NP fields under a $\mathbb{Z}_2$ symmetry which guarantees that they cannot decay into SM fields only. Choosing the DM mass m_{ϕ_3} to be smaller than the mediator mass, i.e. demanding

$$m_\phi < m_\psi\,, \tag{7.8}$$

together with negative mass corrections with $\eta < 0$ then renders ϕ_3 stable.

Chapter 8
Phenomenology

In this chapter we review the phenomenology of our model by analysing constraints placed on its parameter space. We first discuss limits from collider searches, LFV decays, the observed DM relic density and direct as well as indirect detection experiments individually and then conclude this chapter by performing a combined analysis.

8.1 Collider Phenomenology

We use this section to analyse the constraints that collider searches place on the parameter space of our model and particularly on the NP mass parameters m_ψ and m_ϕ. While we focus on LHC searches and signatures that arise from pair-production of the mediator ψ, we also take into account constraints from LEP experiments by demanding the mediator mass to satisfy $m_\psi > 100\,\text{GeV}$ [195, 196].

LHC Signatures from Mediator Pair-Production

The mediator ψ is pair-produced through the annihilation of a quark and antiquark from the initial state protons into an off-shell γ or Z that in turn decays into the pair $\psi\bar{\psi}$. This Drell–Yan process is shown in Figure 8.1a and together with the subsequent decay of the mediator pair from Figure 8.1b it results in the final state $\ell_i\bar{\ell}_j\phi_k\phi_l^\dagger$. Here, the indices i, j, k and l are flavour indices and the $\mathbb{Z}_2$ symmetry discussed in the last section ensures that ψ does not decay into SM particles only. Thus, we find the relevant process at the LHC to be

$$pp \;\to\; \psi\bar{\psi} \;\to\; \ell_i\bar{\ell}_j\phi_k\phi_l^\dagger\,. \tag{8.1}$$

Choosing the flavour indices of the two charged leptons to be equal in this process results in the same-flavour signatures $\ell_i\bar{\ell}_i + \not{E}_T$ while the case $i \neq j$ gives rise to the mixed-flavour signatures $\ell_i\bar{\ell}_j + \not{E}_T$[24].

In non-flavoured DM models (like e.g. SUSY models with neutralino DM) the latter signatures are correlated with the strongly constrained LFV decays $\ell_i \to \ell_j\gamma$ and LHC searches thus typically neglect them. In flavoured DM models however, mixed-flavour final states can be produced at a sizeable rate without flavour violation as they are proportional to the diagonal elements of the coupling matrix that parametrises interactions between DM and the SM. Moreover, flavour violation remains undetected at the LHC for such models, since the dark particles carry away the flavour quantum number. This is similar to the pair-production of W bosons in the SM subsequently decaying into a charged lepton and a neutrino each, where the latter carries away the flavour quantum number as well. We return to these signatures when performing the combined analysis in Section 8.5.

In this section we focus on the same-flavour final states $\ell_i\bar{\ell}_i + \not{E}_T$ and use experimental limits on them in order to constrain our model. The two signatures $e\bar{e}+\not{E}_T$ and $\mu\bar{\mu}+\not{E}_T$ are

[24] We here ignore possible subsequent decays of the heavy dark flavours as they only yield soft and therefore difficult to detect decay products due to the small mass splittings between different dark flavours.

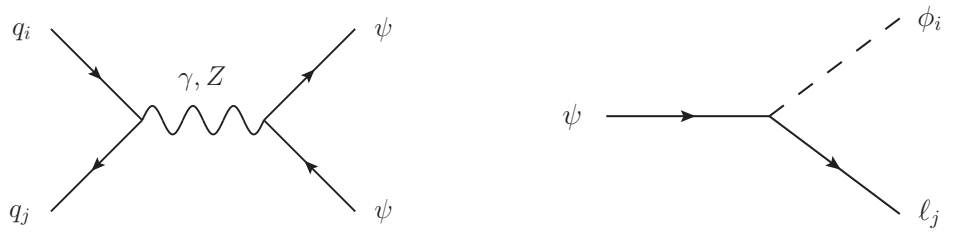

(a) $\psi\bar{\psi}$ production **(b)** ψ decay

Figure 8.1 | Feynman diagrams of ψ pair-production and its subsequent decay.

constrained by searches for supersymmetric *scalar leptons* (sleptons) of the first and second generation while the signature $\tau\bar{\tau}+\not{E}_T$ is constrained by searches for supersymmetric *scalar taus* (staus). Note however, that the kinematics of the SUSY models the experimental limits are obtained for could in principle be different from our case due to distinct spin-statistics. In our model the mediator ψ is a fermion that decays into a scalar and a fermion, while in SUSY models sleptons are scalars that decay into two fermions. Since the cross section of scalars produced in a Drell–Yan process is smaller than for fermions we explicitly implement the pair-production of ψ in our analysis. However, we do not expect the efficiencies of the relevant analyses to strongly depend on the kinematics. We hence assume that they stay the same for our case and compare our signal cross section directly with the experimental upper limits obtained for the SUSY models. In what follows we use the shorthand notation $\ell\bar{\ell}+\not{E}_T$ for the joint signatures $e\bar{e}+\not{E}_T$ and $\mu\bar{\mu}+\not{E}_T$.

Recast of LHC Limits

Relevant experimental searches have been carried out for both signatures at centre-of-mass energies of 13 TeV [197–200] and 8 TeV [201]. For the signature $\ell\bar{\ell}+\not{E}_T$ the most stringent limits are provided by the CMS search of Reference [197], which uses the full LHC run 2 data set corresponding to an integrated luminosity of $137\,\text{fb}^{-1}$. In case of the signature $\tau\bar{\tau}+\not{E}_T$ the leading limits are provided by the ATLAS search of Reference [198] again based on the full LHC run 2 data set.

In order to straightforwardly apply these limits to our model, we first implement the Lagrangian of Equation (7.1) in `FeynRules` [147], generate a `UFO` file [148] and calculate the LO signal cross section $\sigma \times \text{Br}$ for both signatures separately in `MadGraph 5` [149]. We then constrain our model by demanding that the cross section for each signature is smaller than the respective upper limit. When implementing the model into `FeynRules` we follow References [20–22] and our analysis in Section 5.1 in neglecting the mass splittings from Equation (7.6) and assuming a diagonal coupling matrix λ, i.e. we set the mixing angles θ_{ij} and phases δ_{ij} to zero. Small mass splittings only lead to soft and therefore hard to detect decay products of the heavy dark particles, while non-zero mixing angles tend to decrease the branching ratios of the relevant flavour-conserving final states. As this in turn also reduces the relevant signal cross sections and as we are primarily interested in the restrictions that the above mentioned searches place on the NP mass parameters m_ψ and m_ϕ, we set the mixing angles and phases to zero. In this section we further assume the couplings D_1 and D_2 to be degenerate, i.e. we set $D_1 = D_2 = D_\ell$ in order to straightforwardly apply the limits from the searches mentioned above.

The resulting exclusion in the mass plane $m_\psi - m_\phi$ is shown in Figure 8.2. For searches in the final state $\ell\bar{\ell}+\not{E}_T$ shown in Figure 8.2a we find that the excluded area shrinks for growing values of D_3. This is because increasing values of D_3 reduce the branching ratio

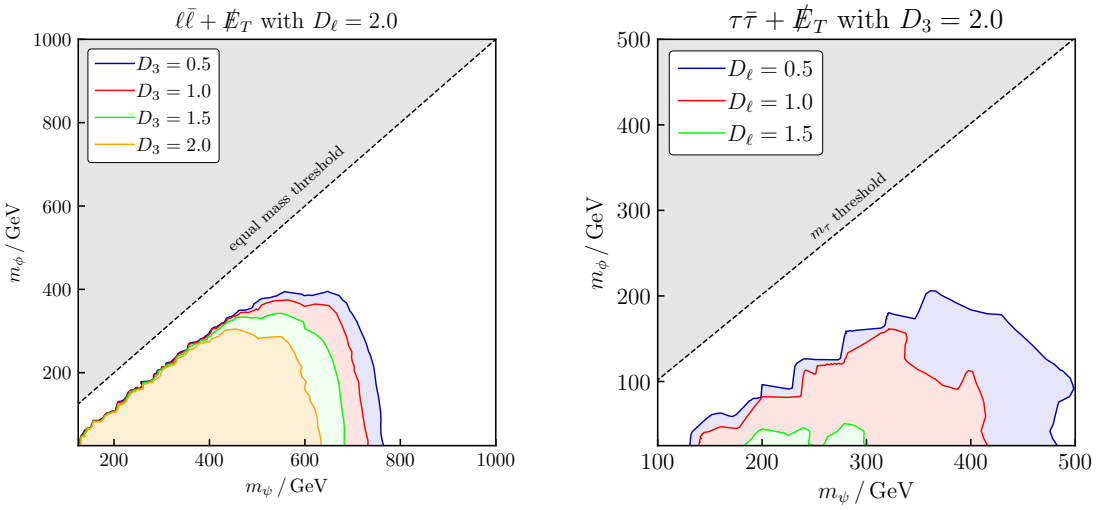

(a) final states with $\ell\bar{\ell} + \not{E}_T$ **(b)** final states with $\tau\bar{\tau} + \not{E}_T$

Figure 8.2 | LHC constraints on the final states $\ell\bar{\ell} + \not{E}_T$ and $\tau\bar{\tau} + \not{E}_T$. The coloured areas are excluded.

of the decay $\psi \to \ell\phi^\dagger$ while they increase the rate of the decay $\psi \to \tau\phi^\dagger$. This in turn reduces the signal cross section which is why we find the largest excluded area for the smallest value of D_3. For a maximal coupling $D_\ell = 2.0$ to electrons as well as muons and a small coupling $D_3 = 0.5$ to taus (blue line) the constraints either enforce $m_\psi \gtrsim 750\,\text{GeV}$ while m_ϕ can be chosen freely or $m_\psi \gtrsim 400\,\text{GeV}$ and $m_\phi \gtrsim 400\,\text{GeV}$. Smaller values of D_3 only marginally increase the excluded area.

For the signature $\tau\bar{\tau} + \not{E}_T$ we find that the resulting restrictions on the masses m_ψ and m_ϕ are much weaker. In this case the excluded area is largest if the coupling D_ℓ to electrons and muons is small compared to the coupling D_3 to taus. The reason for this behaviour again is the increased branching ratio of the final state with taus for decreasing values of D_ℓ. We further find that the relevant branching ratio drops much more quickly and the excluded area shrinks much faster in this case for increasing values of D_ℓ such that there is close to no exclusion at all in the $m_\psi - m_\phi$ plane for near-degenerate couplings $D_\ell \approx D_3$ (green line). This is due to the multiplicity of the final state $\ell\bar{\ell} + \not{E}_T$, as growing values of D_ℓ increase both decay rates $\psi \to e\phi^\dagger$ as well as $\psi \to \mu\phi^\dagger$. For the maximally constrained case with $D_3 = 2.0$ and $D_\ell = 0.5$ we find that the limits can be satisfied by choosing either $m_\psi \gtrsim 500\,\text{GeV}$ and a free m_ϕ or $m_\psi \gtrsim 200\,\text{GeV}$ and $m_\phi \gtrsim 200\,\text{GeV}$. Here again, smaller values of D_ℓ only yield a marginally larger exclusion.

8.2 Flavour Physics Phenomenology

In DMFV, the unrestricted structure of the coupling λ can generally lead to large NP effects in flavour observables. For lepton-flavoured DM the relevant processes are the LFV decays $\ell_i \to \ell_j\gamma$ which are given rise to by FCNCs induced by the NP interaction Lagrangian in Equation (7.1). Identifying flavour-safe scenarios thus puts stringent constraints on the parameter space of the model which we want to discuss in this section. We begin by providing analytic expressions for the NP contributions[25] to the LFV decays and conclude

[25] Note that these decays are forbidden in the SM.

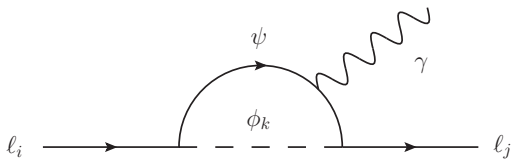

Figure 8.3 | Feynman diagram for the LFV decay $\ell_i \to \ell_j\gamma$. The contribution from the photon coupling to one of the SM leptons is not shown.

the section with a numerical analysis of the constraints.

Lepton Flavour Violating Decays

The LO contribution to the LFV decays $\ell_i \to \ell_j\gamma$ consists of the one-loop diagram shown in Figure 8.3 and is governed by the off-diagonal elements of the coupling matrix λ. Following Reference [202] we express the amplitude of this process according to

$$\mathcal{M}_{\ell_i\ell_j\gamma} = \frac{e}{2m_{\ell_i}}\epsilon^{*\alpha}\bar{u}_{\ell_j}\left[i\sigma_{\beta\alpha}q^\beta\left(a^R_{\ell_i\ell_j\gamma}P_L + a^L_{\ell_i\ell_j\gamma}P_R\right)\right]u_{\ell_i}\,, \tag{8.2}$$

where we have used $\sigma_{\beta\alpha} = i[\gamma_\alpha, \gamma_\beta]/2$. In this expression ϵ^α is the photon polarisation vector and $P_{R/L} = (1 \pm \gamma_5)/2$ are projection operators. We adopt the convention from References [203, 204] according to which the superscript of the coefficients $a_{\ell_i\ell_j\gamma}$ refers to the chirality of the final state lepton. For a generic NP interaction[26] of the form

$$\mathcal{L}_{\text{int}} = c^R_{ij}\,\bar{\ell}_{Ri}\psi\phi_j + c^L_{ij}\,\bar{\ell}_{Li}\psi\phi_j + \text{h.c.}\,, \tag{8.3}$$

with corresponding mass parameters m_ψ and m_{ϕ_i} the expressions of the coefficients $a^{R/L}_{\ell_i\ell_j\gamma}$ are given by [202, 204]

$$a^R_{\ell_i\ell_j\gamma} = \frac{m_{\ell_i}}{16\pi^2}\sum_k\left(\frac{m_{\ell_i}}{12m^2_{\phi_k}}c^{R*}_{ik}c^R_{jk}F(x_k) + \frac{m_\psi}{3m^2_{\phi_k}}c^{L*}_{ik}c^R_{jk}G(x_k)\right)\,, \tag{8.4}$$

$$a^L_{\ell_i\ell_j\gamma} = \frac{m_{\ell_i}}{16\pi^2}\sum_k\left(\frac{m_{\ell_i}}{12m^2_{\phi_k}}c^{L*}_{ik}c^L_{jk}F(x_k) + \frac{m_\psi}{3m^2_{\phi_k}}c^{R*}_{ik}c^L_{jk}G(x_k)\right)\,, \tag{8.5}$$

with $x_k = m^2_\psi/m^2_{\phi_k}$. Here, ψ is a Dirac fermion with electric charge $Q_\psi = -1$, the ϕ_i are scalars and the loop functions F and G are given as [202, 204]

$$F(x) = \frac{2}{(1-x)^4}\left[2 + 3x - 6x^2 + x^3 + 6x\log x\right]\,, \tag{8.6}$$

$$G(x) = -\frac{3}{2(1-x)^3}\left[3 - 4x + x^2 + 2\log x\right]\,. \tag{8.7}$$

The branching ratios of the LFV decays are then given by

$$\text{BR}(\ell_i \to \ell_j\gamma) = \frac{e^2}{64\pi}\frac{m_{\ell_i}}{\Gamma_{\ell_i}}\left(|a^R_{\ell_i\ell_j\gamma}|^2 + |a^L_{\ell_i\ell_j\gamma}|^2\right)\,, \tag{8.8}$$

where Γ_{ℓ_i} denotes the total decay width of the charged lepton ℓ_i.

[26] Such an interaction Lagrangian is only allowed if the fields ψ or ϕ_i are linear combinations of respective gauge eigenstates with different quantum numbers. Otherwise, either of the couplings c^L or c^R has to be zero in order to not violate the gauge symmetry of the SM.

Since the DM flavour triplet ϕ only couples to right-handed charged leptons in our model, contributions with a chirality flip in the loop as well as purely left-handed contributions are absent. Hence, the expressions from above reduce to

$$a^R_{\ell_i\ell_j\gamma} = \frac{m^2_{\ell_i}}{192\pi^2}\sum_k \frac{\lambda^*_{ik}\lambda_{jk}}{m^2_{\phi_k}} F(x_k)\,, \tag{8.9}$$

$$a^L_{\ell_i\ell_j\gamma} = 0\,, \tag{8.10}$$

for which the branching ratios in turn read

$$\mathrm{BR}(\ell_i \to \ell_j\gamma) = \frac{e^2}{64\pi}\frac{m_{\ell_i}}{\Gamma_{\ell_i}}|a^R_{\ell_i\ell_j\gamma}|^2\,. \tag{8.11}$$

Constraints from LFV Decays

For the numerical analysis of the constraints from LFV decays we calculate the branching ratios from Equation (8.11) for randomly generated points in the parameter space and compare them with their respective upper limits. The latter are given at 90% C.L. and read [205–207]

$$\mathrm{BR}(\mu \to e\gamma)_{\max} = 4.2\times 10^{-13}\,, \tag{8.12}$$

$$\mathrm{BR}(\tau \to e\gamma)_{\max} = 3.3\times 10^{-8}\,, \tag{8.13}$$

$$\mathrm{BR}(\tau \to \mu\gamma)_{\max} = 4.2\times 10^{-8}\,. \tag{8.14}$$

The values of the lepton masses m_{ℓ_i} and the decay widths Γ_{ℓ_i} are obtained from Reference [158]. We neglect the mass corrections from Section 7.2 when calculating the branching ratios, since these only lead to higher-order DMFV corrections that we have checked to be negligible here. This further simplifies Equation (8.9) and we find

$$a^R_{\ell_i\ell_j\gamma} = \frac{m^2_{\ell_i}}{192\pi^2}\frac{(\lambda\lambda^\dagger)_{ji}}{m^2_\phi}F(x)\,. \tag{8.15}$$

Using this expression one can already estimate the maximally allowed size of the off-diagonal elements of $\lambda\lambda^\dagger$ in order to not violate the limits from above. In the limit $m_\psi \gg m_\phi$ we for instance find for the most stringently constrained decay $\mu \to e\gamma$ that the coupling matrix has to satisfy

$$\sqrt{|\,(\lambda\lambda^\dagger)_{\mu e}\,|} \lesssim \frac{m_\psi}{15\,\mathrm{TeV}}\,, \tag{8.16}$$

in order to comply with the experimental limit. For NP scales m_ψ of order $\mathcal{O}(\mathrm{TeV})$ this condition reduces to

$$\sqrt{|\,(\lambda\lambda^\dagger)_{\mu e}\,|} \sim \mathcal{O}(0.01-0.1)\,. \tag{8.17}$$

The results of the full analysis are illustrated in Figure 8.4 where we show the viable mixing angles θ_{ij} in dependence of the splittings $\Delta_{ij} = |D_i - D_j|$. As expected, we find the LFV decay limits to mainly place restrictions on the mixing angle θ_{12} while θ_{13} and θ_{23} can be chosen freely even for large splittings Δ_{ij}. We further find that small values of Δ_{ij} generally suppress the LFV decays as all three mixing angles can be chosen freely in the limit of vanishing splittings Δ_{ij}. This is because the product $\lambda\lambda^\dagger$ becomes diagonal in the degeneracy limit $D_i = D_0$, i.e.

$$\lambda\lambda^\dagger = D_0^2\mathbb{1}\,. \tag{8.18}$$

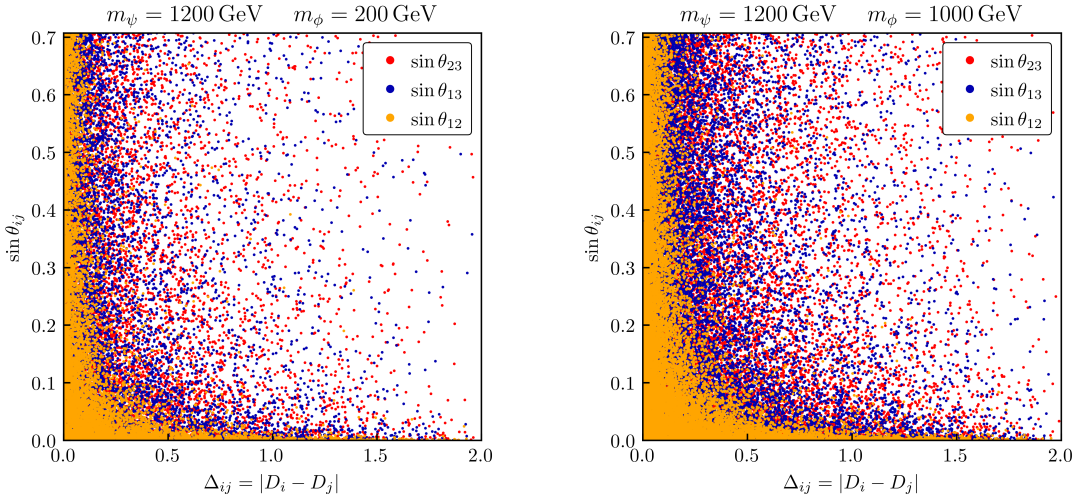

Figure 8.4 | Constraints from LFV decays on the mixing angles θ_{ij} in dependence of the splittings $\Delta_{ij} = |D_i - D_j|$ for $m_\psi = 1200\,\text{GeV}$ and two choices of m_ϕ.

We stress that in contrast to the simple estimate from Equation (8.16) the LFV constraints actually carry a DM mass dependence as can be seen in Figure 8.4. For a close-to-degenerate mass spectrum with $m_\psi \approx m_\phi$ we find larger viable values of Δ_{12} with a free corresponding mixing angle θ_{12}. In total we conclude that the constraints from LFV decays can either be satisfied by choosing the couplings D_1 and D_2 to be close-to-degenerate or by suppressing the mixing angle θ_{12} and allowing for arbitrary couplings to electrons and muons.

Before concluding this section we want to also comment on constraints from measurements of leptonic dipole moments. Generally, lepton-flavoured DM can lead to NP contributions to the electric and magnetic dipole moments of charged leptons through the diagrams shown in Figure 8.3 with $i = j$. We find contributions to the *electric dipole moment* (EDM) d_ℓ to be absent in our case since they are only induced by CP-violating interactions which the NP Lagrangian from Equation (7.1) does not contain due to its chiral structure. While our model can in principle generate contributions to the *magnetic dipole moment* (MDM) a_ℓ, sizeable effects can only be induced for mediator masses of order $\mathcal{O}(100\,\text{GeV})$ which are excluded by the LHC searches discussed in Section 8.1. This again is due to the chiral interaction between DM and the SM because of which a chiral enhancement of a_ℓ is not possible in our model. Thus, it is neither capable of explaining the long-standing tension between the theoretical prediction of the muon MDM a_μ [27] and its experimental measurement [26, 208][27], nor do the MDMs [26, 209, 210] or EDMs [211–213] of charged leptons place relevant constraints on its parameter space.

8.3 Dark Matter Relic Density

In this section we examine the constraints placed on the parameter space of our model by the observed DM relic density. Again, we restrict the analysis to the two thermal

[27] Note that this statement also holds true for the case $m_\psi \approx m_\phi$ although this regime in the NP mass plane is not excluded by the searches from Section 8.1. In the combined analysis of Section 8.5 we will find that the interplay between the relic density and direct detection constraints excludes small mediator masses necessary to generate sizeable effects in a_μ in general.

freeze-out scenarios discussed in Section 3.2. We first define these scenarios numerically and then continue with a review of relevant contributions to the thermally averaged annihilation cross section. The section is concluded by a numerical analysis of the relic density constraints.

DM Annihilations and Thermal Freeze-Out

Both benchmark scenarios that we identified in Section 3.2 for the thermal freeze-out of DM are defined through the mass splittings between the heavier and the lightest dark particle given as

$$\Delta m_{i3} = \frac{m_{\phi_i}}{m_{\phi_3}} - 1\,, \tag{8.19}$$

with $i \in \{1, 2\}$. In terms of these splittings we define them as follows:

- The QDF scenario is defined through negligible mass splittings and hence we demand Δm_{i3} to be smaller than 1% in this case. To suppress the corrections in Equation (7.6) we set $\eta = -0.01$. Smaller absolute values are not justified as the mass corrections are at least generated through one-loop RG running effects.

- For the SFF scenario we require Δm_{i3} to satisfy

$$10\% < \Delta m_{i3} < 30\%\,, \tag{8.20}$$

  in order have significant splittings but at the same time guarantee that the spurion expansion of the mass matrix M_ϕ^2 converges. To this end we set $\eta = -0.075$ in Equation (7.6) which we have tested to lead to maximal splittings of $\Delta m_{i3} \simeq 30\%$.

We further assume the thermal freeze-out of DM to take place at $m_{\phi_3}/T_f \approx 20$ in both scenarios.

In Figure 8.5 we have gathered possible annihilation processes of the NP fields. When calculating the thermally averaged annihilation rate we neglect coannihilations between DM and the mediator as well as annihilations of the mediator itself, shown in Figure 8.5b and 8.5c, respectively. Coannihilations are suppressed by the smallness of the fine structure constant α_{em} and additionally receive a Boltzmann suppression by the factor

$$k = e^{-\frac{m_\psi - m_{\phi_3}}{T_f}} \simeq e^{-20\frac{m_\psi - m_{\phi_3}}{m_{\phi_3}}}\,, \tag{8.21}$$

while the annihilation of a mediator pair is even further suppressed by k^2. Hence, both processes only lead to non-negligible contributions in the close-to-degenerate case $m_\phi \approx m_\psi$. Other possible contributions to the annihilation rate are related to the Higgs portal coupling $\lambda_{H\phi}$. This coupling governs the annihilation of two DM particles into a pair of Higgs bosons which is proportional to $\lambda_{H\phi}^2$. It also parametrises DM annihilations via a virtual Higgs boson in the s-channel which decays into SM fields. The process with a top–antitop pair in the final state is proportional to $\lambda_{H\phi}^2 y_t^2$ and can thus become sizeable due to the large top Yukawa coupling y_t. However, in this analysis we are primarily interested in the structure of the flavour-violating coupling λ and hence we do not constrain $\lambda_{H\phi}$. We use this freedom and assume that both Higgs portal annihilation processes can always be neglected through the appropriate choice of $\lambda_{H\phi}$.

The only remaining contribution to the thermally averaged annihilation rate then is related to the t-channel DM annihilation process shown in Figure 8.5a. Evaluating the diagram we find

$$\overline{|M|^2} = \sum_{ijkl} \frac{|\lambda_{ik}|^2 |\lambda_{jl}|^2}{(t - m_\psi^2)^2} \left[\left(m_{\phi_j}^2 - m_{\ell_l}^2 - t \right) \left(t + m_{\ell_k}^2 - m_{\phi_i}^2 \right) - t \left(s - m_{\ell_k}^2 - m_{\ell_l}^2 \right) \right]\,, \tag{8.22}$$

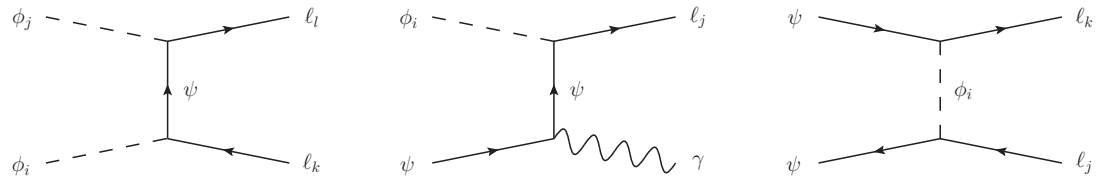

(a) $\phi_i\phi_j$ annihilation **(b)** $\phi_i\psi$ coannihilation **(c)** $\psi\psi$ annihilation

Figure 8.5 | Representative Feynman diagrams for annihilations of the new particles into SM matter.

for the flavour-averaged squared amplitude $\overline{|M|^2}$. The Mandelstam variables are defined as $s = (p_1 + p_2)^2$ and $t = (p_1 - p_3)^2$, and we sum over the flavour indices i, j, k and l.

Using this amplitude together with the techniques provided by References [121, 123] we calculate the coefficients a and b of the low-velocity expansion from Equation (3.12) given as

$$\langle \sigma v \rangle_{\text{eff}} = \frac{f_{\text{sc}}}{2} \left[a + b \langle v^2 \rangle + \mathcal{O}\left(\langle v^4 \rangle \right) \right] . \tag{8.23}$$

Here we have used $f_{\text{nat}} = 1/2$ since DM is a complex scalar in this model. The average squared velocity reads $\langle v^2 \rangle = 6T_f/m_{\phi_3} \simeq 0.3$ and the factor f_{sc} depends on the freeze-out scenario. In the limit of vanishing final state masses $m_{\ell_i} = 0$ and equal initial state masses $m_{\phi_i} = m_\phi$ the coefficients read[28]

$$a = 0 , \tag{8.24}$$

$$b = \sum_{ij} \sum_{kl} \frac{|\lambda_{ik}|^2 |\lambda_{jl}|^2}{48\pi m_\psi^2} \frac{\mu}{(1+\mu)^2} , \tag{8.25}$$

with $\mu = m_\phi^2/m_\psi^2$. Therefore, we find that in the limit of negligible final state masses—well justified by the smallness of the lepton masses—the annihilation rate suffers from a p-wave suppression as the s-wave coefficient a vanishes. This suppression is due to the fact that the annihilation of two scalars in the s-wave corresponds to a $J = 0$ state. Angular momentum conservation implies that the final state must also have $J = 0$, which in turn involves both lepton chiralities. Since the Lagrangian from Equation (7.1) involves a chiral interaction, the s-wave annihilation vanishes in the limit $m_{\ell_i} = 0$. Nevertheless, in the numerical analysis we use the expressions for a and b including the full final state mass dependence which can be found in Appendix B.1.

In Equation (8.25) the DM mass m_ϕ needs to be understood as m_{ϕ_3} for the SFF scenario. Moreover, using equal initial state masses is also justified for the QDF scenario, since the DM masses m_{ϕ_i} are only split by at most one percent in this case which we have checked to be negligible. The aforementioned approximation of using zero final state masses is also well justified since we generally consider $m_\tau \ll m_\phi$.

Constraints from the DM Relic Density

In the numerical analysis we calculate the thermally averaged annihilation rate using the partial wave expansion from above and compare it with the value necessary to yield the correct relic abundance. For DM masses $m_{\phi_3} > 10\,\text{GeV}$ this rate is found to be [162, 163]

$$\langle \sigma v \rangle_{\text{eff}}^{\text{exp}} = 2.2 \times 10^{-26}\,\text{cm}^3\,\text{s}^{-1} , \tag{8.26}$$

[28] Remember that the sum over initial state flavours i and j is absent for the SFF scenario, as in this case only ϕ_3 contributes to the thermal freeze-out of DM.

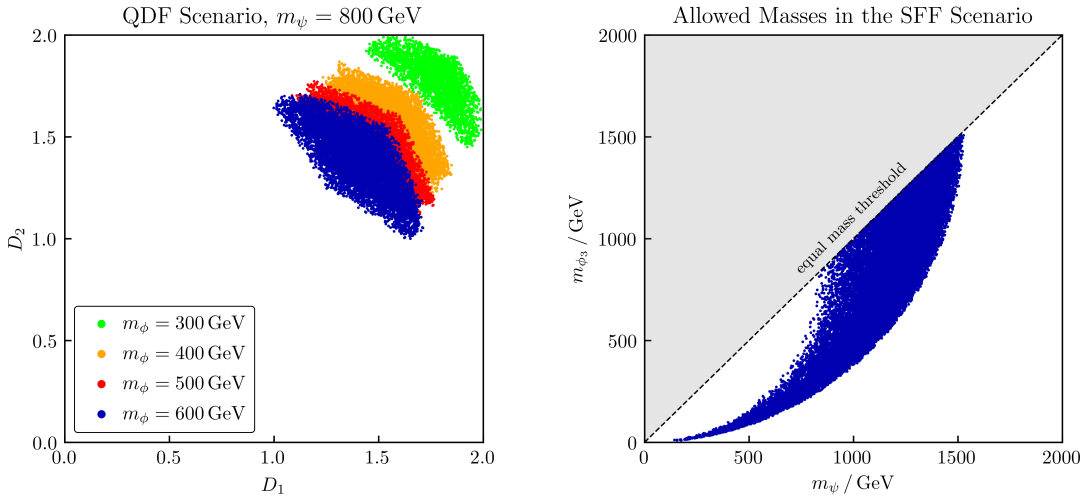

(a) Viable values of D_1 and D_2 with a varying m_ϕ and $m_\psi = 800\,\text{GeV}$ for τ-flavoured DM in the QDF scenario.

(b) Viable masses m_ψ and m_{ϕ_3} in the SFF scenario.

Figure 8.6 | Constraints from the observed DM relic density on the model parameters.

and we demand the calculated annihilation rates to comply with this value within a 10% tolerance range. For the lepton masses m_{ℓ_i} we use the values given in Reference [158].

The results are gathered in Figure 8.6. For the QDF scenario the p-wave coefficient b in the limit $m_\phi \gg m_{\ell_i}$ reads

$$b = \frac{1}{48\pi} \frac{m_\phi^2}{(m_\phi^2 + m_\psi^2)^2} (D_1^2 + D_2^2 + D_3^2)^2 \,, \tag{8.27}$$

where we have performed the sum over initial and final state flavours yielding

$$\sum_{ij} \sum_{kl} |\lambda_{ik}|^2 |\lambda_{jl}|^2 = \text{Tr}\left[\lambda^\dagger \lambda\right]^2 = \text{Tr}\left[D^2\right]^2 \,. \tag{8.28}$$

Hence, the relic density limit reduces to a condition on the couplings D_i which corresponds to the shell of a three-dimensional sphere. This sphere is then further deformed by the restrictions that the mass splitting condition of the QDF scenario places on the couplings D_i which in total results in the contours illustrated in Figure 8.6a. We further find that the m_ϕ^2 dependence of b or $\langle \sigma v \rangle_{\text{eff}}$, respectively, requires larger couplings for decreasing DM masses m_ϕ. Most importantly, the p-wave suppression of the annihilation rate requires large couplings $D_i \gtrsim 1.0$ for viable mediator masses $m_\psi \gtrsim 800\,\text{GeV}$ in order to reproduce the correct relic density.

With respect to the masses of the NP fields, we find that the upper limit $D_i \leq 2.0$ causes a mediator mass dependent lower limit on the DM mass m_ϕ since the annihilation rate depends on the sum of $D_i^4\, m_\phi^2 / m_\psi^4$. This lower limit can be seen explicitly in Figure 8.6b for the SFF scenario. In the latter scenario there also exists an upper limit on the DM mass m_ϕ, since it demands one of the masses

$$m_{\phi_i} = m_\phi \sqrt{1 - |\eta|\, D_j^2} \,, \tag{8.29}$$

where the indices i and j are determined by the hierarchy $m_{\phi_1} > m_{\phi_2} > m_{\phi_3}$, to be significantly split from the other two. This in turn means that in the SFF scenario one coupling $D_{\max} = \max(D_1, D_2, D_3)$ is always large and needs to satisfy $D_{\max} \gtrsim 1.5$ in order to generate mass splittings of at least 10%. Hence, for sufficiently small mediator masses m_ψ the DM mass m_ϕ may not grow arbitrarily large as this would result in a too large annihilation rate. For mediator masses $m_\psi \gtrsim 800\,\text{GeV}$ however, the annihilation rate is sufficiently suppressed by the mediator mass such that values for m_{ϕ_3} up to the equal mass threshold $m_{\phi_3} = m_\psi$ become viable.

8.4 Dark Matter Detection Experiments

Phenomenologically, lepton-flavoured DM models are particularly interesting due to the absence of tree-level contributions to DM–nucleon scattering. This advantage however comes at the cost of potentially more stringent constraints from indirect detection experiments, as in these models DM is directly coupled to positrons. To shed light on how strongly the absence of signal in DM detection experiments restricts the parameter space of our model we examine both direct as well as indirect detection constraints in this section.

Relevant Processes for Direct Detection

Despite the above mentioned one-loop suppression of leading contributions to the DM–nucleon scattering cross section, coupling DM to leptons generally leads to a very rich direct detection phenomenology. The reason is the direct coupling of DM to electrons, which renders these models subject to constraints on a variety of interactions relevant for the direct detection of DM. The latter interactions can be summarised as follows [214]:

a) *DM–nucleon scattering*: In this process the DM particle scatters off nuclei, which results in nuclear recoil signals. For lepton-flavoured DM the leading contribution is generated at the one-loop level through diagrams like the one shown in Figure 8.7a.

b) *DM–electron scattering*: Scatterings between DM and electrons can either take place elastically or inelastically. In the latter case DM scatters off bound electrons in an atom, which ionises the atom as the electron absorbs the whole recoil and is kicked out of it. On the other hand, elastic scatterings between DM and free electrons in the early Universe inhibit structure formation and thus suppress CMB anisotropies. This process is shown in Figure 8.7b.

c) *DM–atom scattering*: In this process DM scatters off bound electrons such that the overall recoil is absorbed by the atom the electron is bound in. This again can take place either elastically, where the electron wave-function remains the same or inelastically, where the scattering excites the electron to an outer shell.

Among this variety of interactions we find scatterings between DM and nuclei to be the most relevant ones for direct detection. This is because comparisons between the event rates of DM–nucleon scattering, inelastic DM–electron scattering and DM–atom scattering show that the former process strongly dominates over the latter two [214]. In both processes, inelastic DM–electron scattering and DM–atom scattering, the event rate suffers from a severe wave-function suppression as the electron has to carry a non-negligible momentum $p_e \sim \mathcal{O}(\text{MeV})$ in order to generate sizeable signals. Hence, these processes are negligible compared to DM–nucleon scattering. For elastic DM–electron scattering we find that it only puts constraints on our model for sub-MeV DM as the limits carry a strong DM mass dependence [215].

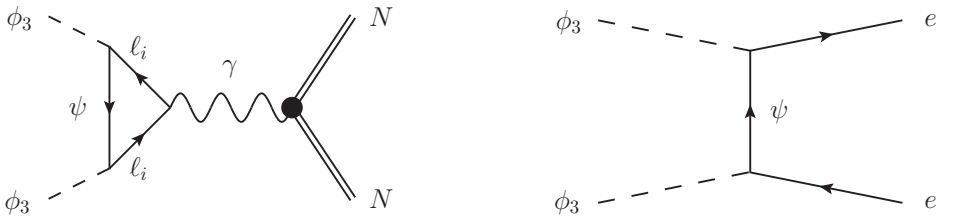

(a) one-loop DM–nucleon scattering **(b)** s-channel DM–electron scattering

Figure 8.7 | Representative Feynman diagrams of relevant interactions for direct detection signals. Note that for the photon penguin there is also a diagram where the photon is emitted by the mediator ψ.

Note that aside the one-loop penguin shown in Figure 8.7a, relevant contributions to the DM–nucleon scattering rate can also be induced by Higgs portal interactions. The quartic coupling $\lambda_{H\phi}$ gives rise to a tree-level scattering diagram in which a Higgs boson is exchanged in the t-channel. This process is proportional to $\lambda_{H\phi}^2 y_N^2$, where $y_N \simeq 0.3$ is the Higgs–nucleon coupling [194][29]. Following our arguments from Section 7.1 and 8.3 we neglect these contributions as we are primarily interested in the structure of the flavour-violating coupling matrix λ. Moreover, there also exists a Z boson mediated version of the penguin diagram in Figure 8.7a, in which DM couples to the quark vector current of the nucleon. This process is suppressed by $m_{\ell_i}^2/m_\psi^2$ where m_{ℓ_i} is the mass of the lepton in the loop and can thus be safely neglected [193].

In summary, this leaves us with the one-loop photon penguin shown in Figure 8.7a. This interaction is induced by the charge-radius operator

$$\mathcal{O}_\gamma = \partial^\mu \phi \, \partial^\nu \phi^\dagger F_{\mu\nu} \,, \tag{8.30}$$

and in the limit of negligible lepton masses $m_{\ell_i} \ll m_\psi$ its matched matrix element f_γ is given by [190]

$$f_\gamma = -\sum_i \frac{e\,|\lambda_{i3}|^2}{16\pi^2\, m_\psi^2} \left[1 + \frac{2}{3} \log\left(\frac{m_{\ell_i}^2}{m_\psi^2}\right)\right] . \tag{8.31}$$

In this expression the electron mass m_e needs to be replaced by the momentum transfer $|\vec{q}| = \mathcal{O}(3-10)\,\text{MeV}$ for the case $i = 1$, i.e. for an electron–positron pair in the loop [190]. The averaged SI DM–nucleon scattering cross section is given by

$$\sigma_{\text{SI}} = \frac{Z^2\, e^2\, \mu^2}{8\pi\, A^2}\, f_\gamma^2 \,, \tag{8.32}$$

where Z and A are the atomic and mass number of the element that the nucleons constitute and μ is the reduced mass of the DM–nucleon system defined as $\mu = m_N m_{\phi_3}/(m_N + m_{\phi_3})$.

Constraints from Direct Detection

In our numerical analysis of the direct detection constraints we generate random points in the parameter space of our model, calculate the DM–nucleon scattering cross section through Equation (8.32) and compare it with its experimental upper limit. The latter

[29] Note that even without a direct coupling of the DM fields to the Higgs boson an effective coupling is generated at the one-loop level through the same diagram as in Figure 8.7a with a Higgs boson instead of a photon. These contributions are proportional to $y_{\ell_i}^2 y_N^2 |\lambda_{i3}|^4$, and hence they are negligible due to the smallness of the lepton Yukawa couplings y_{ℓ_i}.

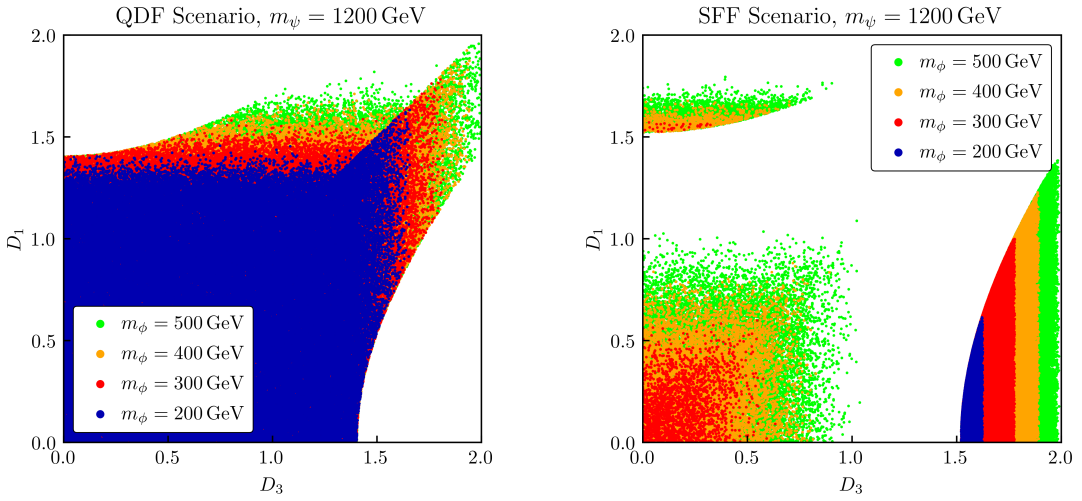

(a) QDF scenario **(b)** SFF scenario

Figure 8.8 | Direct detection bounds on the couplings D_1 and D_3. The mediator mass is fixed to $m_\psi = 1200\,\text{GeV}$ and the tree-level DM mass parameter m_ϕ varies.

is given at 90% C.L. and is obtained from the XENON1T experiment [177]. The values of the lepton masses are taken from Reference [158] and we use $|\vec{q}| = 10\,\text{MeV}$ for the momentum transfer mentioned above. The atomic and mass numbers of Xenon read $Z = 54$ and $A = 131$. Note that we ignore the impact of Xenon isotopes on the DM–nucleon scattering rate here, since it was found to be small in Reference [21]. The results are shown in Figure 8.8.

We find that in both scenarios τ-flavoured DM, i.e. points with $D_3 > D_{1,2}$ generally allow for larger couplings D_i than e- or μ-flavoured DM. The reason is the logarithmic m_{ℓ_i} dependence of the DM–nucleon scattering cross section. As can be seen in Equation (8.31), the amplitude f_γ grows for a decreasing mass of the lepton in the loop. Since the tau mass m_τ is significantly larger than the muon mass m_μ or the momentum transfer $|\vec{q}|$, we find the largest restrictions to be placed on D_1 and D_2. As far as the NP masses are concerned, we find that in both scenarios increasing DM masses m_{ϕ_3} allow for larger couplings D_i. While being suppressed by two powers of the mediator mass m_ψ, the amplitude f_γ however does not depend on the DM mass m_ϕ. This parameter only appears in the reduced mass μ for which we find $\mu \approx m_N$ since we generally consider $m_{\phi_3} \gg m_N$. The above mentioned m_ϕ dependence of the viable points in Figure 8.8 is hence solely due to the XENON1T upper limit itself, which reaches its minimum for $m_{\phi_3} \simeq 30\,\text{GeV}$ and increases with a growing DM mass.

In the QDF scenario shown in Figure 8.8a the points above the diagonal correspond to either e- or μ-flavoured DM while the points below the diagonal represent either μ- or τ-flavoured DM. For the latter case we find the overall viable coupling size to be the largest, as D_3 may grow as large as its maximal value $D_3 = 2.0$ for a DM mass of $m_\phi = 500\,\text{GeV}$ (green points). Viable points in the $D_3 - D_1$ plane are shown for the SFF scenario in Figure 8.8b and here the points with a large D_3 or D_1 represent τ-flavoured DM or e-flavoured DM, respectively. The points close to the origin with $D_{1,3} \lesssim 1.0$ correspond to μ-flavoured DM. Since the SFF scenario demands one coupling D_i to be large, e- and μ-flavoured DM are not viable for small DM masses. This is due to the interplay between the above mentioned logarithmic lepton mass dependence of the DM–nucleon scattering

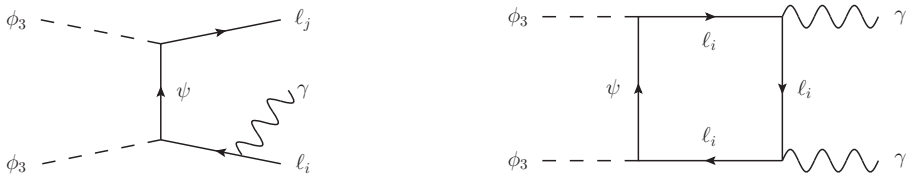

(a) t-channel annihilation to $\ell\bar{\ell}\gamma$ **(b)** one-loop annihilation to $\gamma\gamma$

Figure 8.9 | Representative Feynman diagrams for relevant higher-order annihilation processes.

rate and the DM mass dependence of the experimental upper limit. This can be seen explicitly in Figure 8.8b as there are no viable points with e- or μ-flavoured DM for small masses $m_\phi = 200\,\text{GeV}$ (blue points).

Relevant Processes for Indirect Detection

For lepton-flavoured DM the direct coupling of the DM triplet to electrons and positrons together with the increased number of annihilation channels with a positron in the final state can generally lead to sizeable electron-positron fluxes. Hence, depending on the model details, they can be subject to restrictive constraints from indirect detection experiments. However, for our case of complex scalar DM coupling to SM leptons this is not necessarily the case. As discussed in Section 8.3, in our model the DM annihilation rate is p-wave suppressed which translates into a severe velocity suppression of $\langle\sigma v\rangle_{\text{eff}}$ since the DM halo velocity in the Milky Way today is given by $\langle v^2\rangle \simeq 10^{-6}$.

In order to lift this suppression and provide a proper analysis of the restrictions that indirect detection experiments place on the parameter space of our model, we hence include the higher order diagrams shown in Figure 8.9 into our calculation of the DM annihilation rate. The process of two dark particles ϕ_3 annihilating into the three-body final state $\ell_i\bar{\ell}_j\gamma$ is shown in Figure 8.9a and lifts the p-wave suppression of the process $\phi_3\phi_3^\dagger \to \ell_i\bar{\ell}_j$. On the other hand, the one-loop process of two DM particles annihilating into two photons shown in Figure 8.9b gives comparable contributions and is particularly relevant for searches in γ-ray line spectra. Note that neither of these processes is relevant for the thermal freeze-out of DM. Annihilations into the three-body final state are parametrically suppressed by $\alpha_{\text{em}}/\pi \simeq 10^{-3}$ while one-loop annihilations into photons are even further suppressed by $\alpha_{\text{em}}^2/(4\pi)^2 \simeq 10^{-7}$. In contrast, the p-wave suppression of tree-level DM annihilations only translates into a much less severe velocity suppression by $\langle v^2\rangle \simeq 0.3$ in the early Universe.

In the limit of vanishing lepton masses $m_{\ell_i} \to 0$, the annihilation rates $\langle\sigma v\rangle_{\ell\bar{\ell}\gamma}$ and $\langle\sigma v\rangle_{\gamma\gamma}$ of both processes shown in Figure 8.9 read [216, 217]

$$\langle\sigma v\rangle_{\ell\bar{\ell}\gamma} = \frac{\alpha_{\text{em}}}{32\pi^2 m_{\phi_3}^2}\sum_{ij}|\lambda_{i3}|^2|\lambda_{j3}|^2\mathcal{A}(\mu)\,, \tag{8.33}$$

$$\langle\sigma v\rangle_{\gamma\gamma} = \frac{\alpha_{\text{em}}^2}{64\pi^3 m_{\phi_3}^2}\left(\sum_i|\lambda_{i3}|^2\right)^2|\mathcal{B}(\mu)|^2\,. \tag{8.34}$$

The functions $\mathcal{A}$ and $\mathcal{B}$ are defined as

$$\begin{aligned}\mathcal{A}(\mu) = (\mu+1)\left(\frac{\pi^2}{6} - \log^2\left[\frac{\mu+1}{2\mu}\right] - 2\text{Li}_2\left[\frac{\mu+1}{2\mu}\right]\right)\\ + \frac{4\mu+3}{\mu+1} + \frac{4\mu^2-3\mu-1}{2\mu}\log\left[\frac{\mu-1}{\mu+1}\right]\,,\end{aligned} \tag{8.35}$$

$$\mathcal{B}(\mu) = 2 - 2\log\left[1 - \frac{1}{\mu}\right] - 2\mu \arcsin\left[\frac{1}{\sqrt{\mu}}\right]^2 , \tag{8.36}$$

where $\mu = m_\psi^2/m_{\phi_3}^2$ and $\mathrm{Li}_2(z)$ is the dilogarithm. The rate $\langle\sigma v\rangle_{\ell\bar{\ell}}$ for the tree-level annihilation into a pair of leptons ℓ is the same as the thermal annihilation cross section for the SFF scenario discussed in Section 8.3 without the sum over final state flavours.

Constraints from Indirect Detection

In the numerical analysis we use limits obtained by the AMS [218], Fermi–LAT [219] and H.E.S.S. [220] experiments in order to constrain our model. Reference [221] has calculated an upper limit $\langle\sigma v\rangle_{\bar{e}}^{\max}$ for DM annihilations into an electron–positron pair with a branching ratio of 100% based on AMS-02 measurements of the positron flux. The latter signal generally includes both prompt as well as secondary positrons from decays of muons and taus. However, since the energy spectrum is shifted towards lower energies for secondary positrons and since they additionally suffer from a smeared momentum distribution, the signal is mainly dominated by prompt positrons. To constrain our model we hence sum over all annihilation channels with a positron in the final state and compare the resulting annihilation rate with the experimental upper limit. Here we also include the radiative corrections of Figure 8.9a since we expect the shift in the DM mass dependence for the three-body final state compared to the two-body final state for which the limits from Reference [221] are calculated to be negligible. In summary, we demand that the annihilation rate

$$\langle\sigma v\rangle_{\bar{e}} = \sum_\ell \left(\langle\sigma v\rangle_{\ell\bar{e}} + \langle\sigma v\rangle_{\ell\bar{e}\gamma}\right) , \tag{8.37}$$

is smaller than the experimental upper limit $\langle\sigma v\rangle_{\bar{e}}^{\max}$.

Using measurements of the γ-ray continuum spectrum measured by the Fermi–LAT satellite, Reference [222] provides a respective upper limit $\langle\sigma v\rangle_{\tau}^{\max}$ for DM annihilations into a tau–antitau pair. Similar to the positron flux being most sensitive to prompt positrons, this signal is mainly dominated by taus or antitaus in the final state as they produce significantly more photons through subsequent decays than electrons and muons. We thus calculate the total annihilation rate into final states with at least one tau or antitau, i.e. we calculate the rate

$$\langle\sigma v\rangle_{\tau} = \langle\sigma v\rangle_{\tau\bar{\tau}} + \langle\sigma v\rangle_{\tau\bar{\tau}\gamma} + \frac{1}{2}\sum_{\ell=e,\mu}\left(\langle\sigma v\rangle_{\ell\bar{\tau}} + \langle\sigma v\rangle_{\bar{\ell}\tau} + \langle\sigma v\rangle_{\ell\bar{\tau}\gamma} + \langle\sigma v\rangle_{\bar{\ell}\tau\gamma}\right) , \tag{8.38}$$

and compare it with the upper limit $\langle\sigma v\rangle_{\tau}^{\max}$. In this expression we have included annihilations into the three-body final state for the same reason as above. The factor of $1/2$ for final states with a single tau or antitau is due to the fact that the respective upper limit was derived for a tau–antitau pair in the final state.

Finally, we also constrain our model based on searches in the γ-ray line spectrum, since both processes of Figure 8.9 exhibit a line-like photon energy spectrum. The energy distribution of the one-loop process induced by the box diagram of Figure 8.9b peaks at $E_\gamma = m_{\phi_3}$. In spite of being a three-body process, the diagram depicted in Figure 8.9a on the other hand produces a line-like signal. The reason is that this process is dominated by internal bremsstrahlung photons emitted from the virtual ψ which exhibit a sharply peaked energy spectrum just below the DM mass [223]. To constrain our model we use limits obtained by Reference [223], which based on H.E.S.S. and Fermi–LAT data has calculated an upper limit $\langle\sigma v\rangle_{\gamma}^{\max}$ on the annihilation rate

$$\langle\sigma v\rangle_{\gamma} = \sum_\ell \langle\sigma v\rangle_{\ell\bar{\ell}\gamma} + 2\langle\sigma v\rangle_{\gamma\gamma} . \tag{8.39}$$

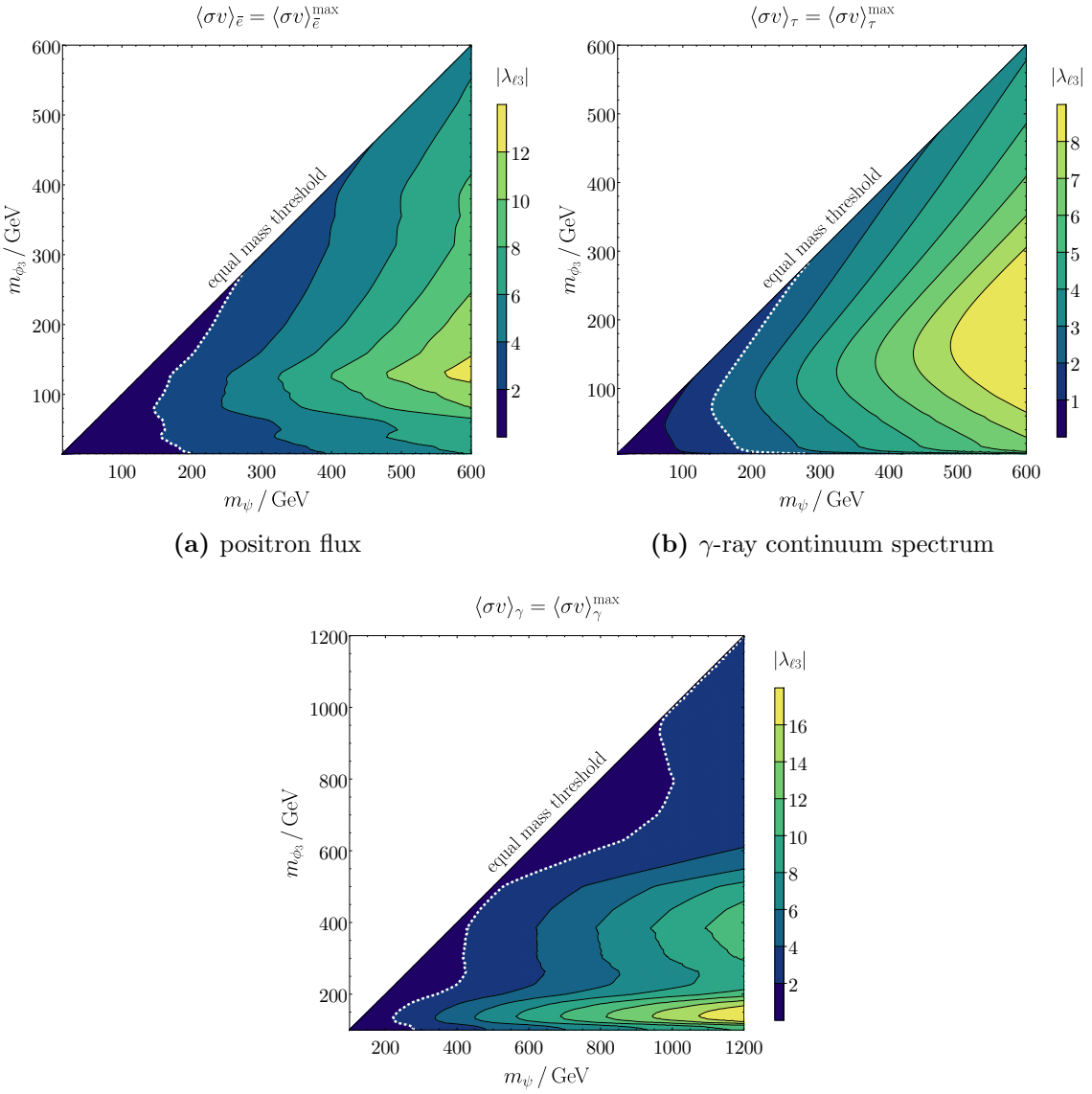

(a) positron flux

(b) γ-ray continuum spectrum

(c) γ-ray line spectrum

Figure 8.10 | Restrictions on the model parameters from indirect detection experiments. The area included by the white dashed line and the equal mass diagonal indicates in which mass regime the constraints are relevant.

We estimate the impact of the constraints on our model by determining the coupling strength for which each of the annihilation rates $\langle\sigma v\rangle_{\bar{e}}$, $\langle\sigma v\rangle_{\tau}$ and $\langle\sigma v\rangle_{\gamma}$ saturates its respective experimental upper limit. To this end, we scan over the mass parameters m_{ψ} and m_{ϕ_3} and take the limit of degenerate couplings $|\lambda_{i3}| = |\lambda_{\ell 3}|$ when calculating the rates of Equations (8.37)–(8.39). The results are gathered in Figure 8.10.

In all three panels the white dashed line indicates the contour with $|\lambda_{i3}| = 2.0$. We only expect constraints on our model in the area that is enclosed by the equal mass diagonal and this contour, since the couplings D_i are limited to $D_i \leq 2.0$ which translates to the condition $|\lambda_{ij}| \leq 2.0$. We find that the constraints from measurements of the positron flux or the γ-ray continuum spectrum only place restrictions on the model parameters for NP scales which are already excluded by the LHC searches discussed in Section 8.1. In Figure 8.10a we see that the limit on annihilations into a single positron constrains our

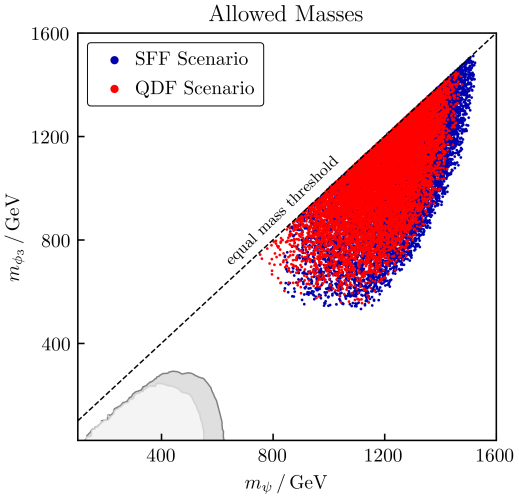

Figure 8.11 | Viable masses in both scenarios when fulfilling all constraints simultaneously. We further show the largest possible exclusion contours coming from the LHC searches for same-flavour final states $\ell\bar{\ell} + \not{E}_T$ with $\ell = e, \mu$ in both scenarios. The grey contour corresponds to the QDF scenario with $D_1 = D_2 = D_3 = 2.0$. The light-grey contour represents the largest possible exclusion in the SFF scenario with $D_1 = D_2 = 1.5$ and $D_3 = 2.0$.

model for mediator masses $m_\psi \lesssim 250\,\text{GeV}$, where in the range $200\,\text{GeV} \lesssim m_\psi \lesssim 250\,\text{GeV}$ it is only relevant in the close-to-degenerate region $m_\psi \approx m_{\phi_3}$. A similar conclusion holds true for annihilations into final states with a tau or antitau, with the sole difference that in this case limits can be relevant up to NP scales $m_\psi \simeq 300\,\text{GeV}$, see Figure 8.10b. The limits from searches in the γ-ray line spectrum are illustrated in Figure 8.10c. We find them to be more restrictive, as they lead to relevant constraints for masses up to $m_\psi \simeq 1000\,\text{GeV}$. However, these limits are again mainly relevant in the near-degeneracy regime $m_\psi \approx m_{\phi_3}$. In total, we conclude that the indirect detection constraints remain rather weak compared to limits from LHC searches, LFV decays, the observed DM relic density or direct detection experiments.

8.5 Combined Analysis

In the combined analysis we impose all constraints simultaneously and demand that they are fulfilled. The results are gathered in Figures 8.11–8.13.

Figure 8.11 illustrates viable points in the $m_\psi - m_{\phi_3}$ plane for both scenarios. We additionally show the largest possible LHC exclusion for both scenarios in form of the grey and light-grey contours. The results show that the combined analysis demands the NP mass parameters to satisfy $m_\psi \gtrsim 750\,\text{GeV}$ and $m_{\phi_3} \gtrsim 550\,\text{GeV}$. This can be tracked down to the interplay of the relic density and direct detection constraints. In Section 8.3 we had found that the p-wave suppression of the DM annihilation rate requires large couplings D_i in order to yield the correct relic density. At the same time, the direct detection limits discussed in Section 8.4 can only be satisfied for sufficiently large mediator masses m_ψ if the couplings D_i are large. As sizeable mediator masses also suppress the DM annihilation rate, this then needs to be compensated for by comparably large DM masses which we had found to enhance the annihilation rate in Section 8.3. We further find that for mediator masses

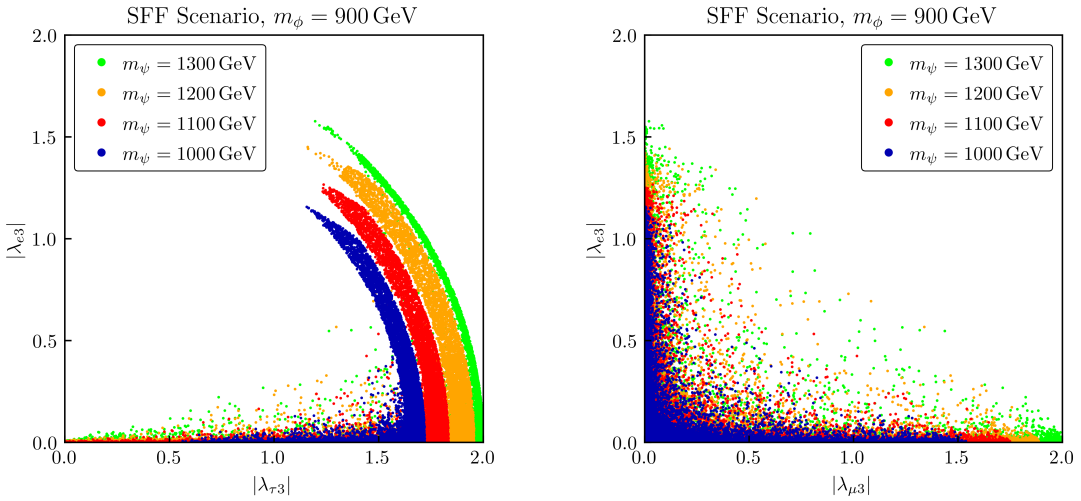

(a) $|\lambda_{\tau 3}| - |\lambda_{e3}|$ plane **(b)** $|\lambda_{\mu 3}| - |\lambda_{e3}|$ plane

Figure 8.12 | Viable couplings $|\lambda_{i3}|$ for $m_\phi = 900\,\text{GeV}$ and varying m_ψ based on all constraints in the SFF scenario.

$750\,\text{GeV} \lesssim m_\psi \lesssim 1200\,\text{GeV}$ the suppression of the DM–nucleon scattering amplitude f_γ through m_ψ alone is not sufficient to compensate for sizeable couplings D_i. In this region the DM mass needs to be larger than what the relic density constraint alone would require, since increasing DM masses do not only enhance the DM annihilation rate but also loosen the XENON1T upper limit on DM–nucleon scattering for $m_{\phi_3} \gtrsim 30\,\text{GeV}$. Hence, for increasing values of m_{ϕ_3} the direct detection constraints allow for larger couplings D_i while the relic density constraint can be satisfied with smaller couplings D_i. We further find that the LHC constraints yield the largest exclusion in the $m_\psi - m_{\phi_3}$ plane for the QDF scenario. This is due to the sign of the parameter η from Equation (7.6) which we have chosen to be negative. As we have additionally assumed $D_1 = D_2 = D_\ell$ in order to straightforwardly recast the LHC searches studied in Section 8.1, the couplings D_i need to satisfy $D_3 > D_{1,2}$ in the SFF scenario to yield the correct mass hierarchy. Hence, in this case one is always left with a larger coupling to taus than to electrons and muons which reduces the relevant branching ratio into final states with the latter two. This in turn leads to a smaller signal cross section in the SFF scenario compared to the QDF scenario, as the couplings D_i are close to equal in the latter case. Moreover, we find that the LHC constraints only exclude the parameter space which is already ruled out by the above explained interplay between the relic density and direct detection constraints. As far as the mixed-flavour final states $\ell_i \bar{\ell}_j + \not{E}_T$ mentioned in Section 8.1 are concerned, we find that their signal cross section is highly suppressed and yields values of order $\mathcal{O}(\text{ab})$, since only large masses m_ψ and m_{ϕ_3} are viable. The SM background on the other hand, is dominated by the production of $t\bar{t}$ and WW pairs, with significantly larger cross sections than $\psi\bar{\psi}$ pair-production in our model: we find the background to be of order $\mathcal{O}(\text{pb})$ and thus expect the mixed-flavour final states to not exhibit a significant discovery potential.

The viable structure of the coupling matrix λ in the SFF scenario is illustrated in Figure 8.12 and is mainly determined by the flavour, relic density and direct detection constraints. The circular bands that can be seen in Figure 8.12a are a result of the interplay between the flavour and relic density constraints. In the SFF scenario the coupling matrix

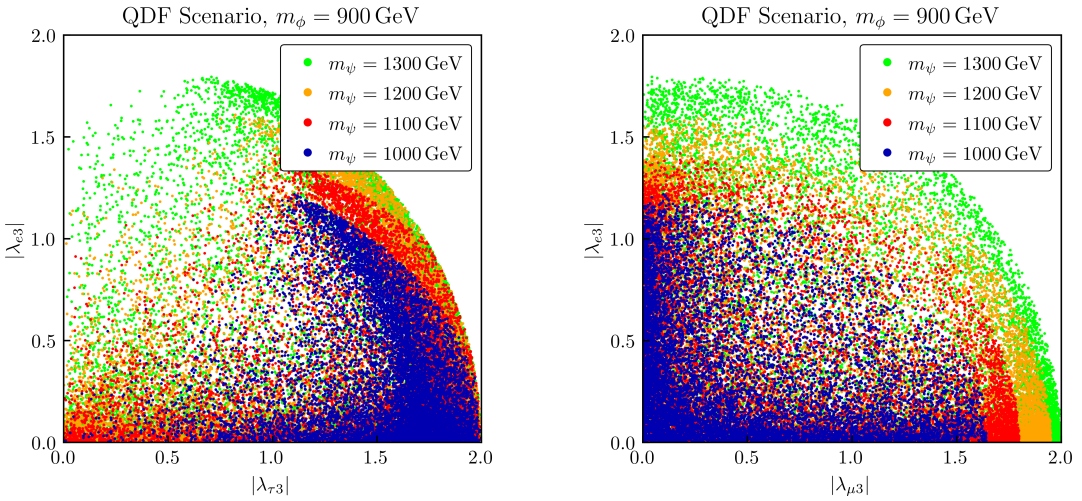

(a) $|\lambda_{\tau 3}| - |\lambda_{e3}|$ plane **(b)** $|\lambda_{\mu 3}| - |\lambda_{e3}|$ plane

Figure 8.13 | Viable couplings $|\lambda_{i3}|$ for $m_\phi = 900\,\text{GeV}$ and varying m_ψ based on all constraints in the QDF scenario.

λ needs to satisfy the spherical condition

$$|\lambda_{e3}|^2 + |\lambda_{\mu 3}|^2 + |\lambda_{\tau 3}|^2 \approx \text{const.}\,, \tag{8.40}$$

in order to yield the correct relic density. This causes the outer edge of the bands shown in Figure 8.12a. The inner edge, on the other hand, is due to the limits from the LFV decay $\mu \to e\gamma$ discussed in Section 8.2. As can be seen in Figure 8.12b, these limits force the product of $|\lambda_{e3}|$ and $|\lambda_{\mu 3}|$ to be small, i.e. either $|\lambda_{e3}|$ can be large while $|\lambda_{\mu 3}|$ is small or vice versa. The points with a sizeable DM–electron coupling $|\lambda_{e3}|$ then cause the circular bands while the points with sizeable couplings $|\lambda_{\mu 3}|$ are scattered at the bottom in Figure 8.12a. In Figure 8.12b we can also see the impact of the direct detection constraints as the maximum of the viable values is larger for $|\lambda_{\mu 3}|$ than for $|\lambda_{e3}|$ for all choices of the mediator mass m_ψ. For large enough values of $|\lambda_{e3}|$ the DM–nucleon scattering constraints become dominant over the relic density constraints. This can be seen in Figure 8.12a as the circular bands become thinner for growing values of $|\lambda_{e3}|$ above this threshold. For even larger values of $|\lambda_{e3}|$ we find that the direct detection and relic density constraints cannot be satisfied simultaneously, which strongly disfavours the case of e-flavoured DM, i.e. $|\lambda_{e3}| > |\lambda_{\mu 3}|, |\lambda_{\tau 3}|$. As the DM–nucleon scattering rate is significantly larger for an electron in the loop in Figure 8.7a, we find that in spite of the $1/m_\psi^2$ suppression of f_γ even for large masses $m_\psi \gtrsim 1200\,\text{GeV}$ the DM particle ϕ_3 needs to be mainly μ- or τ-flavoured.

The viable structure of λ in the QDF scenario is shown in Figure 8.13. While it generally exhibits analogous features as the SFF scenario, we find these features to be far less pronounced due to the different dynamics of the thermal freeze-out of DM. As all dark particles contribute to the freeze-out in this case, the relic density constraint reduces to the condition

$$\sum_{ij} |\lambda_{ij}|^2 \approx \text{const.}\,, \tag{8.41}$$

i.e. it demands the couplings $|\lambda_{ij}|$ to form the shell of a nine-dimensional sphere. This condition causes the outer circular edge that can be seen in both Figure 8.13a and 8.13b.

Moreover, we find the flavour constraints to be weaker than in the SFF scenario, since in this case the couplings D_i are close-to-degenerate which translates to a close-to-diagonal coupling matrix λ. This can be seen explicitly in Figure 8.13b where in spite of the higher point density close to the axes points with comparable values for $|\lambda_{e3}|$ and $|\lambda_{\mu 3}|$ are also viable. This at the same time is the reason for why there is no inner edge for the contours in the $|\lambda_{\tau 3}| - |\lambda_{e3}|$ plane in the QDF scenario as shown in Figure 8.13a. The impact of the direct detection limits on the parameter space can again be seen in both panels of Figure 8.13. For a mediator mass $m_\psi = 1000\,\text{GeV}$ (blue points), for example, the coupling of DM to tau leptons may become maximal with $|\lambda_{\tau 3}| = 2.0$, while the couplings to muons and electrons are limited to $|\lambda_{\mu 3}| \simeq 1.7$ and $|\lambda_{e3}| \simeq 1.2$. The maximally viable values of the latter two couplings moreover increase with a growing mediator mass, as the DM–nucleon scattering rate is suppressed by two powers of it. In Figure 8.13a we further see that the direct detection constraint is dominant over the relic density constraint for a larger range of allowed values for $|\lambda_{e3}|$ than in the SFF scenario. In terms of the flavour of ϕ_3 we again find that most of the viable points correspond to τ-flavoured DM while—contrary to the SFF scenario—in this case a significant part of the viable parameter space also represents μ- and e-flavoured DM.

Chapter 9
Summary

In this part we have studied a simplified DMFV model of lepton-flavoured DM in which the SM is extended by the complex scalar DM flavour triplet $\phi = (\phi_1, \phi_2, \phi_3)^T$ and the charged fermion ψ which couples the DM triplet to right-handed charged leptons ℓ_R. This interaction is governed by a new coupling matrix λ which according to the DMFV ansatz is assumed to constitute the only new source of flavour-violation aside from the SM Yukawa couplings. After having discussed the details of this model in Chapter 7 we examined constraints from collider searches, LFV decays, the observed relic density and direct as well as indirect detection experiments in Chapter 8 in order to constrain the parameter space of this model.

Section 8.1 was dedicated to the analysis of constraints from LHC searches and here we have found that the largest restrictions are placed on our model by SUSY searches for first and second generation sleptons. To study these constraints we recasted a CMS search in the final states $\ell\bar{\ell} + \not{E}_T$ and $\bar{\tau}\tau + \not{E}_T$ based on the full run 2 LHC data set. The constraints from searches in τ-flavoured final states are significantly less restrictive than the limits coming from searches in $\ell\bar{\ell} + \not{E}_T$. For the latter signature, the exclusion in the mass plane $m_\psi - m_\phi$ is the largest for sizeable couplings D_ℓ to electrons and muons together with small couplings D_3 to taus, as otherwise the branching ratio into the relevant final states is reduced. The LHC constraints maximally exclude NP scales of $m_\psi \lesssim 750\,\text{GeV}$.

The flavour structure of the coupling matrix λ was studied in Section 8.2 where we discussed constraints from LFV decays. Here, the strongest restrictions are placed on the model by the decay $\mu \to e\gamma$ which in the limit of negligible DM masses $m_\psi \gg m_\phi$ was estimated to demand the coupling matrix λ to satisfy $|\left(\lambda\lambda^\dagger\right)_{\mu e}|^{1/2} \lesssim m_\psi/15\,\text{TeV}$. More generally, the constraints from LFV decays can either be fulfilled by vanishing mixing angles θ_{ij} or by degenerate couplings D_i which both render the coupling matrix λ diagonal. We concluded this section by commenting on possible constraints from leptonic EDMs and MDMs and found that in our model sizeable contributions to these observables can only be generated at NP scales of $\mathcal{O}(100\,\text{GeV})$, which are already excluded by LHC searches.

In Section 8.3 we have studied the constraints that the observed DM relic density implies for our model. Here we have limited our analysis to the two benchmark scenarios for the thermal freeze-out of DM introduced in Section 3.2 and found the DM annihilation rate to be p-wave suppressed in both. This generally requires the couplings D_i to be sizeable in order to compensate for this suppression and yield the correct relic density. Moreover, the p-wave suppression of the DM annihilation rate requires comparably large DM masses $m_{\phi_3} \gtrsim 300\,\text{GeV}$ for mediator masses $m_\psi \gtrsim 1000\,\text{GeV}$ in order to satisfy the experimental limit.

The restrictions placed on the parameter space of our model by detection experiments were examined in Section 8.4. We first discussed constraints from direct detection experiments by identifying relevant interactions between DM and the SM. The dominant interaction is induced by a one-loop photon penguin diagram contributing to SI DM–nucleon scattering. Using XENON1T data we then constrained our model to find that the

limits from direct detection are generally strong. Further, the DM–nucleon scattering rate is enhanced for a small mass of the lepton in the loop and hence the strongest restrictions are placed on the DM–electron coupling. Moving to constraints from indirect detection experiments, we found that the p-wave suppression of the DM annihilation rate requires the inclusion of higher order diagrams in order to derive meaningful constraints on our model. To this end we included the sub-leading annihilation of DM into two photons as well as the annihilation into the three-body final state with two charged leptons and a photon into our calculation. Nevertheless, the indirect detection constraints are weak compared to other constraints as only measurements of the γ-ray spectrum yield relevant limits for mediator masses up to $m_\psi \simeq 1000\,\text{GeV}$ in the near-degeneracy region $m_\psi \approx m_{\phi_3}$.

To provide a global picture we then used Section 8.5 to perform a combined analysis of all constraints. Here, the combination of relic density and direct detection constraints renders LHC limits irrelevant and forces the masses to roughly lie in the ranges $750\,\text{GeV} \lesssim m_\psi \lesssim 1550\,\text{GeV}$ and $550\,\text{GeV} \lesssim m_{\phi_3} < m_\psi$. Further, the allowed values for the couplings $|\lambda_{i3}|$ are mainly determined by the interplay of relic density, flavour and direct detection constraints in both freeze-out scenarios. Finally, we also studied which flavour of DM is preferred by experimental data and found that while in the SFF scenario only μ- and τ-flavoured DM are viable, the QDF scenario also allows for e-flavoured DM.

We conclude that lepton-flavoured complex scalar DM is a viable DM candidate governed by a rich phenomenology. The interplay of various experiments yields important information on the structure of the model and with future improved sensitivities, we may hope to discover first hints of lepton-flavoured DM in the laboratory.

Part IV

Lepton-Flavoured Scalar Dark Matter II

This part is based on

> H. Acaroğlu, P. Agrawal and M. Blanke, *Flavoured* $(g-2)_\mu$ *with Dark Lepton Seasoning*, 2212.08142.

We here propose a simplified model of lepton-flavoured complex scalar DM as a joint solution for the muon $(g-2)$ anomaly and the DM problem. This model extends the SM by a dark triplet of complex scalars which couple to both left- and right-handed leptons of the SM. These interactions are mediated by two fermion representations—an $SU(2)_L$ doublet which couples the DM triplet to left-handed leptons and a singlet which mediates right-handed interactions. Both representations are additionally coupled to the SM Higgs doublet through a new Yukawa coupling, leading to a mass mixing between the two charged mediators. We study the phenomenology of this model by examining constraints from collider searches, LFV decays, precision tests of the SM, the observed DM relic density and direct as well as indirect detection experiments. We first discuss each of these constraints individually and then perform a combined analysis by demanding that all constraints are satisfied simultaneously. Using the results of this combined analysis we then check if the model is capable of generating sizeable NP contributions to the muon anomalous magnetic moment a_μ. We find that in all benchmark scenarios considered the central value of its experimental measurement $\Delta a_\mu^{\text{exp}}$ can be reproduced without the introduction of fine-tuned lepton masses.

Chapter 10
Model Details

Among the large variety of different DM models those which are capable of addressing other problems, puzzles or anomalies of physics appear particularly appealing. Most prominently, the discrepancy between experimental measurements [26] and state of the art SM predictions [27][30] of the muon anomalous magnetic dipole moment a_μ currently constitutes one of the most significant hints at NP. This tension between data and theory is referred to as the muon $(g-2)$ anomaly and renders lepton-flavoured DM models [190–193] particularly worth investigating, since they assume the DM field to couple to leptons and can therefore generate potentially sizeable contributions to $(g-2)_\mu$.

For the lepton-flavoured DM model studied in the previous part of this work however, we had found that the absence of left-handed interactions forbids sizeable NP contributions to a_μ at viable NP scales, as enhanced diagrams with a chirality flip inside the loop are absent. In order to address both DM and the $(g-2)_\mu$ anomaly at the same time, we hence extend the model from Part III by left-handed interactions between DM and leptons. To this end we introduce an $SU(2)_L$ doublet containing a neutral and charged fermion that mediates interactions between DM and neutrinos or left-handed charged leptons, respectively. This new doublet and the new fermion already present in the purely right-handed version of this model from the previous part are additionally coupled to the SM Higgs doublet through a Yukawa coupling. This model does not belong to the DMFV class, as the additional fields and interactions ultimately lead to the absence of a new flavour symmetry the DM triplet can be associated with. Nevertheless, it represents an interesting benchmark case of flavoured DM potentially capable of explaining both the muon $(g-2)_\mu$ anomaly and the DM problem.

We use this chapter to introduce the model outlined above and present its details. We first review its field content and identify the most important NP interactions. After discussing and parametrising all NP couplings, we conclude the chapter with an analysis of the model's mass spectrum and a discussion of the stability of DM.

10.1 Field Content and Interactions

We present a simplified lepton-flavoured DM model in which the SM is extended by the dark triplet $\phi = (\phi_1, \phi_2, \phi_3)^T$. The fields ϕ_i are complex scalars represented by $(\mathbf{1}, \mathbf{1}, 0)_0$ under $(SU(3)_c, SU(2)_L, U(1)_Y)_{\text{spin}}$ and are coupled to left-handed as well as right-handed leptons of the SM. These interactions are mediated by two new fermion representations—the $SU(2)_L$ doublet $\Psi = (\psi_0, \psi_1')^T$ represented by $(\mathbf{1}, \mathbf{2}, -1/2)_{1/2}$ and the singlet ψ_2' which transforms as $(\mathbf{1}, \mathbf{1}, -1)_{1/2}$, respectively. The two fields Ψ and ψ_2' are additionally coupled to the SM Higgs doublet H through the Yukawa coupling y_ψ and we again assume the lightest dark scalar to account for the observed amount of DM in the Universe. An overview of the NP fields and their representations under the SM gauge group is given in Table 10.1.

[30] See References [225–244] for relevant original work.

The Lagrangian of this model reads

$$\begin{aligned}\mathcal{L} = \mathcal{L}_{\text{SM}} &+ \bar{\Psi}(i\not{D} - m_\Psi)\Psi + \bar{\psi}_2'(i\not{D} - m_\psi)\psi_2' + (\partial_\mu\phi)^\dagger(\partial^\mu\phi) - \phi^\dagger M_\phi^2\phi \\ &- (\lambda_{ij}^R\, \bar{\ell}_{Ri}\psi_2'\,\phi_j + \lambda_{ij}^L\, \bar{L}_i\Psi\,\phi_j + y_\psi\, \bar{\Psi}\psi_2'\,H + \text{h.c.}) \\ &+ \lambda_{H\phi}\,\phi^\dagger\phi\,H^\dagger H + \lambda_{\phi\phi}\left(\phi^\dagger\phi\right)^2 . \end{aligned} \tag{10.1}$$

In this expression the field L_i is defined as $L_i = (\nu_{Li}, \ell_{Li})^T$ and the two coupling matrices λ^R and λ^L are complex 3×3 matrices. To keep the total number of free model parameters manageable, we assume that the left-handed coupling is related to the right-handed coupling through the relation

$$\lambda^L = \xi\,\lambda^R = \xi\,\lambda\,. \tag{10.2}$$

This ansatz ensures that the coupling of DM to the lepton sector of the SM is parametrised by a single new flavour-violating coupling λ. While this simplifying assumption is similar to the DMFV hypothesis, we here stress that the model does not belong to the DMFV class, since the ansatz from above cannot be traced back to a new flavour symmetry the DM fields can be associated with. To overcome the ad-hoc nature of the ansatz in Equation (10.2) and to ensure that the model's phenomenology is captured in its entirety we assume the scaling parameter ξ to be a complex number. In this way we ensure that effects generated by a relative phase between λ^L and λ^R can still be present. In Section 11.2 we will find that this scaling parameter is particularly relevant for constraints from LFV decays, since potentially sizeable contributions from chirality-flipping diagrams can be suppressed through it. At the same time left-handed interactions may not be suppressed too strongly, as similar diagrams with a chirality flip inside the loop are necessary in order to generate sizeable NP effects in the muon anomalous magnetic moment a_μ. We thoroughly study this interplay between different experimental constraints on our model and their implications for the scaling parameter ξ in our phenomenological analysis in Chapter 11.

The mass parameters m_Ψ and m_ψ as well as the mass matrix M_ϕ are discussed in detail in Section 10.2. As already stated for the version of this model with purely right-handed interactions from Part III, the quartic couplings $\lambda_{H\phi}$ and $\lambda_{\phi\phi}$ represent a characteristic feature of scalar DM. For the self-coupling $\lambda_{\phi\phi}$ we again find that the perturbative contact interactions this coupling can give rise to are negligible for the viable DM masses that we find in the combined analysis of Section 11.6. We further neglect contributions generated by the Higgs portal coupling $\lambda_{H\phi}$ but comment on possible implications of it whenever necessary. Since there is no new flavour symmetry which forces these couplings to be diagonal or expressed in terms of λ, both could in principle be generic.

We stress that due to the absence of a new flavour symmetry all parameters of the coupling matrix λ remain physical for this model in contrast to the DMFV models studied

Table 10.1 | NP fields and their definitions as well as their representations under the SM gauge group.

Field	Definition	$SU(3)_C$	$SU(2)_L$	$U(1)_Y$	Spin
ϕ	$(\phi_1, \phi_2, \phi_3)^T$	**1**	**1**	0	0
Ψ	$(\psi_0, \psi_1')^T$	**1**	**2**	$-1/2$	$1/2$
ψ_2'	–	**1**	**1**	-1	$1/2$

in References [20–24], in Part II and particularly in Part III. Hence, we write λ in terms of nine real parameters and nine complex phases, i.e.

$$\lambda_{ij} = |\lambda_{ij}|\, e^{i\,\delta_{ij}} \,. \tag{10.3}$$

Together with the NP mass parameters m_Ψ, m_ψ and the three m_{ϕ_i}, the Yukawa coupling y_ψ and the complex scaling parameter

$$\xi = |\xi|\, e^{i\delta_\xi} \,, \tag{10.4}$$

this yields a total number of 26 model parameters. To ensure perturbativity and avoid a double-counting of the parameter space we restrict the coupling parameters to lie within the ranges

$$|\lambda_{ij}| \in [0, 2]\,, \quad \delta_{ij} \in [0, 2\pi)\,, \quad y_\psi \in [0, 2]\,, \quad |\xi| \in (0, 1]\,, \quad \delta_\xi \in [0, 2\pi)\,, \tag{10.5}$$

for the analyses performed in Chapter 11. Note that the Yukawa coupling y_ψ can be taken real and positive without loss of generality. As far as the parameter ξ is concerned, we restrict its absolute value to be smaller than one, since we only want to minimally extend the model that we have studied in Part III to reproduce the experimental central value of the muon anomalous magnetic moment $(g-2)_\mu$.

10.2 Mass Spectrum and Dark Matter Stability

In the Lagrangian of Equation (10.1) the Yukawa interaction between Ψ, ψ_2' and the Higgs doublet H introduces a mixing between the two charged states ψ_1' and ψ_2' with the corresponding mass matrix

$$M_\psi = \begin{pmatrix} m_\Psi & \frac{v\,y_\psi}{\sqrt{2}} \\ \frac{v\,y_\psi}{\sqrt{2}} & m_\psi \end{pmatrix} \,, \tag{10.6}$$

where $v = 246\,\text{GeV}$ is the *vacuum expectation value* (vev) of the Higgs field. We use the ansatz

$$\begin{pmatrix} \psi_1' \\ \psi_2' \end{pmatrix} = \begin{pmatrix} \cos\theta_\psi & -\sin\theta_\psi \\ \sin\theta_\psi & \cos\theta_\psi \end{pmatrix} \begin{pmatrix} \psi_1 \\ \psi_2 \end{pmatrix} \,, \tag{10.7}$$

and diagonalise this mass matrix to find the eigenvalues

$$m_{\psi_1} = \frac{1}{2}\left(m_\Psi + m_\psi + \sqrt{(m_\Psi - m_\psi)^2 + 2\,y_\psi^2 v^2}\right) \,, \tag{10.8}$$

$$m_{\psi_2} = \frac{1}{2}\left(m_\Psi + m_\psi - \sqrt{(m_\Psi - m_\psi)^2 + 2\,y_\psi^2 v^2}\right) \,, \tag{10.9}$$

and the corresponding mixing angle

$$\theta_\psi = \frac{1}{2}\arccos\left(\frac{(m_\Psi - m_\psi)}{\sqrt{(m_\Psi - m_\psi)^2 + 2\,y_\psi^2 v^2}}\right) \,. \tag{10.10}$$

Using these expressions, the Lagrangian from Equation (10.1) can then be written in terms of the mass eigenstates ψ_1 and ψ_2, yielding

$$\begin{aligned} \mathcal{L} = \mathcal{L}_{\text{SM}} &+ \bar{\psi_0}(i\not{D} - m_{\psi_0})\psi_0 + \bar{\psi_1}(i\not{D} - m_{\psi_1})\psi_1 + \bar{\psi_2}(i\not{D} - m_{\psi_2})\psi_2 + (\partial_\mu\phi)^\dagger(\partial^\mu\phi) \\ &- \phi^\dagger M_\phi^2 \phi + \lambda_{H\phi}\,\phi^\dagger\phi\, H^\dagger H + \lambda_{\phi\phi}\left(\phi^\dagger\phi\right)^2 - \left\{\xi\lambda_{ij}\bar{\nu}_i P_R \psi_0 \phi_j + \text{h.c.}\right\} \end{aligned}$$

$$- \left\{ \lambda_{ij} \bar{\ell}_i \left[(\cos\theta_\psi P_L - \xi \sin\theta_\psi P_R)\, \psi_2 + (\sin\theta_\psi P_L + \xi \cos\theta_\psi P_R)\, \psi_1 \right] \phi_j + \text{h.c.} \right\}$$
$$- \frac{y_\psi}{\sqrt{2}} \left\{ \sin 2\theta_\psi \left[\bar{\psi}_2 \psi_2 - \bar{\psi}_1 \psi_1 \right] h + \cos 2\theta_\psi \left[\bar{\psi}_1 \psi_2 + \bar{\psi}_2 \psi_1 \right] h \right\} . \tag{10.11}$$

In this expression we have defined $m_{\psi_0} = m_\Psi$.

For the DM mass matrix M_ϕ we cannot adopt the usual spurion expansion from MFV [15], since there is no new flavour symmetry in this model that the DM triplet can be associated with. Hence, we choose M_ϕ to be diagonal and write

$$M_\phi^2 = \text{diag}(m_{\phi_1}^2, m_{\phi_2}^2, m_{\phi_3}^2) \,, \tag{10.12}$$

while again demanding the DM mass parameters to satisfy the conventional hierarchy condition

$$m_{\phi_1} > m_{\phi_2} > m_{\phi_3} \,. \tag{10.13}$$

This means that in contrast to the DMFV models presented in References [20–24] as well as the two models studied in the previous parts of this work, the masses m_{ϕ_i} are free parameters here, i.e. the mass splittings between different dark flavours are not restricted. However, to keep the results of our analysis comparable to the mentioned studies we adopt the upper limit from DMFV models. There, the mass corrections are restricted to a maximum of 30% in order to ensure the convergence of the spurion expansion. To guarantee the stability of the lightest state ϕ_3 we again impose a $\mathbb{Z}_2$ symmetry under which only the new fields ϕ_i and ψ_α[31] are charged. This makes sure that the NP fields do not decay into SM-only final states which in turn ensures that ϕ_3 is stable as long as it constitutes the lightest NP state. Recalling that ψ_0 is neutral while ψ_1 and ψ_2 carry electric charge -1, we thus always obtain the hierarchy

$$m_{\psi_1} \geq m_{\psi_0} \geq m_{\psi_2} > m_{\phi_3} \,. \tag{10.14}$$

Regarding neutrinos, we work in the limit of vanishing masses $m_{\nu_i} = 0$ throughout this analysis, which holds to an excellent approximation.

[31] We use Greek indices when generally referring to any of the mass eigenstates ψ_0, ψ_1 and ψ_2 throughout this analysis. This should not be confused with the usual convention of using Greek letters as spinor or four-vector indices.

Chapter 11
Phenomenology

In this chapter we study the phenomenology of the model presented above by examining constraints from collider searches, LFV decays, precision measurements of leptonic dipole moments, the observed DM relic density and direct as well as indirect detection experiments. After discussing each of these constraints independently we perform a combined analysis and determine the viable parameter space of our model. Based on the results of this analysis we then conclude this chapter by reviewing whether the model can generate large enough NP contributions to the muon anomalous magnetic moment a_μ to accommodate the experimental central value.

11.1 Collider Phenomenology

For the analysis of constraints coming from collider experiments we use the same approach as for the purely right-handed version of this model studied in Part III. We focus on LHC searches in signatures that arise through the pair-production of the mediators ψ_α in Drell–Yan. To also fulfil the limits from LEP searches [195, 196] we demand the lightest charged mediator ψ_2 to satisfy $m_{\psi_2} > 100\,\text{GeV}$.

Relevant LHC Signatures

The mediators ψ_α are pair-produced through the Drell–Yan process shown in Figure 11.1, in which the initial state particles annihilate into an off-shell boson that subsequently decays into $\bar{\psi}_\alpha \psi_\beta$ with $\alpha, \beta \in \{0, 1, 2\}$. The indices of the final state produced by this process depend on the off-shell boson in the s-channel—pairs of one neutral and one charged mediator can only be produced if the Drell–Yan process is mediated by a W boson, while h or Z mediated channels can also produce final states with mixed pairs of ψ_1 and ψ_2. The state with a ψ_0 pair can only be produced if the initial state particles annihilate into a Z boson while the photon-mediated process produces either ψ_1 or ψ_2 pairs.

Depending on the actual constellation of the intermediate state, the subsequent decay of the mediator pairs illustrated in Figure 11.2 then gives rise to a variety of signatures. The charged mediators $\psi_{1,2}$ decay into a dark particle and a charged lepton, while the decay products of the neutral mediator entirely remain undetected as it decays into a dark scalar and a neutrino. Hence, pair-production of the mediators can lead to mono- or di-lepton signatures in association with missing transverse energy. Signatures with more particles in the final state arise from cascade decays of the heavier mediators ψ_α into lighter mediators ψ_β and a Higgs or electroweak gauge boson. The subsequent decay of the boson into leptons and the lighter mediator's decay into a lepton and a dark scalar then give rise to signatures with three or more charged leptons and missing energy. Collecting all these decay channels, we find the following relevant processes for LHC searches:

$$pp \;\to\; \bar{\psi}_0 \psi_\alpha \;\to\; \bar{\nu}_i \ell_j \phi_k^\dagger \phi_l \,,$$

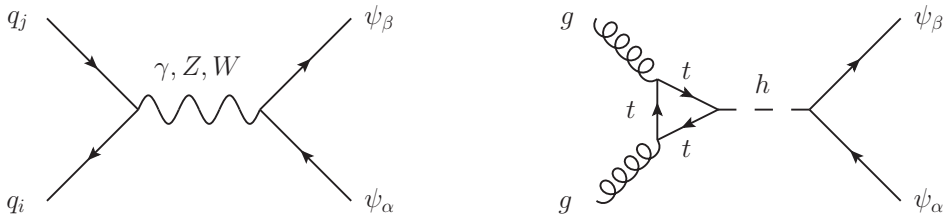

Figure 11.1 | Feynman diagrams for the production of $\bar{\psi}_\alpha \psi_\beta$ pairs through a Drell–Yan process mediated by electroweak gauge bosons or by a Higgs boson produced by gluon fusion.

$$\begin{aligned} pp &\to \bar{\psi}_\alpha \psi_\beta \to \ell_i \bar{\ell}_j \phi_k^\dagger \phi_l \,, \\ pp &\to \bar{\psi}_0 \psi_1 \to \bar{\nu}_i \bar{\ell}_j \ell_j \ell_k \phi_l^\dagger \phi_m \,, \\ pp &\to \bar{\psi}_0 \psi_2 \to \bar{\ell}_j \bar{\nu}_i \ell_i \ell_k \phi_l^\dagger \phi_m \,, \end{aligned} \tag{11.1}$$

where $\alpha, \beta \in \{1, 2\}$ and i, j, k, l and m are flavour indices. Here we have omitted charge conjugated processes and final states with more than three leptons for brevity. In summary, the processes described above yield the signatures $\ell_i + \not{E}_T$, $\ell_i \bar{\ell}_j + \not{E}_T$, $\bar{\ell}_i \ell_i \ell_j + \not{E}_T$ and $\bar{\ell}_i \ell_j \ell_k + \not{E}_T$.

Since existing searches for the mono-lepton signature [245, 246] consider NP cases with different kinematics, a proper recasting is necessary in order to derive meaningful constraints on our model's parameter space. However, this signature suffers from a large SM background stemming from the production of a W boson in the s-channel which subsequently decays into a charged lepton and a neutrino. We hence neglect mono-leptonic final states in our analysis as we expect them to only yield subleading constraints. The two signatures with three final state leptons, $\bar{\ell}_i \ell_i \ell_j + \not{E}_T$ and $\bar{\ell}_i \ell_j \ell_k + \not{E}_T$ only differ by final states with an electron, a muon and a tau, i.e. by the case with $i \neq j \neq k$. The latter final states are typically neglected in LHC searches, since they are correlated with the strongly constrained LFV decays in many models. As far as the signature $\bar{\ell}_i \ell_i \ell_j + \not{E}_T$ is concerned, we again find that existing searches consider models with different final state kinematics [247]. Hence, a thorough recasting of the relevant searches would also be required in this case in order to derive applicable constraints for our model. We leave this for future work and thus focus on the signature $\ell_i \bar{\ell}_j + \not{E}_T$ in this analysis.

This signature again consists of same- and mixed-flavour final states. We neglect the latter case with $i \neq j$ although in our model these final states are not correlated with LFV decays since these signatures are proportional to the diagonal elements of the coupling matrix λ and hence do not require flavour violation. In Part III we have found for the version of this model with purely right-handed interactions that searches in same-flavour final states already exclude the region of the parameter space in which the mixed-flavour final states yield rates comparable to the SM background. We expect this to also hold true for the model at hand. In summary, this leaves us with the same-flavour signatures $e\bar{e} + \not{E}_T$, $\mu\bar{\mu} + \not{E}_T$ and $\tau\bar{\tau} + \not{E}_T$. We further neglect searches in the latter final states containing a pair of taus [198], since we showed in Section 8.1 that they yield significantly weaker limits than searches in final states with light leptons. We hence only consider limits derived for the joint signature $\ell\bar{\ell} + \not{E}_T$ with $\ell = e, \mu$, where in the experimental analyses $\mu - e$ universality is commonly assumed. The latter analyses consist of searches for pair-produced sleptons of the first and second generation that subsequently decay into a neutralino and a charged lepton.

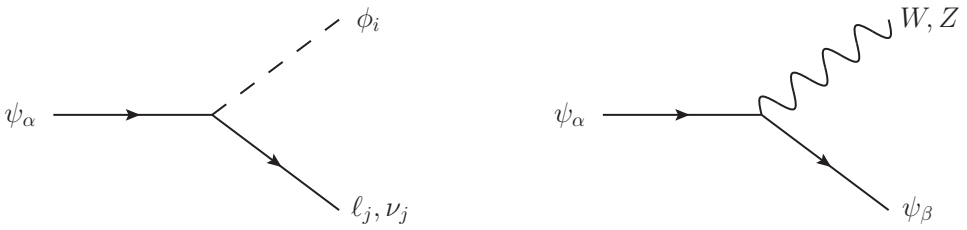

Figure 11.2 | Feynman diagrams for the decay of ψ_α into leptons and dark matter (left) and gauge bosons and lighter mediators ψ_β with $m_{\psi_\beta} < m_{\psi_\alpha}$ (right). For the latter we only show decays into electroweak gauge bosons and ψ_β while decays into a Higgs boson and ψ_β are possible as well.

Recast of LHC Limits

As discussed in Section 8.1, the CMS search in Reference [197] based on the full run 2 data set with an integrated luminosity of $137\,\text{fb}^{-1}$ places the most stringent constraints on NP models that produce the signature $\ell\bar{\ell} + \not{E}_T$. We have obtained the upper limits that this search places on the signal cross section from the `SModelS` [248] database. To constrain the parameter space of our model, we implement the Lagrangian from Equation (10.1) in `FeynRules` [147], generate a `UFO` file [148] and calculate the LO signal cross section of relevant processes in `MadGraph 5` [149]. Since we have two charged mediators $\psi_{1,2}$ in our model, we calculate the signal cross sections of the two processes $pp \to \psi_1\bar{\psi}_1 \to \ell\bar{\ell}+\not{E}_T$ and $pp \to \psi_2\bar{\psi}_2 \to \ell\bar{\ell} + \not{E}_T$ and compare each signal with the experimental upper limits from Reference [197] to draw exclusion contours in both the $m_{\psi_1} - m_\phi$ as well as the $m_{\psi_2} - m_\phi$ plane[32]. In doing so we neglect the kinematic interplay between the two intermediate states as well as the off-diagonal contributions from the mixed intermediate state with ψ_1 and ψ_2, which we expect all to only marginally increase the exclusion in the above mentioned NP mass planes. Note that we also neglect the impact of the potentially different final state kinematics due to the different spin-statistics in our model relative to the SUSY case for the reasons discussed in Section 8.1.

We further follow References [20–22] as well as our analyses from the previous two parts of this work in ignoring the mass splittings amongst the three dark states ϕ_i discussed in Section 10.2 and assuming a diagonal coupling matrix for the numerical analysis of the LHC constraints. Small mass splittings only lead to difficult-to-detect soft decay products of heavy flavours into lighter states, while flavour-violating effects weaken the signal of a given same-flavour final state and thus reduce the exclusion in the $m_{\psi_{1,2}} - m_\phi$ planes which we are primarily interested in. Finally, we set $|\lambda_{e1}| = |\lambda_{\mu 2}| = |\lambda_{\ell\ell}|$ in this section as the relevant CMS analysis assumes a $\mu - e$ universality.

Note that the value of the scaling parameter ξ defined in Equation (10.2) has no impact on the signal cross section, as the relative size of left- and right-handed couplings does not change the hierarchy between the couplings $|\lambda_{ii}|$ to different lepton flavours. This in turn means that the branching ratios of the charged mediators are independent of ξ. As far as the mixing between the charged mediators ψ_1 and ψ_2 is concerned, we assume it to be maximal with $\theta_\psi = \pi/4$ which corresponds to the case of equal gauge eigenstate mass parameters $m_\Psi = m_\psi$.

The results of this recasting procedure are shown in Figure 11.3. In all four panels we have fixed the coupling of DM to light leptons to $|\lambda_{\ell\ell}| = 2.0$ while the DM–tau coupling

[32] Remember that for a maximum mixing angle $\theta_\psi = \pi/4$ the masses m_{ψ_1} and m_{ψ_2} are linearly connected through $m_{\psi_1} = m_{\psi_2} + \sqrt{2} y_\psi v$.

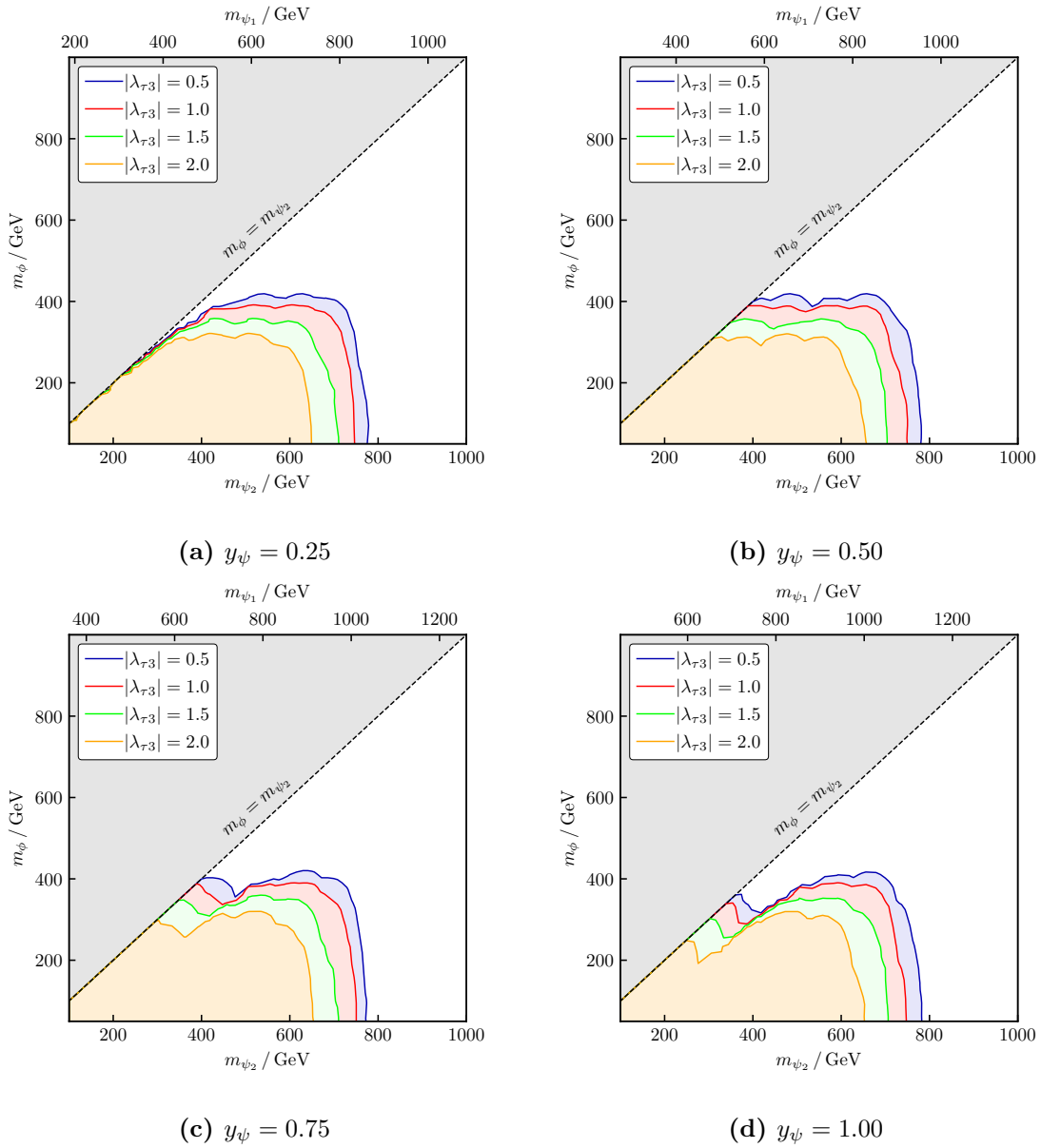

(a) $y_\psi = 0.25$ **(b)** $y_\psi = 0.50$

(c) $y_\psi = 0.75$ **(d)** $y_\psi = 1.00$

Figure 11.3 | Constraints on the final state $\ell\bar{\ell} + \not{E}_T$ for several values of y_ψ, $|\lambda_{\ell\ell}| = 2.0$ and maximum mixing with $m_\Psi = m_\psi$ and $\theta_\psi = \pi/4$. The coloured areas are excluded.

$|\lambda_{\tau 3}|$ varies. We show the overlay of the exclusion in the $m_{\psi_1} - m_\phi$ and $m_{\psi_2} - m_\phi$ plane by using the linear connection between the masses of both charged mediators. The excluded regions in both planes shrink for growing values of $|\lambda_{\tau 3}|$ as this increases the branching ratio of both intermediate states $\bar{\psi}_1\psi_1$ and $\bar{\psi}_2\psi_2$ into a tau–antitau pair and missing energy. This in turn decreases the decay rate into the relevant light lepton final states which ultimately yields a smaller signal. We further find that increasing values of the Yukawa coupling y_ψ have no impact on the maximum extension of the exclusion contour, which indicates that the contributions to the signal cross section from Higgs mediated Drell–Yan processes are negligible. However, varying Yukawa couplings y_ψ have a significant impact on constraints in the soft final state region $m_\phi \approx m_{\psi_2}$. The exclusion in this region is due to contributions from the heavier charged mediator ψ_1, since for $\theta_\psi = \pi/4$ the masses of

the two mediators are split according to

$$\Delta m_\psi = m_{\psi_1} - m_{\psi_2} = \sqrt{2} y_\psi v \,. \tag{11.2}$$

Hence, even if the final state leptons stemming from ψ_2 are produced softly and thus evade the constraints, leptons produced through the decay of ψ_1 can still lead to exclusions in the region $m_\phi \approx m_{\psi_2}$ provided Δm_ψ is large enough. For this reason we find that the exclusion in the near-degeneracy region between m_ϕ and m_{ψ_2} grows for Yukawa couplings up to $y_\psi \simeq 0.50$, see Figure 11.3a and 11.3b. As can be seen in Figures 11.3b–11.3d, the restrictions in this region reach their maximum and exclude masses up to $m_\phi \approx m_{\psi_2} \simeq 400\,\text{GeV}$ between $0.50 \lesssim y_\psi \lesssim 1.00$. For even larger values of y_ψ the splitting Δm_ψ becomes so sizeable that for masses $m_\phi \approx m_{\psi_2} \simeq 400\,\text{GeV}$ the corresponding value of m_{ψ_1} suppresses the pair-production of ψ_1 sufficiently. Hence, for increasing values $y_\psi \gtrsim 1.00$ the exclusion in the near-degeneracy region shrinks. Away from the equal mass threshold, we find that constraints from $\ell\bar{\ell} + \not{E}_T$ searches reach up to mediator masses $m_{\psi_2} \simeq 750\,\text{GeV}$ and DM masses $m_\phi \simeq 400\,\text{GeV}$. For even smaller DM–tau couplings $|\lambda_{\tau 3}| < 0.5$ not shown in Figure 11.3 the excluded area is only increased marginally.

11.2 Flavour Physics Phenomenology

In the previous parts of this work we have found that the constraints from flavour physics experiments can place significant restrictions on flavoured DM models. As discussed in detail in Section 8.2, for the case of lepton-flavoured DM these constraints stem from LFV decays and the process $\ell_i \to \ell_j \gamma$ in particular. Moreover, these constraints have proven to be even more restrictive than limits from neutral meson mixing relevant for quark-flavoured DM [20–24]. This statement also holds true for the model studied in Part III of this work, in which enhanced contributions with a chirality flip inside the loop were found to be absent. However, since the latter contributions are present in the model at hand, the constraints are even tightened. We hence use this section to carefully analyse the restrictions that LFV decays place on the parameter space of our model and determine flavour-safe scenarios.

Lepton Flavour Violating Decays

In Section 8.2 we have discussed the decay rates for the LFV process shown in Figure 11.4 based on References [202, 204] for the generic interaction Lagrangian from Equation (8.3). There we have found

$$\text{BR}(\ell_i \to \ell_j \gamma) = \frac{e^2}{64\pi} \frac{m_{\ell_i}}{\Gamma_{\ell_i}} \left(|a^R_{\ell_i \ell_j \gamma}|^2 + |a^L_{\ell_i \ell_j \gamma}|^2 \right) , \tag{11.3}$$

for the relevant branching ratios and[33]

$$a^R_{\ell_i \ell_j \gamma} = \frac{m_{\ell_i}}{16\pi^2} \sum_k \left(\frac{m_{\ell_i}}{12 m^2_{\phi_k}} c^{R*}_{ik} c^R_{jk} F(x_k) + \frac{m_\psi}{3 m^2_{\phi_k}} c^{L*}_{ik} c^R_{jk} G(x_k) \right) , \tag{11.4}$$

$$a^L_{\ell_i \ell_j \gamma} = \frac{m_{\ell_i}}{16\pi^2} \sum_k \left(\frac{m_{\ell_i}}{12 m^2_{\phi_k}} c^{L*}_{ik} c^L_{jk} F(x_k) + \frac{m_\psi}{3 m^2_{\phi_k}} c^{R*}_{ik} c^L_{jk} G(x_k) \right) , \tag{11.5}$$

with $x_k = m^2_\psi / m^2_{\phi_k}$ for the coefficients $a^{R/L}$. The loop functions $F(x)$ and $G(x)$ were

[33] Recall that we use the convention in which the superscript refers to the chirality of the final state.

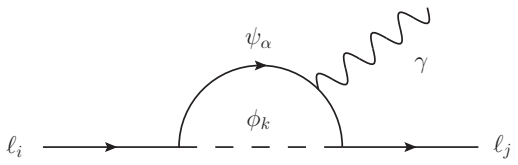

Figure 11.4 | Feynman diagram for the LFV decay $\ell_i \to \ell_j\gamma$. The index α here only refers to the charged mediators, i.e. $\alpha \in \{1,2\}$ while the indices i, j and k are flavour indices. The contribution from the photon coupling to one of the SM leptons is not shown.

obtained from References [202, 204] and are defined in Equation (8.6) and (8.7).

Since it contains two charged mediators, we obtain the following four coefficients when mapping the expressions from above to our model:

$$a^{R,1}_{\ell_i\ell_j\gamma} = \frac{m_{\ell_i}}{16\pi^2}\sum_k \left(\frac{m_{\ell_i}\sin^2\theta_\psi}{12m^2_{\phi_k}}\lambda^*_{ik}\lambda_{jk}F(x_{k,1}) + \frac{m_{\psi_1}\xi^*\sin 2\theta_\psi}{6m^2_{\phi_k}}\lambda^*_{ik}\lambda_{jk}G(x_{k,1})\right), \tag{11.6}$$

$$a^{R,2}_{\ell_i\ell_j\gamma} = \frac{m_{\ell_i}}{16\pi^2}\sum_k \left(\frac{m_{\ell_i}\cos^2\theta_\psi}{12m^2_{\phi_k}}\lambda^*_{ik}\lambda_{jk}F(x_{k,2}) - \frac{m_{\psi_2}\xi^*\sin 2\theta_\psi}{6m^2_{\phi_k}}\lambda^*_{ik}\lambda_{jk}G(x_{k,2})\right), \tag{11.7}$$

$$a^{L,1}_{\ell_i\ell_j\gamma} = \frac{m_{\ell_i}}{16\pi^2}\sum_k \left(\frac{m_{\ell_i}|\xi|^2\cos^2\theta_\psi}{12m^2_{\phi_k}}\lambda^*_{ik}\lambda_{jk}F(x_{k,1}) + \frac{m_{\psi_1}\xi\sin 2\theta_\psi}{6m^2_{\phi_k}}\lambda^*_{ik}\lambda_{jk}G(x_{k,1})\right), \tag{11.8}$$

$$a^{L,2}_{\ell_i\ell_j\gamma} = \frac{m_{\ell_i}}{16\pi^2}\sum_k \left(\frac{m_{\ell_i}|\xi|^2\sin^2\theta_\psi}{12m^2_{\phi_k}}\lambda^*_{ik}\lambda_{jk}F(x_{k,2}) - \frac{m_{\psi_2}\xi\sin 2\theta_\psi}{6m^2_{\phi_k}}\lambda^*_{ik}\lambda_{jk}G(x_{k,2})\right). \tag{11.9}$$

Here we have defined $x_{k,\alpha} = m^2_{\psi_\alpha}/m^2_{\phi_k}$ and used $\sin 2\theta_\psi = 2\sin\theta_\psi\cos\theta_\psi$. In this notation the relevant branching ratios are then given as

$$\mathrm{BR}(\ell_i \to \ell_j\gamma) = \frac{e^2}{64\pi}\frac{m_{\ell_i}}{\Gamma_{\ell_i}}\left(|a^{R,1}_{\ell_i\ell_j\gamma} + a^{R,2}_{\ell_i\ell_j\gamma}|^2 + |a^{L,1}_{\ell_i\ell_j\gamma} + a^{L,2}_{\ell_i\ell_j\gamma}|^2\right). \tag{11.10}$$

We use this expression to constrain the parameter space of our model in the following.

Constraints from LFV Decays

To constrain our model parameters based on LFV decays we calculate the relevant branching ratios through Equation (11.10) and compare them with the same 90% C.L. upper limits as in Section 8.2. The latter were obtained from References [205–207] and read

$$\mathrm{BR}(\mu \to e\gamma)_{\max} = 4.2\times 10^{-13}, \tag{11.11}$$

$$\mathrm{BR}(\tau \to e\gamma)_{\max} = 3.3\times 10^{-8}, \tag{11.12}$$

$$\mathrm{BR}(\tau \to \mu\gamma)_{\max} = 4.2\times 10^{-8}. \tag{11.13}$$

For the lepton masses and decay widths we use the values given in Reference [158].

At the NP scales allowed by the LHC searches discussed in Section 11.1, the LFV rates are generally dominated by chirality-flipping contributions. To obtain a rough estimate of the restrictions these decays place on our model, we hence neglect chirality preserving contributions, i.e. we set the first summand in Equations (11.6)–(11.9) to zero, and expand Equation (11.10) for $m_{\psi_{1,2}} \gg m_\phi$. For the most stringently constrained decay $\mu \to e\gamma$,

the according experimental bound is then satisfied if

$$\sqrt{(\lambda\lambda^\dagger)_{\mu e}} \lesssim \frac{1}{2200\,\text{TeV}} \sqrt{\frac{m_{\psi_1} m_{\psi_2}}{y_\psi |\xi|}}\,, \tag{11.14}$$

where we assume maximum mixing between ψ_1 and ψ_2 with $\theta_\psi = \pi/4$. For a NP scale m_{ψ_1} of order $\mathcal{O}(\text{TeV})$ together with an $\mathcal{O}(1)$ Yukawa coupling y_ψ this condition reduces to[34]

$$\sqrt{(\lambda\lambda^\dagger)_{\mu e}} \lesssim 3.7 \times \frac{10^{-4}}{\sqrt{|\xi|}}\,. \tag{11.15}$$

Moving away from this rough estimation, we want to examine how strongly the LFV decays actually constrain the coupling matrix λ. To this end we draw contours in the $|\xi| - y_\psi$ plane that illustrate how large the values of the DM–lepton couplings $|\lambda_{\ell i}|$ may maximally grow to saturate the respective upper limit. We further assume a maximum mixing angle $\theta_\psi = \pi/4$ and fix the mass of the light charged mediator to $m_{\psi_2} = 1300\,\text{GeV}$. Depending on the value of y_ψ this maximally yields $m_{\psi_1} \simeq 2000\,\text{GeV}$. As far as the DM mass is concerned, we again ignore the mass splittings between different dark scalars and fix their masses to one value $m_\phi = 200\,\text{GeV}$. The resulting contours are shown for all three LFV decays in Figure 11.5.

In Figure 11.5a we show the restrictions placed on the DM–electron couplings $|\lambda_{ei}|$ by the decay $\mu \to e\gamma$. Since we ultimately want to explain the $(g-2)_\mu$ anomaly in this analysis, we have fixed the DM–muon couplings to $|\lambda_{\mu i}| = 1$ to not suppress NP contributions to a_μ. As expected and as our rough estimate from Equation (11.15) already suggests, the upper limit on $|\lambda_{ei}|$ strongly depends on $|\xi|$ while it only mildly varies with y_ψ. This holds true within the range $|\xi| \sim \mathcal{O}(10^{-4} - 10^{0})$, in which contributions with a chirality flip inside the loop dominate. The reason for the mild dependence on y_ψ is connected to our choice of the masses. Since we have fixed the light charged mediator's mass to $m_{\psi_2} = 1300\,\text{GeV}$, growing values of y_ψ only increase the mass of m_{ψ_1}. Hence, the contributions from diagrams with ψ_2 to the branching ratio of Equation (11.10) stay the same. The absolute value of the contributions from diagrams with ψ_1 in the loop on the other hand, is enhanced by the increased value of m_{ψ_1} but at the same time suppressed by the loop function G.[35] As a result of both effects, the relevant branching ratio only marginally grows for increasing values of y_ψ. For a stronger suppression of left-handed interactions with $|\xi| \lesssim 0.5 \times 10^{-4}$ the right-handed chirality-preserving contributions, i.e. the first summands of Equation (11.6) and (11.7) become dominant, as all other contributions are sufficiently suppressed by the small value of $|\xi|$. In this regime the y_ψ dependence is turned around and larger values of y_ψ allow for larger couplings $|\lambda_{ei}|$. The reason is that contrary to chirality-flipping diagrams, the chirality-preserving contributions do not depend on the product of m_{ψ_α} and G but solely depend on the loop function F. Hence, in this case increasing values of y_ψ lead to a suppression of the coefficient $a_{\mu e\gamma}^{R,1}$ through the loop function F. This in turn allows for larger DM–electron couplings $|\lambda_{ei}|$. In summary we conclude that depending on the choice of y_ψ and $|\xi|$ the DM–electron couplings vary between the values $|\lambda_{ei}| \sim \mathcal{O}\left(10^{-4} - 10^{-1}\right)$. As smaller mediator masses demand even smaller values of $|\lambda_{ei}|$, we restrict the range of these couplings to $|\lambda_{ei}| \in [10^{-6}, 10^{-1}]$ when scanning over the parameter space of our model in the remainder of our analysis.

The constraints that the LFV decay $\tau \to e\gamma$ places on the coupling matrix λ are shown in Figure 11.5b. In this case we have set the DM–electron couplings to their maximally viable value $|\lambda_{ei}| = 0.1$ in order to quantify how strongly this decay constrains the DM–tau

[34] Recall that for $\theta_\psi = \pi/4$ the two masses m_{ψ_1} and m_{ψ_2} are connected through $m_{\psi_1} - m_{\psi_2} = \sqrt{2} y_\psi v$.
[35] Note that both $F(x_{k,\alpha})$ and $G(x_{k,\alpha})$ decrease for increasing values $x_{k,\alpha}$.

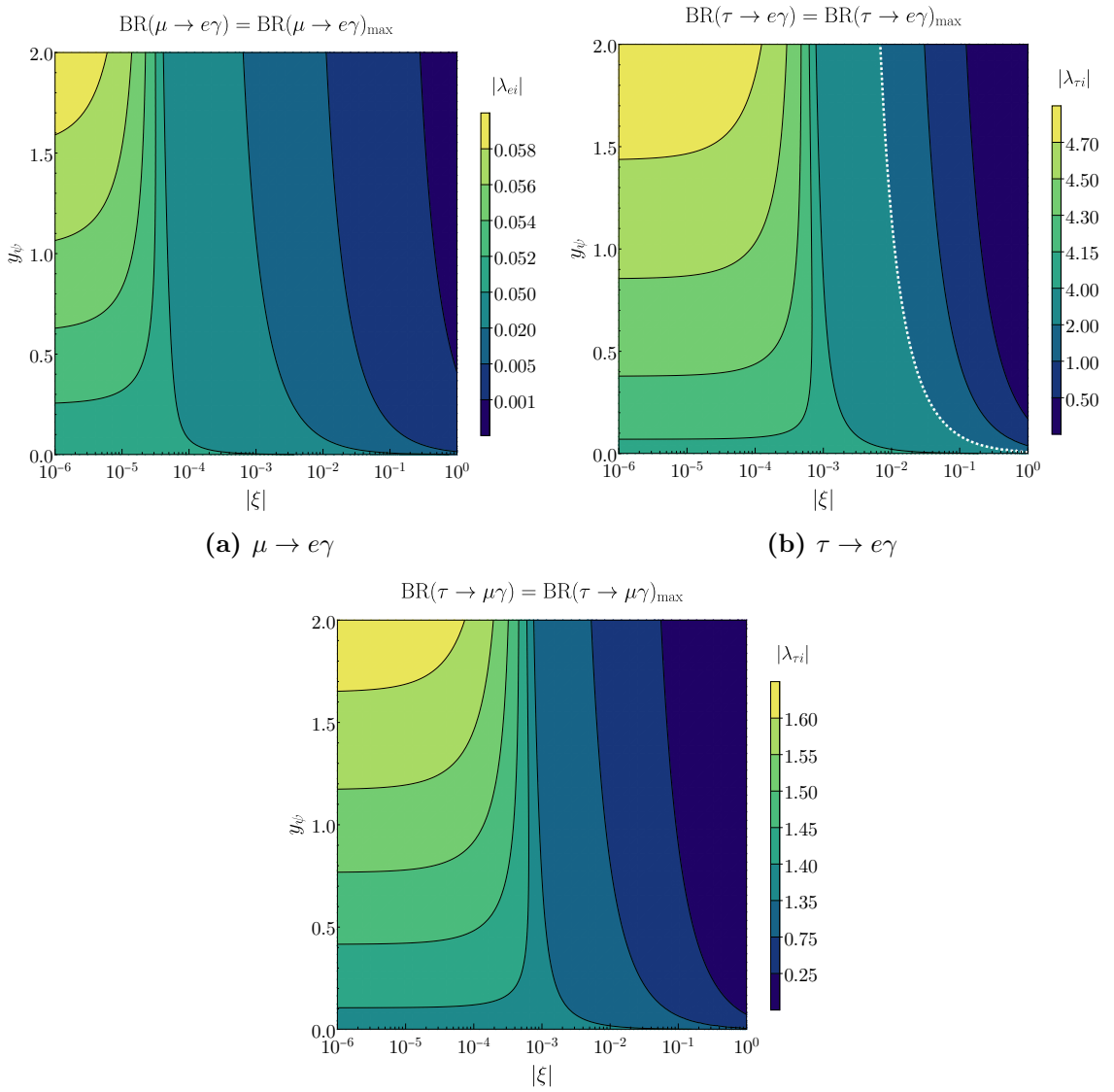

(a) $\mu \to e\gamma$ **(b)** $\tau \to e\gamma$

(c) $\tau \to \mu\gamma$

Figure 11.5 | Constraints from LFV decays on the coupling matrix λ. In all three panels maximum mixing with $\theta_\psi = \pi/4$ is assumed and the DM mass is set to $m_\phi = 200\,\text{GeV}$. We further set $m_{\psi_2} = 1300\,\text{GeV}$, and the value of m_{ψ_1} varies according to the value of y_ψ.

couplings. We find that the dependence of the coupling $|\lambda_{\tau i}|$ on y_ψ and $|\xi|$ is qualitatively the same as in Figure 11.5a. However, in this case the chirality-flipping contribution is dominant for a smaller range of values of the scaling parameter $|\xi| \gtrsim 10^{-3}$. The reason is that the chirality-preserving contribution is proportional to the square of the mass of the lepton that decays, see Equations (11.6)–(11.9). Since at the same time the tau mass is roughly a factor of 17 larger than the muon mass, the threshold upon which the chirality-preserving contribution starts to dominate is shifted towards larger values of $|\xi|$. The white dashed line in Figure 11.5b indicates in which part of the $|\xi| - y_\psi$ plane we expect constraints on $|\lambda_{\tau i}|$ from the decay $\tau \to e\gamma$, as we have limited the couplings to $|\lambda_{ij}| \in [0, 2]$ in Chapter 10. We find that this LFV decay only constrains the DM–tau couplings for values $|\xi| \gtrsim 10^{-2}$.

Finally, we also show the restrictions placed on λ by the decay $\tau \to \mu\gamma$ in Figure 11.5c. In this case we have again set the DM–muon coupling to $|\lambda_{\mu i}| = 1$ to not suppress contributions to $(g-2)_\mu$. Figure 11.5c hence illustrates the constraints on the DM–tau couplings $|\lambda_{\tau i}|$. In terms of the dependence on y_ψ and $|\xi|$ the contours exhibit the same features as in the previous cases. We find that this decay restricts the DM–tau couplings to the range $|\lambda_{\tau i}| \sim \mathcal{O}(10^{-1} - 10^{0})$.

11.3 Precision Measurements of Dipole Moments

Lepton-flavoured DM models can generally be subject to restrictive constraints from precision measurements of leptonic EDMs d_ℓ and MDMs a_ℓ. In Part III of this work we had found that these constraints are irrelevant for the model with purely right-handed couplings of DM to leptons. The reason was related to the lack of chirality enhanced contributions, due to which sizeable effects in these observables can only be generated at NP scales excluded by collider searches. For the model at hand however, we expect more significant constraints to be placed on the coupling matrix λ since the DM triplet is coupled to both right- as well as left-handed leptons. Hence, this model cannot only generate potentially sizeable contributions to the muon anomalous magnetic moment a_μ but also to the MDM and EDM of other charged leptons. While we relegate the discussion of NP effects in a_μ to Section 11.7, we use this section to identify the parameter space of our model consistent with the experimental measurement of other MDMs and EDMs.

Lepton EDM and MDM

The NP contributions to the EDM d_{ℓ_i} and MDM a_{ℓ_i} of the lepton ℓ_i are induced through vertex corrections of its coupling to photons. The Feynman diagram of the corresponding LO process is obtained when setting $i = j$ in the diagram shown in Figure 11.4. Following our notation from the previous section and Reference [249], its amplitude can be written as

$$\mathcal{M}_{\ell_i\ell_i\gamma} = \frac{e}{2m_{\ell_i}}\epsilon^{*\alpha}\bar{u}_{\ell_i}\left[i\sigma_{\beta\alpha}q^\beta\left(a^R_{\ell_i\ell_i\gamma}P_L + a^L_{\ell_i\ell_i\gamma}P_R\right)\right]u_{\ell_i} + \epsilon^{\mu*}\bar{u}_{\ell_i}\left[\sigma_{\nu\mu}\gamma_5 q^\nu d_{\ell_i}\right]u_{\ell_i}\,, \tag{11.16}$$

where $\sigma_{\beta\alpha} = i[\gamma_\alpha, \gamma_\beta]/2$, ϵ is the photon polarisation vector, q is the photon momentum and $P_{R/L} = (1 \pm \gamma_5)/2$ are projection operators. For the generic Lagrangian

$$\mathcal{L}_{\text{int}} = c^R_{ij}\,\bar{\ell}_{Ri}\psi\phi_j + c^L_{ij}\,\bar{\ell}_{Li}\psi\phi_j + \text{h.c.}\,, \tag{11.17}$$

which we had already introduced in Equation (8.3) the NP contributions to the MDM and the EDM[36] of the lepton ℓ_i then read [249, 252]

$$\begin{aligned}\Delta a_{\ell_i} &= a^R_{\ell_i\ell_i\gamma} + a^L_{\ell_i\ell_i\gamma}\,,\\ &= \frac{m_{\ell_i}}{16\pi^2}\sum_k\left(\frac{m_{\ell_i}}{12m^2_{\phi_k}}(|c^R_{ik}|^2 + |c^L_{ik}|^2)F(x_k) + \frac{2m_\psi}{3m^2_{\phi_k}}\text{Re}\left[c^{L*}_{ik}c^R_{ik}\right]\,G(x_k)\right)\,,\end{aligned} \tag{11.18}$$

and

$$d_{\ell_i} = -\frac{e}{16\pi^2}\sum_k\frac{m_\psi}{3m^2_{\phi_k}}\text{Im}\left[c^R_{ik}c^{L*}_{ik}\right]\,G(x_k)\,. \tag{11.19}$$

[36] Note that since leptonic EDMs arise at the four-loop level [250] in the SM, estimates [251] provide an upper limit of $d_e^{\text{SM}} < 10^{-38}\,e\,\text{cm}$. We hence ignore SM contributions to the lepton EDMs and denote the NP contributions as d_{ℓ_i} instead of Δd_{ℓ_i}.

Here, the coefficients $a^{R/L}_{\ell_i\ell_i\gamma}$ as well as the loop functions F and G are the same as in the previous section and Section 8.2. We stress that an EDM d_{ℓ_i} is only induced if the Lagrangian $\mathcal{L}_{\text{int}}$ from Equation (11.17) is CP-violating [253], i.e. if the couplings defined in Equation (11.17) satisfy

$$\text{Im}\left[c^R c^{L*}\right] \neq 0\,. \tag{11.20}$$

Since there are two charged mediators in our model, we define the two contributions

$$\Delta a^1_{\ell_i} = a^{R,1}_{\ell_i\ell_i\gamma} + a^{L,1}_{\ell_i\ell_i\gamma}\,, \tag{11.21}$$

$$\Delta a^2_{\ell_i} = a^{R,2}_{\ell_i\ell_i\gamma} + a^{L,2}_{\ell_i\ell_i\gamma}\,, \tag{11.22}$$

which when mapping the expressions from above to our model read

$$\Delta a^1_{\ell_i} = \frac{m_{\ell_i}}{16\pi^2}\sum_k \left(\frac{m_{\ell_i}|\lambda_{ik}|^2}{12m^2_{\phi_k}}(s^2_\theta + |\xi|^2 c^2_\theta)F(x_{k,1}) + \frac{m_{\psi_1} s_{2\theta}\,|\lambda_{ik}|^2}{3m^2_{\phi_k}}\text{Re}\,\xi\, G(x_{k,1})\right)\,, \tag{11.23}$$

$$\Delta a^2_{\ell_i} = \frac{m_{\ell_i}}{16\pi^2}\sum_k \left(\frac{m_{\ell_i}|\lambda_{ik}|^2}{12m^2_{\phi_k}}(c^2_\theta + |\xi|^2 s^2_\theta)F(x_{k,2}) - \frac{m_{\psi_2} s_{2\theta}\,|\lambda_{ik}|^2}{3m^2_{\phi_k}}\text{Re}\,\xi\, G(x_{k,2})\right)\,. \tag{11.24}$$

Here we have defined $s_\theta = \sin\theta_\psi$, $c_\theta = \cos\theta_\psi$ as well as $s_{2\theta} = \sin 2\theta_\psi$ for brevity of notation and again used $x_{k,\alpha} = m^2_{\psi_\alpha}/m^2_{\phi_k}$. The total NP contribution Δa_{ℓ_i} to the MDM of the lepton ℓ_i is then obtained by adding both contributions, i.e.

$$\Delta a_{\ell_i} = \Delta a^1_{\ell_i} + \Delta a^2_{\ell_i}\,. \tag{11.25}$$

Likewise, we define the EDM d_{ℓ_i} of the lepton ℓ_i as $d_{\ell_i} = d^1_{\ell_i} + d^2_{\ell_i}$ yielding

$$d_{\ell_i} = -\frac{e}{16\pi^2}\sum_k \frac{c_\theta s_\theta\,|\lambda_{ik}|^2}{3m^2_{\phi_k}}\text{Im}\,\xi\Big(m_{\psi_2}G(x_{k,2}) - m_{\psi_1}G(x_{k,1})\Big)\,. \tag{11.26}$$

For a non-negligible scaling parameter ξ and NP scales of $\mathcal{O}(1\,\text{TeV})$ allowed by the LHC constraints discussed in Section 11.1, the MDMs are dominated by contributions with a chirality flip inside the loop in the diagram of Figure 11.4. However, these contributions are only positive if the real part of the scaling parameter ξ is negative. At the same time solving the $(g-2)_\mu$ anomaly requires sizeable positive NP contributions to a_μ and hence we only consider the case $\text{Re}\,\xi < 0$ in the remainder of this part.

Constraints from Dipole Moments

Regarding the experimental measurement of leptonic EDMs and MDMs the most restrictive constraints are related to both dipole moments of the electron. Measurements of the electron EDM d_e for instance, currently yield a 90% C.L. upper limit of [211]

$$d_e^{\text{max}} = 1.1\times 10^{-29} e\,\text{cm}\,. \tag{11.27}$$

In comparison, the according upper limits on the muon EDM d_μ [212] and tau EDM d_τ [213] are ten orders of magnitude weaker and hence negligible. The same holds true for the tau MDM a_τ, which has not been measured precisely enough yet [158, 210, 254] to provide meaningful constraints on NP models at all. In spite of having been measured at a very high precision [209], the electron MDM a_e on the other hand is subject to a tension caused by disagreeing measurements of the fine-structure constant α_{em}. This tension ultimately yields different SM predictions a_e^{SM} for the electron MDM depending

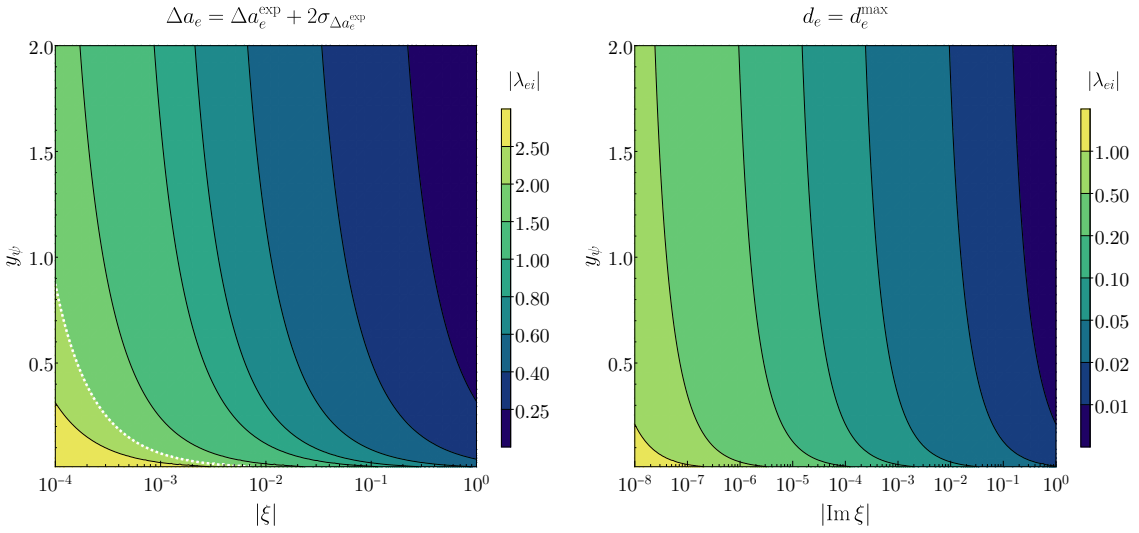

(a) constraints on $|\lambda_{ei}|$ from a_e **(b)** constraints on $|\lambda_{ei}|$ from d_e

Figure 11.6 | Constraints from the electron EDM and MDM on the DM–electron couplings. In all three panels maximum mixing with $\theta_\psi = \pi/4$ is assumed. We further set $m_\phi = 200\,\text{GeV}$, $m_{\psi_2} = 1300\,\text{GeV}$ and the value of m_{ψ_1} varies according to the value of y_ψ. In the left panel the white dashed line shows the contour with $|\lambda_{ei}| = 2.0$.

on which value is used for α_{em}. If the latter constant is obtained from measurements based on ^{133}Cs atoms [255] the difference between the SM prediction and experimental measurement reads [256]

$$\Delta a_e^{\text{exp}}(\text{Cs}) = (-8.8 \pm 3.6) \times 10^{-13}\,, \tag{11.28}$$

where Δa_e^{exp} is generally defined as $\Delta a_e^{\text{exp}} = a_e^{\text{exp}} - a_e^{\text{SM}}$. This corresponds to a deviation of 2.4σ between theory and experiment. If on the other hand the value of α_{em} is obtained from measurements in ^{87}Rb atoms [257], the deviation between theory and experiment reduces to 1.6σ and reads [258]

$$\Delta a_e^{\text{exp}}(\text{Rb}) = (4.8 \pm 3.0) \times 10^{-13}\,. \tag{11.29}$$

In the last section we however have fixed the scaling parameter's sign to $\text{Re}\,\xi < 0$ in order to obtain the correct sign for the NP corrections to the muon MDM a_μ. Hence, as a conservative approach we use the limit $\Delta a_e^{\text{exp}}(\text{Rb})$ from Equation (11.29) in order to further constrain our model parameters and the DM–electron couplings in particular.

In our numerical analysis of constraints from the electron EDM and MDM we follow the same procedure as for the flavour constraints in Section 11.2. We fix all DM–electron couplings to one universal value $|\lambda_{ei}|$, demand the MDM Δa_e as well as the EDM d_e to saturate their respective upper limit and draw contours in the $|\xi| - y_\psi$ plane indicating the maximally allowed values of $|\lambda_{ei}|$. In terms of the NP masses we again assume maximum mixing with $\theta_\psi = \pi/4$, set $m_\phi = 200\,\text{GeV}$, $m_{\psi_2} = 1300\,\text{GeV}$ and let m_{ψ_1} vary according to the value of y_ψ. The results are shown in Figure 11.6.

In Figure 11.6a we show the constraints placed on the DM–electron couplings by the electron MDM a_e. Here we demand that the experimental limit is satisfied at the 2σ level, while the white dashed line illustrates the contour with maximal couplings $|\lambda_{ei}| = 2.0$. We find that for free couplings $|\lambda_{ei}|$ the MDM a_e can yield stringent constraints as it forces

the DM–electron couplings to satisfy $|\lambda_{ei}| \lesssim 0.60$ within the range $|\xi| \gtrsim 10^{-2}$. Combining this result with our findings from the previous section however shows that for couplings $|\lambda_{ei}| < 10^{-1}$ necessary to satisfy the constraints from the LFV decay $\mu \to e\gamma$ while allowing for $\mathcal{O}(1)$ DM–muon couplings, the constraints from a_e are basically rendered irrelevant.

The constraints from measurements of the electron EDM d_e are shown in Figure 11.6b. In this case we show the $|\mathrm{Im}\,\xi| - y_\psi$ plane since the condition from Equation (11.20) reduces to $\mathrm{Im}\,\xi \neq 0$ in our model. Here we find that the stringent upper limit on d_e places strong restrictions on a relative phase between the left-handed and right-handed coupling of DM to leptons. To render order $\mathcal{O}(1)$ DM–electron couplings together with non-vanishing Yukawa couplings y_ψ viable, the scaling parameter needs to be practically real as this demands $\mathrm{Im}\,\xi \lesssim 10^{-8}$. If on the other hand the DM–electron couplings are restricted to $|\lambda_{ei}| \sim \mathcal{O}\left(10^{-4} - 10^{-1}\right)$ as required by the flavour constraints, we find that the viable values for the imaginary part of the scaling parameter lie within the range $|\mathrm{Im}\,\xi| \sim \mathcal{O}(10^{-4}{-}10^{0})$. We hence conclude that in combination with the flavour constraints the EDM bound allows for an order $\mathcal{O}(1)$ imaginary part of ξ.

Before concluding this section we want to also comment on possible constraints on the parameter space of our model coming from electroweak precision observables. In general, the NP interactions of our model can induce vertex corrections to the couplings of leptons to electroweak gauge bosons at the one-loop level. These corrections in turn have an impact on the Fermi constant G_F as well as the Z boson couplings to leptons which potentially poses a problem for the global electroweak fit. However, we expect these contributions to be negligible since they are suppressed by a loop factor as well as the NP scale $m_{\mathrm{NP}} \sim \mathcal{O}(\mathrm{TeV})$.

11.4 Dark Matter Relic Density

In this section we study the constraints placed on the model parameters by the observed amount of DM in the Universe. We again consider the two benchmark scenarios for the thermal freeze-out of DM defined in Section 3.2. After identifying and discussing relevant annihilations during the early Universe, we conclude this section by a numerical analysis of the relic density constraints.

DM Annihilations and Thermal Freeze-Out

A central difference between our model and DMFV models is that the mass splittings between the different dark states ϕ_i are not parametrised by the coupling matrix λ in this case due to the absence of a new flavour symmetry the NP fields can be associated with. Hence, the parameters m_{ϕ_i} are basically free, which is why the definition of the two freeze-out scenarios introduced in Section 3.2 does not depend on λ either. This means that in our model the two freeze-out scenarios only depend on the choice of the masses m_{ϕ_i} and the resulting mass splitting

$$\Delta m_{i3} = \frac{m_{\phi_i}}{m_{\phi_3}} - 1\,, \tag{11.30}$$

between the lightest state ϕ_3 and the heavier states with $i \in \{1, 2\}$. For the QDF scenario we demand this splitting to satisfy $\Delta m_{i3} < 1\%$, while the SFF scenario is defined by significant splittings $10\% < \Delta m_{i3} < 30\%$. Here, the upper limit is only applied in order to keep our results comparable to our findings from the previous parts as well as studies in the DMFV framework in general, see Section 10.2. In both scenarios we again assume the thermal freeze-out to take place at $T_f \approx m_{\phi_3}/20$.

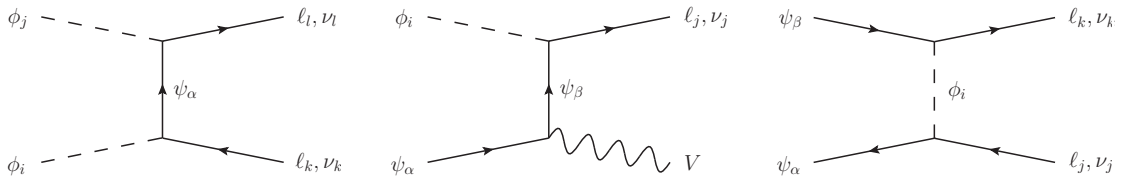

(a) $\phi_i\phi_j$ annihilation **(b)** $\phi_i\psi_\alpha$ coannihilation **(c)** $\psi_\alpha\psi_\beta$ annihilation

Figure 11.7 | Representative Feynman diagrams for annihilations of the new particles into SM matter. Here, V represents any of the SM gauge bosons γ, W, Z but also h and we have only chosen the letter V and a curly line as most of them are vector bosons.

The rich NP field content of this model gives rise to a variety of tree-level annihilations of the new particles into SM matter during the early Universe, see Figure 11.7. The process shown in Figure 11.7a only produces a pair of neutrinos $\bar{\nu}_k\nu_l$ if the particle in the t-channel is the neutral mediator ψ_0. In Figure 11.7b we show coannihilations between dark particles and the mediators, which only yield a neutrino and a W boson in the final state for $\beta = 0$ and $\alpha \in \{1, 2\}$, while the process with $\alpha = \beta = 0$ produces a neutrino and a Z boson. The off-diagonal contributions with $\alpha = 1$, $\beta = 2$ and vice versa produce either of the final states $\ell_j Z$ or $\ell_j h$, while the diagonal case $\alpha = \beta \in \{1, 2\}$ can additionally produce the final state $\ell_j\gamma$. Annihilations between the mediators ψ_α and ψ_β are shown in Figure 11.7c and produce final states with either two charged leptons, two neutrinos or one neutrino and one charged lepton.

We stress that all coannihilations gathered in 11.7b are suppressed by the Boltzmann factor

$$k_\alpha = e^{-\frac{m_{\psi_\alpha} - m_{\phi_3}}{T_f}} \simeq e^{-20\frac{m_{\psi_\alpha} - m_{\phi_3}}{m_{\phi_3}}}\,, \tag{11.31}$$

while the ones shown in 11.7c receive an even stronger suppression by $k_\alpha k_\beta$. We hence neglect these contributions, since we do not consider near-degenerate scenarios between the masses m_{ψ_2} and m_{ϕ_3} in this analysis. Following the arguments provided in the previous part and in Chapter 10, we further neglect annihilations into a pair of Higgs bosons as well as annihilations into a pair of top quarks mediated by an off-shell Higgs in the s-channel. Both processes are induced by the Higgs portal coupling and are proportional to $\lambda_{H\phi}^2$ or $\lambda_{H\phi}^2 y_t^2$, respectively.

The only process that we consider when calculating the DM annihilation rate is thus the t-channel mediator exchange shown in Figure 11.7a. Its total flavour-averaged squared amplitude reads

$$\overline{|M|^2} = \overline{|M_0|^2} + \overline{|M_1|^2} + \overline{|M_2|^2} + 2\,\mathrm{Re}\,\overline{M_{12}}\,, \tag{11.32}$$

where the index represents the index of the mediator ψ_α exchanged in the t-channel. For the expressions of the individual contributions M_α and the interference term $\overline{M_{12}}$ we find

$$\overline{|M_0|^2} = \sum_{ij}\sum_{kl} \frac{|\lambda_{ik}|^2|\lambda_{jl}|^2}{(t - m_{\psi_0}^2)^2} f_{ij}^0\,, \tag{11.33}$$

$$\overline{|M_1|^2} = \sum_{ij}\sum_{kl} \frac{|\lambda_{ik}|^2|\lambda_{jl}|^2}{(t - m_{\psi_1}^2)^2} f_{ijkl}^1\,, \tag{11.34}$$

$$\overline{|M_2|^2} = \sum_{ij}\sum_{kl} \frac{|\lambda_{ik}|^2|\lambda_{jl}|^2}{(t - m_{\psi_2}^2)^2} f_{ijkl}^2\,, \tag{11.35}$$

$$\overline{M_{12}} = \sum_{ij}\sum_{kl} \frac{|\lambda_{ik}|^2|\lambda_{jl}|^2}{(t-m_{\psi_1}^2)(t-m_{\psi_2}^2)} f_{ijkl}^{12}\,, \tag{11.36}$$

with the functions f^α defined as

$$f_{ij}^0 = |\xi|^4 \left(\left(m_{\phi_j}^2 - t\right)\left(t - m_{\phi_i}^2\right) - ts \right)\,, \tag{11.37}$$

$$\begin{aligned} f_{ijkl}^1 &= A_{ijkl}\left(s_\theta^4 + |\xi|^4 c_\theta^4\right) + c_\theta^2 s_\theta^2 \left(2|\xi|^2 C_{kl} + m_{\psi_1}^2 D_{kl}\right) \\ &\quad + 2c_\theta s_\theta\, m_{\psi_1}\, \mathrm{Re}B_{ijkl}\left(s_\theta^2 + |\xi|^2 c_\theta^2\right), \end{aligned} \tag{11.38}$$

$$\begin{aligned} f_{ijkl}^2 &= A_{ijkl}\left(c_\theta^4 + |\xi|^4 s_\theta^4\right) + c_\theta^2 s_\theta^2 \left(2|\xi|^2 C_{kl} + m_{\psi_2}^2 D_{kl}\right) \\ &\quad - 2c_\theta s_\theta\, m_{\psi_2}\, \mathrm{Re}B_{ijkl}\left(c_\theta^2 + |\xi|^2 s_\theta^2\right), \end{aligned} \tag{11.39}$$

$$\begin{aligned} f_{ijkl}^{12} &= s_\theta^2 c_\theta^2 \left(A_{ijkl}(1+|\xi|^4) - m_{\psi_1} m_{\psi_2} D_{kl}\right) + C_{kl}|\xi|^2\left(c_\theta^4 + s_\theta^4\right) \\ &\quad + c_\theta s_\theta \left(B_{ijkl} c_\theta^2 \left(m_{\psi_1} - |\xi|^2 m_{\psi_2}\right) - B_{ijkl}^* s_\theta^2 \left(m_{\psi_2} - |\xi|^2 m_{\psi_1}\right)\right)\,. \end{aligned} \tag{11.40}$$

The indices i, j, k and l are flavour indices here and we have again used the short hand notation $s_\theta = \sin\theta_\psi$ and $c_\theta = \cos\theta_\psi$. The expressions of the functions $A_{ijkl}, B_{ijkl}, C_{kl}$ and D_{kl} can be found in Appendix C.1 and depend on the masses $m_{\phi_i}, m_{\phi_j}, m_{\ell_k}$ and m_{ℓ_l} as well as the Mandelstam variables $s = (p_1 + p_2)^2$ and $t = (p_1 - p_3)^2$.

For the calculation of the thermally averaged annihilation cross section we use the low-velocity expansion from Equation (3.12), which in this case again reduces to

$$\langle\sigma v\rangle_{\mathrm{eff}} = \frac{f_{\mathrm{sc}}}{2}\left[a + b\,\langle v^2\rangle + \mathcal{O}\left(\langle v^4\rangle\right)\right]\,, \tag{11.41}$$

as we have $f_{\mathrm{nat}} = 1/2$ for complex scalar DM. Also recall that the factor f_{sc} is equal to one in the SFF scenario while we have $f_{\mathrm{sc}} = 1/9$ for the QDF scenario. The mean velocity square is given by $\langle v^2\rangle = 6T_f/m_{\phi_3} \simeq 0.3$. Following the previous parts, we use equal initial state state masses for the calculation of the expansion coefficients a and b in both freeze-out scenarios. The splittings Δm_{ij} are negligible in the QDF scenario while the only particle that contributes to the freeze-out in the SFF scenario is ϕ_3. Hence, in the latter case the masses m_{ϕ_i} and m_{ϕ_j} in the functions A_{ijkl} and B_{ijkl} need to be replaced by m_{ϕ_3} and the sum over initial state flavours needs to be omitted. In the remainder of this section we hence use m_{ϕ_3} whenever we refer to the DM mass in both freeze-out scenarios.

In Section 8.3 we had found for the version of this model with purely right-handed interactions between DM and leptons that the DM annihilation rate is p-wave suppressed for zero final state masses. In this case however, DM can also annihilate in the s-wave as it couples to both right- as well as left-handed leptons. The reason is that the p-wave suppression of the annihilation rate in Section 8.3 ultimately represents a chirality suppression which is trivially lifted in this model due to the additional coupling of DM to left-handed leptons [216]. Hence, the s-wave coefficient a does not vanish and reads

$$a = \sum_{ij}\sum_{kl} \frac{|\lambda_{ik}|^2|\lambda_{jl}|^2}{16\pi m_{\phi_3}^2} \frac{\left(\mu_2 - \mu_1\right)^2\left(\mu_1\mu_2 - 1\right)^2 |\xi|^2 \sin^2 2\theta_\psi}{\left(1+\mu_1^2\right)^2\left(1+\mu_2^2\right)^2}\,, \tag{11.42}$$

where we have used $\mu_\alpha = m_{\psi_\alpha}/m_{\phi_3}$. The dependence of this coefficient on the scaling parameter ξ is due to our ansatz from Equation (10.2). In the case of non-suppressed left-handed interactions the annihilation rate is thus dominated by this contribution. The respective p-wave contribution for this case can be found in Appendix C.1. If in contrast left-handed interactions are suppressed, i.e. if ξ approaches zero, we re-encounter the

aforementioned p-wave suppression of the annihilation rate. Then, the coefficients of the low-velocity expansion read

$$a = 0\,, \tag{11.43}$$

$$b = \sum_{ij}\sum_{kl} \frac{|\lambda_{ik}|^2|\lambda_{jl}|^2}{32\pi m_{\phi_3}^2} \frac{\left(2+\mu_1^2+\mu_2^2+\left(\mu_1^2-\mu_2^2\right)\cos 2\theta_\psi\right)^2}{\left(1+\mu_1^2\right)^2\left(1+\mu_2^2\right)^2}\,. \tag{11.44}$$

Note that in the limit of equal charged mediator masses $m_{\psi_1} = m_{\psi_2}$, i.e. for $y_\psi = 0$ the p-wave coefficient b reduces to the expression which we had found for the model studied in Part III, see Equation (8.25)[37]. Also note that while all the coefficients above are given for vanishing lepton masses, we use the expressions with the full final state mass dependence in our numerical analysis.

Constraints from the DM Relic Density

In order to study the relic density constraints numerically we calculate the thermally averaged annihilation rate $\langle\sigma v\rangle_{\text{eff}}$ from Equation (11.41) for randomly generated points of our parameter space and compare it with the value necessary to obtain the correct abundance of DM. The latter rate is approximately constant for DM masses $m_{\phi_3} > 10\,\text{GeV}$ and reads [162, 163]

$$\langle\sigma v\rangle_{\text{eff}}^{\text{exp}} = 2.2\times 10^{-26}\,\text{cm}^3\,\text{s}^{-1}\,. \tag{11.45}$$

We consider points that yield rates which equal this value within a 10% tolerance range as viable. For the calculation of $\langle\sigma v\rangle_{\text{eff}}$ we always include both the s- and p-wave contribution containing the full final state mass dependence. The lepton masses are adopted from Reference [158]. Due to our findings from Section 11.2 we restrict the DM–electron couplings to $|\lambda_{ei}| \in [10^{-6}, 10^{-1}]$ when generating random points in the parameter space of our model and the value of y_ψ is randomly generated within the range $y_\psi \in [0, 2]$. Regarding the scaling parameter ξ we restrict the analysis to the two cases $|\xi| = 0.01$ and $|\xi| = 1.00$, i.e. we consider the two limiting cases of a significant suppression and no suppression of left-handed interactions between DM and leptons. The results are gathered in Figure 11.8 and 11.9.

In Figure 11.8 we show the restrictions that the relic density constraints place on the coupling matrix λ in the SFF scenario. Here we have assumed maximum mixing, i.e. we have set $m_\Psi = m_\psi$ which yields $\theta_\psi = \pi/4$. The DM mass is fixed to $m_{\phi_3} = 600\,\text{GeV}$ while the gauge eigenstate mass parameters $m_\Psi = m_\psi$ vary. Since we generally consider DM masses that satisfy $m_{\phi_3} \gg m_{\ell_i}$ in our analysis, the relic density constraint reduces to the spherical condition

$$|\lambda_{e3}|^2 + |\lambda_{\mu 3}|^2 + |\lambda_{\tau 3}|^2 \approx \text{const.}\,, \tag{11.46}$$

for the SFF scenario. At the same time we satisfy the flavour constraints by restricting the DM–electron couplings to be suppressed, which further reduces this condition to

$$|\lambda_{\mu 3}|^2 + |\lambda_{\tau 3}|^2 \approx \text{const.} \tag{11.47}$$

This explains the discrete circular bands in the in the $|\lambda_{\mu 3}|-|\lambda_{\tau 3}|$ plane in Figure 11.8. The width of these bands corresponds to the 10% tolerance region that we allow for when comparing our annihilation rate with $\langle\sigma v\rangle_{\text{eff}}^{\text{exp}}$. Regarding the choice for the scaling parameter ξ we find that suppressed left-handed interactions with $|\xi| = 0.01$ require larger couplings

[37] Note the different definitions of the mass ratio μ, which in Equation (8.25) is defined as the inverse squared of the definition we use here.

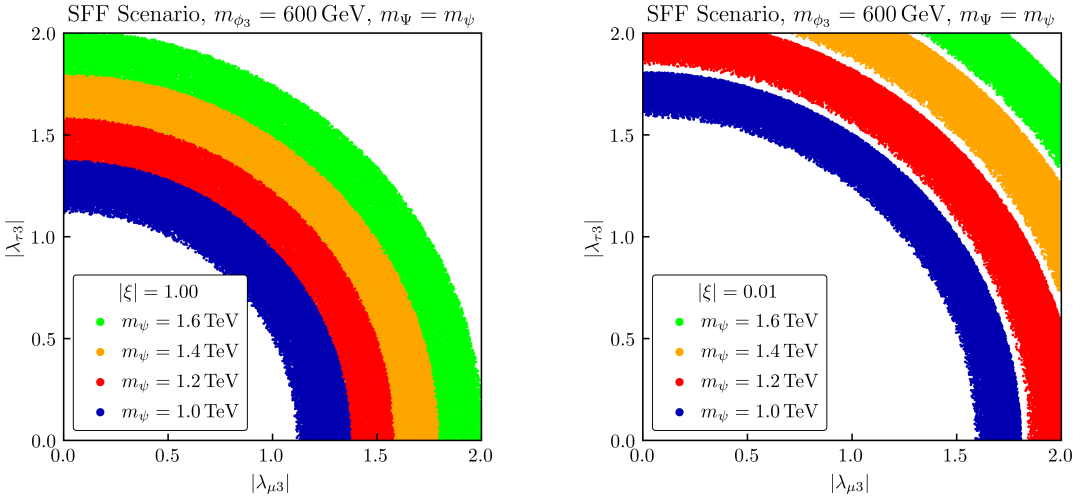

(a) $|\xi| = 1.00$ **(b)** $|\xi| = 0.01$

Figure 11.8 | Constraints on $|\lambda_{\mu 3}|$ and $|\lambda_{\tau 3}|$ from the observed DM relic density in the SFF scenario for maximum mixing with $\theta_\psi = \pi/4$. The DM mass is set to $m_{\phi_3} = 600\,\text{GeV}$ and the mass parameters $m_\Psi = m_\psi$ vary.

to satisfy the constraint since in this case the annihilation rate is p-wave suppressed. This can be seen in Figure 11.8b. If in contrast left-handed interactions may be sizeable, the p-wave suppression is lifted and the correct annihilation rate can also be obtained with comparably smaller couplings, see Figure 11.8a. We stress that DM annihilations into a pair of neutrinos through the t-channel exchange of the neutral mediator ψ_0 only lead to sub-dominant contributions for both choices of $|\xi|$. As this annihilation channel is purely governed by left-handed interactions, it is chirality-suppressed for any choice of ξ and only contributes to the p-wave. For the case of non-suppressed left-handed interactions with $|\xi| = 1.00$ these annihilations are thus sub-leading to the contribution from annihilations into a pair of leptons in the s-wave given in Equation (11.42). In the case of suppressed left-handed couplings with $|\xi| = 0.01$, the additional annihilation channel into a pair of neutrinos does not yield relevant contributions at all, since it is proportional to $|\xi|^4$. In Figure 11.8 we further see that for both choices for the scaling parameter ξ growing masses $m_\psi = m_\Psi$ require larger couplings. This is due to the $1/m^2_{\psi_\alpha}$ suppression of the s-wave coefficient a and the $1/m^4_{\psi_\alpha}$ suppression of the p-wave coefficient b, respectively. We also note that moving away from the case of maximum mixing between ψ_1 and ψ_2, i.e. considering cases with $m_\psi \neq m_\Psi$ has no qualitative impact on our findings. This behaviour is trivial for suppressed left-handed interactions with $|\xi| = 0.01$, since in this case the restrictions on λ solely depend on m_ψ, which is the mass parameter of the gauge eigenstate ψ_2' that couples the dark scalars to right-handed leptons. For the case of non-suppressed left-handed interactions we find that the case $m_\psi \neq m_\Psi$ increases the mass splitting

$$\Delta m_\psi = m_{\psi_1} - m_{\psi_2} = \sqrt{(m_\Psi - m_\psi)^2 + 2y_\psi^2 v^2}\,, \tag{11.48}$$

which the s-wave coefficient a is proportional to, while it at the same time increases the $1/m^2_{\psi_\alpha}$ suppression of a. Ultimately, this increased suppression dominates over the growth in Δm_ψ when choosing $m_\Psi \neq m_\psi$, such that the interplay of both effects only leads to a small shift of the contours from Figure 11.8a to larger couplings in this case.

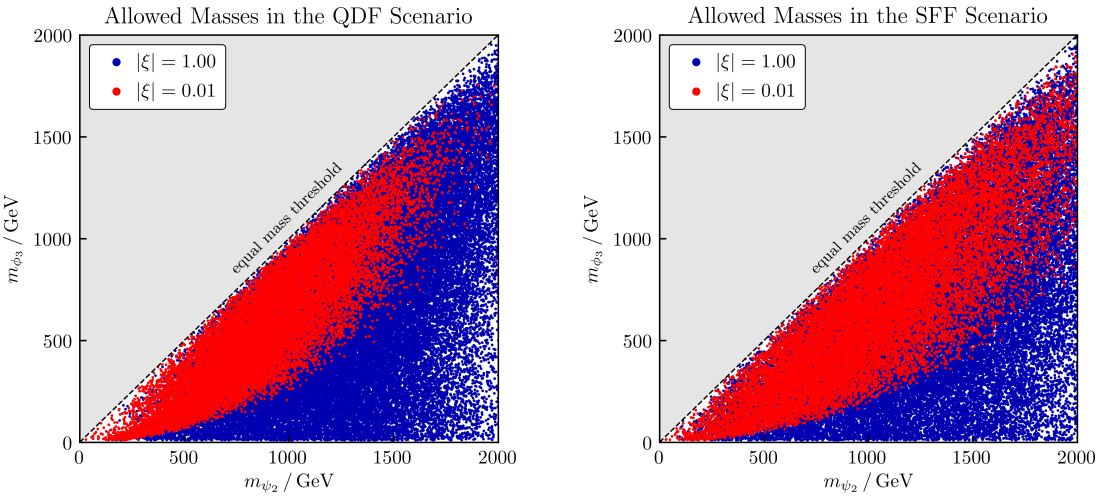

(a) QDF scenario **(b)** SFF scenario

Figure 11.9 | Viable masses m_{ψ_2} and m_{ϕ_3} for both freeze-out scenarios. The red points correspond to the case of a significant suppression of left-handed interactions and the blue points correspond to the case of no suppression.

In the QDF scenario the relic density constraints restrict all entries of the coupling matrix λ as they demand it to satisfy

$$\sum_{ij} |\lambda_{ij}|^2 \approx \text{const.}\,, \tag{11.49}$$

in the case of negligible lepton masses. As this condition yields much less apparent constraints, we waive showing them here but instead comment on the most important features of the parameter space that we find to be viable. The condition from above demands the couplings $|\lambda_{ij}|$ to form the shell of a nine-dimensional sphere, which is why the outer edge of the contours from Figure 11.8a is also present in the QDF case. However, the QDF freeze-out leads to smaller DM annihilation rates in general, which is due to the flavour-averaging factor $f_{\text{sc}} = 1/9$.[38] Hence, in this scenario the outer edge is shifted towards larger couplings. Due to the higher dimensionality of the relevant parameter space, we further find that in spite of suppressed DM–electron couplings the contours in the $|\lambda_{\mu 3}| - |\lambda_{\tau 3}|$ plane do not exhibit an inner edge in this freeze-out scenario, i.e. both $|\lambda_{\mu 3}|$ and $|\lambda_{\tau 3}|$ may become arbitrarily small at the same time.

Figure 11.9 illustrates the restrictions that the relic density constraints place on the NP masses. We here only show the $m_{\psi_2} - m_{\phi_3}$ plane as the largest contributions to the annihilation rate come from processes where the light charged mediator ψ_2 is exchanged in the t-channel. Diagrams with a ψ_1-exchange suffer from an additional suppression by a larger NP scale since we conventionally chose $m_{\psi_1} > m_{\psi_2}$. We find that for the case of suppressed left-handed interactions (red points) a lower limit arises for the value of the DM mass m_{ϕ_3} in both scenarios. This is due to the p-wave suppression of the DM annihilation rate for $|\xi| = 0.01$. For negligible lepton masses, i.e. in the case $m_\ell \ll m_{\phi_3} \ll m_{\psi_2}$ the

[38] The origin of this flavour-averaging factor was explained in Section 3.2.

p-wave coefficient b behaves like[39]

$$b = \sum_{ij} \sum_{kl} \frac{|\lambda_{ik}|^2 |\lambda_{jl}|^2}{16\pi} \frac{m_{\phi_3}^2}{m_{\psi_1}^2 m_{\psi_2}^2} \,, \tag{11.50}$$

and hence the DM mass m_{ϕ_3} may not be arbitrarily small in order to compensate for the velocity suppression of the annihilation rate. As can be seen in Figure 11.9 and inferred from the expression above, this lower limit on m_{ϕ_3} increases with growing mediator masses $m_{\psi_{1,2}}$ since the annihilation rate is suppressed by the latter. Comparing Figure 11.9a and 11.9b we find that in the QDF scenario the lower limit on m_{ϕ_3} is more stringent, due to the generally smaller annihilation rate in this freeze-out case. If on the other hand left-handed interactions are not suppressed (blue points), DM can also annihilate in the s-wave which is why the above discussed lower limit on m_{ϕ_3} is absent in this case. Here we find that even very large values for m_{ψ_2} allow for any DM mass $m_{\phi_3} < m_{\psi_2}$.

11.5 Dark Matter Detection Experiments

Our previous analyses in this work as well as earlier studies in the DMFV framework [20–24] have shown that flavoured DM models can be subject to restrictive constraints from direct detection experiments. Even for the case of lepton-flavoured DM, where the leading contributions to DM–nucleon scattering arise at the one-loop level, we found this statement to hold true in Part III of this work. As far as constraints from indirect detection are concerned, we there found for the version of this model with purely right-handed interactions that the p-wave suppression of the DM annihilation rate renders them irrelevant for large parts of the parameter space. However, since in this model DM is additionally coupled to left-handed leptons, we expect constraints from both direct as well as indirect detection experiments to be more restrictive, since the new left-handed interactions between DM and leptons do not only lead to additional contributions to DM–nucleon scatterings but most importantly also lift the p-wave suppression of the DM annihilation rate. We hence use this section and examine constraints coming from direct and indirect detection experiments.

Relevant Processes for Direct Detection

In Section 8.4 we have discussed in detail that in spite of generally exhibiting a rich direct detection phenomenology, the most stringent constraints for lepton-flavoured DM are related to DM–nucleon scattering. Constraints from other processes such as DM–atom or DM–electron scattering can be safely neglected, as these either suffer from a severe wave-function suppression [214] or as they are only relevant for sub-MeV DM [215].

Following these findings we thus focus on DM–nucleon scattering here. Relevant contributions to this process are generated through the one-loop penguins shown in Figure 11.10. The penguin diagram shown in Figure 11.10a is only mediated by a photon γ if the mediators in the loop are charged and carry the same index $\alpha = \beta \in \{1, 2\}$. All other diagrams included in this figure are mediated by a Z boson and we also note that only if the indices satisfy $\alpha = \beta = 0$ the lepton in the loop is a neutrino ν_i. Most importantly, all Z penguin contributions are proportional to the external momentum and can hence be safely neglected. The Higgs mediated penguin diagram shown in Figure 11.10b only exist for the

[39] Recall that the sum over initial state flavours is absent for the SFF case and the initial state flavour indices satisfy $i = j = 3$.

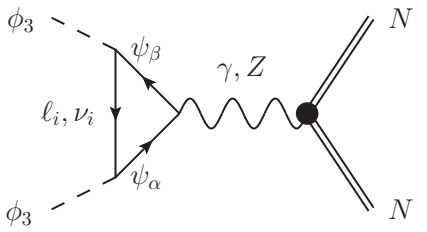

(a) one-loop DM–nucleon scattering mediated by γ or Z

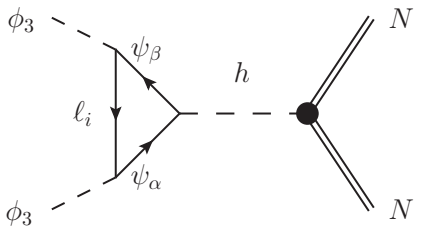

(b) one-loop DM–nucleon scattering mediated by h

Figure 11.10 | Representative Feynman diagrams of relevant interactions for direct detection signals. Note that for both penguins there is also a diagram with two leptons and one mediator in the loop where the bosons are emitted from the two leptons.

cases $\alpha, \beta \in \{1, 2\}$. Diagrams in which the Higgs boson is emitted from two charged leptons in the loop are negligible, since these processes are proportional to $y_{\ell_i} y_N |\lambda_{i3}|^2$, where $y_N \simeq 0.3$ is the Higgs-nucleon coupling [194]. On the other hand, the case where the Higgs boson is emitted from two charged mediators is proportional to $y_\psi y_N |\lambda_{i3}|^2$ and can thus become potentially sizeable. However, we find that the amplitude of this diagram is divergent and contributes to the renormalisation of the Higgs portal coupling $\lambda_{H\phi}$, which induces tree-level scatterings between DM and nucleons where a Higgs boson is exchanged in the t-channel.[40] In line with the arguments provided in Chapter 10, we use our freedom towards the quartic coupling $\lambda_{H\phi}$ and always choose it in such a way that the tree-level and one-loop contributions cancel.

Thus, the only relevant contribution that we consider for the calculation of the DM–nucleon scattering rate is the one-loop photon penguin diagram shown in Figure 11.10a. This process is induced by the charge-radius operator given in Equation (8.30). In the limit of negligible lepton masses $m_\ell \ll m_{\phi_3}$ the matched Wilson coefficients $f_{\gamma,1}$ and $f_{\gamma,2}$ of the contributions with the charged mediators ψ_1 and ψ_2 in the loop read [190]

$$f_{\gamma,1} = -\sum_i \frac{e\,|\lambda_{i3}|^2\,(s_\theta^2 + |\xi|^2 c_\theta^2)}{16\pi^2\, m_{\psi_1}^2} \left[1 + \frac{2}{3}\log\left(\frac{m_{\ell_i}^2}{m_{\psi_1}^2}\right)\right], \tag{11.51}$$

$$f_{\gamma,2} = -\sum_i \frac{e\,|\lambda_{i3}|^2\,(c_\theta^2 + |\xi|^2 s_\theta^2)}{16\pi^2\, m_{\psi_2}^2} \left[1 + \frac{2}{3}\log\left(\frac{m_{\ell_i}^2}{m_{\psi_2}^2}\right)\right]. \tag{11.52}$$

The expressions above do not include contributions with a chirality flip inside the loop, since for closed loops these are proportional to the mass of the lepton in the loop and are therefore negligible. Also note that the mass m_{ℓ_i} needs to be replaced by the momentum transfer $|\vec{q}| = \mathcal{O}(3-10)\,\text{MeV}$ for first generation leptons in the loop, i.e. in the case $i = 1$, since the momentum transfer $|\vec{q}|$ is much larger than the electron mass m_e [190]. The averaged SI DM–nucleon scattering cross section is given in terms of these two coefficients and reads

$$\sigma_{\text{SI}} = \frac{Z^2\, e^2\, \mu^2}{8\pi\, A^2} \left|f_{\gamma,1} + f_{\gamma,2}\right|^2, \tag{11.53}$$

where Z and A are the atomic and mass numbers of the nucleon while μ is the reduced mass of the DM–nucleon system defined as $\mu = m_N m_{\phi_3}/(m_N + m_{\phi_3})$.

[40] For large parts of the parameter space this contribution is comparable to the photon penguin for $\lambda_{H\phi} \sim \mathcal{O}(1)$ couplings, see Appendix C.2 for details.

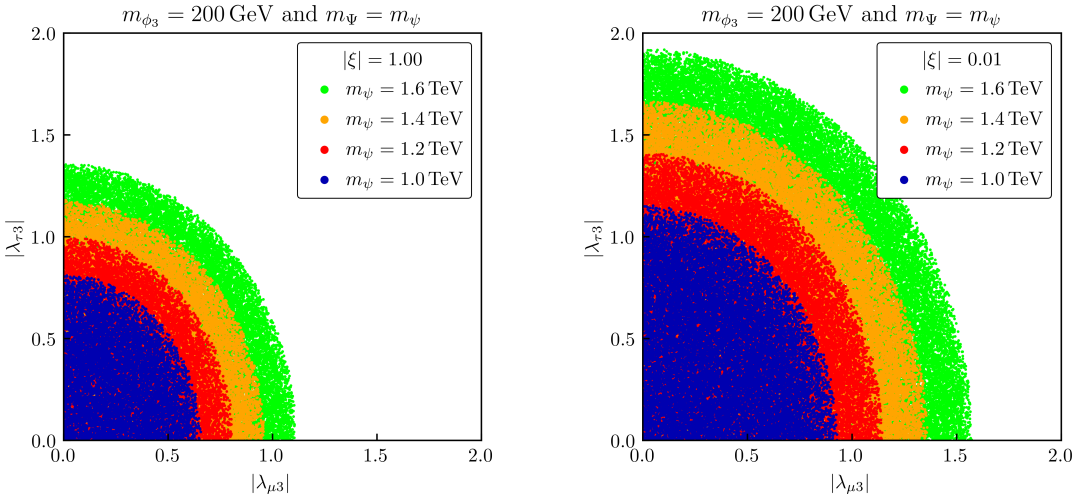

(a) $|\xi| = 1.00$ **(b)** $|\xi| = 0.01$

Figure 11.11 | Direct detection constraints on $|\lambda_{\mu 3}|$ and $|\lambda_{\tau 3}|$ for both choices of $|\xi|$ and various values for $m_\Psi = m_\psi$, while assuming maximum mixing with $\theta_\psi = \pi/4$. The DM mass is fixed to $m_{\phi_3} = 200\,\text{GeV}$.

Constraints from Direct Detection

To determine the parameter space of our model that is consistent with constraints from direct detection experiments we calculate the DM–nucleon scattering rate through Equation (11.53) for randomly generated points and compare it with the experimental upper limit on WIMP–nucleon scattering. The most stringent limits for the latter interactions are set by the XENON1T experiment [177] and are given at 90% C.L. We again neglect the impact of Xenon isotopes here, since Reference [21] found it to be small. For the lepton masses we use the values adopted from Reference [158] and we further set the momentum transfer mentioned above to $|\vec{q}| = 10\,\text{MeV}$. When generating random points in the parameter space of our model, we follow our findings from Section 11.2 and restrict the DM–electron couplings to $|\lambda_{ei}| \in [10^{-6}, 10^{-1}]$. Note that due to the absence of a flavour symmetry in this model, the mass hierarchy between the different dark scalars is not driven by the coupling matrix λ. Hence, in contrast to the models studied in the previous parts of this work the direct detection constraints carry no dependence on the freeze-out scenario in this case.

In Figure 11.11 we show the restrictions that the direct detection constraints place on the model parameters. We again consider the case of maximum mixing between the charged mediators ψ_1 and ψ_2 and let the mass parameters $m_\psi = m_\Psi$ vary while the DM mass is fixed to $m_{\phi_3} = 200\,\text{GeV}$. We do not show varying DM masses here, since the DM–nucleon scattering rate from Equation (11.53) does not depend on the DM mass m_{ϕ_3}. The reason is that for $m_{\phi_3} \gg m_N$ the reduced mass of the DM–nucleon system is approximately $\mu \approx m_N$. However, for $m_{\phi_3} > 30\,\text{GeV}$ growing DM masses yield a less stringent experimental upper limit and hence increasing DM masses trivially allow for larger couplings. In Figure 11.11 we observe the same behaviour for increasing mediator masses $m_\psi = m_\Psi$ or m_{ψ_α}, respectively[41], which is due to the $1/m^2_{\psi_\alpha}$ suppression of the

[41] Recall that the masses m_{ψ_1} and m_{ψ_2} denote the mass parameters of the mass eigenstates ψ_1 and ψ_2 while m_ψ and m_Ψ are respective mass parameters of the gauge eigenstates ψ_1' and ψ_2'.

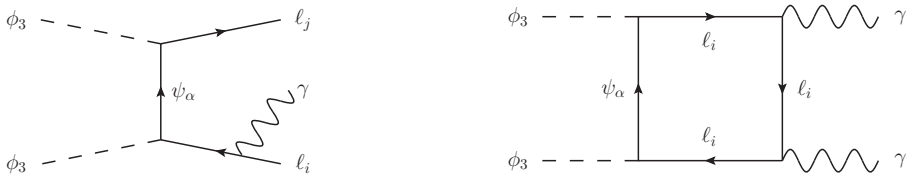

(a) t-channel annihilation to $\ell\bar{\ell}\gamma$ **(b)** one-loop annihilation to $\gamma\gamma$

Figure 11.12 | Representative Feynman diagrams for relevant higher-order annihilation processes. The index only refers to charged mediators, i.e. $\alpha \in \{1, 2\}$.

Wilson coefficients $f_{\gamma,\alpha}$. Hence, for both choices of the scaling parameter ξ the distribution of viable points in the $|\lambda_{\mu 3}| - |\lambda_{\tau 3}|$ plane in Figure 11.11 is shifted towards larger values for increasing masses $m_\Psi = m_\psi$. Regarding the dependence on the scaling parameter ξ, the case of suppressed left-handed interactions shown in Figure 11.11b trivially allows for larger couplings than the case of non-suppressed left-handed couplings shown in Figure 11.11a. With respect to the overall size of the couplings we find that due to the logarithmic dependence of the coefficients $f_{\gamma,\alpha}$ on the lepton mass m_{ℓ_i} the DM–tau coupling $|\lambda_{\tau 3}|$ may grow larger than the DM–muon coupling $|\lambda_{\mu 3}|$, since the muon mass is much smaller than the tau mass. We do not show the DM–electron coupling here as we assumed it to be small in order to satisfy the stringent flavour constraints discussed in Section 11.2.

Relevant Processes for Indirect Detection

For the discussion of constraints from indirect DM detection experiments we follow our analysis from Section 8.4 and include the higher order diagrams shown in Figure 11.12 to the calculation of the DM annihilation rate. These diagrams may become particularly relevant for the case $|\xi| = 0.01$, i.e. the case with suppressed left-handed interactions, since for this choice the DM annihilation rate is p-wave suppressed. As the DM halo velocity in the Milky Way today reads $\langle v^2 \rangle \simeq 10^{-6}$, the p-wave contribution is severely velocity suppressed which renders the inclusion of the diagrams shown in Figure 11.12 necessary in order to provide a thorough analysis of the indirect detection phenomenology.

The annihilation of two dark scalars into two leptons and a photon is shown in Figure 11.12a and lifts the p-wave suppression of according tree-level annihilations without a photon in the final state [259]. This process is proportional to $\alpha_{\text{em}}/\pi \sim 10^{-3}$ while the box diagram of Figure 11.12b is even further suppressed by $\alpha_{\text{em}}^2/(4\pi)^2 \sim 10^{-7}$, but gives comparable contributions to the overall annihilation rate in parts of the parameter space. Both processes are not relevant for the thermal freeze-out of DM, since the velocity suppression during the early Universe is significantly less severe than today and reads $\langle v^2 \rangle \simeq 0.3$.

Since there are two charged mediators in our model, we write

$$\langle \sigma v \rangle_{\gamma\gamma} = \langle \sigma v \rangle_{\gamma\gamma}^1 + \langle \sigma v \rangle_{\gamma\gamma}^2 + 2\langle \sigma v \rangle_{\gamma\gamma}^{12} , \tag{11.54}$$

for the total rate of the $2 \to 2$ process shown in Figure 11.12b. Here the superscript denotes the contributions from diagrams with either ψ_1 or ψ_2 in the loop and the interference term between both diagrams. Just as for the penguin diagram from Figure 11.10a, contributions from processes with a chirality flip inside the loop again vanish since we consider the chiral limit $m_\ell \to 0$ [217]. In this limit, the expressions of the single contributions from

Equation (11.54) read [217]

$$\langle\sigma v\rangle^1_{\gamma\gamma} = \frac{\alpha_{\rm em}^2\left(s_\theta^2+|\xi|^2c_\theta^2\right)^2}{64\pi^3 m_{\phi_3}^2}\left(\sum_i|\lambda_{i3}|^2\right)^2|\mathcal{B}(\mu_1)|^2\,, \tag{11.55}$$

$$\langle\sigma v\rangle^2_{\gamma\gamma} = \frac{\alpha_{\rm em}^2\left(c_\theta^2+|\xi|^2s_\theta^2\right)^2}{64\pi^3 m_{\phi_3}^2}\left(\sum_i|\lambda_{i3}|^2\right)^2|\mathcal{B}(\mu_2)|^2\,, \tag{11.56}$$

$$\langle\sigma v\rangle^{12}_{\gamma\gamma} = \frac{\alpha_{\rm em}^2\left(c_\theta^2+|\xi|^2s_\theta^2\right)\left(s_\theta^2+|\xi|^2c_\theta^2\right)}{64\pi^3 m_{\phi_3}^2}\left(\sum_i|\lambda_{i3}|^2\right)^2|\mathcal{B}(\sqrt{\mu_1\mu_2})|^2\,, \tag{11.57}$$

where the loop function $\mathcal{B}$ is defined as

$$\mathcal{B}(\mu_\alpha) = 2 - 2\log\left[1-\frac{1}{\mu_\alpha}\right] - 2\mu_\alpha\arcsin\left[\frac{1}{\sqrt{\mu_\alpha}}\right]^2\,, \tag{11.58}$$

with $\mu_\alpha = \psi_\alpha^2/m_{\phi_3}^2$. We also decompose the total annihilation rate of the $2\to3$ process shown in Figure 11.12a by writing

$$\langle\sigma v\rangle_{\ell\bar\ell\gamma} = \langle\sigma v\rangle^1_{\ell\bar\ell\gamma} + \langle\sigma v\rangle^2_{\ell\bar\ell\gamma} + 2\langle\sigma v\rangle^{12}_{\ell\bar\ell\gamma}\,. \tag{11.59}$$

Similar to the penguin and box diagrams from Figure 11.10a and 11.12b, respectively, contributions with a chirality flip on either of the final state leptons vanish for this process in the chiral limit. While not vanishing identically, the process with a chirality flip on the virtual mediator in the t-channel however only yields p-wave suppressed contributions and can thus be safely neglected. This p-wave suppression is due to the conservation of the total angular momentum, since the annihilation of two scalars in the s-wave implies $J=0$ while the photon only has two polarisations with $J_z\in\{-1,1\}$.[42] On the other hand, the calculation of the interference term between the contributions from ψ_1 and ψ_2 is much less trivial than for the box diagram of Figure 11.12b due to the three-body phase space. Following the techniques provided by References [262, 263] we have obtained an expression for $\langle\sigma v\rangle^{12}_{\ell\bar\ell\gamma}$ that can be found in Appendix C.3 and was tested to yield the correct total annihilation rate $\langle\sigma v\rangle_{\ell\bar\ell\gamma}$ in the limit $|\xi| = y_\psi = 0$. The other two contributions in Equation (11.59) are given by [259, 264]

$$\langle\sigma v\rangle^1_{\ell\bar\ell\gamma} = \frac{\alpha_{\rm em}\left(s_\theta^2+|\xi|^2c_\theta^2\right)^2}{32\pi^2 m_{\phi_3}^2}\sum_{ij}|\lambda_{i3}|^2|\lambda_{j3}|^2\mathcal{A}(\mu_1)\,, \tag{11.60}$$

$$\langle\sigma v\rangle^2_{\ell\bar\ell\gamma} = \frac{\alpha_{\rm em}\left(c_\theta^2+|\xi|^2s_\theta^2\right)^2}{32\pi^2 m_{\phi_3}^2}\sum_{ij}|\lambda_{i3}|^2|\lambda_{j3}|^2\mathcal{A}(\mu_2)\,, \tag{11.61}$$

where the phase space function $\mathcal{A}(\mu_\alpha)$ is defined as

$$\begin{aligned}\mathcal{A}(\mu_\alpha) = (\mu_\alpha+1)\left(\frac{\pi^2}{6} - \log^2\left[\frac{\mu_\alpha+1}{2\mu_\alpha}\right] - 2\mathrm{Li}_2\left[\frac{\mu_\alpha+1}{2\mu_\alpha}\right]\right)\\ + \frac{4\mu_\alpha+3}{\mu_\alpha+1} + \frac{4\mu_\alpha^2-3\mu_\alpha-1}{2\mu_\alpha}\log\left[\frac{\mu_\alpha-1}{\mu_\alpha+1}\right]\,.\end{aligned} \tag{11.62}$$

In this expression $\mathrm{Li}_2(z)$ is the dilogarithm and we have again used $\mu_\alpha = \psi_\alpha^2/m_{\phi_3}^2$. The annihilation rate for the tree-level process $\phi_3\phi_3^\dagger\to\bar\ell_i\ell_j$ is the same as the one that we obtained for the thermal annihilation rate in the SFF scenario in Section 11.4.

[42] Note that this finding holds true for any $2\to3$ annihilation process with a massless vector boson in the final state, where the according $2\to2$ process without the vector boson is p-wave suppressed. A well known example with different spin statistics are according annihilations of neutralino DM in SUSY, see References [260, 261].

Constraints from Indirect Detection

For the numerical analysis of the indirect detection limits we follow the same approach as in Section 8.4 and consider constraints derived from the positron flux and the γ-ray continuum as well as line spectrum. The constraints for the positron flux are based on AMS-02 measurements and given in form of an upper limit $\langle\sigma v\rangle_{\bar{e}}^{\max}$ on the annihilation rate into final states with positrons [221]. Based on Fermi-LAT measurements of the γ-ray continuum spectrum, Reference [222] provides an equivalent upper limit $\langle\sigma v\rangle_{\tau}^{\max}$ for annihilations into final states with tau flavour. Lastly, Reference [223] has calculated an upper limit $\langle\sigma v\rangle_{\gamma}^{\max}$ for annihilations into photons with a line-like energy spectrum based on Fermi-LAT and H.E.S.S. measurements of the γ-ray line spectrum. Note that the limit on the positron flux signal is mainly dominated by prompt positrons, while the limit on continuum γ-rays mainly constrains the production of taus and antitaus, since they produce significantly more photons than muons and electrons. Thus, to provide constraints on our model parameters we define the three annihilation rates

$$\langle\sigma v\rangle_{\bar{e}} = \sum_{\ell} \left(\langle\sigma v\rangle_{\ell\bar{e}} + \langle\sigma v\rangle_{\ell\bar{e}\gamma}\right) , \tag{11.63}$$

$$\langle\sigma v\rangle_{\tau} = \langle\sigma v\rangle_{\tau\bar{\tau}} + \langle\sigma v\rangle_{\tau\bar{\tau}\gamma} + \frac{1}{2}\sum_{\ell=e,\mu} \left(\langle\sigma v\rangle_{\ell\bar{\tau}} + \langle\sigma v\rangle_{\bar{\ell}\tau} + \langle\sigma v\rangle_{\ell\bar{\tau}\gamma} + \langle\sigma v\rangle_{\bar{\ell}\tau\gamma}\right) , \tag{11.64}$$

$$\langle\sigma v\rangle_{\gamma} = \sum_{\ell} \langle\sigma v\rangle_{\ell\bar{\ell}\gamma} + 2\langle\sigma v\rangle_{\gamma\gamma} , \tag{11.65}$$

and compare them with the respective limits. Here we have included the radiative corrections shown in Figure 11.12a in the rates $\langle\sigma v\rangle_{\bar{e}}$ and $\langle\sigma v\rangle_{\tau}$, since we expect the shift in the m_{ϕ_3} dependence of the three-body final state in comparison with the two-body final state to be negligible. The factor of $1/2$ for final states with a single tau or antitau in $\langle\sigma v\rangle_{\tau}$ is due to the fact that $\langle\sigma v\rangle_{\tau}^{\max}$ was derived for annihilations into a tau–antitau pair.

In order to illustrate the indirect detection constraints in dependence of the NP masses m_{ϕ_3} and m_{ψ_2} we set the DM–lepton couplings to a universal value $|\lambda_{i3}| = |\lambda_{\ell 3}|$, calculate all three rates from above and compare them with the respective experimental upper limit. We then draw contours in the $m_{\psi_2} - m_{\phi_3}$ plane which correspond to the maximum allowed value of $|\lambda_{\ell 3}|$ for which the respective experimental limit is saturated. With respect to the mass spectrum we assume the mixing between ψ_1 and ψ_2 to be maximal corresponding to $\theta_{\psi} = \pi/4$, which fixes the mass of the heavy charged mediator to $m_{\psi_1} = m_{\psi_2} + \sqrt{2} y_{\psi} v$ for given values of m_{ψ_2}. The results of this procedure are gathered in Figure 11.13, where we show the case of non-suppressed left-handed interactions with $|\xi| = 1.00$. Both annihilation rates $\langle\sigma v\rangle_{\bar{e}}$ and $\langle\sigma v\rangle_{\tau}$ are dominated by the s-wave contribution from Equation (11.42), which is proportional to the mass difference $\Delta m_{\psi} = m_{\psi_1} - m_{\psi 2} = \sqrt{2} y_{\psi} v$. Hence, in Figure 11.13a and 11.13b we have set the mediator–Higgs Yukawa coupling to its maximum value $y_{\psi} = 2.0$ in order to determine the largest possible constraints. In Figure 11.13c we have set $y_{\psi} = 0$, since $\langle\sigma v\rangle_{\gamma}$ does not depend on Δm_{ψ} and hence increasing values of y_{ψ} only lead to a larger mass m_{ψ_1} for fixed values of m_{ψ_2}. This in turn suppresses the contributions of relevant diagrams with ψ_1 in the t-channel or loop, respectively, which ultimately yields less stringent constraints. The white dashed line indicates the region, where we expect the indirect detection constraints to become relevant, as the DM–lepton couplings are required to be smaller than the maximally allowed value $|\lambda_{\ell 3}| = 2.0$ within the area enclosed by this line and the equal mass threshold.

We find that constraints based on measurements of the γ-ray continuum spectrum shown in Figure 11.13b are the most stringent ones. They yield restrictions on $|\lambda_{\ell 3}|$ for DM masses $m_{\phi_3} \lesssim 600\,\text{GeV}$ over the complete range of mediator masses m_{ψ_2}. In

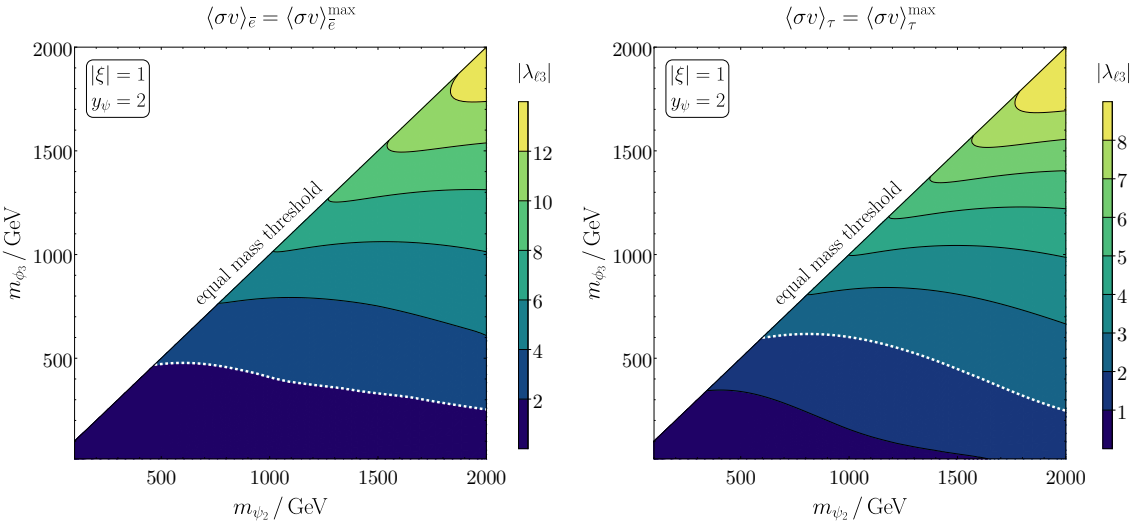

(a) constraints from the positron flux **(b)** constraints from the γ continuum spectrum

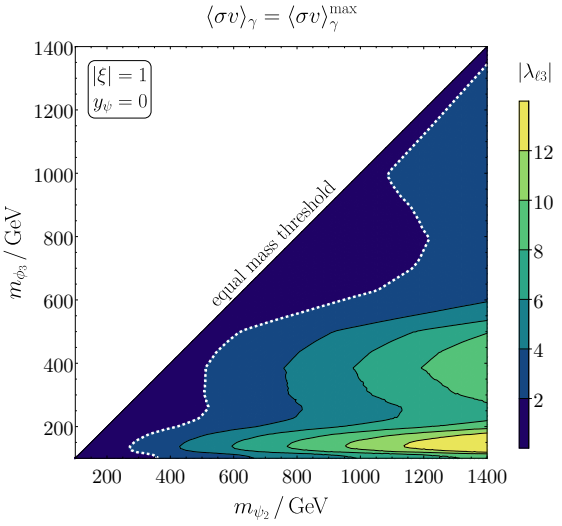

(c) constraints from the γ line spectrum

Figure 11.13 | Restrictions on the model parameters from indirect detection experiments for non-suppressed left-handed interactions. In all three panels we assume maximum mixing with $\theta_\psi = \pi/4$. The area included by the white dashed line and the equal mass diagonal indicates in which mass regime the constraints are relevant.

comparison, we find the constraints on the positron flux shown in Figure 11.13a to be only relevant for DM masses $m_{\phi_3} \lesssim 450\,\text{GeV}$. On the other hand, we see in Figure 11.13c that searches in the γ-ray line spectrum are relevant close to the equal mass threshold, where for $m_{\psi_2} \lesssim 1200\,\text{GeV}$ these limits can also become relevant for larger mass splittings between m_{ψ_2} and m_{ϕ_3} in parts of the $m_{\psi_2} - m_{\phi_3}$ plane.

We do not show the case of suppressed left-handed couplings with $|\xi| = 0.01$ here but relegate it to Appendix C.3, since in this case the resulting exclusion contours are exactly the same as the ones we obtained for the purely right-handed version of this model in Section 8.4. There we had found that the indirect detection constraints are generally weak due to the p-wave suppression of tree-level annihilations $\phi_3\phi_3^\dagger \to \bar{\ell}_i\ell_j$. In summary we conclude that in spite of yielding much more stringent restrictions on the model parameters

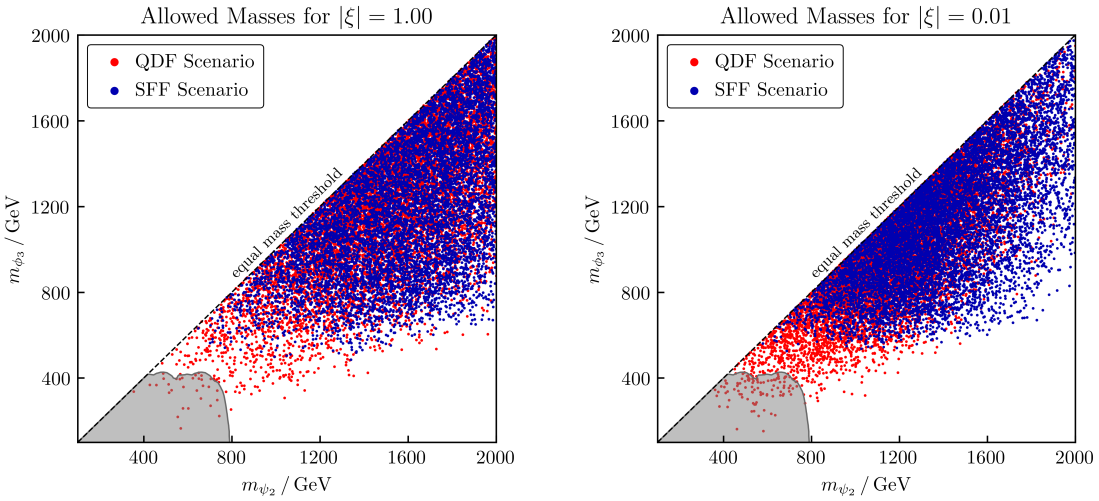

(a) $|\xi| = 1.00$ **(b)** $|\xi| = 0.01$

Figure 11.14 | Viable masses m_{ψ_2} and m_{ϕ_3} while satisfying all constraints simultaneously. We show both freeze-out scenarios and both cases of $|\xi|$. The grey area shows the largest possible exclusion from LHC searches for same-flavour final states $\ell\bar{\ell}+\not{E}_T$ with $\ell = e, \mu$ discussed in Section 11.1 and corresponds to the case $|\lambda_{\ell 3}| = 2.0$, $|\lambda_{\tau 3}| = 0.0$ and $y_\psi = 0.25$.

for non-suppressed left-handed interactions with $|\xi| = 1.00$, the indirect detection limits are still rather mild in comparison to the constraints from LFV decays, the DM relic density or direct DM detection experiments.

11.6 Combined Analysis

We use this section to perform a combined analysis of all experimental constraints discussed above in order to identify the viable parameter space of our model. We generate random points and demand that all relevant limits are satisfied simultaneously. The results of this combined numerical analysis are shown in Figures 11.14–11.16.

In Figure 11.14 we show viable points in the $m_{\psi_2} - m_{\phi_3}$ plane for both freeze-out scenarios and both cases of $|\xi|$. The constraints that LHC searches place on these two masses are shown in form of the grey exclusion contour.[43] Regarding the latter, we find that only for the QDF scenario (red points) LHC searches exclude additional parameter space for both choices of the scaling parameter ξ.

For the SFF scenario (blue points) we find that the viable masses in Figure 11.14 are roughly the same for both suppressed as well as non-suppressed left-handed interactions. The distribution of the viable points in this case is mainly determined by the interplay of direct detection and relic density constraints. In both cases, $|\xi| = 1.00$ and $|\xi| = 0.01$ we find a lower bound on the DM mass m_{ϕ_3} for a given value of m_{ψ_2}. For suppressed left-handed interactions this lower bound was already present in Figure 11.9 where we have solely considered the relic density constraints. In Figure 11.14, we find that this lower

[43] Strictly speaking these limits do not straightforwardly apply here, since they assume $e-\mu$ universality while we have limited the DM–electron couplings to $|\lambda_{ei}| \in [10^{-6}, 10^{-1}]$ and allow for abitraty DM–muon couplings in the combined analysis. We hence expect the actual exclusion from LHC searches to be smaller than the area shown in Figure 11.14 and only include it here for illustration purposes.

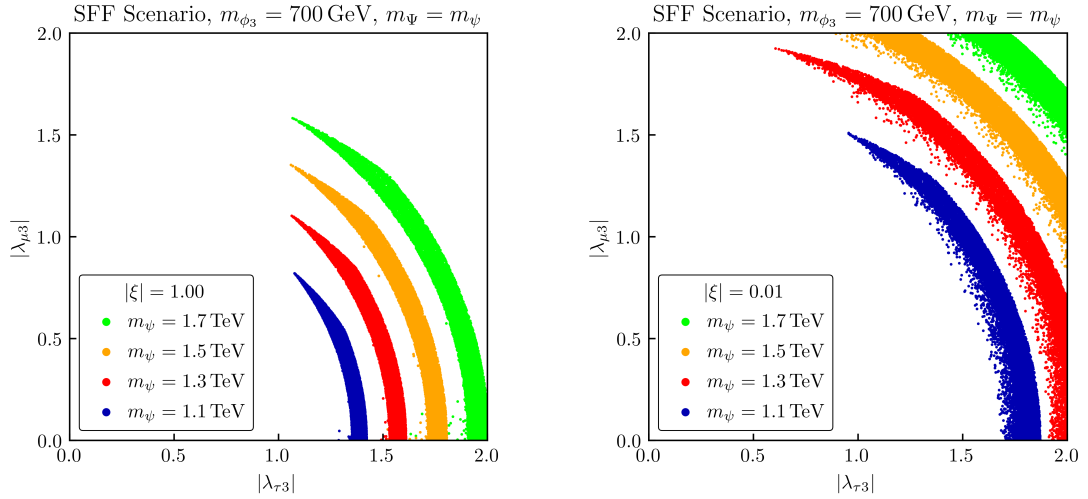

(a) $|\xi| = 1.00$ **(b)** $|\xi| = 0.01$

Figure 11.15 | Viable couplings $|\lambda_{\tau 3}|$ and $|\lambda_{\mu 3}|$ while satisfying all constraints simultaneously in the SFF scenario for both cases of $|\xi|$. We assume maximum mixing with $\theta_\psi = \pi/4$. The DM mass is fixed to $m_{\phi_3} = 700\,\text{GeV}$ and the mass parameters $m_\Psi = m_\psi$ vary.

bound on m_{ϕ_3} is strengthened since the DM–lepton couplings are additionally restricted by the direct detection bound here and may not grow arbitrarily large. Due to the same reason we encounter a lower limit on m_{ϕ_3} for non-suppressed left handed couplings with $|\xi| = 1.00$—for the maximum coupling strengths allowed by the direct detection constraints the DM mass needs to be accordingly large in order to enhance the DM annihilation rate sufficiently and satisfy the relic density limit. For both choices of the scaling parameter ξ we find that this interplay requires $m_{\psi_2} \gtrsim 800\,\text{GeV}$ and $m_{\phi_3} \gtrsim 600\,\text{GeV}$ in order to satisfy both the direct detection and relic density constraints at the same time. Smaller mediator masses $m_{\psi_2} \lesssim 800\,\text{GeV}$ are excluded for both choices of $|\xi|$, since in this region the direct detection constraints force the DM–lepton couplings $|\lambda_{\ell 3}|$ to be so small that even for maximum DM masses $m_{\phi_3} \approx m_{\psi_2}$[44] the resulting DM annihilation rate is too small to satisfy the relic density bound.

In the QDF scenario (red points) the distribution of the viable masses in Figure 11.14 follows a similar pattern as for the SFF scenario. While the overall picture is again determined by the direct detection and relic density constraints, we find that in this case the region of viable mediator masses is extended to include the range $400\,\text{GeV} \lesssim m_{\psi_2} \lesssim 800\,\text{GeV}$. The reason is that in this freeze-out scenario the relic density constraint can in principle also be satisfied through annihilations of the heavier dark states ϕ_1 and ϕ_2 alone. As the direct detection bound solely constrains the couplings of ϕ_3, the correct DM annihilation rate can also be obtained for comparably small mediator masses $m_{\psi_2} \lesssim 800\,\text{GeV}$ since the couplings of ϕ_1 and ϕ_2 may still be sizeable. Regardless of the choice of $|\xi|$, the lower limit on the DM mass m_{ϕ_3} is also present in this freeze-out scenario for the same reasons as for the SFF scenario discussed above.

In Figure 11.15 we show the viable values for $|\lambda_{\tau 3}|$ and $|\lambda_{\mu 3}|$ in the SFF scenario for both cases of $|\xi|$ and for maximum mixing between ψ_1 and ψ_2. In both cases the distribution

[44] Note that scenarios with such small mass splittings between m_{ϕ_3} and m_{ψ_2} are not properly treated in our analysis, since we have neglected coannihilations in Section 11.4.

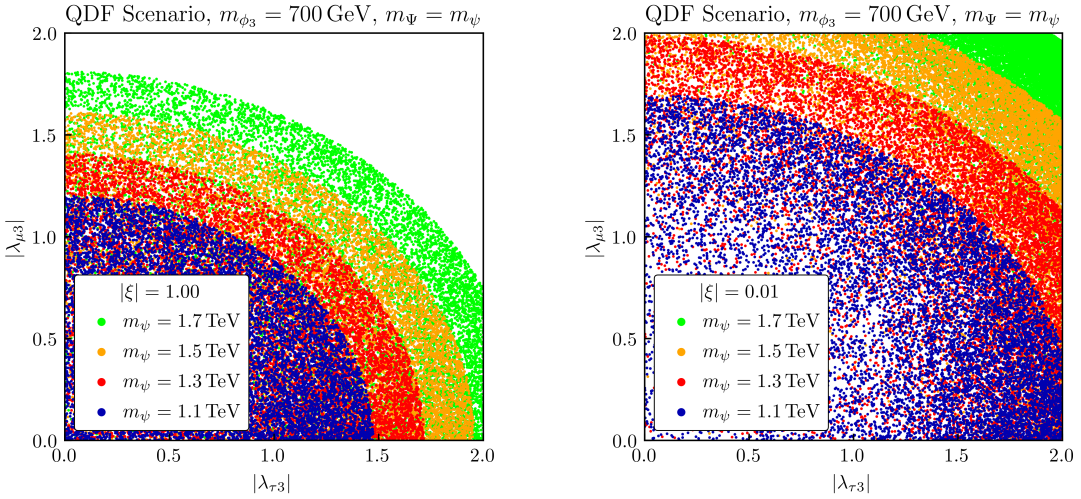

(a) $|\xi| = 1.00$ **(b)** $|\xi| = 0.01$

Figure 11.16 | Viable couplings $|\lambda_{\tau 3}|$ and $|\lambda_{\mu 3}|$ while satisfying all constraints simultaneously in the QDF scenario for both cases of $|\xi|$. We assume maximum mixing with $\theta_\psi = \pi/4$. The DM mass is fixed to $m_{\phi_3} = 700\,\text{GeV}$ and the mass parameters $m_\Psi = m_\psi$ vary.

of viable points is mainly determined by the flavour, relic density and direct detection constraints. Since we have limited the DM–electron couplings to $|\lambda_{ei}| \in [10^{-6}, 10^{-1}]$, the relic density constraint approximately requires the DM–muon and DM–tau couplings to satisfy the circular condition

$$|\lambda_{\mu 3}|^2 + |\lambda_{\tau 3}|^2 \approx \text{const.}\,, \tag{11.66}$$

which causes the discrete bands that can be observed in Figure 11.15. The inner edge of these bands is due to negligible DM–electron couplings, while the outer edge is due to the relic density bound over large parts of the parameter space. If however the DM–muon coupling $|\lambda_{\mu 3}|$ exceeds an m_ψ-dependent threshold, the direct detection constraints start to dominate over the relic density limit, giving rise to the spikes at the upper end of the bands. The limits from direct detection only dominate for large enough DM–muon couplings $|\lambda_{\mu 3}|$, since due to the logarithm of the mass m_{ℓ_i} in Equation (11.51) and (11.52) they are generally more stringent for light leptons in the loop. Regarding the choice of the scaling parameter ξ, we find that the case of suppressed left-handed interactions shown in Figure 11.15b requires larger couplings $|\lambda_{\mu 3}|$ and $|\lambda_{\tau 3}|$. This is mainly due to the p-wave suppression of the DM annihilation rate but also due to suppressed left-handed contributions to the DM–nucleon scattering cross section. The choice of $|\xi|$ has thus important implications for the flavour of DM. While the case of e-flavoured DM is generally excluded due to the severe restrictions from LFV decays on the DM–electron couplings[45] for both choices of $|\xi|$, we find that the case $|\xi| = 1.00$ mainly requires τ-flavoured DM while for $|\xi| = 0.01$ a significant part of the viable parameter space also corresponds to μ-flavoured DM. The latter finding especially holds true for mediator masses $m_\psi \gtrsim 1400\,\text{GeV}$

[45] Remember that in the most general case the flavour constraints could also be satisfied by accordingly restricted DM–muon couplings. However, in this analysis we disregard such scenarios since we ultimately want to solve the $(g-2)_\mu$ anomaly.

for which μ- and τ-flavoured DM are equally favoured. For the case of non-suppressed left-handed interactions we find that only a tiny part of the viable parameter space represents μ-flavoured DM for masses $m_\psi \gtrsim 1300\,\text{GeV}$.

The viable points in the $|\lambda_{\tau 3}| - |\lambda_{\mu 3}|$ plane are shown for the QDF scenario in Figure 11.16. In this case we find their distribution to be much less pronounced, since the relic density constraints restrict each entry of the coupling matrix λ. As all dark species contribute to the thermal freeze-out of DM, the correct DM annihilation rate can in this scenario also be obtained through annihilations of the heavier states ϕ_1 and ϕ_2 alone, which is why the dominant constraints on the DM–lepton couplings $|\lambda_{\mu 3}|$ and $|\lambda_{\tau 3}|$ stem from direct detection. For non-suppressed left-handed couplings with $|\xi| = 1.00$ shown in Figure 11.16a this holds true for each choice of $m_\Psi = m_\psi$. In the case $|\xi| = 0.01$ shown in Figure 11.16b the relic density constraints yield a lower limit on the couplings $|\lambda_{\tau 3}|$ and $|\lambda_{\mu 3}|$ for sizeable mediator masses $m_\psi \gtrsim 1600\,\text{GeV}$. This is due to the p-wave suppression of the DM annihilation rate in this case, which together with such large mediator masses requires sizeable couplings in order to yield the correct DM relic density. Regarding the flavour of ϕ_3 we find that in the QDF scenario both μ- as well as τ-flavoured DM is viable. Here, the latter case is slightly favoured over the former, due to stronger direct detection constraints for DM coupling predominantly to muons.

11.7 Muon Anomalous Magnetic Moment

As already mentioned in Chapter 10 we propose this model as a joint solution for the DM problem and the long-standing muon $(g-2)$ anomaly. After having identified its viable parameter space in the last section, we are now prepared to examine if NP contributions to a_μ sizeable enough to solve the latter anomaly can be generated within our model.

Theoretical Approach

Precision measurements of the muon anomalous magnetic moment [26, 208] yield a world average of

$$a_\mu^{\text{exp}} = (116592061 \pm 41) \times 10^{-11}\,, \tag{11.67}$$

while state-of-the-art SM calculations [225–244] predict the value [27]

$$a_\mu^{\text{SM}} = (116591810 \pm 43) \times 10^{-11}\,. \tag{11.68}$$

Comparing both of these values accounts to a difference of

$$\Delta a_\mu^{\text{exp}} = a_\mu^{\text{exp}} - a_\mu^{\text{SM}} = (2.51 \pm 0.59) \times 10^{-9}\,, \tag{11.69}$$

which corresponds to a 4.2σ deviation[46] between the theory prediction and experimental measurement. We interpret this tension as a hint at NP and propose that the missing contributions $\Delta a_\mu^{\text{exp}}$ originate from our model.

In the latter, the NP contributions Δa_μ are generated through the diagram shown in Figure 11.4 with $\ell_i = \ell_j = \mu$ and read

$$\Delta a_\mu = \Delta a_\mu^1 + \Delta a_\mu^2\,. \tag{11.70}$$

[46] Using recent lattice determinations of the hadronic vacuum polarisation significantly softens the tension between data and the SM [265–268]. However, in that case, a tension emerges in low-energy $\sigma(e^+e^- \to \text{hadrons})$ data [269–271] that requires further investigation. We hence disregard the lattice results and consider the discrepancy as given in Equation (11.69) in this analysis.

(a) chirality flip on external muon line **(b)** chirality flip in the loop

Figure 11.17 | Representative Feynman diagrams for NP contributions Δm_μ to the muon mass.

Here, a single summand Δa_μ^α denotes the contribution coming from the charged mediator ψ_α and the respective expression of each contribution is obtained by setting $i = 2$ in Equation (11.23) and (11.24). Since the operator that induces the magnetic moment of the muon given in Equation (11.16) involves both chiralities, contributions to Δa_μ with a chirality flip inside the loop receive a strong enhancement. In our model, the source of these chirality-flipping contributions is the parameter y_ψ, which couples the fields Ψ and ψ_2' to the SM Higgs doublet and thereby induces a mixing between the two charged mediators. In contrast to contributions with a chirality flip on an external muon line, these diagrams are hence not proportional to the muon mass m_μ but to the mass splitting $\Delta m_\psi = m_{\psi_1} - m_{\psi_2}$. For approximately equal gauge eigenstate mass parameters $m_\Psi \approx m_\psi$ this difference is given by

$$\Delta m_\psi \approx \sqrt{2} y_\psi v \,, \tag{11.71}$$

yielding $\Delta m_\psi \gg m_\mu$ for the scale of the relevant NP that invoke the chirality flip, provided the mediator–Higgs Yukawa coupling satisfies $y_\psi \gtrsim 10^{-3}$.

As the latter condition holds true over large parts of the parameter space, neglecting the first term in Equation (11.23) and (11.24) gives a very good approximation of Δa_μ and reads

$$\Delta a_\mu = \frac{m_\mu}{16\pi^2} \sum_k \frac{\sin 2\theta_\psi \, |\lambda_{\mu k}|^2}{3 m_{\phi_k}^2} \mathrm{Re}\, \xi \left(m_{\psi_1} G(x_{k,1}) - m_{\psi_2} G(x_{k,2}) \right) . \tag{11.72}$$

Given that the mixing angle θ_ψ as defined in Equation (10.10) lies within the range

$$0 \leq \theta_\psi \leq \pi/4 \,, \tag{11.73}$$

such that $\sin 2\theta_\psi > 0$ and that the loop function G defined in Equation (8.7) satisfies

$$m_{\psi_2} G(x_{k,2}) > m_{\psi_1} G(x_{k,1}) \,, \tag{11.74}$$

positive NP contributions Δa_μ require the scaling parameter's real part to be negative, i.e. $\mathrm{Re}\, \xi < 0$.

Since the Yukawa coupling y_ψ also gives rise to the self-energy diagrams of Figure 11.17, NP contributions to the muon anomalous magnetic moment a_μ are typically accompanied by according and potentially sizeable contributions to the muon mass m_μ. In our model, the total muon mass is hence given by the relation

$$m_\mu = \frac{y_\mu v}{\sqrt{2}} + \Delta m_\mu \,, \tag{11.75}$$

which induces a potential fine-tuning problem. The NP contributions to both a_μ and m_μ can be estimated parametrically which yields [272, 273]

$$\Delta a_\mu = \mathcal{C}_{\mathrm{NP}} \frac{m_\mu^2}{m_{\mathrm{NP}}^2} \,, \tag{11.76}$$

$$\Delta m_\mu = \mathcal{O}\left(\mathcal{C}_{\mathrm{NP}}\right) m_\mu \,, \tag{11.77}$$

where the factor $\mathcal{C}_{\mathrm{NP}}$ depends on the details of the model. Using these expressions one can derive an approximate upper bound on the NP scale m_{NP} up to which the experimental value $\Delta a_\mu^{\mathrm{exp}}$ can be reproduced without introducing a fine-tuned muon mass m_μ. Following the convention from Reference [272] we consider scenarios in which the NP corrections Δm_μ to the muon mass are larger than the physical muon mass as fine-tuned. Combined with the parametric estimates from above, this yields an upper limit on the NP scale of [272]

$$m_{\mathrm{NP}} \lesssim 2100\,\mathrm{GeV}\,. \tag{11.78}$$

In addition to this general estimate, we also check explicitly in our numerical analysis which regions of the viable parameter space of our model correspond to fine-tuned scenarios by calculating Δm_μ through [273]

$$\Delta m_\mu = -\frac{\sin 2\theta_\psi \mathrm{Re}\,\xi}{16\pi^2} \sum_k |\lambda_{\mu k}|^2 \left(m_{\psi_1} B_0(0, m_{\psi_1}, m_{\phi_k}) - m_{\psi_2} B_0(0, m_{\psi_2}, m_{\phi_k}) \right), \tag{11.79}$$

where the function $B_0(p^2, m_1, m_2)$ is a standard Passarino–Veltman two-point function renormalised according to the $\overline{\mathrm{MS}}$ scheme. Here we only consider contributions to Δm_μ with an internal chirality flip shown in Figure 11.17b. The process with a chirality flip on an external muon line shown in Figure 11.17a is proportional to m_μ and is hence negligible compared to the contribution from Equation (11.79).

Results

In order to examine whether our model is capable of solving the $(g-2)_\mu$ anomaly, we calculate the NP contributions Δa_μ to the muon anomalous magnetic moment within the regions of the parameter space that were found to be viable in the combined analysis of Section 11.6. In the numerical analysis we use the full expression for Δa_μ given in Equation (11.70), which includes diagrams with a chirality flip on any of the external muon lines as well. For the calculation of the NP contributions Δm_μ to the muon mass we use the expression from Equation (11.79). Following the previous sections, we only consider the case of maximum mixing between ψ_1 and ψ_2 corresponding to $\theta_\psi = \pi/4$ here. The results are gathered in Figures 11.18–11.20.

In Figure 11.18 we show for which values of $|\xi|$ and y_ψ the value of $\Delta a_\mu^{\mathrm{exp}}$ can be reproduced within the experimental 2σ band while satisfying all constraints discussed in the previous sections. The results are shown for both freeze-out scenarios. For non-suppressed left-handed interactions with $|\xi| = 1.00$ we find that the mediator-Higgs Yukawa coupling needs to satisfy $y_\psi \lesssim 10^{-1}$ in order to stay consistent with the 2σ band of the experimental measurement in both freeze-out scenarios. For suppressed left-handed interactions with $|\xi| = 0.01$ we in contrast find that the 2σ band can be reached for values $0.3 \lesssim y_\psi < 2.0$. Further, the overall dependence on the freeze-out scenario is found to be small, as in the QDF scenario shown in Figure 11.18b the viable points are slightly shifted towards smaller values of $|\xi|$. This is due to the fact that the latter scenario allows for larger couplings than the SFF scenario, see Section 11.6. We also find the distribution of viable points to only very leniently depend on the mediator mass. As can be seen in both Figure 11.18a and 11.18b, increasing the mass parameter $m_\Psi = m_\psi$ only slightly shrinks the viable area in the $|\xi| - y_\psi$ plane. The reason is that larger masses $m_\Psi = m_\psi$ allow for larger couplings $|\lambda_{\mu i}|$ while they at the same time suppress the value of Δa_μ. An increased maximum value of the couplings $|\lambda_{\mu i}|$ reduces both the maximally viable value of y_ψ as well as $|\xi|$ in

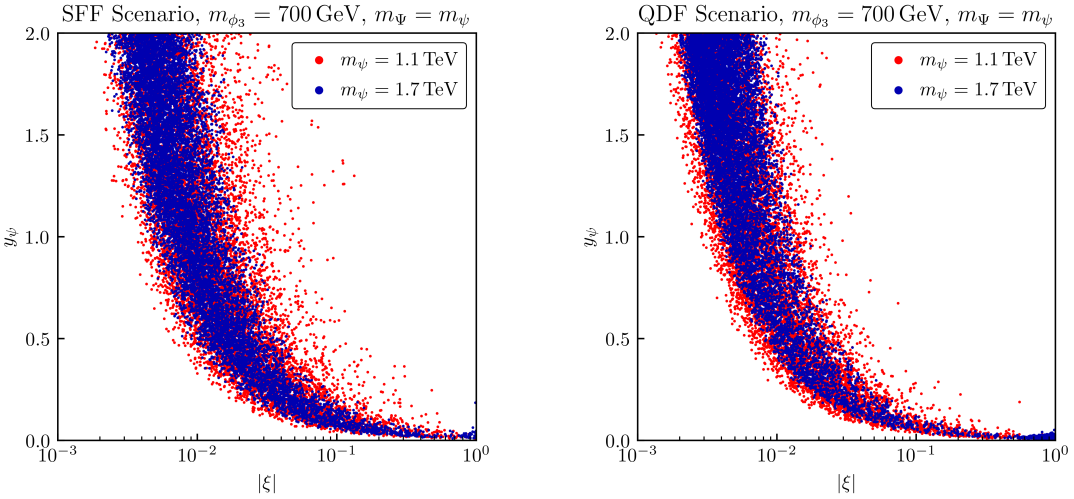

(a) SFF scenario **(b)** QDF scenario

Figure 11.18 | Viable points in the $|\xi| - y_\psi$ plane while demanding that Δa_μ lies within the 2σ band of $\Delta a_\mu^{\text{exp}}$.

order to not yield a too large Δa_μ. Hence, in this case the upper edge of the distribution of viable points is shifted towards smaller values of $|\xi|$ and y_ψ. On the other hand, the suppression of Δa_μ through large mediator masses raises the minimally required value of y_ψ and $|\xi|$ in order to not yield too small NP contributions to a_μ. This in turn causes the lower edge of the viable areas in Figure 11.18 to be shifted towards larger values of y_ψ and $|\xi|$.

The dependence of Δa_μ on the Yukawa coupling y_ψ is shown for the SFF scenario in Figure 11.19a and 11.19b. For both choices of the scaling parameter ξ we find that the experimental central value of $\Delta a_\mu^{\text{exp}}$ can be reproduced. In the case of non-suppressed left-handed interactions shown in Figure 11.19a this requires Yukawa couplings of at least $y_\psi \simeq 0.006$ for masses $m_\psi = 1100\,\text{GeV}$, while larger values $y_\psi \simeq 0.008$ are required for $m_\psi = 1700\,\text{GeV}$. If left-handed interactions are suppressed, i.e. for the case $|\xi| = 0.01$ shown in Figure 11.19b we find that the experimental central value is obtained for couplings $y_\psi \simeq 0.6$ and $m_\psi = 1100\,\text{GeV}$ or $y_\psi \simeq 0.8$ and $m_\psi = 1700\,\text{GeV}$, respectively. We further find that sizeable values of $m_\Psi = m_\psi$ shrink the area of the viable values Δa_μ for a given coupling y_ψ. In the case of suppressed left-handed interactions they even cause a lower limit on the viable values of Δa_μ, as can be seen in Figure 11.19b. This lower limit is due to the relic density constraint, which for suppressed left-handed interactions and masses $m_\psi \gtrsim 1500\,\text{GeV}$ requires the DM–muon coupling to satisfy $|\lambda_{\mu 3}| \gtrsim 1.0$ in order to compensate for the p-wave suppression of the DM annihilation rate, see Figure 11.15b. For non-suppressed left-handed interactions DM can also annihilate in the s-wave and hence the lower bound is absent in this case, since the DM–muon coupling may become arbitrarily small, see Figure 11.15a. Since growing mediator masses at the same time suppress Δa_μ, the upper edge of accessible values shrinks for both cases of $|\xi|$ for increasing mediator masses.

Qualitatively we find this behaviour to also hold true for the QDF scenario shown in Figure 11.19c and 11.19d. In this case however, the area of viable values Δa_μ for a given Yukawa coupling y_ψ shrinks more rapidly with increasing masses $m_\Psi = m_\psi$ as the lower limit is strengthened. This can be seen particularly well for the case of suppressed left-

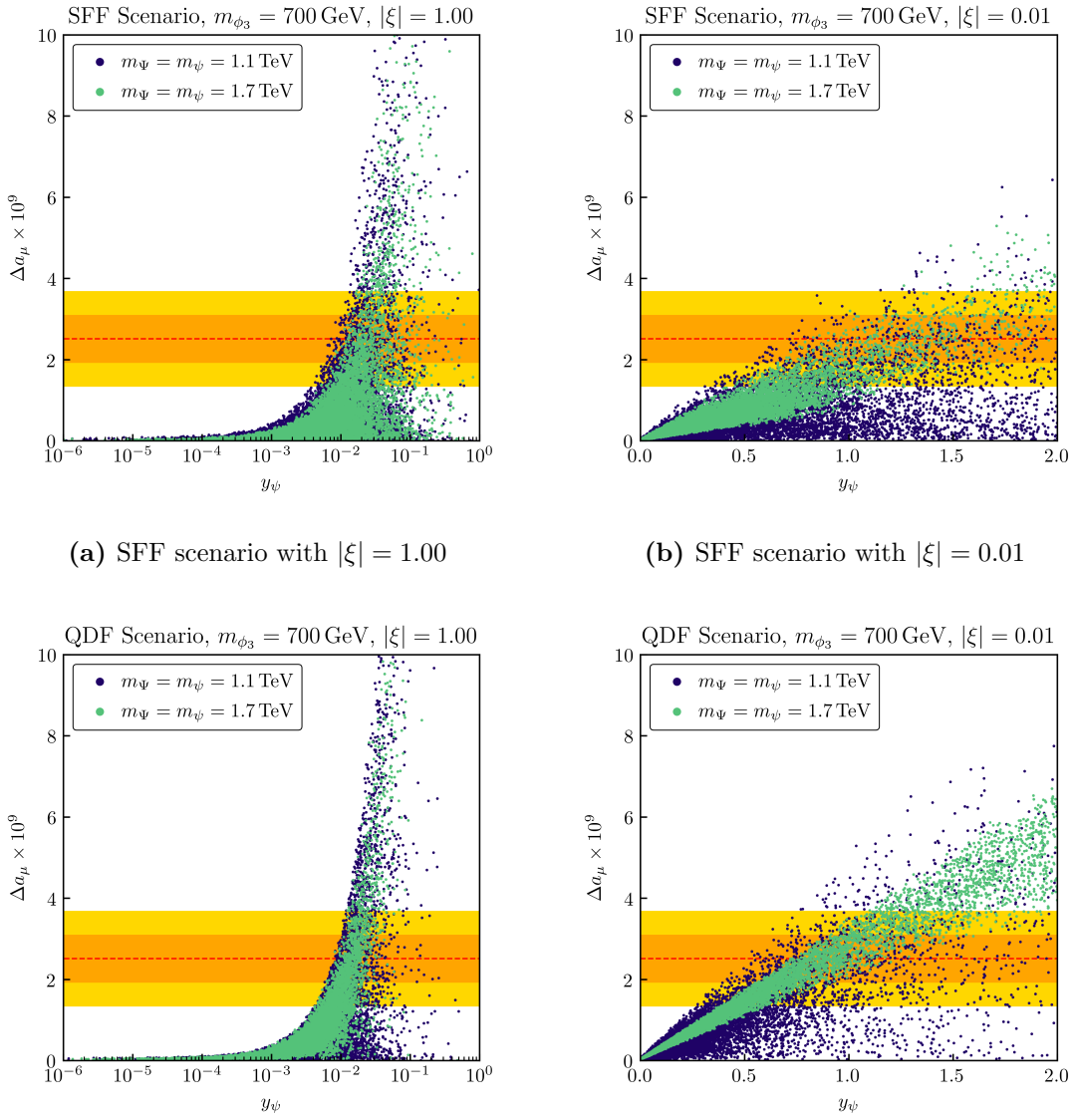

(a) SFF scenario with $|\xi| = 1.00$

(b) SFF scenario with $|\xi| = 0.01$

(c) QDF scenario with $|\xi| = 1.00$

(d) QDF scenario with $|\xi| = 0.01$

Figure 11.19 | Dependence of the NP contributions Δa_μ on the Yukawa coupling y_ψ for both freeze-out scenarios and both choices of $|\xi|$. The red dashed line shows the mean value of $\Delta a_\mu^{\text{exp}}$ and the orange and yellow areas show the 1σ and 2σ bands, respectively.

handed interactions shown in Figure 11.19d. The reason are again the constraints from the DM relic density—in the QDF scenario all couplings $|\lambda_{\mu i}|$ need to be accordingly large in order to compensate for the small DM–electron couplings for sizeable mass parameters $m_\Psi = m_\psi$. Hence, the lower limit on the minimally viable value of Δa_μ is increased with respect to the SFF case, see Figure 11.19b and 11.19d. The more rapidly reduced upper limit on Δa_μ on the other hand, is due to the fact that even for comparably small masses $m_\psi = 1100\,\text{GeV}$ the QDF scenario already allows for close-to-maximal couplings $|\lambda_{\mu 3}| \simeq 1.7$, see Figure 11.16b. Hence, the increased suppression of Δa_μ for increased values of $m_\Psi = m_\psi$ can be less compensated for by growing couplings $|\lambda_{\mu 3}|$ as they are limited to $|\lambda_{\mu 3}| \leq 2.0$. For the QDF scenario we find that for $|\xi| = 1.00$ the experimental central

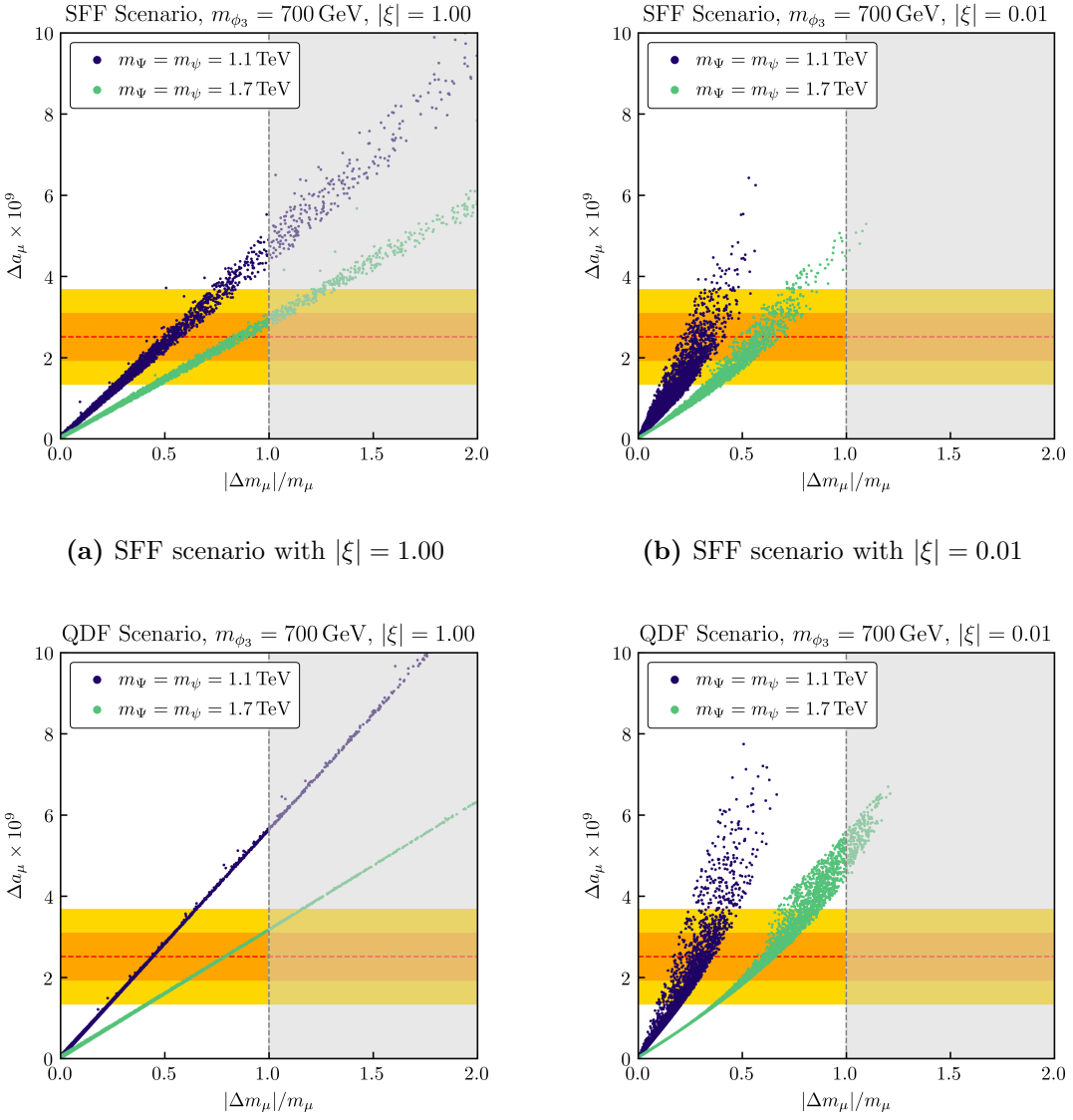

(a) SFF scenario with $|\xi| = 1.00$

(b) SFF scenario with $|\xi| = 0.01$

(c) QDF scenario with $|\xi| = 1.00$

(d) QDF scenario with $|\xi| = 0.01$

Figure 11.20 | Correlation between Δa_μ and $|\Delta m_\mu|$ in both freeze-out scenarios and for both choices of $|\xi|$. The greyed-out area indicates the region with $|\Delta m_\mu|/m_\mu > 1$ which we consider fine-tuned. The red dashed line shows the mean value of $\Delta a_\mu^{\text{exp}}$ and the orange and yellow areas show the 1σ and 2σ bands, respectively.

value of $\Delta a_\mu^{\text{exp}}$ can be reproduced for $y_\psi \simeq 0.008$ and masses $m_\psi = 1100\,\text{GeV}$, while we find $y_\psi \simeq 0.01$ for $m_\psi = 1700\,\text{GeV}$. If in contrast left-handed interactions are suppressed we find that $y_\psi \simeq 0.5$ is required for masses $m_\psi = 1100\,\text{GeV}$ while for $m_\psi = 1700\,\text{GeV}$ the Yukawa coupling needs to satisfy $y_\psi \simeq 0.8$.

The correlation between NP contributions to a_μ and m_μ is illustrated in Figure 11.20 for both freeze-out scenarios and both choices of $|\xi|$. Here we show how large the corrections Δa_μ are for a given value of $|\Delta m_\mu|$ normalised to the physical muon mass m_μ. In Figure 11.20a and 11.20b we find that in the SFF scenario the central value of Δa_μ can be reproduced without exceeding the threshold $|\Delta m_\mu|/m_\mu = 1$, i.e. without intro-

ducing a fine-tuned muon mass for both choices of the scaling parameter ξ and masses $m_\Psi = m_\psi$. Increasing mediator masses lead to smaller values of Δa_μ for a given value of Δm_μ, indicating that NP contributions to a_μ receive a stronger suppression from growing masses $m_\Psi = m_\psi$ than according corrections to m_μ. Likewise, non-suppressed left-handed interactions require larger accompanying corrections Δm_μ for sizeable NP effects in a_μ. For $|\xi| = 1.00$ the combined analysis generally requires $y_\psi \sim \mathcal{O}(10^{-4} - 10^{-1})$ for which the mass of the lightest charged mediator m_{ψ_2}[47] is larger than in the case of suppressed left-handed couplings which allow for Yukawa couplings $y_\psi \sim \mathcal{O}(1)$. While this suppresses both Δa_μ as well as Δm_μ, we find that the function

$$\frac{m_{\psi_1}}{m^2_{\phi_k}} G(x_{k,1}) - \frac{m_{\psi_2}}{m^2_{\phi_k}} G(x_{k,2}) \,, \tag{11.80}$$

responsible for the suppression of Δa_μ is steeper than

$$m_{\psi_2} B_0(0, m_{\psi_2}, m_{\phi_k}) - m_{\psi_1} B_0(0, m_{\psi_1}, m_{\phi_k}) \,, \tag{11.81}$$

which causes the suppression of $|\Delta m_\mu|$. Hence, the slope of the distribution of viable points is steeper in Figure 11.20b than in Figure 11.20a.

The results for the QDF scenario are shown in Figure 11.20c and 11.20d. Again, for both choices of $|\xi|$ the central value of $\Delta a_\mu^{\text{exp}}$ can be accommodated for corrections $|\Delta m_\mu| < m_\mu$. With respect to the correlation between Δa_μ and Δm_μ we find that just as for the SFF scenario larger mediator masses yield larger accompanying corrections Δm_μ for sizeable NP effects in a_μ. We observe the same behaviour when comparing the two cases for $|\xi|$ with each other, as for suppressed left-handed interactions the slope of the distribution of viable points again is stepper than for $|\xi| = 1.00$. However, in this freeze-out scenario the viable points lie on a thin band for the latter case shown in Figure 11.20c. This is due to the very small range of y_ψ values that allow for sizeable NP contributions Δa_μ in this case, as can be seen in Figure 11.19c. In that range the ratio $\Delta a_\mu / |\Delta m_\mu|$ is approximately constant in this freeze-out scenario, leading to the thin strips of Figure 11.20c.

Note that we have also checked if equivalent contributions to the electron or tau mass are generated and found those effects to be negligibly small. Hence, we conclude that in both scenarios and for both cases of $|\xi|$ our model is capable of accommodating $\Delta a_\mu^{\text{exp}}$ without introducing fine-tuned lepton masses and a fine-tuned muon mass in particular.

Further, we stress that similar diagrams as the ones shown in Figure 11.17 induce one-loop contributions to the lepton Yukawa couplings. However, the leading contribution does not modify the Higgs decay rates to leptons as it equally affects the lepton mass and the respective Yukawa coupling. The leading processes that have an effect on the relevant decay rates suffer from an additional $v^2/m^2_{\psi_\alpha}$ suppression factor and are hence smaller than the LHC sensitivity.

[47] Recall that for maximum mixing with $m_\Psi = m_\psi$ this mass is given by $m_{\psi_2} = m_\psi - y_\psi v/\sqrt{2}$.

Chapter 12

Summary

In this part we have studied a simplified model of lepton-flavoured complex scalar DM coupling to both left- as well as right-handed leptons. The right-handed interactions between DM and leptons are mediated by a new charged Dirac fermion, while left-handed interactions are mediated by an $SU(2)_L$ doublet containing one charged and one neutral Dirac fermion. The coupling strength of both of these interactions is parametrised by a new flavour-violating 3×3 complex matrix λ, while we allow the strength of the left-handed interactions to be scaled by a complex parameter ξ. Further, the two mediator fields interact with the SM Higgs doublet through the Yukawa coupling y_ψ. We have studied this model's phenomenology by examining constraints from collider searches, LFV decays, precision tests of the SM, the DM relic density and direct as well indirect detection experiments. After performing a combined analysis of all constraints, we concluded the phenomenological analysis by studying if sizeable effects in the muon anomalous magnetic moment a_μ can be generated.

Section 11.1 was dedicated to the analysis of constraints from LHC searches for sleptons in the same-flavour final state $\ell\bar{\ell} + \not{E}_T$ with $\ell = e, \mu$. Here we found that the largest exclusion in the $m_{\psi_2} - m_{\phi_3}$ plane is obtained for maximal couplings $|\lambda_{\ell 3}| = 2.0$ to electrons and muons and a vanishing DM–tau coupling $|\lambda_{\tau 3}|$. The search we investigated excludes mediator masses up to $m_{\psi_2} \simeq 750\,\text{GeV}$ and DM masses up to $m_{\phi_3} \simeq 400\,\text{GeV}$. Further, the existence of two charged mediators in this model leads to significant exclusions in the near-degeneracy region $m_{\phi_3} \approx m_{\psi_2}$ for values $0.25 \lesssim y_\psi \lesssim 1.00$. For larger values of y_ψ these exclusions shrink with increasing couplings y_ψ.

To determine the flavour structure of λ we then studied limits from LFV decays in Section 11.2. Since in this model the mediator-Higgs Yukawa coupling y_ψ invokes enhanced contributions with an internal chirality flip, the bound on the LFV decay $\mu \to e\gamma$ yields very stringent constraints. Only if the DM–electron couplings are suppressed to lie within the range $|\lambda_{ei}| \sim \mathcal{O}(10^{-6} - 10^{-1})$, this limit allows for DM–muon couplings $|\lambda_{\mu i}| \sim \mathcal{O}(1)$, necessary to generate sizeable NP effects in a_μ. Other LFV decays place less severe restrictions on the coupling matrix λ due to weaker experimental limits.

We then turned to the analysis of the constraints that precision tests of the SM place on the parameter space of our model in Section 11.3. While we found that the EDM d_e and MDM a_e of the electron generally place constraints on the DM–electron couplings $|\lambda_{ei}|$, the resulting restrictions are very lenient if the latter couplings are already suppressed according to the limits from LFV decays. In this case the restrictions stemming from the MDM a_e are automatically satisfied, while the bound coming from the EDM d_e allows for $\mathcal{O}(1)$ imaginary parts of the scaling parameter ξ.

In Section 11.4 we examined which part of the parameter space reproduces the correct DM relic density. For both freeze-out scenarios, we here studied the two cases of suppressed and non-suppressed left-handed interactions between DM and the SM with $|\xi| = 0.01$ and $|\xi| = 1.00$, respectively. In all cases the relic density constraint allows for large couplings $|\lambda_{ij}| \sim \mathcal{O}(1)$ while the case $|\xi| = 0.01$ requires larger couplings in general since it yields a

p-wave suppressed DM annihilation rate.

The phenomenology of DM detection experiments was studied in Section 11.5. Regarding the direct detection constraints we found that the leading contribution to DM–nucleon scattering constrained by XENON1T data consists of a one-loop photon penguin diagram, proportional to the logarithm of the mass of the lepton in the loop. Hence, the largest constraints are placed on the DM–muon coupling, since the DM–electron coupling is already suppressed due to the flavour constraints. With respect to limits from indirect detection we found that in the case of non-suppressed left-handed interactions the constraints from measurements of the positron flux and the γ-ray continuum spectrum yield restrictions on λ for DM masses $m_{\phi_3} \lesssim 450\,\text{GeV}$ and $m_{\phi_3} \lesssim 600\,\text{GeV}$, respectively. The γ-ray line spectrum only places constraints on λ in the near-degeneracy region $m_{\phi_3} \approx m_{\psi_2}$. In summary, the indirect detection constraints are lenient in comparison to other limits.

To obtain a global picture of this model's viable parameter space we then performed a combined analysis in Section 11.6. Here we found that the distribution of viable points is mainly determined by flavour, relic density and direct detection constraints. In both freeze-out scenarios the case of non-suppressed left-handed interactions with $|\xi| = 1.00$ allows for smaller couplings $|\lambda_{\tau 3}|$ and $|\lambda_{\mu 3}|$ than the case with $|\xi| = 0.01$. In the SFF scenario the interplay between the flavour and relic density constraints requires the viable points to lie in a circular band in the $|\lambda_{\tau 3}| - |\lambda_{\mu 3}|$ plane. For small enough DM–tau couplings the direct detection constraints become dominant and yield a more stringent upper limit on $|\lambda_{\mu 3}|$ than the relic density limits. For the QDF scenario the direct detection constraints are dominant. In this case simultaneously small values of $|\lambda_{\tau 3}|$ and $|\lambda_{\mu 3}|$ are also viable, if the mediator mass is sufficiently small and satisfies $m_{\psi_2} \lesssim 1500\,\text{GeV}$ such that the relic density constraint can also be satisfied through annihilations of the heavier states ϕ_1 and ϕ_2 alone.

Finally, we used our results from Section 11.6 to examine if our model is able to account for the discrepancy between the SM and experiment in the muon anomalous magnetic moment a_μ in Section 11.7. To this end we calculated Δa_μ in the regions identified as viable in the combined analysis and compared it with the experimental value. We further calculated accompanying corrections Δm_μ to the muon mass and checked if sizeable effects in a_μ introduce a fine-tuned muon mass. We found that in both freeze-out scenarios the central value of $\Delta a_\mu^{\text{exp}}$ can be reached within the region of parameter space that we regard as non-fine-tuned for both cases of ξ, requiring different values for the mediator-Higgs coupling y_ψ. Noteworthy, for non-suppressed left-handed interactions larger corrections to the muon mass are generated for a given value of Δa_μ than for $|\xi| = 0.01$.

We conclude that lepton-flavoured DM with couplings to both left- and right-handed leptons accompanied by Higgs portal interactions of the corresponding mediators elegantly connects the current most convincing hints at NP: the DM problem and the muon $(g-2)$ anomaly. In spite of exhibiting a very rich phenomenology spanning over several branches of particle physics and thus being subject to many constraints, this model still allows for a joint explanation of both. Hence, it qualifies as an attractive DM candidate waiting to be further probed with increased sensitivity by future experiments.

Part V

Conclusion and Appendices

Chapter 13
Conclusion

In this thesis we have studied three simplified models of flavoured DM that all exhibit a rich phenomenology capable of ameliorating the tension between the WIMP paradigm and the absence of signal in various DM searches. This finding alone already constitutes an important global result, since it emphasises the main phenomenological advantage of flavoured DM models: the existence of multiple DM generations with couplings to the SM softens the restrictions placed on the model parameters by the observed DM relic density as well as direct detection experiments and hereby eases the pressure put on the WIMP paradigm. The mechanism that gives rise to this effect is the increased number of annihilation channels of DM that allows for a much more dynamic freeze-out phenomenology than the non-flavoured case, ultimately allowing to obtain the correct DM relic density while at the same time satisfying the strong constraints coming from direct detection experiments. While we have found this behaviour to hold true for all three models analysed in this thesis, each model also exhibited additional specific phenomenological advantages determined by the choice of the particle nature of DM and the SM fields it couples to.

In Part II of this work we studied a Majorana fermionic up-type flavoured DM model set-up in the DMFV framework. In this model DM is assumed to couple to the right-handed up-type quarks of the SM and we found the Majorana nature of DM to have a severe impact on this model's phenomenology. Aside from constraints from collider searches, this impact relaxes the restrictions placed on the model parameters by several experiments. In terms of the flavour constraints we here found that the Majorana nature gives rise to an additional box diagram for neutral D meson mixing with crossed fermion lines that destructively interferes with the usual box contribution. For the thermal freeze-out of DM the Majorana nature also proved to make a crucial difference, as Majorana specific u-channel annihilations lead to a p-wave suppression of the annihilation rate of a single dark flavour into massless final states ultimately rendering constraints from indirect detection irrelevant. Aside of its direct coupling to up quarks in this model, constraints from direct detection experiments are lenient in this case since leading contributions to DM–nucleon scattering vanish for Majorana DM with chiral interactions. In spite of strengthened constraints from LHC searches due to additional same-sign signatures, we worked out that the latter are worth investigating as they can be utilised in order to gain insights on the particle nature of quark-flavoured DM. The Majorana nature of DM in this model did not only render it a viable DM candidate with a rich phenomenology but also allowed it to reproduce large effects in CP violating charm decays as measured by the LHCb collaboration.

A simplified model of lepton-flavoured complex scalar DM was the subject of Part III. This model again belongs to the DMFV class and here we found the main phenomenological advantage to be connected to the choice of the SM fields that DM couples to—since DM interacts with the SM through the lepton portal in this model, constraints from collider searches and direct detection are weaker than in the quark-flavoured case. Regarding

LHC searches we found that for lepton-flavoured DM in general, the respective mediator is pair-produced in Drell–Yan, which ultimately yields a smaller signal cross section due to an s-channel suppression of the production rate. For DM–nucleon scattering we on the other hand found that leading contributions arise at the one-loop level and hence suffer from a loop suppression. At the same time the direct coupling of DM to leptons gives rise to stringent constraints from LFV decays and potentially strong restrictions from indirect detection experiments. Regarding the latter, the choice for the particle nature of DM turned out to be advantageous: the annihilation rate of complex scalar DM into massless fermions is p-wave suppressed which implies a severe velocity suppression of relevant annihilations for indirect detection experiments. Regarding precision tests of the SM, we found that due to purely right-handed interactions of DM with leptons, relevant restrictions only arise at NP scales already excluded by LHC searches due to the absence of chirality-flipping contributions. The interplay of these features in total proved this model to constitute a viable DM candidate with a rich phenomenology allowing for sizeable couplings of DM to leptons.

To profit from this phenomenological freedom and connect the DM problem with the $(g-2)_\mu$ anomaly, we then studied an extended version of the model from above in Part IV. Here we included an additional fermion representation, which is an $SU(2)_L$ doublet and mediates interactions between left-handed leptons and DM. Additionally, we Yukawa-coupled this new field as well as the fermion that mediates interactions between right-handed leptons and DM to the Higgs doublet to allow for chirality-flipping contributions to the anomalous magnetic moment of the muon and address the $(g-2)_\mu$ anomaly. To keep the number of parameters manageable we expressed the couplings of DM to both left- and right-handed leptons in terms of a single flavour-violating coupling matrix while allowing for a complex scaling of the coupling strength of left-handed interactions. Phenomenologically, the additional source for chirality-flipping contributions renders constraints from the LFV decay $\mu \to e\gamma$ much more restrictive and requires strongly suppressed DM–electron couplings when allowing for sizeable DM–muon couplings necessary to not preclude a solution to the $(g-2)_\mu$ anomaly. At the same time these contributions give rise to restrictions from precision measurements of dipole moments of the electron, which however are automatically satisfied once the DM–electron coupling is suppressed according to the flavour constraints. Since the additional coupling to left-handed leptons also lifts the p-wave suppression of the DM annihilation rate, constraints from indirect detection gain importance in this model, while they are still sub-leading to the bounds from LFV decays, direct detection and the DM relic density. In summary, we found that this model is capable of accommodating the experimental central value of $(g-2)_\mu$ without introducing fine-tuned lepton masses in a large part of the viable parameter space, ultimately rendering it a particularly attractive solution to the DM problem.

In conclusion, flavoured DM models provide an elegant connection of the DM problem to an aspect of the SM, which in spite of being very well described is least understood on a fundamental level: flavour. Introducing DM as a flavour triplet turns out to yield many phenomenological advantages, which depending on its particle nature and the choice of the SM fields that DM interacts with allows for a connection of the DM problem with other problems, anomalies or puzzles of particle physics. Future improved experimental sensitivities will hence hopefully be able to shed light on the properties of DM and let us *taste its flavour*.

Appendix A
Up-Type Flavoured Majorana Dark Matter

A.1 Dark Matter Relic Density

For the partial wave expansion of Equation (5.38) we find with $m_{q_k} = m_k$ and $m_{q_l} = m_l$

$$
\begin{aligned}
a = &\sum_{ijkl} \frac{3\sqrt{-2m_k^2\left(m_l^2+4m_\chi^2\right)+m_k^4+\left(m_l^2-4m_\chi^2\right)^2}}{512\pi m_\chi^4\left(m_k^2+m_l^2-2\left(m_\chi^2+m_\phi^2\right)\right)^2} \\
&\times\Big\{8m_\chi^2\left(m_k^2+m_l^2\right)\mathrm{Re}\,c_{ijkl}^{tu}-\left(m_k^2-m_l^2\right)^2\left(c_{ijkl}^{u}+c_{ijkl}^{t}\right) \\
&-16m_\chi^4\left(2\mathrm{Re}\,c_{ijkl}^{tu}-c_{ijkl}^{u}-c_{ijkl}^{t}\right)\Big\},
\end{aligned}
\tag{A.1}
$$

$$
\begin{aligned}
b = &\sum_{ijkl} \frac{\sqrt{-2m_k^2\left(m_l^2+4m_\chi^2\right)+m_k^4+\left(m_l^2-4m_\chi^2\right)^2}}{4096\pi m_\chi^4\left(m_k^2+m_l^2-2\left(m_\chi^2+m_\phi^2\right)\right)^4} \\
&\times\Big\{-4\big(-2m_k^2\big(m_l^4\left((c_{ijkl}^{t}+c_{ijkl}^{u})m_\phi^2-m_\chi^2\left(9(c_{ijkl}^{t}+c_{ijkl}^{u})+c_{ijkl}^{tu}\right)\right) \\
&-2m_l^2\big(m_\chi^4(c_{ijkl}^{t}+c_{ijkl}^{u}-16c_{ijkl}^{tu})-2(c_{ijkl}^{t}+c_{ijkl}^{u})m_\chi^2m_\phi^2+(c_{ijkl}^{t}+c_{ijkl}^{u})m_\phi^4\big) \\
&-8\big(-\left(m_\chi^6(c_{ijkl}^{t}+c_{ijkl}^{u}-12c_{ijkl}^{tu})\right)+8(c_{ijkl}^{t}+c_{ijkl}^{u})m_\chi^4m_\phi^2+(c_{ijkl}^{t}+c_{ijkl}^{u})m_\chi^2m_\phi^4\big) \\
&+3(c_{ijkl}^{t}+c_{ijkl}^{u})m_l^6\big)-2m_k^6\left(m_\chi^2\left(c_{ijkl}^{t}+c_{ijkl}^{u}+c_{ijkl}^{tu}\right)+(c_{ijkl}^{t}+c_{ijkl}^{u})\left(3m_l^2-m_\phi^2\right)\right) \\
&+2m_k^4\big(m_l^2\big(m_\chi^2\left(9(c_{ijkl}^{t}+c_{ijkl}^{u})+c_{ijkl}^{tu}\right)-(c_{ijkl}^{t}+c_{ijkl}^{u})m_\phi^2\big)+5(c_{ijkl}^{t}+c_{ijkl}^{u})m_l^4 \\
&-(c_{ijkl}^{t}+c_{ijkl}^{u})\left(9m_\chi^4+14m_\chi^2m_\phi^2+m_\phi^4\right)\big)+2m_l^6\left((c_{ijkl}^{t}+c_{ijkl}^{u})m_\phi^2\right. \\
&\left.-m_\chi^2\left(c_{ijkl}^{t}+c_{ijkl}^{u}+c_{ijkl}^{tu}\right)\right)+16m_l^2m_\chi^2\left(-m_\chi^4(c_{ijkl}^{t}+c_{ijkl}^{u}-12c_{ijkl}^{tu})\right. \\
&\left.+8(c_{ijkl}^{t}+c_{ijkl}^{u})m_\chi^2m_\phi^2+(c_{ijkl}^{t}+c_{ijkl}^{u})m_\phi^4\right)+32m_\chi^4\left(m_\chi^4(c_{ijkl}^{t}+c_{ijkl}^{u}-10c_{ijkl}^{tu})\right. \\
&\left.+6m_\chi^2m_\phi^2(c_{ijkl}^{t}+c_{ijkl}^{u}-2c_{ijkl}^{tu})+m_\phi^4(6c_{ijkl}^{tu}-7(c_{ijkl}^{t}+c_{ijkl}^{u}))\right)+(c_{ijkl}^{t}+c_{ijkl}^{u})m_k^8 \\
&-2(c_{ijkl}^{t}+c_{ijkl}^{u})m_l^4\left(9m_\chi^4+14m_\chi^2m_\phi^2+m_\phi^4\right)+(c_{ijkl}^{t}+c_{ijkl}^{u})m_l^8\big) \\
&+9\left(m_k^2+m_l^2-2\left(m_\chi^2+m_\phi^2\right)\right)^2-16m_\chi^4(c_{ijkl}^{t}+c_{ijkl}^{u}-2c_{ijkl}^{tu}) \\
&+(c_{ijkl}^{t}+c_{ijkl}^{u})\left(m_k^2-m_l^2\right)^2-8c_{ijkl}^{tu}m_\chi^2\left(m_k^2+m_l^2\right) \\
&+\frac{3\left(-16m_\chi^2\left(m_k^2+m_l^2\right)+3\left(m_k^2-m_l^2\right)^2+16m_\chi^4\right)\left(m_k^2+m_l^2-2\left(m_\chi^2+m_\phi^2\right)\right)^2}{-2m_k^2\left(m_l^2+4m_\chi^2\right)+m_k^4+\left(m_l^2-4m_\chi^2\right)^2} \\
&\times\Big(-16m_\chi^4(c_{ijkl}^{t}+c_{ijkl}^{u}-2c_{ijkl}^{tu})+(c_{ijkl}^{t}+c_{ijkl}^{u})\left(m_k^2-m_l^2\right)^2 \\
&-8c_{ijkl}^{tu}m_\chi^2\left(m_k^2+m_l^2\right)\Big)\Big\}.
\end{aligned}
\tag{A.2}
$$

A.2 Direct Detection

The Wilson coefficents f_G, $g_G^{(1)}$ and $g_G^{(2)}$ from Equation (5.63) read [165]

$$
\begin{aligned}
f_G = \sum_{i=u,c,t} \alpha_s |\tilde{\lambda}_{i3}|^2 m_{\chi_3} \Big[& -12 m_i^2 m_\phi^4 m_{\chi_3}^2 (m_i^2 - m_\phi^2 + m_{\chi_3}^2) \Lambda_i(m_{\chi_3}^2; m_i, m_\phi) \\
& - (m_i - m_\phi - m_{\chi_3})(m_i + m_\phi - m_{\chi_3})(m_i - m_\phi + m_{\chi_3}) \\
& \times (m_i + m_\phi + m_{\chi_3}) \{ m_i^6 - 3 m_i^4 (2 m_\phi^2 + m_{\chi_3}^2) \\
& + m_i^2 (3 m_\phi^4 + 2 m_\phi^2 m_{\chi_3}^2 + 3 m_{\chi_3}^4) + (m_\phi^2 - m_{\chi_3}^2)^2 (2 m_\phi^2 - m_{\chi_3}^2) \} \Big] \\
& \times \frac{(m_i - m_\phi + m_{\chi_3})^{-3} (m_i + m_\phi + m_{\chi_3})^{-3}}{192 \pi m_\phi^2 (m_i - m_\phi - m_{\chi_3})^3 (m_i + m_\phi - m_{\chi_3})^3} \,,
\end{aligned}
\tag{A.3}
$$

$$
\begin{aligned}
\frac{g_G^{(2)}}{m_{\chi_3}^2} = \sum_{i=u,c,t} \alpha_s |\tilde{\lambda}_{i3}|^2 \Big[& 2 m_{\chi_3}^2 \{ 10 m_{\chi_3}^4 (m_i^6 - m_\phi^6) + m_{\chi_3}^8 (m_i^2 - 5 m_\phi^2) - 5 m_{\chi_3}^2 (m_i^2 - m_\phi^2)^3 \\
& \times (m_i^2 + m_\phi^2) + (m_i^2 - m_\phi^2)^5 + 2 m_{\chi_3}^6 (-4 m_i^4 + 2 m_i^2 m_\phi^2 + 5 m_\phi^4) + m_{\chi_3}^{10} \} \\
& \times \Lambda_i(m_{\chi_3}^2; m_i, m_\phi) - (m_i - m_\phi - m_{\chi_3})(m_i + m_\phi - m_{\chi_3})(m_i - m_\phi + m_{\chi_3}) \\
& \times (m_i + m_\phi + m_{\chi_3}) \Big\{ 7 m_{\chi_3}^4 (m_i^4 - m_\phi^4) - 2 m_{\chi_3}^6 (m_i^2 - 4 m_\phi^2) - 2 m_{\chi_3}^2 (m_i^2 - m_\phi^2)^3 \\
& + 2 (m_i^4 - 2 m_i^2 (m_\phi^2 + m_{\chi_3}^2) + (m_\phi^2 - m_{\chi_3}^2)^2)^2 \log\left(\frac{m}{m_\phi}\right) - 3 m_{\chi_3}^8 \Big\} \Big] \\
& \times \frac{(m_i - m_\phi + m_{\chi_3})^{-3} (m_i + m_\phi + m_{\chi_3})^{-3}}{48 \pi m_{\chi_3}^5 (m_i - m_\phi - m_{\chi_3})^3 (m_i + m_\phi - m_{\chi_3})^3} \,,
\end{aligned}
\tag{A.4}
$$

$$
\begin{aligned}
\frac{g_G^{(1)}}{m_{\chi_3}} = \sum_{i=u,c,t} \alpha_s |\tilde{\lambda}_{i3}|^2 \Big[& 2 m_{\chi_3}^2 (3 m_{\chi_3}^2 (m_\phi^4 - m_i^4) + m_{\chi_3}^4 (5 m_i^2 + m_\phi^2) + (m_i^2 - m_\phi^2)^3 - 3 m_{\chi_3}^6) \\
& \times \Lambda_i(m_{\chi_3}^2; m_i, m_\phi) + 2 (m_i + m_\phi - m_{\chi_3})(m_i - m_\phi + m_{\chi_3})(m_i + m_\phi + m_{\chi_3}) \\
& \Big\{ m_{\chi_3}^2 (m_i - m_\phi - m_{\chi_3})(m_i^2 - m_\phi^2 - 3 m_{\chi_3}^2) - (m_i + m_\phi - m_{\chi_3})(m_i - m_\phi + m_{\chi_3}) \\
& \times (-m_i + m_\phi + m_{\chi_3})^2 (m_i + m_\phi + m_{\chi_3}) \log\left(\frac{m_i}{m_\phi}\right) \Big\} \Big] \\
& \times \frac{(-m_i + m_\phi + m_{\chi_3})^{-2} (m_i + m_\phi + m_{\chi_3})^{-2}}{192 \pi m_{\chi_3}^4 (m_i + m_\phi - m_{\chi_3})^2 (m_i - m_\phi + m_{\chi_3})^2} \,,
\end{aligned}
\tag{A.5}
$$

with

$$
\begin{aligned}
\Lambda_i(m_{\chi_3}^2; m_i, m_\phi) &= \frac{\lambda_i}{m_{\chi_3}^2} \log\left(\frac{m_i^2 + \lambda_i + m_\phi^2 - m_{\chi_3}^2}{2 m_i m_\phi} \right) \\
\lambda_i &= \sqrt{m_i^4 - 2 m_i^2 m_\phi^2 - 2 m_i^2 m_{\chi_3}^2 + m_\phi^4 - 2 m_\phi^2 m_{\chi_3}^2 + m_{\chi_3}^4} \,.
\end{aligned}
\tag{A.6}
$$

Appendix B

Lepton-Flavoured Scalar Dark Matter I

B.1 Dark Matter Relic Density

The coefficients from the partial wave expansion of the thermal averaged annihilation cross section from Equation (8.23) with the full final state mass dependence read

$$
\begin{aligned}
a = \sum_{ijkl} |\lambda_{ik}|^2 |\lambda_{jl}|^2 & \frac{\sqrt{-2m_{\ell_k}^2\left(m_{\ell_l}^2+4m_\phi^2\right)+m_{\ell_k}^4+\left(m_{\ell_l}^2-4m_\phi^2\right)^2}}{128\pi m_\phi^4\left(m_{\ell_k}^2+m_{\ell_l}^2-2m_\psi^2-2m_\phi^2\right)^2} \\
& \times \left(4m_\phi^2\left(m_{\ell_k}^2+m_{\ell_l}^2\right)-6m_{\ell_k}^2 m_{\ell_l}^2+m_{\ell_k}^4+m_{\ell_l}^4\right) , \qquad \text{(B.1)}
\end{aligned}
$$

$$
\begin{aligned}
b = \sum_{ijkl} |\lambda_{ik}|^2 |\lambda_{jl}|^2 & \frac{\sqrt{-2m_{\ell_k}^2\left(m_{\ell_l}^2+4m_\phi^2\right)+m_{\ell_k}^4+\left(m_{\ell_l}^2-4m_\phi^2\right)^2}}{3072\pi m_\phi^4\left(m_{\ell_k}^2+m_{\ell_l}^2-2m_\psi^2-2m_\phi^2\right)^4} \\
& \times \Bigg\{ 3\left(-4m_\phi^2\left(m_{\ell_k}^2+m_{\ell_l}^2\right)+6m_{\ell_k}^2 m_{\ell_l}^2+m_{\ell_k}^4+m_{\ell_l}^4\right)\left(m_{\ell_k}^2+m_{\ell_l}^2-2m_\psi^2-2m_\phi^2\right)^2 \\
& - \frac{3\left(-16m_\phi^2\left(m_{\ell_k}^2+m_{\ell_l}^2\right)+3\left(m_{\ell_k}^2-m_{\ell_l}^2\right)^2+16m_\phi^4\right)}{-2m_{\ell_l}^2\left(m_{\ell_k}^2+4m_\phi^2\right)+\left(m_{\ell_k}^2-4m_\phi^2\right)^2+m_{\ell_l}^4} \\
& \times \left(4m_\phi^2\left(m_{\ell_k}^2+m_{\ell_l}^2\right)-6m_{\ell_k}^2 m_{\ell_l}^2-m_{\ell_k}^4-m_{\ell_l}^4\right)\left(m_{\ell_k}^2+m_{\ell_l}^2-2m_\psi^2-2m_\phi^2\right)^2 \\
& + 8\Bigg[-\left(m_{\ell_k}^2-m_{\ell_l}^2\right)^2\left(m_\psi^2\left(m_{\ell_k}^2+m_{\ell_l}^2\right)+3m_{\ell_k}^2 m_{\ell_l}^2+m_\psi^4\right) \\
& + 8m_\phi^6\left(8m_\psi^2-7\left(m_{\ell_k}^2+m_{\ell_l}^2\right)\right) \\
& + m_\phi^4\left(-96m_\psi^2\left(m_{\ell_k}^2+m_{\ell_l}^2\right)+66m_{\ell_k}^2 m_{\ell_l}^2+31m_{\ell_k}^4+31m_{\ell_l}^4+32m_\psi^4\right) \\
& + 2m_\phi^2\Bigg(4m_\psi^4\left(m_{\ell_k}^2+m_{\ell_l}^2\right)+m_\psi^2\left(46m_{\ell_k}^2 m_{\ell_l}^2+9m_{\ell_k}^4+9m_{\ell_l}^4\right) \\
& - 2\left(m_{\ell_k}^2+m_{\ell_l}^2\right)\left(4m_{\ell_k}^2 m_{\ell_l}^2+m_{\ell_k}^4+m_{\ell_l}^4\right)\Bigg)+32m_\phi^8\Bigg]\Bigg\} . \qquad \text{(B.2)}
\end{aligned}
$$

Appendix C

Lepton-Flavoured Scalar Dark Matter II

C.1 Dark Matter Relic Density

The functions $A_{ijkl}, B_{ijkl}, C_{kl}$ and D_{kl} from Equations (11.37)–(11.40) read

$$A_{ijkl} = (m_{\phi_j}^2 - m_{\ell_l}^2 - t)(t + m_{\ell_k}^2 - m_{\phi_i}^2) - t(s - m_{\ell_k}^2 - + m_{\ell_l}^2)\,, \tag{C.1}$$

$$B_{ijkl} = \xi^* m_{\ell_l}(m_{\phi_i}^2 - m_{\ell_k}^2 - t) + \xi m_{\ell_k}(m_{\phi_j}^2 - m_{\ell_l}^2 - t)\,, \tag{C.2}$$

$$C_{kl} = -2 m_{\ell_k} m_{\ell_l} t\,, \tag{C.3}$$

$$D_{kl} = 2|\xi|^2(s - m_{\ell_k}^2 - m_{\ell_l}^2) - 2 m_{\ell_k} m_{\ell_l}\left(\xi^{*2} + \xi^2\right)\,. \tag{C.4}$$

The p-wave contribution to the thermally averaged annihilation cross section from Equation (11.41) for $\xi \neq 0$ is given by

$$\begin{aligned} b =& \frac{1}{9}\sum_{ijkl}\frac{|\lambda_{ik}|^2|\lambda_{jl}|^2}{32\pi m_{\phi_3}^2}\Bigg\{\frac{\left(2+\mu_2^2+\mu_1^2+\left(\mu_1^2-\mu_2^2\right)\cos 2\theta_\psi\right)^2}{\left(1+\mu_2^2\right)^2\left(1+\mu_1^2\right)^2} \\ &- \frac{|\xi|^2\sin^2 2\theta_\psi(\mu_2-\mu_1)^2}{(1+\mu_2^2)^4(1+\mu_1^2)^4}\Big[3\left(\mu_2^6+6\mu_2^4+\mu_1^2\right)\mu_2^6 \\ &+ 2\mu_1\left(\mu_1^2-5\right)\left(3\mu_1^2+1\right)\mu_2^5+\left(18\mu_1^6+31\mu_1^4+4\mu_1^2+3\right)\mu_2^4 \\ &- 4\mu_1\left(7\mu_1^4+26\mu_1^2+7\right)\mu_2^3+\left(3\mu_1^6+4\mu_1^4+31\mu_1^2+18\right)\mu_2^2 \\ &- 2\mu_1\left(\mu_1^2+3\right)\left(5\mu_1^2-1\right)\mu_2+3\mu_1^2\left(\mu_1^2+6\right)+3\Big] \\ &+ 4|\xi|^4\Bigg[\frac{\cos^4(\theta_\psi)}{\left(\mu_1^2+1\right)^2}+\frac{\sin^2(\theta_\psi)}{\left(\mu_2^2+1\right)^2}\Bigg(\frac{2\left(\mu_2^2+1\right)\cos^2(\theta_\psi)}{\mu_1^2+1} \\ &+ \sin^2(\theta_\psi)\Bigg)+\frac{1}{\left(\mu_0^2+1\right)^2}\Bigg]\Bigg\}\,, \end{aligned} \tag{C.5}$$

in the limit of equal initial state masses and vanishing final state masses. Here we have used $\mu_\alpha = m_{\psi_\alpha}/m_{\phi_3}$.

C.2 Direct Detection

The averaged DM–nucleon cross section for t-channel scatterings through the Higgs portal reads [194]

$$\sigma_{\mathrm{SI}}^{H\phi} = \frac{\lambda_{H\phi}^2 y_N^2}{4\pi}\frac{\mu^2 m_N^2}{m_H^4 m_{\phi_3}^2}\,, \tag{C.6}$$

where m_N is the nucleon mass and $\mu = m_{\phi_3} m_N/(m_{\phi_3}+m_N)$ is the reduced mass of the DM–nucleon system. In order to estimate in which parts of the parameter space these

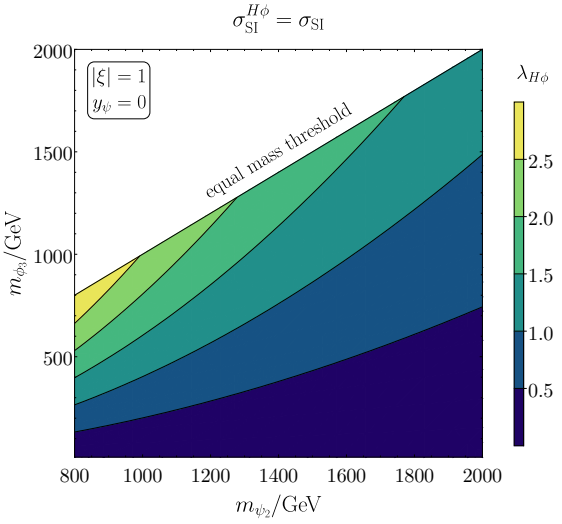

Figure C.1 | Maximum allowed values of $\lambda_{H\phi}$ in order to give at most equal contributions to the DM–nucleon scattering cross section as the photon penguin diagram.

contributions grow larger than the photon one-loop penguin from Figure 11.10a, we fix the couplings to $|\lambda_{i3}| = 2$ and $|\xi| = 1$ as well as $y_\psi = 0$ in Equation (11.53) and assume maximum mixing with $\theta_\psi = \pi/4$. Comparing the scattering rate from Equation (11.53) with the one in Equation (C.6) then gives the maximum allowed value of the Higgs portal coupling $\lambda_{H\phi}$ for at most equal scattering cross sections. This illustrated by the contours shown in Figure C.1.

C.3 Indirect Detection

The expression for the interference term of ψ_1 and ψ_2 for the internal bremsstrahlung process of Figure 11.12a is given by

$$
\begin{aligned}
\langle\sigma v\rangle^{12}_{\ell\bar{\ell}\gamma} = \sum_{ij} \frac{-\alpha_{\mathrm{em}}|\lambda_{i3}|^2|\lambda_{j3}|^2\left(c_\theta^2+|\xi|^2 s_\theta^2\right)\left(s_\theta^2+|\xi|^2 c_\theta^2\right)}{128 m_{\phi_3}^2\pi^2(\mu_2-\mu_1)^2}\Big\{ & -4p_1\mu_2(1+\mu_2)^2 \\
& + 4p_2\mu_2(1+\mu_2)^2 - 2(\mu_2-\mu_1)^2 - 4p_3\mu_1(1+\mu_1)^2 + 4p_4\mu_1(1+\mu_1)^2 \\
& + p_5(\mu_2+\mu_1)(2+\mu_2(2+\mu_2)+\mu_1(2+\mu_1)) \\
& - p_6(\mu_2+\mu_1)(2+\mu_2(2+\mu_2)+\mu_1(2+\mu_1)) \\
& + p_7(\mu_2+\mu_1)(2+\mu_2(2+\mu_2)+\mu_1(2+\mu_1)) \\
& - p_8(\mu_2+\mu_1)(2+\mu_2(2+\mu_2)+\mu_1(2+\mu_1)) + \mu_2^3(4l_1^2 - l_2l_3 + l_3l_4 - 3l_5 - l_3l_5 \\
& + l_4l_5 + 4l_5l_6 + l_1(3+l_2+l_3-2l_4-4l_5-4l_6-l_8) + l_5l_8) + \mu_2^2(8l_1^2 \\
& - 2l_2(1+l_3) + 2l_4(1+l_3+l_5) - 2l_5(l_3-4l_6) + 2l_1(l_2+l_3-2(l_4+2(l_5+l_6))) \\
& - l_1l_9 + l_5l_9 \\
& + (-l_2(-2+l_3) + l_1(-1+l_2+l_3-2l_4) + (-2+l_3)l_4 + (1-l_3+l_4)l_5)\mu_1) \\
& + \mu_2(4l_1^2 - l_2(3+2l_3) + 2l_3l_4 - 2l_3l_5 + 2l_4l_5 \ + 3(l_4+l_5) + 4l_5l_6 \\
& + l_1(-3+2l_2+2l_3-4l_4-4l_5-4l_6-l_8) + l_5l_8 + \mu_1(2(l_2-2l_2l_3 \\
& + l_1(-1+2l_2+2l_3-4l_4) - l_4 + 2l_3l_4 + l_5 - 2l_3l_5 + 2l_4l_5) \\
& + (l_2 - l_2l_3 + l_1(-2+l_2+l_3-2l_4) + (-1+l_3)l_4 + (2-l_3+l_4)l_5)\mu_1))
\end{aligned}
$$

$$
\begin{aligned}
&+\mu_1(l_1(3+2l_2+2l_3-4l_4)+2l_3l_4+4l_4^2-2l_3l_5+2l_4l_5-3(l_4+l_5)\\
&-4l_4l_7-l_4l_8+l_2(3-2l_3-4l_4+4l_7+l_8)+\mu_1(2l_1(1+l_2+l_3-2l_4)\\
&-2(l_5+l_3(-l_4+l_5)+l_2(l_3+4l_4-4l_7)-l_4(4l_4+l_5-4l_7))+(l_2-l_4)l_9\\
&+(l_1(l_3-2l_4)+3l_4+l_3l_4+4l_4^2-l_3l_5+l_4l_5-4l_4l_7-l_4l_8+\\
&l_2(-3+l_1-l_3-4l_4+4l_7+l_8))\mu_1))\Big\}\,,
\end{aligned}
\tag{C.7}
$$

with the logarithms l_i and polylogarithms p_i defined as

$$
\begin{aligned}
&l_1=\log(1+\mu_2)\,, \quad l_2=\log(\mu_1-1)\,, \quad l_3=\log(\mu_2+\mu_1)\,,\\
&l_4=\log(1+\mu_1)\,, \quad l_5=\log(\mu_2-1)\,, \quad l_6=\log(\mu_2)\,,\\
&l_7=\log(\mu_1)\,, \qquad l_8=\log(16)\,, \qquad l_9=\log(256)\,,
\end{aligned}
\tag{C.8}
$$

and

$$
\begin{aligned}
&p_1=\mathrm{Li}_2\left(\frac{\mu_2-1}{2\mu_2}\right)\,, \quad p_2=\mathrm{Li}_2\left(\frac{1+\mu_2}{2\mu_2}\right)\,, \quad p_3=\mathrm{Li}_2\left(\frac{\mu_1-1}{2\mu_1}\right)\,,\\
&p_4=\mathrm{Li}_2\left(\frac{1+\mu_1}{2\mu_1}\right)\,, \quad p_5=\mathrm{Li}_2\left(\frac{\mu_2-1}{\mu_2+\mu_1}\right)\,, \quad p_6=\mathrm{Li}_2\left(\frac{1+\mu_2}{\mu_2+\mu_1}\right)\,,\\
&p_7=\mathrm{Li}_2\left(\frac{\mu_1-1}{\mu_2+\mu_1}\right)\,, \quad p_8=\mathrm{Li}_2\left(\frac{1+\mu_1}{\mu_2+\mu_1}\right)\,.
\end{aligned}
\tag{C.9}
$$

The constraint coming from indirect detection experiments for the case of suppressed left-handed interactions is shown in Figure C.2.

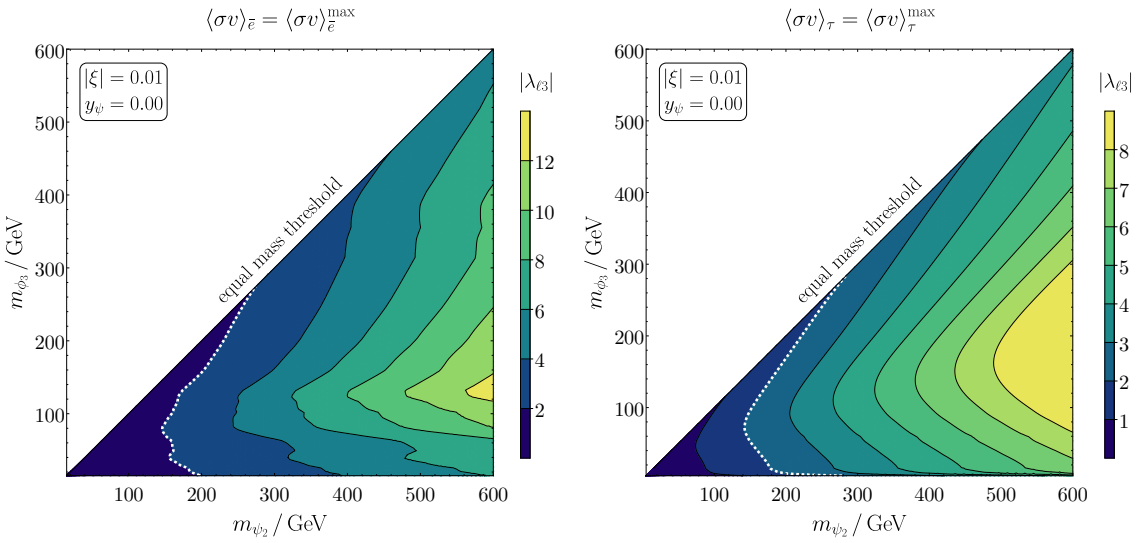

(a) constraints from the positron flux

(b) constraints from the γ continuum spectrum

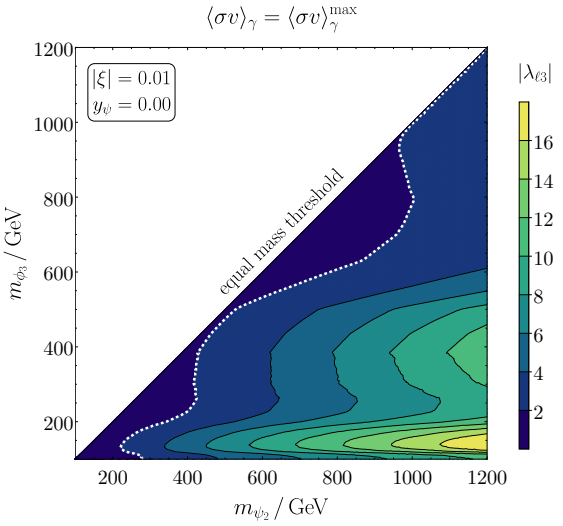

(c) constraints from the γ line spectrum

Figure C.2 | Restrictions on the model parameters from indirect detection experiments for suppressed left-handed interactions. In all three panels we have assumed maximum mixing with $\theta_\psi = \pi/4$. The area included by the white dashed line and the equal mass diagonal indicates in which mass regime the constraints are relevant.

Bibliography

[1] G. Bertone, D. Hooper and J. Silk, *Particle dark matter: Evidence, candidates and constraints*, *Phys. Rept.* **405** (2005) 279 [hep-ph/0404175].

[2] Planck collaboration, *Planck 2018 results. VI. Cosmological parameters*, *Astron. Astrophys.* **641** (2020) A6 [1807.06209].

[3] J. Kile and A. Soni, *Flavored Dark Matter in Direct Detection Experiments and at LHC*, *Phys. Rev. D* **84** (2011) 035016 [1104.5239].

[4] J. F. Kamenik and J. Zupan, *Discovering Dark Matter Through Flavor Violation at the LHC*, *Phys. Rev. D* **84** (2011) 111502 [1107.0623].

[5] B. Batell, J. Pradler and M. Spannowsky, *Dark Matter from Minimal Flavor Violation*, *JHEP* **08** (2011) 038 [1105.1781].

[6] P. Agrawal, S. Blanchet, Z. Chacko and C. Kilic, *Flavored Dark Matter, and Its Implications for Direct Detection and Colliders*, *Phys. Rev. D* **86** (2012) 055002 [1109.3516].

[7] B. Batell, T. Lin and L.-T. Wang, *Flavored Dark Matter and R-Parity Violation*, *JHEP* **01** (2014) 075 [1309.4462].

[8] J. Kile, *Flavored Dark Matter: A Review*, *Mod. Phys. Lett. A* **28** (2013) 1330031 [1308.0584].

[9] J. Kile, A. Kobach and A. Soni, *Lepton-Flavored Dark Matter*, *Phys. Lett. B* **744** (2015) 330 [1411.1407].

[10] L. Lopez-Honorez and L. Merlo, *Dark matter within the minimal flavour violation ansatz*, *Phys. Lett. B* **722** (2013) 135 [1303.1087].

[11] A. Kumar and S. Tulin, *Top-flavored dark matter and the forward-backward asymmetry*, *Phys. Rev. D* **87** (2013) 095006 [1303.0332].

[12] Y. Zhang, *Top Quark Mediated Dark Matter*, *Phys. Lett. B* **720** (2013) 137 [1212.2730].

[13] G. Arcadi, M. Dutra, P. Ghosh, M. Lindner, Y. Mambrini, M. Pierre et al., *The waning of the WIMP? A review of models, searches, and constraints*, *Eur. Phys. J. C* **78** (2018) 203 [1703.07364].

[14] A. J. Buras, P. Gambino, M. Gorbahn, S. Jager and L. Silvestrini, *Universal unitarity triangle and physics beyond the standard model*, *Phys. Lett. B* **500** (2001) 161 [hep-ph/0007085].

[15] G. D'Ambrosio, G. F. Giudice, G. Isidori and A. Strumia, *Minimal flavor violation: An Effective field theory approach*, *Nucl. Phys. B* **645** (2002) 155 [hep-ph/0207036].

[16] A. J. Buras, *Minimal flavor violation*, *Acta Phys. Polon. B* **34** (2003) 5615 [hep-ph/0310208].

[17] R. S. Chivukula and H. Georgi, *Composite Technicolor Standard Model*, *Phys. Lett. B* **188** (1987) 99.

[18] L. J. Hall and L. Randall, *Weak scale effective supersymmetry*, *Phys. Rev. Lett.* **65** (1990) 2939.

[19] V. Cirigliano, B. Grinstein, G. Isidori and M. B. Wise, *Minimal flavor violation in the lepton sector*, *Nucl. Phys. B* **728** (2005) 121 [hep-ph/0507001].

[20] P. Agrawal, M. Blanke and K. Gemmler, *Flavored dark matter beyond Minimal Flavor Violation*, *JHEP* **10** (2014) 072 [1405.6709].

[21] M. Blanke and S. Kast, *Top-Flavoured Dark Matter in Dark Minimal Flavour Violation*, *JHEP* **05** (2017) 162 [1702.08457].

[22] M. Blanke, S. Das and S. Kast, *Flavoured Dark Matter Moving Left*, *JHEP* **02** (2018) 105 [1711.10493].

[23] T. Jubb, M. Kirk and A. Lenz, *Charming Dark Matter*, *JHEP* **12** (2017) 010 [1709.01930].

[24] M.-C. Chen, J. Huang and V. Takhistov, *Beyond Minimal Lepton Flavored Dark Matter*, *JHEP* **02** (2016) 060 [1510.04694].

[25] LHCb collaboration, *Observation of CP Violation in Charm Decays*, *Phys. Rev. Lett.* **122** (2019) 211803 [1903.08726].

[26] Muon g-2 collaboration, *Measurement of the Positive Muon Anomalous Magnetic Moment to 0.46 ppm*, *Phys. Rev. Lett.* **126** (2021) 141801 [2104.03281].

[27] T. Aoyama et al., *The anomalous magnetic moment of the muon in the Standard Model*, *Phys. Rept.* **887** (2020) 1 [2006.04822].

[28] G. Bertone, D. Hooper and J. Silk, *Particle Dark Matter: Observations, Models and Searches*. Cambridge Univ. Press, Cambridge, 2010, 10.1017/CBO9780511770739.

[29] G. Bertone and D. Hooper, *History of dark matter*, *Rev. Mod. Phys.* **90** (2018) 045002 [1605.04909].

[30] V. C. Rubin and W. K. Ford, Jr., *Rotation of the Andromeda Nebula from a Spectroscopic Survey of Emission Regions*, *Astrophys. J.* **159** (1970) 379.

[31] K. C. Freeman, *On the disks of spiral and SO Galaxies*, *Astrophys. J.* **160** (1970) 811.

[32] R. N. Whitehurst and M. S. Roberts, *High-Velocity Neutral Hydrogen in the Central Region of the Andromeda Galaxy*, *Astrophys. J.* **175** (1972) 347.

[33] D. H. Rogstad and G. S. Shostak, *Gross Properties of Five Scd Galaxies as Determined from 21-CENTIMETER Observations*, *Astrophys. J.* **176** (1972) 315.

[34] M. S. Roberts and A. H. Rots, *Comparison of Rotation Curves of Different Galaxy Types*, *Astron. Astrophys.* **26** (1973) 483.

[35] J. Einasto, A. Kaasik and E. Saar, *Dynamic evidence on massive coronas of galaxies*, *Nature* **250** (1974) 309.

[36] J. P. Ostriker, P. J. E. Peebles and A. Yahil, *The Size and Mass of Galaxies, and the Mass of the Universe*, *Astrophys. J. Lett.* **193** (1974) L1.

[37] M. S. Roberts and R. N. Whitehurst, *The rotation curve and geometry of M31 at large galactocentric distances.*, *Astrophys. J.* **201** (1975) 327.

[38] E. E. Salpeter, *Rotation Curves in the Outer Parts of Galaxies from HI Observations*, in *Structure and Properties of Nearby Galaxies*, E. M. Berkhuijsen and R. Wielebinski, eds., vol. 77, p. 23, Jan., 1978.

[39] A. Bosma, *The distribution and kinematics of neutral hydrogen in spiral galaxies of various morphological types*, Ph.D. thesis, University of Groningen, Netherlands, Mar., 1978.

[40] V. C. Rubin, W. K. Ford, Jr. and N. Thonnard, *Extended rotation curves of high-luminosity spiral galaxies. IV. Systematic dynamical properties, Sa through Sc*, *Astrophys. J. Lett.* **225** (1978) L107.

[41] E. V. Karukes, P. Salucci and G. Gentile, *The dark matter distribution in the spiral NGC 3198 out to 0.22 R_{vir}*, *Astron. Astrophys.* **578** (2015) A13 [1503.04049].

[42] J. F. Navarro, C. S. Frenk and S. D. M. White, *The Structure of cold dark matter halos*, *Astrophys. J.* **462** (1996) 563 [astro-ph/9508025].

[43] G. Gentile, G. I. G. Jozsa, P. Serra, G. H. Heald, W. J. G. de Blok, F. Fraternali et al., *HALOGAS: Extraplanar gas in NGC 3198*, *Astron. Astrophys.* **554** (2013) A125 [1304.4232].

[44] M. Markevitch, *Chandra observation of the most interesting cluster in the universe*, *ESA Spec. Publ.* **604** (2006) 723 [astro-ph/0511345].

[45] D. Clowe, M. Bradac, A. H. Gonzalez, M. Markevitch, S. W. Randall, C. Jones et al., *A direct empirical proof of the existence of dark matter*, *Astrophys. J. Lett.* **648** (2006) L109 [astro-ph/0608407].

[46] F. Zwicky, *Die Rotverschiebung von extragalaktischen Nebeln*, *Helv. Phys. Acta* **6** (1933) 110.

[47] B. Ryden, *Introduction to cosmology*. Cambridge University Press, 1970, 10.1017/9781316651087.

[48] S. Profumo, *An Introduction to Particle Dark Matter*. World Scientific, 2017, 10.1142/q0001.

[49] K. Freese, *Status of Dark Matter in the Universe*, *Int. J. Mod. Phys.* **1** (2017) 325 [1701.01840].

[50] A. Berlin, D. Hooper, G. Krnjaic and S. D. McDermott, *Severely Constraining Dark Matter Interpretations of the 21-cm Anomaly*, *Phys. Rev. Lett.* **121** (2018) 011102 [1803.02804].

[51] C. Creque-Sarbinowski, L. Ji, E. D. Kovetz and M. Kamionkowski, *Direct millicharged dark matter cannot explain the EDGES signal*, *Phys. Rev. D* **100** (2019) 023528 [1903.09154].

[52] CDF collaboration, *The Collider Detector at Fermilab (CDF)*, *IEEE Trans. Nucl. Sci.* **33** (1986) 40.

[53] CDF collaboration, *The CDF Detector: An Overview*, *Nucl. Instrum. Meth. A* **271** (1988) 387.

[54] D0 collaboration, *The D0 Detector*, *Nucl. Instrum. Meth. A* **338** (1994) 185.

[55] D0 collaboration, *The Upgraded D0 detector*, *Nucl. Instrum. Meth. A* **565** (2006) 463 [physics/0507191].

[56] Belle-II collaboration, *Belle II Technical Design Report*, 1011.0352.

[57] ALEPH collaboration, *ALEPH: A detector for electron-positron annnihilations at LEP*, *Nucl. Instrum. Meth. A* **294** (1990) 121.

[58] DELPHI collaboration, *The DELPHI detector at LEP*, *Nucl. Instrum. Meth. A* **303** (1991) 233.

[59] L3 collaboration, *The Construction of the L3 Experiment*, *Nucl. Instrum. Meth. A* **289** (1990) 35.

[60] OPAL collaboration, *The OPAL detector at LEP*, *Nucl. Instrum. Meth. A* **305** (1991) 275.

[61] ATLAS collaboration, *The ATLAS Experiment at the CERN Large Hadron Collider*, *JINST* **3** (2008) S08003.

[62] CMS collaboration, *The CMS Experiment at the CERN LHC*, *JINST* **3** (2008) S08004.

[63] LHCb collaboration, *The LHCb Detector at the LHC*, *JINST* **3** (2008) S08005.

[64] CDEX collaboration, *Introduction to the CDEX experiment*, *Front. Phys. (Beijing)* **8** (2013) 412 [1303.0601].

[65] SuperCDMS collaboration, *Low-mass dark matter search with CDMSlite*, *Phys. Rev. D* **97** (2018) 022002 [1707.01632].

[66] SuperCDMS collaboration, *The SuperCDMS Experiment*, in *5th International Heidelberg Conference on Dark Matter in Astro and Particle Physics*, 2, 2005, astro-ph/0502435.

[67] COSINE-100 collaboration, *Dark Matter Searches with the COSINE-100 Experiment*, *J. Phys. Conf. Ser.* **1468** (2020) 012066.

[68] CRESST collaboration, *The CRESST dark matter search*, *Astropart. Phys.* **12** (1999) 107 [hep-ex/9904005].

[69] DAMA collaboration, *The DAMA/LIBRA apparatus*, *Nucl. Instrum. Meth. A* **592** (2008) 297 [0804.2738].

[70] DAMIC collaboration, *The DAMIC dark matter experiment*, *PoS* **ICRC2015** (2016) 1221 [1510.02126].

[71] DAMIC-M collaboration, *DAMIC-M Experiment: Thick, Silicon CCDs to search for Light Dark Matter*, *Nucl. Instrum. Meth. A* **958** (2020) 162933 [2001.01476].

[72] DarkSide collaboration, *Low-Mass Dark Matter Search with the DarkSide-50 Experiment*, *Phys. Rev. Lett.* **121** (2018) 081307 [1802.06994].

[73] DEAP-3600 collaboration, *The DEAP-3600 Experiment*, *PoS* **ICRC2021** (2021) 527.

[74] DARWIN collaboration, *DARWIN: towards the ultimate dark matter detector*, *JCAP* **11** (2016) 017 [1606.07001].

[75] PICASSO collaboration, *The PICASSO dark matter search project*, *PoS* **IDM2008** (2008) 010.

[76] PICO collaboration, *Dark Matter Search Results from the PICO-60 C_3F_8 Bubble Chamber*, *Phys. Rev. Lett.* **118** (2017) 251301 [1702.07666].

[77] EDELWEISS collaboration, *The EDELWEISS experiment and Dark Matter Direct Detection*, in *Proceedings of the 5th Patras Workshop on Axions, WIMPs and WISPs (PATRAS 2009)*, 6, 2003, astro-ph/0306233.

[78] EDELWEISS collaboration, *Dark matter searches with the experiment EDELWEISS-II*, in *12th Marcel Grossmann Meeting on General Relativity*, pp. 879–881, 7, 2009, DOI.

[79] EDELWEISS collaboration, *The EDELWEISS-III Dark Matter Search: Status and Perspectives*, in *20th International Conference on Particles and Nuclei*, pp. 378–381, 9, 2014, DOI.

[80] LUX collaboration, *The Large Underground Xenon (LUX) Experiment*, *Nucl. Instrum. Meth. A* **704** (2013) 111 [1211.3788].

[81] LZ collaboration, *The LUX-ZEPLIN (LZ) Experiment*, *Nucl. Instrum. Meth. A* **953** (2020) 163047 [1910.09124].

[82] NEWS-G collaboration, *The search for light dark matter with the NEWS-G spherical proportional counter*, *J. Phys. Conf. Ser.* **1312** (2019) 012008.

[83] PandaX collaboration, *PandaX: A Liquid Xenon Dark Matter Experiment at CJPL*, *Sci. China Phys. Mech. Astron.* **57** (2014) 1476 [1405.2882].

[84] PandaX-II collaboration, *Progress and Prospect of PandaX Experiment*, *Nucl. Phys. Rev.* **34** (2017) 290.

[85] PandaX collaboration, *Dark matter direct search sensitivity of the PandaX-4T experiment*, *Sci. China Phys. Mech. Astron.* **62** (2019) 31011 [1806.02229].

[86] XENON100 collaboration, *The XENON100 Dark Matter Experiment*, *Astropart. Phys.* **35** (2012) 573 [1107.2155].

[87] XENON1T collaboration, *The XENON1T Dark Matter Search Experiment*, *Springer Proc. Phys.* **148** (2013) 93 [1206.6288].

[88] MAGIC collaboration, *The MAGIC telescope*, *Nucl. Phys. B Proc. Suppl.* **114** (2003) 247.

[89] VERITAS collaboration, *The first VERITAS telescope*, *Astropart. Phys.* **25** (2006) 391 [astro-ph/0604119].

[90] HAWC collaboration, *The HAWC observatory*, *Nucl. Instrum. Meth. A* **692** (2012) 72.

[91] IceCube collaboration, *The IceCube Neutrino Observatory: Instrumentation and Online Systems*, *JINST* **12** (2017) P03012 [1612.05093].

[92] ANTARES collaboration, *ANTARES: the first undersea neutrino telescope*, *Nucl. Instrum. Meth. A* **656** (2011) 11 [1104.1607].

[93] Super-Kamiokande collaboration, *The Super-Kamiokande detector*, *Nucl. Instrum. Meth. A* **501** (2003) 418.

[94] PAMELA collaboration, *The PAMELA experiment in space*, *Nucl. Instrum. Meth. A* **461** (2001) 262.

[95] Pierre Auger collaboration, *The Pierre Auger Cosmic Ray Observatory*, *Nucl. Instrum. Meth. A* **798** (2015) 172 [1502.01323].

[96] Fermi-LAT collaboration, *The Large Area Telescope on the Fermi Gamma-ray Space Telescope Mission*, *Astrophys. J.* **697** (2009) 1071 [0902.1089].

[97] H.E.S.S. collaboration, *The Status of the H.E.S.S. project*, *New Astron. Rev.* **48** (2004) 331 [astro-ph/0403052].

[98] AMS collaboration, *The Alpha Magnetic Spectrometer (AMS)*, *Nucl. Instrum. Meth. A* **478** (2002) 119.

[99] AMS 02 collaboration, *The antimatter spectrometer (AMS-02): A particle physics detector in space*, *Nucl. Instrum. Meth. A* **588** (2008) 227.

[100] G. R. Blumenthal, S. M. Faber, J. R. Primack and M. J. Rees, *Formation of Galaxies and Large Scale Structure with Cold Dark Matter*, *Nature* **311** (1984) 517.

[101] J. S. Bullock, T. S. Kolatt, Y. Sigad, R. S. Somerville, A. V. Kravtsov, A. A. Klypin et al., *Profiles of dark haloes. Evolution, scatter, and environment*, *Mon. Not. Roy. Astron. Soc.* **321** (2001) 559 [astro-ph/9908159].

[102] A. J. Benson, A. Farahi, S. Cole, L. A. Moustakas, A. Jenkins, M. Lovell et al., *Dark Matter Halo Merger Histories Beyond Cold Dark Matter: I - Methods and Application to Warm Dark Matter*, *Mon. Not. Roy. Astron. Soc.* **428** (2013) 1774 [1209.3018].

[103] M. R. Lovell, C. S. Frenk, V. R. Eke, A. Jenkins, L. Gao and T. Theuns, *The properties of warm dark matter haloes*, *Mon. Not. Roy. Astron. Soc.* **439** (2014) 300 [1308.1399].

[104] R. Kennedy, C. Frenk, S. Cole and A. Benson, *Constraining the warm dark matter particle mass with Milky Way satellites*, *Mon. Not. Roy. Astron. Soc.* **442** (2014) 2487 [1310.7739].

[105] S. D. McDermott, H.-B. Yu and K. M. Zurek, *Turning off the Lights: How Dark is Dark Matter?*, *Phys. Rev. D* **83** (2011) 063509 [1011.2907].

[106] F. J. Sanchez-Salcedo, E. Martinez-Gomez and J. Magana, *On the fraction of dark matter in charged massive particles (CHAMPs)*, *JCAP* **02** (2010) 031 [1002.3145].

[107] B. Audren, J. Lesgourgues, G. Mangano, P. D. Serpico and T. Tram, *Strongest model-independent bound on the lifetime of Dark Matter*, *JCAP* **12** (2014) 028 [1407.2418].

[108] F. S. Queiroz and K. Sinha, *The Poker Face of the Majoron Dark Matter Model: LUX to keV Line*, *Phys. Lett. B* **735** (2014) 69 [1404.1400].

[109] M. G. Baring, T. Ghosh, F. S. Queiroz and K. Sinha, *New Limits on the Dark Matter Lifetime from Dwarf Spheroidal Galaxies using Fermi-LAT*, *Phys. Rev. D* **93** (2016) 103009 [1510.00389].

[110] Y. Mambrini, S. Profumo and F. S. Queiroz, *Dark Matter and Global Symmetries*, *Phys. Lett. B* **760** (2016) 807 [1508.06635].

[111] G. Giesen, M. Boudaud, Y. Génolini, V. Poulin, M. Cirelli, P. Salati et al., *AMS-02 antiprotons, at last! Secondary astrophysical component and immediate implications for Dark Matter*, *JCAP* **09** (2015) 023 [1504.04276].

[112] B.-Q. Lu and H.-S. Zong, *Limits on dark matter from AMS-02 antiproton and positron fraction data*, *Phys. Rev. D* **93** (2016) 103517 [1510.04032].

[113] T. R. Slatyer and C.-L. Wu, *General Constraints on Dark Matter Decay from the Cosmic Microwave Background*, *Phys. Rev. D* **95** (2017) 023010 [1610.06933].

[114] H.-B. Jin, Y.-L. Wu and Y.-F. Zhou, *Astrophysical background and dark matter implication based on latest AMS-02 data*, *Astrophys. J.* **901** (2020) 80 [1701.02213].

[115] D. Scott, *The standard model of cosmology: A skeptic's guide*, *Proc. Int. Sch. Phys. Fermi* **200** (2020) 133 [1804.01318].

[116] A. Del Popolo and M. Le Delliou, *Small scale problems of the ΛCDM model: a short review*, *Galaxies* **5** (2017) 17 [1606.07790].

[117] D. N. Spergel and P. J. Steinhardt, *Observational evidence for selfinteracting cold dark matter*, *Phys. Rev. Lett.* **84** (2000) 3760 [astro-ph/9909386].

[118] J. L. Feng, *Dark Matter Candidates from Particle Physics and Methods of Detection*, *Ann. Rev. Astron. Astrophys.* **48** (2010) 495 [1003.0904].

[119] M. Trodden and S. M. Carroll, *TASI lectures: Introduction to cosmology*, in *Theoretical Advanced Study Institute in Elementary Particle Physics (TASI 2002): Particle Physics and Cosmology: The Quest for Physics Beyond the Standard Model(s)*, pp. 703–793, 1, 2004, astro-ph/0401547.

[120] D. Hooper, *Particle Dark Matter*, in *Theoretical Advanced Study Institute in Elementary Particle Physics: The Dawn of the LHC Era*, pp. 709–764, 2010, 0901.4090, DOI.

[121] P. Gondolo and G. Gelmini, *Cosmic abundances of stable particles: Improved analysis*, *Nucl. Phys. B* **360** (1991) 145.

[122] M. Srednicki, R. Watkins and K. A. Olive, *Calculations of Relic Densities in the Early Universe*, *Nucl. Phys. B* **310** (1988) 693.

[123] J. D. Wells, *Annihilation cross-sections for relic densities in the low velocity limit*, hep-ph/9404219.

[124] L. Roszkowski, *A Simple way of calculating cosmological relic density*, *Phys. Rev. D* **50** (1994) 4842 [hep-ph/9404227].

[125] K. Griest and D. Seckel, *Three exceptions in the calculation of relic abundances*, *Phys. Rev. D* **43** (1991) 3191.

[126] J. D. Wells, *Mass density of neutralino dark matter*, *Adv. Ser. Direct. High Energy Phys.* **21** (2010) 269 [hep-ph/9708285].

[127] J. Edsjo and P. Gondolo, *Neutralino relic density including coannihilations*, *Phys. Rev. D* **56** (1997) 1879 [hep-ph/9704361].

[128] H. Acaroğlu, M. Blanke, J. Heisig, M. Krämer, M. Mühlleitner and L. Rathmann, *Phenomenological Details of Flavoured Majorana Dark Matter*, *in preparation* (2023) .

[129] H. Acaroğlu and M. Blanke, *Tasting flavoured Majorana dark matter*, *JHEP* **05** (2022) 086 [2109.10357].

[130] G. Jungman, M. Kamionkowski and K. Griest, *Supersymmetric dark matter*, *Phys. Rept.* **267** (1996) 195 [hep-ph/9506380].

[131] H. Führ and Z. Rzeszotnik, *A note on factoring unitary matrices*, *Linear Algebra and its Applications* **547** (2018) 32.

[132] M. Blanke, A. J. Buras, A. Poschenrieder, S. Recksiegel, C. Tarantino, S. Uhlig et al., *Another look at the flavour structure of the littlest Higgs model with T-parity*, *Phys. Lett. B* **646** (2007) 253 [hep-ph/0609284].

[133] T. Takagi, *On an algebraic problem reluted to an analytic theorem of carathéodory and fejér and on an allied theorem of landau*, *Japanese journal of mathematics: transactions and abstracts* **1** (1924) 83.

[134] L. Autonne, *Sur les matrices hypohermitiennes et sur les matrices unitaires*, no. Bd. 38 in Annales de l'Université de Lyon: Sciences, médecine. J.-B. Baillière et fils, 1915.

[135] M. Papucci, A. Vichi and K. M. Zurek, *Monojet versus the rest of the world I: t-channel models*, *JHEP* **11** (2014) 024 [1402.2285].

[136] A. D. Martin, W. J. Stirling, R. S. Thorne and G. Watt, *Parton distributions for the LHC*, *Eur. Phys. J. C* **63** (2009) 189 [0901.0002].

[137] M. Blanke, P. Pani, G. Polesello and G. Rovelli, *Single-top final states as a probe of top-flavoured dark matter models at the LHC*, *JHEP* **01** (2021) 194 [2010.10530].

[138] T. Hurth and W. Porod, *Flavour violating squark and gluino decays*, *JHEP* **08** (2009) 087 [0904.4574].

[139] M. Blanke, G. F. Giudice, P. Paradisi, G. Perez and J. Zupan, *Flavoured Naturalness*, *JHEP* **06** (2013) 022 [1302.7232].

[140] P. Agrawal and C. Frugiuele, *Mixing stops at the LHC*, *JHEP* **01** (2014) 115 [1304.3068].

[141] M. Arana-Catania, S. Heinemeyer and M. J. Herrero, *Updated Constraints on General Squark Flavor Mixing*, *Phys. Rev. D* **90** (2014) 075003 [1405.6960].

[142] M. Backović, A. Mariotti and M. Spannowsky, *Signs of Tops from Highly Mixed Stops*, *JHEP* **06** (2015) 122 [1504.00927].

[143] M. Blanke, B. Fuks, I. Galon and G. Perez, *Gluino Meets Flavored Naturalness*, *JHEP* **04** (2016) 044 [1512.03813].

[144] CMS collaboration, *Searches for physics beyond the standard model with the M_{T2} variable in hadronic final states with and without disappearing tracks in proton-proton collisions at $\sqrt{s} = 13$ TeV*, *Eur. Phys. J. C* **80** (2020) 3 [1909.03460].

[145] ATLAS collaboration, *Search for R-parity-violating supersymmetry in a final state containing leptons and many jets with the ATLAS experiment using $\sqrt{s} = 13TeV$ proton–proton collision data*, *Eur. Phys. J. C* **81** (2021) 1023 [2106.09609].

[146] CMS collaboration, *Search for supersymmetry in proton-proton collisions at 13 TeV in final states with jets and missing transverse momentum*, *JHEP* **10** (2019) 244 [1908.04722].

[147] A. Alloul, N. D. Christensen, C. Degrande, C. Duhr and B. Fuks, *FeynRules 2.0 - A complete toolbox for tree-level phenomenology*, *Comput. Phys. Commun.* **185** (2014) 2250 [1310.1921].

[148] C. Degrande, C. Duhr, B. Fuks, D. Grellscheid, O. Mattelaer and T. Reiter, *UFO - The Universal FeynRules Output*, *Comput. Phys. Commun.* **183** (2012) 1201 [1108.2040].

[149] J. Alwall, R. Frederix, S. Frixione, V. Hirschi, F. Maltoni, O. Mattelaer et al., *The automated computation of tree-level and next-to-leading order differential cross sections, and their matching to parton shower simulations*, *JHEP* **07** (2014) 079 [1405.0301].

[150] CMS collaboration, *Search for physics beyond the standard model in events with jets and two same-sign or at least three charged leptons in proton-proton collisions at $\sqrt{s} = 13$ TeV*, *Eur. Phys. J. C* **80** (2020) 752 [2001.10086].

[151] G. Buchalla, A. J. Buras and M. E. Lautenbacher, *Weak decays beyond leading logarithms*, *Rev. Mod. Phys.* **68** (1996) 1125 [hep-ph/9512380].

[152] A. J. Buras, *Weak Hamiltonian, CP violation and rare decays*, in *Les Houches Summer School in Theoretical Physics, Session 68: Probing the Standard Model of Particle Interactions*, pp. 281–539, 6, 1998, hep-ph/9806471.

[153] ATLAS collaboration, *Search for flavour-changing neutral currents in processes with one top quark and a photon using 81 fb^{-1} of pp collisions at $\sqrt{s} = 13$ TeV with the ATLAS experiment*, *Phys. Lett. B* **800** (2020) 135082 [1908.08461].

[154] A. Crivellin and M. Davidkov, *Do squarks have to be degenerate? Constraining the mass splitting with Kaon and D mixing*, *Phys. Rev. D* **81** (2010) 095004 [1002.2653].

[155] N. Carrasco et al., *$D^0 - \bar{D}^0$ mixing in the standard model and beyond from N_f =2 twisted mass QCD*, *Phys. Rev. D* **90** (2014) 014502 [1403.7302].

[156] Flavour Lattice Averaging Group collaboration, *FLAG Review 2019: Flavour Lattice Averaging Group (FLAG)*, *Eur. Phys. J. C* **80** (2020) 113 [1902.08191].

[157] A. J. Buras, S. Jager and J. Urban, *Master formulae for Delta F=2 NLO QCD factors in the standard model and beyond*, *Nucl. Phys. B* **605** (2001) 600 [hep-ph/0102316].

[158] Particle Data Group collaboration, *Review of Particle Physics*, *PTEP* **2020** (2020) 083C01.

[159] HFLAV collaboration, *Averages of b-hadron, c-hadron, and τ-lepton properties as of 2018*, *Eur. Phys. J. C* **81** (2021) 226 [1909.12524].

[160] I. I. Bigi, M. Blanke, A. J. Buras and S. Recksiegel, *CP Violation in D0 - anti-D0 Oscillations: General Considerations and Applications to the Littlest Higgs Model with T-Parity*, *JHEP* **07** (2009) 097 [0904.1545].

[161] A. A. Petrov, *Long-distance effects in charm mixing*, in *6th International Workshop on Charm Physics*, 12, 2013, 1312.5304.

[162] G. Steigman, B. Dasgupta and J. F. Beacom, *Precise Relic WIMP Abundance and its Impact on Searches for Dark Matter Annihilation*, *Phys. Rev. D* **86** (2012) 023506 [1204.3622].

[163] G. Steigman, *CMB Constraints On The Thermal WIMP Mass And Annihilation Cross Section*, *Phys. Rev. D* **91** (2015) 083538 [1502.01884].

[164] M. Garny, A. Ibarra and S. Vogl, *Signatures of Majorana dark matter with t-channel mediators*, *Int. J. Mod. Phys. D* **24** (2015) 1530019 [1503.01500].

[165] K. A. Mohan, D. Sengupta, T. M. P. Tait, B. Yan and C. P. Yuan, *Direct detection and LHC constraints on a t-channel simplified model of Majorana dark matter at one loop*, *JHEP* **05** (2019) 115 [1903.05650].

[166] J. Herrero-Garcia, E. Molinaro and M. A. Schmidt, *Dark matter direct detection of a fermionic singlet at one loop*, *Eur. Phys. J. C* **78** (2018) 471 [1803.05660].

[167] D. G. Cerdeño, A. Cheek, P. Martín-Ramiro and J. M. Moreno, *B anomalies and dark matter: a complex connection*, *Eur. Phys. J. C* **79** (2019) 517 [1902.01789].

[168] M. Drees, M. M. Nojiri, D. P. Roy and Y. Yamada, *Light Higgsino dark matter*, *Phys. Rev. D* **56** (1997) 276 [hep-ph/9701219].

[169] A. Djouadi, M. Drees, P. Fileviez Perez and M. Muhlleitner, *Loop induced Higgs and Z boson couplings to neutralinos and implications for collider and dark matter searches*, *Phys. Rev. D* **65** (2002) 075016 [hep-ph/0109283].

[170] M. Freytsis and Z. Ligeti, *On dark matter models with uniquely spin-dependent detection possibilities*, *Phys. Rev. D* **83** (2011) 115009 [1012.5317].

[171] M. Drees and M. Nojiri, *Neutralino - nucleon scattering revisited*, *Phys. Rev. D* **48** (1993) 3483 [hep-ph/9307208].

[172] J. Hisano, K. Ishiwata and N. Nagata, *Gluon contribution to the dark matter direct detection*, *Phys. Rev. D* **82** (2010) 115007 [1007.2601].

[173] R. J. Hill and M. P. Solon, *Standard Model anatomy of WIMP dark matter direct detection I: weak-scale matching*, *Phys. Rev. D* **91** (2015) 043504 [1401.3339].

[174] R. J. Hill and M. P. Solon, *Standard Model anatomy of WIMP dark matter direct detection II: QCD analysis and hadronic matrix elements*, *Phys. Rev. D* **91** (2015) 043505 [1409.8290].

[175] K. G. Chetyrkin, J. H. Kuhn and M. Steinhauser, *RunDec: A Mathematica package for running and decoupling of the strong coupling and quark masses*, *Comput. Phys. Commun.* **133** (2000) 43 [hep-ph/0004189].

[176] PICO collaboration, *PICO-60 Results and PICO-40L Status*, *J. Phys. Conf. Ser.* **1468** (2020) 012043.

[177] XENON collaboration, *Dark Matter Search Results from a One Ton-Year Exposure of XENON1T*, *Phys. Rev. Lett.* **121** (2018) 111302 [1805.12562].

[178] A. Khodjamirian and A. A. Petrov, *Direct CP asymmetry in $D \to \pi^-\pi^+$ and $D \to K^-K^+$ in QCD-based approach*, *Phys. Lett. B* **774** (2017) 235 [1706.07780].

[179] J. Brod, A. L. Kagan and J. Zupan, *Size of direct CP violation in singly Cabibbo-suppressed D decays*, *Phys. Rev. D* **86** (2012) 014023 [1111.5000].

[180] Y. Grossman and S. Schacht, *The emergence of the $\Delta U = 0$ rule in charm physics*, *JHEP* **07** (2019) 020 [1903.10952].

[181] W. Altmannshofer, R. Primulando, C.-T. Yu and F. Yu, *New Physics Models of Direct CP Violation in Charm Decays*, *JHEP* **04** (2012) 049 [1202.2866].

[182] Y. Grossman, A. L. Kagan and Y. Nir, *New physics and CP violation in singly Cabibbo suppressed D decays*, *Phys. Rev. D* **75** (2007) 036008 [hep-ph/0609178].

[183] UTfit collaboration, *The 2004 UTfit collaboration report on the status of the unitarity triangle in the standard model*, *JHEP* **07** (2005) 028 [hep-ph/0501199].

[184] LHCb collaboration, *Measurement of the time-integrated CP asymmetry in $D^0 \to K^-K^+$ decays*, 2209.03179.

[185] G. Hiller, M. Jung and S. Schacht, *SU(3)-flavor anatomy of nonleptonic charm decays*, *Phys. Rev. D* **87** (2013) 014024 [1211.3734].

[186] Y. Grossman and D. J. Robinson, *SU(3) Sum Rules for Charm Decay*, *JHEP* **04** (2013) 067 [1211.3361].

[187] D. Pirtskhalava and P. Uttayarat, *CP Violation and Flavor SU(3) Breaking in D-meson Decays*, *Phys. Lett. B* **712** (2012) 81 [1112.5451].

[188] S. Schacht, *A U-Spin Anomaly in Charm CP Violation*, 2207.08539.

[189] H. Acaroğlu, P. Agrawal and M. Blanke, *Lepton-Flavoured Scalar Dark Matter in Dark Minimal Flavour Violation*, 2211.03809.

[190] Y. Bai and J. Berger, *Lepton Portal Dark Matter*, *JHEP* **08** (2014) 153 [1402.6696].

[191] C.-J. Lee and J. Tandean, *Lepton-Flavored Scalar Dark Matter with Minimal Flavor Violation*, *JHEP* **04** (2015) 174 [1410.6803].

[192] A. Hamze, C. Kilic, J. Koeller, C. Trendafilova and J.-H. Yu, *Lepton-Flavored Asymmetric Dark Matter and Interference in Direct Detection*, *Phys. Rev. D* **91** (2015) 035009 [1410.3030].

[193] J. Kawamura, S. Okawa and Y. Omura, *Current status and muon $g-2$ explanation of lepton portal dark matter*, *JHEP* **08** (2020) 042 [2002.12534].

[194] J. M. Cline, K. Kainulainen, P. Scott and C. Weniger, *Update on scalar singlet dark matter*, *Phys. Rev. D* **88** (2013) 055025 [1306.4710].

[195] ALEPH collaboration, *Search for charginos nearly mass degenerate with the lightest neutralino in e+ e- collisions at center-of-mass energies up to 209-GeV*, *Phys. Lett. B* **533** (2002) 223 [hep-ex/0203020].

[196] DELPHI collaboration, *Searches for supersymmetric particles in e+ e- collisions up to 208-GeV and interpretation of the results within the MSSM*, *Eur. Phys. J. C* **31** (2003) 421 [hep-ex/0311019].

[197] CMS collaboration, *Search for supersymmetry in final states with two oppositely charged same-flavor leptons and missing transverse momentum in proton-proton collisions at $\sqrt{s} = 13$ TeV*, *JHEP* **04** (2021) 123 [2012.08600].

[198] ATLAS collaboration, *Search for direct stau production in events with two hadronic τ-leptons in $\sqrt{s} = 13$ TeV pp collisions with the ATLAS detector*, *Phys. Rev. D* **101** (2020) 032009 [1911.06660].

[199] ATLAS collaboration, *Search for electroweak production of charginos and sleptons decaying into final states with two leptons and missing transverse momentum in $\sqrt{s} = 13$ TeV pp collisions using the ATLAS detector*, *Eur. Phys. J. C* **80** (2020) 123 [1908.08215].

[200] CMS collaboration, *Search for supersymmetric partners of electrons and muons in proton-proton collisions at $\sqrt{s} = 13$ TeV*, *Phys. Lett. B* **790** (2019) 140 [1806.05264].

[201] ATLAS collaboration, *Search for direct production of charginos, neutralinos and sleptons in final states with two leptons and missing transverse momentum in pp collisions at $\sqrt{s} = 8$ TeV with the ATLAS detector*, *JHEP* **05** (2014) 071 [1403.5294].

[202] J. Kersten, J.-h. Park, D. Stöckinger and L. Velasco-Sevilla, *Understanding the correlation between $(g-2)_\mu$ and $\mu \to e\gamma$ in the MSSM*, *JHEP* **08** (2014) 118 [1405.2972].

[203] J. Hisano, T. Moroi, K. Tobe and M. Yamaguchi, *Lepton flavor violation via right-handed neutrino Yukawa couplings in supersymmetric standard model*, *Phys. Rev. D* **53** (1996) 2442 [hep-ph/9510309].

[204] Z. Chacko and G. D. Kribs, *Constraints on lepton flavor violation in the MSSM from the muon anomalous magnetic moment measurement*, *Phys. Rev. D* **64** (2001) 075015 [hep-ph/0104317].

[205] MEG collaboration, *Search for the lepton flavour violating decay $\mu^+ \to e^+\gamma$ with the full dataset of the MEG experiment*, *Eur. Phys. J. C* **76** (2016) 434 [1605.05081].

[206] BaBar collaboration, *Searches for Lepton Flavor Violation in the Decays tau+- —> e+- gamma and tau+- —> mu+- gamma*, *Phys. Rev. Lett.* **104** (2010) 021802 [0908.2381].

[207] Belle collaboration, *Search for lepton-flavor-violating tau-lepton decays to $\ell\gamma$ at Belle*, *JHEP* **10** (2021) 19 [2103.12994].

[208] Muon g-2 collaboration, *Final Report of the Muon E821 Anomalous Magnetic Moment Measurement at BNL*, *Phys. Rev. D* **73** (2006) 072003 [hep-ex/0602035].

[209] D. Hanneke, S. Fogwell and G. Gabrielse, *New measurement of the electron magnetic moment and the fine structure constant*, *Phys. Rev. Lett.* **100** (2008) 120801.

[210] DELPHI collaboration, *Study of tau-pair production in photon-photon collisions at LEP and limits on the anomalous electromagnetic moments of the tau lepton*, *Eur. Phys. J. C* **35** (2004) 159 [hep-ex/0406010].

[211] ACME collaboration, *Improved limit on the electric dipole moment of the electron*, *Nature* **562** (2018) 355.

[212] Muon (g-2) collaboration, *An Improved Limit on the Muon Electric Dipole Moment*, *Phys. Rev. D* **80** (2009) 052008 [0811.1207].

[213] Belle collaboration, *Search for the electric dipole moment of the tau lepton*, *Phys. Lett. B* **551** (2003) 16 [hep-ex/0210066].

[214] J. Kopp, V. Niro, T. Schwetz and J. Zupan, *DAMA/LIBRA and leptonically interacting Dark Matter*, *Phys. Rev. D* **80** (2009) 083502 [0907.3159].

[215] D. V. Nguyen, D. Sarnaaik, K. K. Boddy, E. O. Nadler and V. Gluscevic, *Observational constraints on dark matter scattering with electrons*, *Phys. Rev. D* **104** (2021) 103521 [2107.12380].

[216] T. Toma, *Internal Bremsstrahlung Signature of Real Scalar Dark Matter and Consistency with Thermal Relic Density*, *Phys. Rev. Lett.* **111** (2013) 091301 [1307.6181].

[217] S. Tulin, H.-B. Yu and K. M. Zurek, *Three Exceptions for Thermal Dark Matter with Enhanced Annihilation to $\gamma\gamma$*, *Phys. Rev. D* **87** (2013) 036011 [1208.0009].

[218] AMS collaboration, *First Result from the Alpha Magnetic Spectrometer on the International Space Station: Precision Measurement of the Positron Fraction in Primary Cosmic Rays of 0.5–350 GeV*, *Phys. Rev. Lett.* **110** (2013) 141102.

[219] T. Bringmann, X. Huang, A. Ibarra, S. Vogl and C. Weniger, *Fermi LAT Search for Internal Bremsstrahlung Signatures from Dark Matter Annihilation*, *JCAP* **07** (2012) 054 [1203.1312].

[220] H.E.S.S. collaboration, *Search for Photon-Linelike Signatures from Dark Matter Annihilations with H.E.S.S.*, *Phys. Rev. Lett.* **110** (2013) 041301 [1301.1173].

[221] A. Ibarra, A. S. Lamperstorfer and J. Silk, *Dark matter annihilations and decays after the AMS-02 positron measurements*, *Phys. Rev. D* **89** (2014) 063539 [1309.2570].

[222] M. Tavakoli, I. Cholis, C. Evoli and P. Ullio, *Constraints on Dark Matter Annihilations from Diffuse Gamma-Ray Emission in the Galaxy*, *JCAP* **01** (2014) 017 [1308.4135].

[223] M. Garny, A. Ibarra, M. Pato and S. Vogl, *Internal bremsstrahlung signatures in light of direct dark matter searches*, *JCAP* **12** (2013) 046 [1306.6342].

[224] H. Acaroğlu, P. Agrawal and M. Blanke, *Flavoured* $(g-2)_\mu$ *with Dark Lepton Seasoning*, 2212.08142.

[225] T. Aoyama, M. Hayakawa, T. Kinoshita and M. Nio, *Complete Tenth-Order QED Contribution to the Muon g-2*, *Phys. Rev. Lett.* **109** (2012) 111808 [1205.5370].

[226] T. Aoyama, T. Kinoshita and M. Nio, *Theory of the Anomalous Magnetic Moment of the Electron*, *Atoms* **7** (2019) 28.

[227] A. Czarnecki, W. J. Marciano and A. Vainshtein, *Refinements in electroweak contributions to the muon anomalous magnetic moment*, *Phys. Rev. D* **67** (2003) 073006 [hep-ph/0212229].

[228] C. Gnendiger, D. Stöckinger and H. Stöckinger-Kim, *The electroweak contributions to* $(g-2)_\mu$ *after the Higgs boson mass measurement*, *Phys. Rev. D* **88** (2013) 053005 [1306.5546].

[229] M. Davier, A. Hoecker, B. Malaescu and Z. Zhang, *Reevaluation of the hadronic vacuum polarisation contributions to the Standard Model predictions of the muon* $g-2$ *and* $\alpha(m_Z^2)$ *using newest hadronic cross-section data*, *Eur. Phys. J. C* **77** (2017) 827 [1706.09436].

[230] A. Keshavarzi, D. Nomura and T. Teubner, *Muon* $g-2$ *and* $\alpha(M_Z^2)$*: a new data-based analysis*, *Phys. Rev. D* **97** (2018) 114025 [1802.02995].

[231] G. Colangelo, M. Hoferichter and P. Stoffer, *Two-pion contribution to hadronic vacuum polarization*, *JHEP* **02** (2019) 006 [1810.00007].

[232] M. Hoferichter, B.-L. Hoid and B. Kubis, *Three-pion contribution to hadronic vacuum polarization*, *JHEP* **08** (2019) 137 [1907.01556].

[233] M. Davier, A. Hoecker, B. Malaescu and Z. Zhang, *A new evaluation of the hadronic vacuum polarisation contributions to the muon anomalous magnetic moment and to* $\boldsymbol{\alpha(m_Z^2)}$, *Eur. Phys. J. C* **80** (2020) 241 [1908.00921].

[234] A. Keshavarzi, D. Nomura and T. Teubner, *$g-2$ of charged leptons, $\alpha(M_Z^2)$, and the hyperfine splitting of muonium*, *Phys. Rev. D* **101** (2020) 014029 [1911.00367].

[235] A. Kurz, T. Liu, P. Marquard and M. Steinhauser, *Hadronic contribution to the muon anomalous magnetic moment to next-to-next-to-leading order*, *Phys. Lett. B* **734** (2014) 144 [1403.6400].

[236] K. Melnikov and A. Vainshtein, *Hadronic light-by-light scattering contribution to the muon anomalous magnetic moment revisited*, *Phys. Rev. D* **70** (2004) 113006 [hep-ph/0312226].

[237] P. Masjuan and P. Sanchez-Puertas, *Pseudoscalar-pole contribution to the $(g_\mu - 2)$: a rational approach*, *Phys. Rev. D* **95** (2017) 054026 [1701.05829].

[238] G. Colangelo, M. Hoferichter, M. Procura and P. Stoffer, *Dispersion relation for hadronic light-by-light scattering: two-pion contributions*, *JHEP* **04** (2017) 161 [1702.07347].

[239] M. Hoferichter, B.-L. Hoid, B. Kubis, S. Leupold and S. P. Schneider, *Dispersion relation for hadronic light-by-light scattering: pion pole*, *JHEP* **10** (2018) 141 [1808.04823].

[240] A. Gérardin, H. B. Meyer and A. Nyffeler, *Lattice calculation of the pion transition form factor with $N_f = 2 + 1$ Wilson quarks*, *Phys. Rev. D* **100** (2019) 034520 [1903.09471].

[241] J. Bijnens, N. Hermansson-Truedsson and A. Rodríguez-Sánchez, *Short-distance constraints for the HLbL contribution to the muon anomalous magnetic moment*, *Phys. Lett. B* **798** (2019) 134994 [1908.03331].

[242] G. Colangelo, F. Hagelstein, M. Hoferichter, L. Laub and P. Stoffer, *Longitudinal short-distance constraints for the hadronic light-by-light contribution to $(g-2)_\mu$ with large-N_c Regge models*, *JHEP* **03** (2020) 101 [1910.13432].

[243] T. Blum, N. Christ, M. Hayakawa, T. Izubuchi, L. Jin, C. Jung et al., *Hadronic Light-by-Light Scattering Contribution to the Muon Anomalous Magnetic Moment from Lattice QCD*, *Phys. Rev. Lett.* **124** (2020) 132002 [1911.08123].

[244] G. Colangelo, M. Hoferichter, A. Nyffeler, M. Passera and P. Stoffer, *Remarks on higher-order hadronic corrections to the muon $g-2$*, *Phys. Lett. B* **735** (2014) 90 [1403.7512].

[245] CMS collaboration, *Search for new physics in the lepton plus missing transverse momentum final state in proton-proton collisions at $\sqrt{s} = 13$ TeV*, *JHEP* **07** (2022) 067 [2202.06075].

[246] ATLAS collaboration, *Search for a new heavy gauge boson resonance decaying into a lepton and missing transverse momentum in 36 fb^{-1} of pp collisions at $\sqrt{s} = 13$ TeV with the ATLAS experiment*, *Eur. Phys. J. C* **78** (2018) 401 [1706.04786].

[247] ATLAS collaboration, *Search for chargino–neutralino pair production in final states with three leptons and missing transverse momentum in $\sqrt{s} = 13$ TeV pp collisions with the ATLAS detector*, *Eur. Phys. J. C* **81** (2021) 1118 [2106.01676].

[248] G. Alguero, J. Heisig, C. K. Khosa, S. Kraml, S. Kulkarni, A. Lessa et al., *Constraining new physics with SModelS version 2*, *JHEP* **08** (2022) 068 [2112.00769].

[249] K. Cheung, O. C. W. Kong and J. S. Lee, *Electric and anomalous magnetic dipole moments of the muon in the MSSM*, *JHEP* **06** (2009) 020 [0904.4352].

[250] M. E. Pospelov and I. B. Khriplovich, *Electric dipole moment of the W boson and the electron in the Kobayashi-Maskawa model*, *Sov. J. Nucl. Phys.* **53** (1991) 638.

[251] M. Pospelov and A. Ritz, *Electric dipole moments as probes of new physics*, *Annals Phys.* **318** (2005) 119 [hep-ph/0504231].

[252] S. P. Martin and J. D. Wells, *Muon Anomalous Magnetic Dipole Moment in Supersymmetric Theories*, *Phys. Rev. D* **64** (2001) 035003 [hep-ph/0103067].

[253] T. Ibrahim and P. Nath, *CP Violation From Standard Model to Strings*, *Rev. Mod. Phys.* **80** (2008) 577 [0705.2008].

[254] ATLAS collaboration, *Observation of the $\gamma\gamma \to \tau\tau$ process in Pb+Pb collisions and constraints on the τ-lepton anomalous magnetic moment with the ATLAS detector*, 2204.13478.

[255] R. H. Parker, C. Yu, W. Zhong, B. Estey and H. Müller, *Measurement of the fine-structure constant as a test of the standard model*, *Science* **360** (2018) 191.

[256] T. Aoyama, T. Kinoshita and M. Nio, *Theory of the anomalous magnetic moment of the electron*, *Atoms* **7** (2019) .

[257] L. Morel, Z. Yao, P. Cladé and S. Guellati-Khélifa, *Determination of the fine-structure constant with an accuracy of 81 parts per trillion*, *Nature* **588** (2020) 61.

[258] T. Aoyama, M. Hayakawa, T. Kinoshita and M. Nio, *Tenth-Order QED Contribution to the Electron g-2 and an Improved Value of the Fine Structure Constant*, *Phys. Rev. Lett.* **109** (2012) 111807 [1205.5368].

[259] F. Giacchino, L. Lopez-Honorez and M. H. G. Tytgat, *Scalar Dark Matter Models with Significant Internal Bremsstrahlung*, *JCAP* **10** (2013) 025 [1307.6480].

[260] L. Bergstrom, T. Bringmann and J. Edsjo, *New Positron Spectral Features from Supersymmetric Dark Matter - a Way to Explain the PAMELA Data?*, *Phys. Rev. D* **78** (2008) 103520 [0808.3725].

[261] T. Bringmann, L. Bergstrom and J. Edsjo, *New Gamma-Ray Contributions to Supersymmetric Dark Matter Annihilation*, *JHEP* **01** (2008) 049 [0710.3169].

[262] P. Ciafaloni, M. Cirelli, D. Comelli, A. De Simone, A. Riotto and A. Urbano, *On the Importance of Electroweak Corrections for Majorana Dark Matter Indirect Detection*, *JCAP* **06** (2011) 018 [1104.2996].

[263] V. Barger, W.-Y. Keung and D. Marfatia, *Bremsstrahlung in dark matter annihilation*, *Phys. Lett. B* **707** (2012) 385 [1111.4523].

[264] A. Ibarra, T. Toma, M. Totzauer and S. Wild, *Sharp Gamma-ray Spectral Features from Scalar Dark Matter Annihilations*, *Phys. Rev. D* **90** (2014) 043526 [1405.6917].

[265] M. Cè et al., *Window observable for the hadronic vacuum polarization contribution to the muon $g-2$ from lattice QCD*, 2206.06582.

[266] S. Borsanyi et al., *Leading hadronic contribution to the muon magnetic moment from lattice QCD*, *Nature* **593** (2021) 51 [2002.12347].

[267] G. Colangelo, A. X. El-Khadra, M. Hoferichter, A. Keshavarzi, C. Lehner, P. Stoffer et al., *Data-driven evaluations of Euclidean windows to scrutinize hadronic vacuum polarization*, *Phys. Lett. B* **833** (2022) 137313 [2205.12963].

[268] C. Alexandrou et al., *Lattice calculation of the short and intermediate time-distance hadronic vacuum polarization contributions to the muon magnetic moment using twisted-mass fermions*, 2206.15084.

[269] A. Crivellin, M. Hoferichter, C. A. Manzari and M. Montull, *Hadronic Vacuum Polarization: $(g-2)_\mu$ versus Global Electroweak Fits*, *Phys. Rev. Lett.* **125** (2020) 091801 [2003.04886].

[270] A. Keshavarzi, W. J. Marciano, M. Passera and A. Sirlin, *Muon $g-2$ and $\Delta\alpha$ connection*, *Phys. Rev. D* **102** (2020) 033002 [2006.12666].

[271] G. Colangelo, M. Hoferichter and P. Stoffer, *Constraints on the two-pion contribution to hadronic vacuum polarization*, *Phys. Lett. B* **814** (2021) 136073 [2010.07943].

[272] P. Athron, C. Balázs, D. H. J. Jacob, W. Kotlarski, D. Stöckinger and H. Stöckinger-Kim, *New physics explanations of a_μ in light of the FNAL muon $g-2$ measurement*, *JHEP* **09** (2021) 080 [2104.03691].

[273] D. Stöckinger and H. Stöckinger-Kim, *On the role of chirality flips for the muon magnetic moment and its relation to the muon mass*, *Front. in Phys.* **10** (2022) 944614.